Dynamics of bright solitary matter-waves

Timothy Peter Wiles

A thesis submitted in partial fulfilment
of the requirements for the degree of
Doctor of Philosophy

Department of Physics
Durham University

June 27, 2013

Dynamics of bright solitary matter-waves

Timothy Peter Wiles

Abstract

This thesis describes the formation of a ^{85}Rb Bose-Einstein condensate and the subsequent creation of a bright solitary matter-wave in a quasi-one-dimensional optical waveguide, with experiments investigating the dynamics of a solitary wave in comparison with a repulsive Bose-Einstein condensate. In the final chapters of this thesis, progress towards the interaction of a solitary wave with a narrow barrier and an attractive atom–surface potential is presented.

Beyond the above, a review of recent soliton and solitary wave theory is presented from the perspective of an experimentalist, culminating in the numerical analysis of a variety of key areas, namely, quantum reflection, solitary wave size and solitary wave profile. The modelling and experimental results relating to the merging of ultracold gases of ^{85}Rb and ^{87}Rb, in order to create isotopic mixtures, is also described within this thesis. Such a scheme could be used as an initial step in the process of forming molecules or undertaking sympathetic cooling. Finally, the creation of a complex LabVIEW based experimental control system is also described within.

Declaration

I confirm that no part of the material offered has previously been submitted by myself for a degree in this or any other University. Where material has been generated through joint work, the work of others has been indicated.

Timothy Peter Wiles
Durham, June 27, 2013

For mum, who is now home, but still with me.
For dad, who continues with me on my walk.

Acknowledgements

The process of undertaking a PhD, and all that has happened outside of it, has been the most turbulent three-and-a-half years of my life. With that in mind, there are a great many people I have to thank, without whom this document would not exist. There are many more people that I would like to thank but I just can't fit them all here—I think my acknowledgements would be as long as my thesis! My apologies in advance to those.

Firstly I would like to thank Simon Cornish for providing the opportunity to work on the soliton project and for guidance throughout the PhD. Steve Hopkins has been a fount of all knowledge, particularly relating to all things electronic or practical. I have also really enjoyed getting to know him personally—maybe one day we'll finish The Planets Suite.

I would like to thank Charles Adams for co-supervising my PhD and the helpful discussions that we've had on a diverse range of topics. I would also like to thank Simon Gardiner for always having an open door to discuss theory related issues and for pastoral support during the PhD. I am forever indebted to Ifan Hughes for always finding the time to chat and discuss things relating to physics and life outside. He has helped keep me sane during a turbulent three-and-a-half years. I also thank the other AtMol staff members, Matt Jones, Kevin Weatherill, Robert Potvliege and David Carty for helpful discussions.

I have much to thank of my fellow Soliton Project members. I am grateful for the hard work Sylvi Händel did in setting up much of the experiment. I would like to thank Anna Marchant for the many careful hours put into the experiment to get it to the stage of producing beautiful ^{85}Rb BECs and solitary waves. I have enjoyed her company during the many hours of lab time and appreciate the helpful advice and guidance she has given on many occasions. Finally, I am pleased to see the experiment in the capable hands of Manfred Yu and it has been a pleasure to run the experiment with him over the last year or so. I look forward to seeing how things progress for the remainder of his PhD.

It has been great to get to know the current and former members of the other Cornish labs over the past three-and-a-half years. To Danny McCarron, Hung Wen Cho, Dan Jenkin, Michael Köppinger and Pete Moloney (Team Mixture) it has been great to enjoy your company and share many helpful discussions.

To Team YbCs, Kirsteen Butler and Stefan Kemp, I have enjoyed the many chats we've had and the help that you have given me in many different ways. I am delighted to know that DExTer is in such capable hands!

I have thoroughly enjoyed the time spent in the office with the three lads—particularly their sense of humour and generally light outlook on life. I've known Lee Weller throughout my time of undergraduate and postgraduate work at Durham and it has been a pleasure to get to know this fellow Welshman. I enjoyed many a chat with Dan Maxwell about the joys and perils of running a cold atom experiment. James Keaveney has been a great person to bounce many programming and physics related ideas off and he has helped get me more quickly to the right answer on many occasions because of this. To my extended office mate Chris Carr, I have always enjoyed our twice yearly catch-up!

I am very much indebted to Christoph Weiss, Tom Billam, Peter Mason, David Holdaway and John Helm, members of the AtMol soliton theory group, for many helpful discussions that have aided in my understanding of what should be going on under-the-hood.

I wish to thank all the other former and current members of AtMol for the supportive and encouraging environment and the many helpful discussions that have made my thesis all the more rich. Of these I would particularly like to thank Jon Pritchard, James Millen, Alfred Millett-Sikking, David Szwer, Christophe Vaillant and Rob Bettles.

Beyond AtMol I have to thank all the members of the mechanical workshop for their hard work in getting many things made for the experiment. I would particularly like to mention Stephen Lishman for always having the time to offer help and for his remarkable way of being able to slot new jobs in to get them done in good time, Malcolm Robertshaw for always being prepared to explain how I should actually be doing things and to Kevin Ring for his humour and encouragement on many occasions.

Outside of academic circles, there are many who have supported me—each in their unique way. When mum passed away, Melody Briggs and Edith Light went above and beyond the call of duty, constantly looking out for me and providing a place to chat and vent. The fact that both of them found the time to fit me in amongst everything that they already did (including looking after their own children) will continue to amaze me for many years to come. Iris Prizeman, Rhoda Clarke and Diana McKenzie have done the most wonderful job of *grandmothering* me—checking up on me every Sunday and having me round for wonderful roast dinners. I thank Mark Lovell, Mad Cockburn, Hazel White, Evelyn and Derek Paddon, Mark and Becca Dobie and family, Pete and Theresa Phillips and family, the Briggs family, the Light family and all those who have been part of the Neville's Cross cell group, for the caring evironment, supportive friendships and massively fun socials. For the promise of thesis cake and her excitment that simply could not be

bottled up, I thank Catherine Marsden. To all my extended family at King's Church Durham, I am so proud to be part of a church with such an inclusive atmosphere, diverse range of ages, backgrounds, disciplines and jobs, keeping Jesus at the centre of it all. Thank you to each of you who have had a part to play in the nearly eight years I've been in Durham. I'm just sorry I can't name you all!

Tom Judge has been like a brother to me for more than a year now and has supported me through ups and down. I'd like to thank him for many deep conversations, PhD support and motivation, always finding a way to make me laugh and for sharing in many good burgers. Dave Fisher has also been like a brother to me. I've thoroughly enjoyed the many hours of Call of Duty, Guitar Hero and Command and Conquer, interspersed amongst supportive conversation and friendship.

To Will Stanley and Stuart Baker, I am immensely thankful for your friendship and support over the years. When I came to university I thought I would make friends for life and the two of you are, without doubt, in that category. I am also particularly grateful to all my other friends that I made during my undergraduate degree and that I am still in touch with now. I would also like to make a special mention of Laura Harpin, who is no longer with us. Her enthusiam for life, her laugh and her kindness will never be forgotten—in fact I am sure her personality rubbed off onto everyone that she met.

To my long-distance-housemate Rialette Pretorius I am very grateful for her friendship and support, particularly over the past three years. I would also like to thank Elena Borodenko for her friendship, having a listening ear, always being encouraging with me and knowing exactly what to say to make me laugh out loud.

I wish to thank all of my extended family for their love and support, particularly during these last three years. I want to especially thank Aunty Sylvia and Aunty Valerie, who came all the way from Italy to Cardiff at such short notice to support me and my dad during our darkest days. I will never forget that. Also to Nicola Crews, I am very appreciative of the constant support she has given me over the past year or so.

To Nan and Grandad, my never ending thanks for everything you have done to support me throughout my entire life. I was pleased to know that at the end of school you would often be coming to pick me up to take me somewhere exciting and my years as a child were infinitely more rich because of you. You both have always believed in me, more than I believed in myself and this PhD is testament to your constant encouragement, even when things are so difficult for you. I hope that I have shown you how much I value all of this. If I can do just 10% of what you have done for me, for any grandchildren I might have, I think I'll be doing alright.

To Mum and Dad, I cannot think of how I could possibly have had a better upbringing than you provided for me. You included me in major decision making from a very young age, encouraged me to be honest and be myself and you loved me unconditionally. With this foundation you created an environment where I was allowed to choose what I wanted to do and try and be the best I could be.

Mum, you were my go-to person, someone I could always rely on to have a listening ear and to give extremely thoughtful and helpful advice. You were here at the start of this journey but didn't make it to the end, but I know you are in a better place. For now, I will miss you dearly—your sense of humour, kindness, smile, hugs and warmth, but I know I carry part of you in me. I just hope that as I continue to live, that I can share as much of your love and compassion with others as you showed to me.

Dad, for your wonderful example of how a father should be, I am immensely grateful. You are patient, always listening, providing advice where needed and always encouraging. I am proud to be your *favourite son* and hope that I can pass on the example you gave to me to any son or daughter that I have in the future. I look forward to sharing in this new chapter in your life.

Rev 7:9-17

Contents

List of Figures

List of Tables

Chapter 1

Introduction

1.1 Bose–Einstein condensation

1.1.1 The prediction

Through a novel derivation of Planck's radiation law by Bose [1], and in his collaboration with Einstein, the theory of integer spin particles, or bosons, was born. From their development of the Bose–Einstein distribution, a theoretical prediction of a new state of matter, the Bose–Einstein condensate (BEC), was proposed [2–4]. It was predicted that a transition to this state of matter would occur for a uniform system if the phase space density D_{ph} of an ideal gas reached a value of ≈ 2.612, where D_{ph} is given as [5]

$$D_{\mathrm{ph}} = n_0 \lambda_{\mathrm{dB}}^3, \tag{1.1}$$

where n_0 is the peak density of the particles and λ_{dB} is the deBroglie wavelength of the particles. For a harmonic trap, commonly used in experiments with ultracold atoms [6], we can substitute for n_0 and λ_{dB}, arriving at

$$D_{\mathrm{ph}} = N \left(\frac{\hbar \omega_{\mathrm{ho}}}{k_{\mathrm{B}} T} \right)^3, \tag{1.2}$$

where $\omega_{\mathrm{ho}} = (\omega_x \omega_y \omega_z)^{1/3}$, ω_x, ω_y and ω_z are the trap frequencies, N is the total number of atoms in the trap and k_{B} is Boltzmann's constant. Substituting in typical numbers ($10^4 < N < 10^7$, $2\pi \times 20 < \omega_{\mathrm{ho}} < 2\pi \times 1000$ Hz) one can obtain critical temperatures between microkelvin and tens of nanokelvin [6].

1.1.2 The first observations

Bose–Einstein condensation was first observed in 1995 by teams at JILA [7] and MIT [8] in clouds of ^{87}Rb and ^{23}Na respectively. In the same year a team at Rice University also presented evidence of the creation of an attractively interacting ^{7}Li BEC [9]. A later study [10, 11] found that they had, indeed, created a ^{7}Li BEC, although the atom number was actually 10^3 as opposed to the original estimate of 10^5. Following these observations, BECs have been created in a number of other elements (*e.g.* H [12], ^{4}He [13], ^{41}K [14] and ^{85}Rb [15]) and in molecules [16, 17]. A comprehensive list of created BECs can be found in [18]. The formation of condensates from a variety of different atomic species has enabled the observation of a wide array of fascinating phenomena [19–28]. There have also been a number of applications of BECs within the field of fundamental physics, such as probing atom–surface interactions [29] and slowing light to very low velocities [30].

As discovered by the group at Rice University, interactions play a very large role in the ability to create stable BECs of varying sizes. The inter-particle scattering length controls the magnitude and sign of interactions among particles that form a BEC; with repulsive interactions favouring the formation of a stable BEC and attractive interactions allowing the creation of solitary waves (see section 1.2).

1.1.3 Bose–Einstein condensation of ^{85}Rb

The scattering length and, hence, the strength and sign of the interactions among atoms within a condensate, was originally fixed in the first BEC experiments. It wasn't until 2000 that the first condensate with widely tunable interactions was formed and manipulated by Cornish *et al.* [15], following work by Gerton *et al.* [31]. By exploiting a Feshbach resonance [6] the condensate interaction energy and size could be adjusted, resulting in both attractive and repulsive interactions in a BEC. Cornish *et al.* observed the first glimpses of the collapse mechanism that would eventually result in the formation of solitons in later experiments.

1.2 Solitons and solitary waves

1.2.1 John Scott Russell and the Union Canal

The first recorded account of the observation of a solitary wave was by John Scott Russell in 1834. This first encounter is described here in his own words [32]:

> *'I was observing the motion of a boat which was rapidly drawn along a narrow channel by a pair of horses, when the boat suddenly stopped—not so the mass of water in the channel which it had put in motion; it accumulated round the prow of the vessel in a state of violent agitation, then suddenly leaving it behind, rolled forward with great velocity, assuming the form of a large solitary elevation, a rounded, smooth and well-defined heap of water, which continued its course along the channel apparently without change of form or diminution of speed. I followed it on horseback, and overtook it still rolling on at a rate of some eight or nine miles an hour, preserving its original figure some thirty feet long and a foot to a foot and a half in height. Its height gradually diminished, and after a chase of one or two miles I lost it in the windings of the channel. Such, in the month of August 1834, was my first chance interview with that singular and beautiful phenomenon which I have called the Wave of Translation.'*

Having been fascinated by the unusual properties of solitary waves, such as their apparent lack of dispersion, he studied them experimentally. This resulted in his *Report on Waves* in 1844 [32], the first experimental study of solitary waves.

Though John Scott Russell created a number of different categories of wave in his *Report on Waves*, one significant observation that he made was that solitary waves can be both positive (bright) and negative (dark). A bright solitary wave is a localised stable peak in density of the medium—a swell—while a dark solitary wave is a localised stable reduction in density of the medium—a dip.

1.2.2 Mathematical formulation

John Scott Russell's initial observations led to the theoretical study of solitary waves by Boussinesq, Rayleigh, Korteweg and de Vries [33, 34], although the terms *solitary wave* and *soliton* were not used at the time. Of the equations developed in these studies, the most commonly quoted is the Korteweg–de Vries (KdV) equation [35]

$$\frac{\partial u}{\partial t} + 6u\frac{\partial u}{\partial t} + \frac{\partial^3 u}{\partial x^3} = 0. \tag{1.3}$$

The term *soliton* was coined by Zabusky and Kruskal in 1965 [36]. In 1967 a method known as the inverse scattering transform was developed by Gardner *et al.* [37] which allowed the KdV equation to be analytically solved. This method was then used by Zakharov and Shabat to solve the nonlinear Schrödinger equation [38], demonstrating the flexibility of the inverse scattering transform in solving another nonlinear equation.

A soliton can be defined as a solitary wave that remains unscathed from binary collisions, up to shifts in phase and position [39]. Strictly speaking, a soliton solution of the KdV equation differs from the solitary waves observed in nature due to the fact that it is the solution of a nonlinear one-dimensional homogeneous equation. An example of a bright soliton solution of the KdV equation is of the form [35]

$$u(x,t) = \frac{V}{2}\,\mathrm{sech}^2\left[\frac{\sqrt{V}}{2}\,(x - Vt)\right], \tag{1.4}$$

where V describes the velocity of the soliton. One can see from (1.4), a soliton with a greater amplitude will consequently have a greater velocity.

Both (1.3) and (1.4) are dimensionless equations, as is evident from the terms within the sech^2 function of (1.4). The dimensionful KdV equation includes terms describing the water surface tension, viscosity, density and depth, as well as the acceleration due to gravity. As, at best, we can only create quasi-one-dimensional systems in our three-dimensional universe the soliton is a purely theoretical entity. The addition of two-dimensions results in the introduction of instabilities in the soliton (see section 2.2.7), based on its size. For clarity this less stable form will be referred to as a *solitary wave*, while

its one-dimensional counterpart will be referred to as a *soliton*. However, in literature the two terms are commonly used interchangeably.

1.2.3 Solitary waves and non-linear media

It wasn't until the 1970's that the study of solitons [40] started to unveil the possibilities of being able to exploit this physics for communication through optical fibres, described by the nonlinear Schrödinger equation. Since then, evidence of the manifestation of solitary waves, and collapse, has been found in such varied areas of nature as water, magnetism, optics, astronomy, the human body and even traffic flow [27, 28, 41–51].

1.2.4 Solitary waves in Bose–Einstein condensates

Experimental observations of soliton formation within a BEC occurred as early as 1999, with the formation of dark solitons via phase imprinting [25]. Interest has continued in this field since the first experiment [52–54]. However, if one wishes to produce bright solitons within a BEC, an entirely different process is necessary. By exploiting a Feshbach resonance, the s-wave scattering length, a, can be tuned from being positive to negative (repulsive to attractive interactions). This causes an instability in the condensate, resulting in an implosion and expulsion of relatively high energy atoms leaving a remnant, much like one observes with a supernova [26]. Hence, the process was given the name 'Bosenova'. The first observations of bright solitary waves occurred in 2002 by groups at Rice University [27] and ENS [28].

Detailed research has already been undertaken in order to characterize the collapse process and stability conditions of a condensate [55]. A later experiment studied the formation of solitary waves after the collapse and the situations in which single or multiple solitary waves can be observed [56]. More recently further theoretical research has been undertaken, using the GPE to simulate binary soliton collisions [57, 58]. These have highlighted the importance of the relative phase of the solitary waves during collisions. Within these areas there is still a significant amount of research required to understand the processes more fully. For example, the process by which multiple stable solitary waves form, which are out of phase with one another, has not been satisfactorily explained.

1.2.5 The JILA experiment

The work we wish to undertake in this project has its foundations in an experiment run in 2005 by Cornish *et al.* [56] in which solitary waves were created and studied in a three-dimensional trap geometry. They observed how the number of solitary waves formed was dependent on the number of atoms in the remnant resulting from the condensate collapse. This was an experimental confirmation of the critical number condition for a BEC [55].

The solitary waves created in the 2005 experiment were seen to oscillate for more than 3 seconds in the harmonic trap, without combining. It was postulated that this was due to repulsive interactions[1] between neighbouring solitary waves that kept this system stable, though there was no direct evidence of the necessary phase relationship between the solitary waves. We hope our continuation of this experiment will provide a greater insight into this possible phase dependence.

1.3 Motivation for this experiment

The broad aim of this experiment is to investigate the formation and dynamics of bright solitary waves created from a BEC of ^{85}Rb and their interaction with a solid surface. Experimental outcomes can be compared with predictions made via mean field theory and we aim to determine the validity of the Gross–Pitaevskii equation (GPE) (see chapter 2) in describing the observed dynamics. The motivation and main application of solitary wave–surface interactions are described in the grant proposal for this project [59]:

> *'This proposal aims to demonstrate the quantum reflection of solitons from a solid surface, as a first step towards measuring the atom–surface interaction. The use of well-localized solitons, coupled to the precise control of their velocity, has the potential to take the study of atom–surface interactions to a new level. Such studies are motivated by the possibility that precision measurements of atom–surface interactions may, in the future, set new limits on short range corrections to gravity due to exotic forces beyond the Standard model.'*

[1] As is necessary in the Gross–Pitaevskii equation framework.

1.3.1 Collapse and the formation of solitary waves

We aim to create a BEC of ^{85}Rb and exploit a Feshbach resonance to tune interparticle interactions from a stable repulsive state at BEC to an attractive state. This will cause a collapse of the atom cloud, resulting in an expulsion of atoms, or 'Bosenova'. This process leaves a stable remnant, the solitary wave, where the typical dispersive property of a wave-packet and the attractive interactions of the ^{85}Rb particles are balanced. We aim to study this collapse and the formation of solitary waves during this process.

1.3.2 Solitary wave dynamics

Once the mechanism for producing solitary waves is characterised, our aim is to release the solitary wave off-centre in a quasi-1D waveguide potential. This will enable us to demonstrate and study the stability of a propagating solitary wave as a number of different parameters are varied, such as scattering length and particle number. These results can then be compared with theoretical predictions.

1.3.3 Binary solitary wave collisions

Theoretical research within the framework of the GPE has been undertaken to try to understand the dynamics of solitary waves during binary collisions [57, 58]. These simulations noted the importance of the relative phase of the solitary waves during collisions. Where no phase difference was present unstable attractive interactions were observed and for a π phase difference stable repulsive interactions were observed. Multiple solitary wave creation with inferred repulsive interactions has been observed in one experiment [27], while multiple solitary wave stability over a few seconds, again with inferred repulsive interactions, has been observed in a later experiment [56]. However, no experimental evidence for a collision outcome dependent on phase has yet been observed; therefore, we intend to settle this debate by undertaking such binary collisions and determining the validity of these theoretical results.

1.3.4 Quantum reflection from a dielectric surface

A plane wave that is incident upon a simple attractive step potential has a probability of reflection expressed by [60]

$$R = \left(\frac{1 - \sqrt{1 - V_0/(E + V_0)}}{1 + \sqrt{1 - V_0/(E + V_0)}} \right), \tag{1.5}$$

where E is the energy of the incoming plane wave and V_0 is the depth of the potential step. What we can see by the above expression is that quantum reflection is maximised by reducing the incident energy of a plane wave (or particle) approaching an attractive potential [61]. Therefore, experiments have typically been undertaken with particles bombarding a surface at grazing angle, in order to reduce the velocity perpendicular to the surface (*e.g.* [62–64]), thus increasing the probability of observing quantum reflection. Typically the process can only be inferred by detecting how many particles return after a surface is bombarded with a 'beam' of these particles. Observing the dynamics of quantum reflection or tunnelling on a single-atom scale has not yet been possible. Other experiments have attempted to reflect BECs from a surface [65, 66], whose dynamics, in comparison with single atoms, can be clearly imaged. Unfortunately observing high reflection probabilities is very difficult in these cases, due to instabilities in the cloud during reflection. This instability is due to the dispersive properties of the BEC wavepacket and the lack of attractive interactions to maintain a constant shape of the cloud.

We propose that solitary waves created from a BEC of ^{85}Rb offer the exciting possibility of high reflection probabilities, without the same inherent instability, while being large enough to image during the process of reflection. We aim to transfer kinetic energy to a solitary wave via a velocity kick or an offset from the trap centre. It will then move towards the surface of a prism, shown in Fig. 1.1 (a) and (c). The dynamics and reflection probabilities of the subsequent interactions will be observed and compared with theoretical simulations. There will be the option of including an additional repulsive evanescent wave potential, allowing us to tune the height of a barrier that the soliton is incident upon, close to the surface, as shown in Fig. 1.1 (b). The presence of the barrier enables an unknown surface potential to be calculated (*e.g.* see [67]), although this is not the only method that can be used [68].

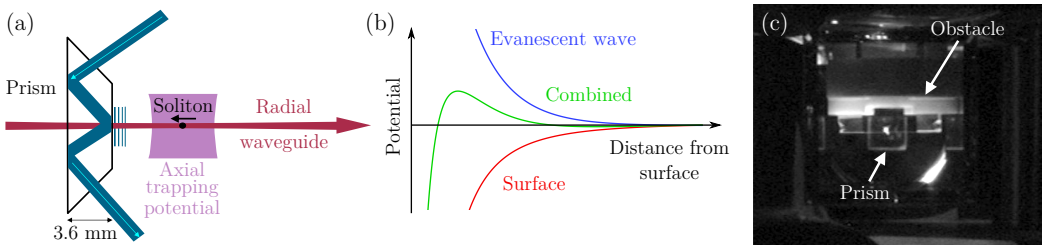

Figure 1.1: (a) (Adapted from [29]) A solitary wave incident upon a prism sees an attractive surface potential (see (b)), however, we also apply a blue detuned laser beam that undergoes total internal reflection. This creates a repulsive evanescent potential that can be adjusted to produce a combined potential with a variable barrier height for an incoming soliton to be incident upon, as shown in (b). (c) The obstacle and prism as viewed from the science cell.

1.4 Thesis context

This thesis is primarily concerned with the final stage of the production of a Bose–Einstein condensate, namely evaporation in an optical dipole trap, followed by the loading of this condensate into a one-dimensional waveguide to form a solitary wave. We investigate the dynamics of a solitary wave in the waveguide and the addition of an attractive barrier in an attempt to observe quantum reflection. The focus throughout this thesis is from the perspective of how to best observe predicted solitary wave phenomena in an experimental context. To this end we undertake an in-depth study of the cutting edge soliton and solitary wave theoretical research and explore parameter regimes available to us in the current manifestation of the experimental apparatus.

This thesis encompasses a time frame over which four postgraduate researchers have contributed to the development of the experimental apparatus and the results obtained. In order of succession, these researchers are Sylvi Händel (SH), Anna Marchant (ALM), the author (TPW) and Manfred Yu (MMHY). Throughout this thesis we will focus on the work undertaken by TPW, which has been varied throughout his time involved with the project. We now discuss the responsibilities of each of these researchers.

The construction of the laser cooling and transport apparatus, as well as the magnetic coils was undertaken by SH. Characterisation of the transport over the obstacle (see figure 1.1 (c)) was undertaken by TPW. All of the other initial stages of BEC production, such as the magneto-optical trap (MOT), magnetic transport and quadrupole trap evaporation, are described in detail in the thesis of SH [69] and will not be presented here. The development of

the MOT optical setup and optical dipole traps was undertaken by SH and ALM, along with optimisation of the apparatus resulting in the production of a ^{87}Rb condensate. During the above period TPW developed a basic 1D GPE code and investigated the dynamics of solitons incident upon a variety of localised potentials, resulting in a MPhys report [70]. TPW also took sole responsibility for the development of reliable experimental control hardware and software that forms the backbone of each experimental cycle.

Simulation of the merging of magnetic traps, in order to combine initially separate clouds of atoms, was undertaken by TPW. This resulted in an accurate but elegant analysis of a three-dimensional problem in one spatial dimension. SH undertook the experiments which confirmed the validity of this model. This work resulted in a publication [71].

Characterisation of the optical dipole trap in the lead-up to the production of a ^{85}Rb BEC was undertaken by ALM and TPW. The initial cooling of ^{85}Rb to degeneracy and the initial production and investigation of ^{85}Rb solitary waves was carried out by ALM; details of this can be found in [72]. The initial loading of the waveguide and its characterisation was achieved by TPW and MMHY. This lead to the production of ^{85}Rb solitary waves and their controlled reflection from a broad Gaussian barrier by ALM. Subsequent experiments on solitary waves, undertaken by TPW and MMHY, have focussed on their study for future interactions with narrow barriers. Optimisation of the experiment, including the loading of the waveguide, was undertaken by TPW while MMHY developed the apparatus for narrow barrier–solitary wave collisions. TPW and MMHY undertook the installation of the narrow attractive barrier and investigated its properties, with the aim of attempting to observe quantum reflection. TPW has also characterised a laser system that could be used to generate an evanescent wave potential, once solitary wave interactions with a surface become the main experimental focus.

Throughout the period in which the work in this thesis has been undertaken, TPW has also helped develop and improve software which analyses images of the ultracold clouds and software which simulates potentials generated by magnetic coils and dipole traps. Finally, having learned from the limitations of the initial experimental control system, TPW has developed an entirely new LabVIEW FPGA powered control system which will be implemented in the soliton experiment and two other experiments [73–76].

1.5 Thesis layout

Due to the eclectic nature of this thesis, various chapters have been grouped into parts as follows: part I contains chapter 2, focussing on the necessary background information required to understand the physics of interacting BECs and solitary waves, giving an insight into cutting edge research and providing details of expected regimes accessible to this experiment; details of the experimental set up are given in part II, which contains chapter 3, presenting a brief overview of the experimental apparatus to give context to the reader and chapter 4 giving a detailed explanation of the control hardware and software developed for this experiment; experiments undertaken by the author are presented in part III, where chapter 5 covers the merging of ultracold gases of ^{87}Rb and ^{85}Rb and chapter 6 investigates the properties of ^{85}Rb condensates and solitary waves; finally part IV presents work undertaken that we hope will eventually lead to the observation of intriguing solitary wave phenomena, such as interactions with a narrow barrier (chapter 7) and a surface (chapter 8), before concluding in chapter 9.

1.6 Publications arising from this work

S. Händel, T. P. Wiles, A. L. Marchant, S. A. Hopkins, C. S. Adams and S. L. Cornish, *Magnetic merging of ultracold atomic gases of ^{85}Rb and ^{87}Rb*, Phys. Rev. A **83**, 053633 (2011). [71]

A. L. Marchant, S. Händel, T. P. Wiles, S. A. Hopkins and S. L. Cornish, *Guided transport of ultracold gases of rubidium up to a room-temperature dielectric surface*, New J. Phys. **13**, 125003 (2011). [77]

S. Händel, A. L. Marchant, T. P. Wiles, S. A. Hopkins and S. L. Cornish, *Magnetic transport apparatus for the production of ultracold atomic gases in the vicinity of a dielectric surface*, Rev. Sci. Instrum. **83**, 013105 (2012). [78]

A. L. Marchant, S. Händel, S. A. Hopkins, T. P. Wiles and S. L. Cornish, *Bose-Einstein condensation of ^{85}Rb by direct evaporation in an optical dipole trap*, Phys. Rev. A **85**, 053647 (2012). [79]

A. L. Marchant, T. P. Billam, T. P. Wiles, M. M. H. Yu, S. A. Gardiner and S. L. Cornish, *Controlled formation and reflection of a bright solitary matter-wave*, Nat. Commun. **4**, 1865 (2013). [80]

Part I

Background material

Chapter 2

Bright soliton theory and experimental predictions

2.1 Introduction

This chapter presents an overview of the theoretical work undertaken in the field of bright solitons formed from Bose–Einstein condensates. This overview will encompass work undertaken in the last 50 years, with a large focus on more recent work from the last few years and is from the perspective of an experimentalist, with an aim to highlight key physical phenomena that could be observed in an experiment. As a result, some basic calculations are provided, as are parameter regimes for expected phenomena.

2.2 Review

Two main branches of research have been investigated by theoretical physicists when describing the dynamics of a dilute Bose gas, namely the mean-field and many-body theories. Solitons are interesting phenomena that can manifest themselves within a dilute Bose gas, and as such have been investigated using both of these approaches. This section presents the starting point for both theories, discusses their merits and disadvantages and presents key areas of research. For some of this section we closely follow the explanations given in [81].

2.2.1 The dilute Bose gas

Over the past 18 years since the first observation of Bose–Einstein condensation, many different degenerate quantum gases have been formed. The densities of these gases are typically $10^{13}\,\mathrm{cm}^{-3}$ – $10^{15}\,\mathrm{cm}^{-3}$. When comparing to the typical densities of air at room temperature and atmospheric pressure ($\sim 10^{19}\ \mathrm{cm}^{-3}$) and liquids or solids ($\sim 10^{22}\ \mathrm{cm}^{-3}$), it can be seen that this gas is very dilute [6].

In 1947 Bogoliubov presented the model of the weakly interacting Bose gas [82] when attempting to describe behaviour observed in superfluid helium. To be in a valid regime for this theory the gas must be dilute—mathematically expressed as $n|a|^3 \ll 1$, where n is the peak density of the BEC and a is the s–wave scattering length.

The Hamiltonian describing a system of weakly interacting Bose particles, in the occupation number representation of second quantisation, can be written as [81, 83]

$$\begin{aligned}\hat{H} = &\int d\mathbf{r}\ \hat{\Psi}^\dagger(\mathbf{r},t)\left[-\frac{\hbar^2}{2m}\nabla^2 + U(\mathbf{r},t)\right]\hat{\Psi}(\mathbf{r},t)\\ &+\frac{1}{2}\iint d\mathbf{r}\,d\mathbf{r}'\ \hat{\Psi}^\dagger(\mathbf{r},t)\hat{\Psi}^\dagger(\mathbf{r}',t)V(\mathbf{r}-\mathbf{r}')\hat{\Psi}(\mathbf{r}',t)\hat{\Psi}(\mathbf{r},t),\end{aligned} \tag{2.1}$$

where $-\hbar^2\nabla^2/(2m)$ is the kinetic energy operator, $U(\mathbf{r},t)$ is the operator describing any external potential the gas is exposed to and $V(\mathbf{r}-\mathbf{r}')$ is the exact two-body interatomic potential. $\hat{\Psi}^\dagger(\mathbf{r},t)$ and $\hat{\Psi}(\mathbf{r},t)$ are the creation and annihilation operators representing the addition or removal of a particle at point $\mathbf{r}$ in space and t in time.

It is important to note that this Hamiltonian is the basis for all theoretical treatments of dilute Bose gases, includes quantum fluctuations and can be used in formalisms that describe scenarios with thermal fluctuations [81].

2.2.2 The effective interaction potential

The interaction potential, $V(\mathbf{r}-\mathbf{r}')$, experienced by alkali-metal atoms consists of a short range repulsive core in addition to a longer range attractive van der Waals interaction. The combination of these two competing potentials is a complex potential giving rise to rich physics such as molecular bound states (see figure 2.1 (a)). Attempting to solve the Schrödinger equation for a Hamiltonian containing such a complex potential is unnecessary for an ultracold dilute Bose gas and has a number of disadvantages [84]:

1. The exact potential is very difficult to calculate. A small error in the potential can lead to a large error in the scattering length.

2. Bose condensed gases are in a metastable state. At experimental temperatures and densities the thermal equilibrium of the system would be solid. This is due to the presence of bound states of the potential with a binding energy much smaller than the temperature of the gas.

3. The potential cannot be treated in the Born approximation due to it being very repulsive at short distances and containing many bound states. Some mean-field approximations which neglect correlations between particles, due to interactions, are implicitly relying on the Born approximation. These cannot use the exact potential.

Instead of using the exact potential we can create an effective potential that greatly simplifies the problem. For the effective potential to be valid, two conditions must be true; the gas must be dilute to the extent that effectively only two-body scattering events occur[1] and the collisions must be low energy ($k \to 0$, where $\hbar k$ is the relative momentum of the colliding atoms). If these conditions are fulfilled we are only interested in the long range effect of the exact potential, which is to shift the phase of a quantum mechanical wavefunction (see figure 2.1 (b)). The effective potential can produce exactly the same result; therefore, for a single atomic species the interaction is only dependent on one parameter; the s-wave scattering length, a. An explanation of the origins of the scattering length is given in figure 2.1 (b-f). The form of

[1] In other words, we are only interested in the asymptotic result of a collision and not the actual dynamics of the collision itself.

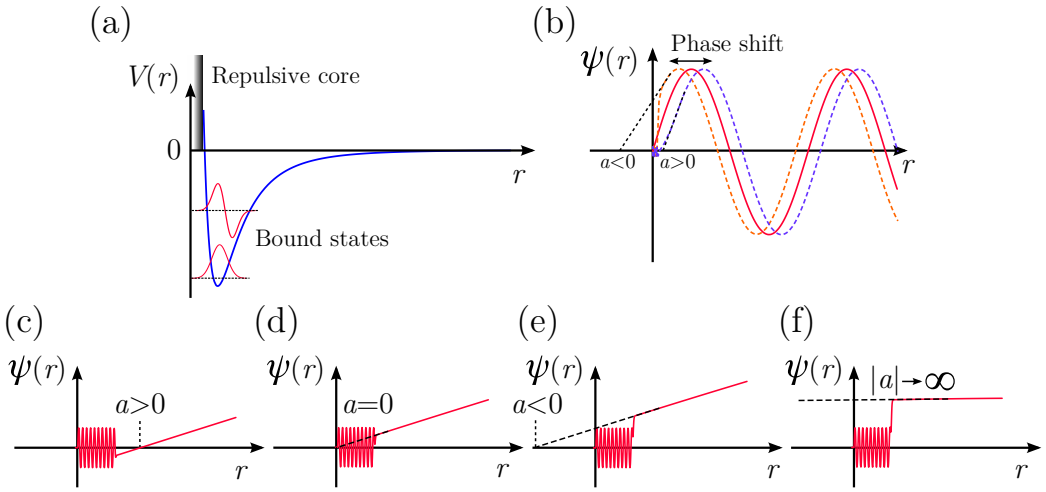

Figure 2.1: Schematic of the interatomic potential and the origin of scattering length. (a) The exact interatomic potential consists of a strong short range repulsive core, due to repulsion of electron clouds, with the addition of a long range attractive interaction, due to a combination of the van der Waals interaction and covalent bonding. In alkali-metal atoms the potential can support many bound states. (b) The presence of bound states can introduce a positive or negative phase shift in the asymptotic wavefunction of a free particle, resulting in a positive or negative a, determined by extrapolating the free particle wavefunction just before it reaches the interparticle potential well. (c-f) Scattering lengths that are positive (repulsive) (c), zero (non-interacting) (d), negative (attractive) (e) and approaching ∞ (strongly repulsive/attractive) (f) can be produced by moving bound states into and out of the potential well. $|a| \to \infty$ when the bound state is on resonance with the free particle collision energy. Small changes in the interatomic potential can have a large effect on a.

this effective contact interaction potential is a variable strength delta function at the origin[2] [81]

$$V(\mathbf{r}-\mathbf{r}') = g\delta(\mathbf{r}-\mathbf{r}'), \tag{2.2}$$

where

$$g = \frac{4\pi\hbar^2 a}{m}, \tag{2.3}$$

is the strength of the interaction. Using the effective potential model, when two atoms collide they will undergo a perfectly elastic collision. By substituing (2.2) into (2.1) we achieve a new simplified Hamiltonian

$$\begin{aligned}\hat{H} = &\int d\mathbf{r}\ \hat{\Psi}^\dagger(\mathbf{r},t)\left[-\frac{\hbar^2}{2m}\nabla^2 + U(\mathbf{r},t)\right]\hat{\Psi}(\mathbf{r},t)\\ &+\frac{g}{2}\int d\mathbf{r}\ \hat{\Psi}^\dagger(\mathbf{r},t)\hat{\Psi}^\dagger(\mathbf{r},t)\hat{\Psi}(\mathbf{r},t)\hat{\Psi}(\mathbf{r},t).\end{aligned} \tag{2.4}$$

What we ultimately want to be able to determine is how the field operator $\hat{\Psi}(\mathbf{r},t)$, or system, evolves with respect to space and time. In the Heisenberg picture, where the time dependence is contained within the operators [85], the equation of motion for the field operator is

$$\begin{aligned}\mathrm{i}\hbar\frac{\partial\hat{\Psi}(\mathbf{r},t)}{\partial t} &= \left[\hat{\Psi}(\mathbf{r},t),\hat{H}\right]\\ &= \left(-\frac{\hbar^2}{2m}\nabla^2 + U(\mathbf{r},t)\right)\hat{\Psi}(\mathbf{r},t) + g\,\hat{\Psi}^\dagger(\mathbf{r},t)\hat{\Psi}(\mathbf{r},t)\hat{\Psi}(\mathbf{r},t).\end{aligned} \tag{2.5}$$

2.2.3 Separating condensate and non-condensate fractions

As we are modelling a Bose–Einstein condensate, we have a macroscopic occupation of the lowest energy state of the system. As a result it now makes sense to split the field operator, $\hat{\Psi}(\mathbf{r},t)$, into an orthogonal basis of an operator representing the condensate, $\hat{\phi}(\mathbf{r},t)$, and another representing the non-condensed fraction, $\hat{\delta}(\mathbf{r},t)$,

$$\hat{\Psi}(\mathbf{r},t) = \hat{\phi}(\mathbf{r},t) + \hat{\delta}(\mathbf{r},t). \tag{2.6}$$

[2]Where this transformation is sufficient for the form of the wavefunction we are concerned with.

We can separate the operator from the wavefunction describing the condensate and other excited states,

$$\hat{\phi}(\mathbf{r},t) = \hat{a}_0(t)\varphi_0(\mathbf{r},t), \qquad \hat{\delta}(\mathbf{r},t) = \sum_{i\neq 0} \hat{a}_i(t)\varphi_i(\mathbf{r},t). \tag{2.7}$$

$\hat{a}_0^\dagger$ and $\hat{a}_0$ are the creation and annihilation operators for the condensate fraction, with the properties,

$$\hat{a}_0^\dagger \left|N_0\right\rangle = \sqrt{N_0+1}\left|N_0+1\right\rangle, \qquad \hat{a}_0 \left|N_0\right\rangle = \sqrt{N_0}\left|N_0-1\right\rangle. \tag{2.8}$$

In order to determine the number of atoms in the condensate one applies the number operator $\hat{N}_0\left|N_0\right\rangle = \hat{a}_0^\dagger\hat{a}_0\left|N_0\right\rangle = N_0\left|N_0\right\rangle$. If $N_0 \gg 1$ then $N_0+1 \approx N_0$, therefore, the effect of applying $\hat{a}_0^\dagger\hat{a}_0$ is approximately the same as applying $\hat{a}_0\hat{a}_0^\dagger$; resulting in the effect of applying $\hat{a}_0^\dagger$ being approximately the same as $\hat{a}_0$, which is the c-number approximation [86]. We are effectively stating that as the condensate number increases the operators $\hat{a}_0^\dagger$ and $\hat{a}_0$ approach a limit where they commute. If $\hat{a}_0^\dagger \approx \hat{a}_0$ and $\hat{a}_0^\dagger\hat{a}_0\left|N_0\right\rangle = N_0\left|N_0\right\rangle$, then in this approximation $\hat{a}_0^\dagger, \hat{a}_0 \approx \sqrt{N_0}$. As a result of this we can replace the operator $\hat{\phi}(\mathbf{r},t)$ with the complex number $\phi(\mathbf{r},t) = \sqrt{N_0}\varphi_0(\mathbf{r},t)$ and rewrite equation (2.6) as

$$\hat{\Psi}(\mathbf{r},t) = \phi(\mathbf{r},t) + \hat{\delta}(\mathbf{r},t). \tag{2.9}$$

The experimentalist is most interested in quantities that can be measured; wavefunctions and field operators will not be the main focus here. Instead, atom density is a quantity that is readily measureable and can be expressed as [81]

$$n(\mathbf{r},t) = \langle\hat{\Psi}^\dagger(\mathbf{r},t)\hat{\Psi}(\mathbf{r},t)\rangle = n_c(\mathbf{r},t) + \tilde{n}(\mathbf{r},t). \tag{2.10}$$

As the condensate is now represented by a complex number, the condensate density is simply $n_c(\mathbf{r},t) = |\phi(\mathbf{r},t)|^2$. The simplest mean-field Gross–Pitaevskii formulation (see section 2.2.4) [87, 88] is essentially just interested in this quantity, whereas extensions to this formalism will also take account of the non-condensate density, $\tilde{n}(\mathbf{r},t) = \langle\hat{\delta}^\dagger(\mathbf{r},t)\hat{\delta}(\mathbf{r},t)\rangle$, to varying degrees of approximation. The specifics of these extensions are outside the scope of this thesis, however, we refer the reader to a wide variety of theoretical approaches taking account of the non-condensate density [89–99].

2.2.4 The Gross–Pitaevskii equation

We can take a zeroth order approximation by assuming that all of the atoms in a system are in the condensate, with negligible fluctuations in the non-condensate; meaning that $T \to 0$. In this situation $\hat{\Psi}(\mathbf{r},t) \to \phi(\mathbf{r},t)$ and $\hat{\Psi}^{\dagger}(\mathbf{r},t) \to \phi^{*}(\mathbf{r},t)$. The many-body dynamics of the system have now been approximated by that of a single wavefunction, with nonlinearity encapsulated in one term—we have undertaken a mean-field approach—and the result is the Gross–Pitaevskii equation (GPE) [100],

$$\mathrm{i}\hbar\frac{\partial\phi\left(\mathbf{r},t\right)}{\partial t} = \left[-\frac{\hbar^{2}}{2m}\nabla^{2} + U\left(\mathbf{r},t\right) + g\left|\phi\left(\mathbf{r},t\right)\right|^{2}\right]\phi\left(\mathbf{r},t\right). \tag{2.11}$$

The GPE has been shown to produce a good approximation to dynamics observed in a BEC in a number of scenarios up to a temperature of $T \approx T_{c}/2$ [81].

If one wishes to find stationary state solutions to the GPE, such as the ground state of a particular trap potential, it is possible to eliminate any time dependence from the GPE by separating the spatial and temporal parts of the wavefunction,

$$\phi(\mathbf{r},t) = \phi_{\mathrm{s}}(\mathbf{r})\exp\left(-\frac{\mathrm{i}\mu t}{\hbar}\right), \tag{2.12}$$

where μ is the chemical potential (the energy required to add or remove a particle from the system). By substituting (2.12) into (2.11) we arrive at the time-independent GPE,

$$\mu\phi_{\mathrm{s}}\left(\mathbf{r}\right) = \left[-\frac{\hbar^{2}}{2m}\nabla^{2} + U\left(\mathbf{r}\right) + g\left|\phi_{\mathrm{s}}\left(\mathbf{r}\right)\right|^{2}\right]\phi_{\mathrm{s}}\left(\mathbf{r}\right). \tag{2.13}$$

It is possible to calculate the total energy of this system by taking the Gross-Pitaevskii energy functional and integrating over all space [101, 102],

$$E = \int d^{3}\mathbf{r}\left[\frac{\hbar^{2}}{2m}\left|\nabla\phi_{\mathrm{s}}\left(\mathbf{r}\right)\right|^{2} + U\left(\mathbf{r}\right)\left|\phi_{\mathrm{s}}\left(\mathbf{r}\right)\right|^{2} + \frac{g}{2}\left|\phi_{\mathrm{s}}\left(\mathbf{r}\right)\right|^{4}\right]. \tag{2.14}$$

It is often sufficient, for the explanation of physical phenomena, to change (2.13) into a 1D equation by integrating out two of the dimensions. This ap-

proximation can be undertaken by assuming that these directions are tightly confined and contribute very little to the excitations observed within the condensate. In order to achieve this, both the chemical potential and temperature of the gas must be lower than the ground state energy of the harmonic potential in the radial direction—$\mu < \hbar\omega_r/2$ and $k_{\mathrm{B}}T < \hbar\omega_r/2$. Most of the essential physics relevant to this thesis is also retained in this 1D picture, while maintaining clarity and simplicity. Taking the confinement in all three dimensions to be harmonic in form and radially symmetric and that the density of the condensate is sufficiently dilute, the 1D condition becomes $\omega_y = \omega_z = \omega_r$ and $\omega_r \gg \omega_x$. The form of the wavefunction in the radial direction is the ground state of the quantum harmonic oscillator (*e.g.* see (2.17)) and the resulting time-independent 1D GPE is [102]

$$\mu\phi_{\mathrm{s}}(x) = \left[-\frac{\hbar^2}{2m}\frac{d^2}{dx^2} + \frac{1}{2}m\omega_x^2x^2 + g_{1\mathrm{D}}\left|\phi_{\mathrm{s}}(x)\right|^2\right]\phi_{\mathrm{s}}(x), \tag{2.15}$$

where $g_{1\mathrm{D}} = g/(2\pi a_r^2)$ and $a_r = \sqrt{\hbar/(m\omega_r)}$ is the radial length scale of the condensate in the trap. In the process of integrating out the radial direction we have incorporated the radial trapping into the strength of the interparticle interactions, therefore, the radial trapping continues to affect the dynamics of the system, but only along the axial direction in this picture. From (2.15) we can now investigate some limits and solutions of the GPE, in its more simplified form.

Non-interacting limit

In the limit that the *s*-wave scattering length $a \to 0$ ($g \to 0$, see (2.3)) the interaction parameter, $g_{1\mathrm{D}}$, becomes zero. This simplifies (2.15), such that it becomes the 1D Schrödinger equation for a particle in a harmonic trapping potential,

$$\mu\phi_{\mathrm{s}}(x) = \left[-\frac{\hbar^2}{2m}\frac{d^2}{dx^2} + \frac{1}{2}m\omega_x^2x^2\right]\phi_{\mathrm{s}}(x). \tag{2.16}$$

The ground state solution of this is the ground state of the quantum harmonic oscillator [85],

$$\phi_{\mathrm{s}}(x) = \left(\frac{m\omega_x}{\pi\hbar}\right)^{1/4}\exp\left(-\frac{m\omega_x x^2}{2\hbar}\right), \tag{2.17}$$

with an energy eigenvalue of $\mu = (1/2)\hbar\omega_x$.

Thomas-Fermi limit

In the limit that $g_{1D} \gg 1$ and $N_0 \gg 1$ we have very strong repulsive interactions and the condensate spreads out in the trap. This action minimises the kinetic energy, while the interaction energy dominates, and, as a result, we can neglect the kinetic energy term from (2.15),

$$\mu\phi_s(x) = \left[\frac{1}{2}m\omega_x^2 x^2 + g_{1D}\left|\phi_s(x)\right|^2\right]\phi_s(x). \tag{2.18}$$

Rearranging (2.18) and remembering that $n_c(\mathbf{r}) = \left|\phi_0(\mathbf{r})\right|^2$, the ground state Thomas-Fermi condensate density is

$$n_c(x) = \frac{\mu - m\omega_x^2 x^2/2}{g_{1D}}. \tag{2.19}$$

The condensate density is a physical, measureable quantity, therefore, it cannot be negative. As a result, we can see from (2.19) that the condensate has a very well defined width, with a sharp cut off, in the Thomas-Fermi limit. The condensate exists in the region $|x| < \left[2\mu/\left(m\omega_x^2\right)\right]^{1/2}$. By normalising n_c to N_0 and integrating over the entire condensate we are able to determine the 1D chemical potential,

$$\mu = \frac{1}{2}\left(\frac{3}{2}\sqrt{m}\omega_x g_{1D} N_0\right)^{2/3}. \tag{2.20}$$

Soliton solutions

Exact soliton solutions can be found for the GPE in the limit where $\omega_x \to 0$. The result of removing the potential term from (2.15) is to give the Nonlinear Schrödinger equation,

$$\mu\phi_s(x) = \left[-\frac{\hbar^2}{2m}\frac{d^2}{dx^2} + g_{1D}\left|\phi_s(x)\right|^2\right]\phi_s(x). \tag{2.21}$$

The form of the stationary soliton solution is

$$\phi_s(x) = N_0\left(\frac{m\left|g_{1D}\right|}{4\hbar^2}\right)^{1/2}\operatorname{sech}\left(\frac{m\left|g_{1D}\right|N_0 x}{2\hbar^2}\right), \tag{2.22}$$

where $a < 0$ and, hence, $g_{1D} < 0$ and $\phi_s(x)$ is normalised to the total number of atoms in the condensate, N_0. It can be seen that increasing the inter-particle interaction strength will attract the condensate inwards, therefore, the width of the soliton becomes narrower. However, perhaps counterintuitively, as the particle number increases the profile of the soliton also becomes narrower, due to the increase in the strength of interactions, as we have increased the number of attractors. Details of the first experiment to report the production of a single soliton can be found in [28].

2.2.5 The importance of dimensionality and further complications

In the previous section one-dimensional solutions to the GPE were presented in order to demonstrate significant limits that can and have been observed experimentally. In each limit the only difference was the strength and sign of the interatomic interaction. While these solutions present a qualitative explanation of BEC and solitary wave behaviour, it is important to note that increasing the analysis to three dimensions introduces further complications.

As discussed in section 1.2.2, a soliton and a solitary wave are two distinct entities. A soliton is a mathematical solution, to certain one-dimensional nonlinear equations, that maintains a stable profile due to a balance between dispersion and attractive nonlinear interaction. However, a solitary wave is a physical manifestation of a soliton in three-dimensional space, which introduces the complications alluded to earlier. These complications include instability beyond certain densities (see sections 2.2.7, 2.2.9 and 2.3.4) and the change in axial profile of the solitary wave due to variation in its confinement in the radial direction (see section 2.3.5).

While analytical soliton solutions can be found in free space, the introduction of weak axial trapping breaks the integrability of the GPE, requiring numerical approaches in order to obtain a solution (see section 2.3.5 for an example of a variational method).

In some sections of the remainder of this chapter the above complications will be discussed in a variety of contexts, estabilishing reasons for their manifestation and presenting possible methods for handling them.

2.2.6 Multiple soliton formation, relative phase and stability

It is possible to rewrite the complex condensate wavefunction, $\phi(\mathbf{r},t)$, in terms of the condensate density, $n(\mathbf{r},t)$, and a phase function, $\theta(\mathbf{r},t)$, via the Madelung transform [103],

$$\phi(\mathbf{r},t) = \sqrt{n(\mathbf{r},t)}\exp\left[i\theta(\mathbf{r},t)\right], \tag{2.23}$$

where $\phi(\mathbf{r},t)$ is normalised to the total condensate atom number, N_0. This allows us to explicitly define a density profile for the soliton while also controlling its phase. It has been shown that soliton–soliton interactions vary sinusoidally with relative phase [104] (see (2.38)). The mechanism by which this relative phase affects the interactions between colliding solitons is described in [105], where it is stated that in-phase (out-of-phase) solitons, with attractive particle–particle interactions, interact attractively (repulsively) due to constructive (destructive) interference when they overlap, leading to an increase (reduction) in the density. A potential method for directly measuring the relative phase between two solitary waves is given in [106], by looking for interference fringes in momentum space, without requiring the automatic assumption that out-of-phase solitary waves repel each other.

So far two experiments have been able to consistently generate multiple bright solitary waves [27, 56]. The first experiment (in ^{7}Li) [27] noted that the appearance of stable moving multiple solitary waves implied a repulsive interaction between neighbouring solitary waves, inferring a π phase difference [104]. Further theoretical studies of this experiment [107, 108] gave credence to the argument of a relative phase of $\approx \pi$ between neighbouring solitons, although the exact method of forming a solitary wave train was under debate. The second experiment (in ^{85}Rb) [56] controllably produced single and multiple solitary waves depending on the total atom number in the condensate prior to collapse. Subsequent modelling [109, 110] suggested that repulsive interactions between neighbouring solitary waves lead to the behaviour observed by Cornish *et al.*

More recent publications [57, 58, 110] have studied the effect of relative phase on collisions of binary solitons in the GPE formalism. One publication [110] attempted to model the behaviour seen in the ^{85}Rb experiment and observed

excellent quantitative agreement between experiment and theory when neighbouring solitary waves had a π phase difference. In-phase soliton–soliton collisions were shown to be very unstable due to their ability to overlap, resulting in the density increasing above the critical density. Above the critical density a solitary wave will be prone to collapse (see section 2.2.7). Martin *et al.* [57] and Parker *et al.* [58] studied the effects of altering the relative phase between colliding solitons and observed that faster soliton collisions were less prone to collapse[3], even when they are in-phase. Population transfer—the scenario where more atoms are seen to congregate in one soliton than another during a collision—was also observed for intermediate phases—not 0 or π—and it was noted that this could eventually lead to collapse of the solitary waves after multiple collisions.

2.2.7 Collapse, stability and critical number

Much like the stability of neutron stars, due to the balance between the competing repulsive quantum degeneracy pressure and gravitational attraction [111], solitary waves remain stable due to the fine balance between dispersion and attractive interparticle interactions. In 1D solitons are stable regardless of how strongly attractive the interparticle interactions are, however, once one decides to investigate 2D and 3D scenarios, solitary waves are no longer infinitely stable from collapse. This can be seen by observing how the kinetic, potential and interaction energies depend on the cloud size and number of dimensions. Firstly, any density must be proportional to the inverse of the size of the cloud, R, to the power of the dimensions, D; for 1D $n_s(x) \sim 1/R$, for 3D $n_s(\mathbf{r}) \sim 1/R^3$, or in general $n_s(\mathbf{r}) \sim 1/R^D$. As $n_s(\mathbf{r}) = |\phi_s(\mathbf{r})|^2$, one simply finds that $\phi_s(\mathbf{r}) \sim 1/R^{D/2}$. Substituting this dependency into (2.14), results in us finding that the kinetic energy (KE), will always be dependent on $1/R^2$, regardless of the dimensions; the interaction energy (IE) is dependent on the density, $1/R^D$; and any external potential we will take to be harmonic, therefore the potential energy (PE) of the cloud is dependent on R^2. Combining these terms results in,

$$E_{\text{tot}} = \text{KE} + \text{IE} + \text{PE} \sim \frac{C_{\text{KE}}}{R^2} + \frac{C_{\text{IE}}}{R^D} + C_{\text{PE}} R^2, \tag{2.24}$$

[3]In other words, the longer that solitons spend colliding with one another, the more opportunity for them to respond to an increase in density and collapse.

where C_{KE}, C_{IE} and C_{PE} are prefactors that can affect the stability of an interacting BEC. It is very important to note that the sign of C_{IE} is negative for a solitary wave and positive for a repulsive BEC. These dependencies are shown in figure 2.2, demonstrating the fine balance between the KE, IE and PE required to stablise a solitary wave in more than one-dimension.

It is possible to characterise the 3D collapse limit via a collapse parameter, k_{cr} [112][4],

$$k_{\mathrm{cr}} = \frac{|a|\, N_{\mathrm{cr}}}{a_{\mathrm{ho}}}, \tag{2.25}$$

where a is the s-wave scattering length, $a_{\mathrm{ho}} = \sqrt{\hbar/\left(m\omega_{\mathrm{ho}}\right)}$ characterises the size of the soliton and $\omega_{\mathrm{ho}} = (\omega_x\omega_y\omega_z)^{1/3}$ is the geometric mean of the trap frequencies. The value of k_{cr} has been tabulated for a wide variety of trap geometries [114], with a value of $k_{\mathrm{cr}} = 0.574$ for a spherically symmetric trap.

A clear observation of condensate collapse from attractive interactions was reported in 2000 by Gerton *et al.* in ^{7}Li [31]. Following this observation, in 2001 a team in JILA realised the controlled collapse of a BEC of ^{85}Rb [26, 55]. The *bosenova*, as it is now known, was initiated by a fast change in the scattering length ($t_{\mathrm{change}} \ll 1/\omega_{\mathrm{ho}}$) by sweeping along a magnetic Feshbach resonance. Based on the number of atoms observed after collapse in this experiment, the collapse parameter was determined to be $k_{\mathrm{cr}} = 0.459$, which is lower than could be accounted for by the non-spherical trapping geometry used. Following improved characterisation of the Feshbach resonance [115] the collapse parameter was revised to be $k_{\mathrm{cr}} = 0.547(58)$, well within error for the predicted value.

Through their detailed study of the dynamics of collapsing BECs [26], the team from JILA observed that there was an initial delay—of the order of 2-14 ms—between the switching to $a_{\mathrm{s}} < 0$ and the collapse of the condensate. The delay became shorter for more negative a_{s} values and collapse then initiated and took the form of a decaying exponential. The collpase time was only observed to be weakly dependent on a_{s} and N_0 and the decay constant[5] was on average 2.8(1) ms.

[4] Originally given in a different form in [113].

[5] For a decaying exponential the decay constant is generally defined as τ where $N_0(t) = N_0(t_0)\exp(-t/\tau)$.

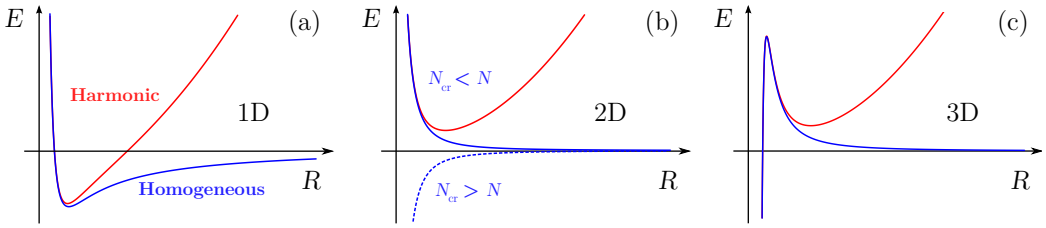

Figure 2.2: Stability of a soliton/solitary wave as a function of the number of dimensions (see (2.24)). (a) In 1D it is possible to create solitons in the homogenous regime (no external trapping potential), due to the balance between KE and IE introducing a minimum in the potential at $R < \infty$ where $E \neq -\infty$ (dark/blue line). Introducing a harmonic potential only serves to reduce the equilibrium size of the cloud (light/red line). (b) Introducing a second dimension results in no finite potential minimum at $R < \infty$ in the homogenous regime, as the IE and KE now have the same dependency ($1/R^2$). Either the cloud size will expand due to |KE| > |IE| (we haven't reached a critical number of atoms) for all values of R (solid dark/blue line), or the cloud will collapse in on itself due to |IE| > |KE| (we have more than the critical number of atoms) for all values of R (dashed dark/blue line). Adding an external potential creates the required minimum to stabilise the cloud. (c) In the full 3D picture there will always be a value of R where the cloud will be susceptible to collapse. The homogenous regime has no finite minimum, resulting in the cloud expanding or collapsing depending on its initial size and the fine balance between the KE and IE. It is possible to stabilise the cloud if we introduce an external potential and ensure that the KE, PE and IE are finely balanced to produce the finite local minimum seen in (c).

More recently (2011) this collapse process has been observed by Altin *et al.* in ^{85}Rb [116] and has been shown to agree qualitatively with simulations using a GPE that includes three-body loss. Collapse has also been observed and studied in the Durham ^{85}Rb experiment (see [103] and [72]).

2.2.8 Beyond the mean-field

A thorough exploration of beyond-mean-field approaches is outside the scope of this thesis, however, in order to discuss some of the exciting phenomena that may be observable in our experiment it is important that we cover some of the key background.

As a solitary wave is a mesoscopic quantum object, it would seem paradoxical to describe this object using a mean-field approach. The reason for this is that mean-field approaches replace a many-body wavefunction with a single-body mean-field wavefunction, essentially treating the condensate or solitary wave as a single particle with a well defined centre of mass. The result of this approximation is a nonlinear classical wave equation—the GPE (see section

2.2.4). The obvious question to ask here is: *why use a classical wave equation to describe an object that should display quantum mechanical behaviour?* The answer to this is two-fold; firstly, this analysis vastly simplifies calculations with a large number of particles ($\gtrsim 100$ atoms), which generally is the case in BEC and solitary wave experiments, and secondly, a mean-field formalism still displays key phenomena observed in non-interacting and interacting BECs, such as ground state solutions, breathing modes[6], solitary wave splitting, reflection and transmission due to a barrier and critical collapse limits.

Recently there have been many examples of publications that go beyond the mean-field, in an attempt to predict interesting quantum mechanical behaviour that would not be manifested in the basic GPE [117–128]. One method of going beyond the mean-field, used in a number of recent papers [117, 118, 122, 127, 128], is the Lieb-Liniger(-McGuire) model, which describes N interacting Bosons [129, 130]. The interacting N-particle Hamiltonian is extremely difficult to solve in more than one-dimension, therefore, often publications investigating this model are limited to a 1D Lieb-Liniger(-McGuire) Hamiltonian, which is a very good approximation to most systems manifesting solitary waves [127, 130],

$$\hat{H} = -\sum_{j=1}^{N} \frac{\hbar^2}{2m}\frac{\partial^2}{\partial x_j^2} + \sum_{j=1}^{N-1}\sum_{n=j+1}^{N} g_{1\mathrm{D}}\,\delta\left(x_j - x_n\right) + \sum_{j=1}^{N} U\left(x_j\right), \tag{2.26}$$

where $U\left(x_j\right)$ is an external potential and, for bright solitons, $g_{1\mathrm{D}} < 0$. As stated earlier, in the mean-field approximation the centre of mass is localised and well defined, however, if one wishes to find solutions to (2.26), with no external potential, these solutions must be translationally invariant [127]. The resulting eigenfunctions have an eigenenergy that is the sum of the ground state energy, $E_0(N)$ and the centre of mass kinetic energy, E_{kin}, where,

$$E_0\left(N\right) = -\frac{1}{24}\frac{m g_{1\mathrm{D}}^2}{\hbar^2} N\left(N^2-1\right) \quad \text{and} \quad E_{\mathrm{kin}} = N\frac{\hbar^2 k^2}{2m}. \tag{2.27}$$

[6]Such as due to a sudden change in the s-wave scattering length.

Holdaway *et al.* [128] separate out the centre of mass Hamiltonian from (2.26), with harmonic trapping, and obtain a resulting wavefunction that describes the centre of mass,

$$\psi_{\mathrm{c}}\left(x_{\mathrm{c}}\right)=\left(\frac{N\gamma}{\pi}\right)^{1/4}\exp\left(-\frac{N\gamma x_{c}^{2}}{2}\right), \tag{2.28}$$

where

$$\gamma=\frac{\hbar^{3}\omega_{x}}{mg_{\mathrm{1D}}^{2}\left(N-1\right)^{2}}, \tag{2.29}$$

and ω_x is the 1D trap frequency. The width of the centre of mass wavefunction can be stated as $\sigma_{\mathrm{sc:CoM}}=1/\sqrt{\gamma N}$, in scaled units of *soliton length*. When converted to absolute units we obtain $\sigma_{\mathrm{ab:CoM}}=\sqrt{\hbar/(Nm\omega_{x})}$. It is clear to see that in the mean-field limit of $N\rightarrow\infty$, $\sigma_{\mathrm{ab:CoM}}\rightarrow 0$—a δ-function—which is exactly what we expect.

N-body approaches have been used to study whether quantum superpositions of mesoscopic objects, such as solitary waves, are possible. Through energy arguments, using (2.27), Gertjerenken *et al.* [127] have identified three key regimes, where it might be possible to create quantum superpositions, such as 'NOON' (Schrödinger cat) states or Schrödinger kitten states[7] and the third, where the GPE is valid. Kinetic energy can to be transferred into interaction energy, through a soliton's interaction with a barrier, resulting in its splitting, and in high-kinetic-energy regimes it is possible for 50:50 splitting to occur because

$$E_{\mathrm{kin}}\gg 2E_{0}\left(\frac{N}{2}\right)-E_{0}\left(N\right). \tag{2.30}$$

When E_{kin} reduces and becomes equal to the right hand side of (2.30), splitting becomes less and less energetically favourable. Eventually the kinetic energy becomes so low that it is impossible for even one particle to split off from the soliton,

$$E_{\mathrm{kin}}<E_{0}\left(N-1\right)-E_{0}\left(N\right). \tag{2.31}$$

[7] These are states not exactly represented by the 'NOON' state given earlier in (2.32), but instead have a small spread of other possible states such as $|N-1,1\rangle$ and $|N-2,2\rangle$.

In this regime, if the energy required to travel over a barrier is equal to the centre of mass kinetic energy of the soliton, a 50:50 quantum superposition state can be created. In this scenario all of the particles will be transmitted or reflected on an individual occasion, however, it is essentially a coin toss as to which side the particles will be found. Using Fock-state notation, this 'NOON' quantum superposition state can be expressed as [127],

$$|\psi\rangle = \frac{1}{\sqrt{2}}\left(|N,0\rangle + e^{\mathrm{i}\alpha}\,|0,N\rangle\right). \tag{2.32}$$

In this low kinetic energy regime, the mean-field solutions have been shown to manifest discontinuities where quantum superpositions may occur [127]. One clear example of this can be found in a publication by Lee and Brand [131]. Gertjerenken *et al.* conjecture that the presence of these discontinuities in a mean-field calculation may indicate that interesting quantum behaviour is occurring, which is presented in detail in [132].

2.2.9 Other interesting phenomena and theoretical predictions

Bright solitary waves can manifest many intriguing phenomena. The aim here is to briefly cover a few examples that would not fall into any of the previous categories. Each of these examples could eventually contribute to an atom optician's toolkit.

A soliton laser: Controllable soliton emission

By exploiting the attractive interparticle interactions required to form a soliton, in 2005 Rodas-Verde *et al.* [133] demonstrated that it would be possible to form a soliton laser using a method they call 'Controllable soliton emission'. They simulated a BEC trapped in a dipole trap with a discontinuous spatial variation of the scattering length. Inside the trap the scattering length is zero, resulting in a non-interacting BEC, and close to one side of the trap the scattering length is discontinuously switched to a negative value. If the BEC is made to overlap with the negative scattering length region, atoms are sucked out of the trap and form a soliton, reducing the size of the trapped BEC. The soliton can then propagate in space, outside of the trap. While

this soliton propagates, the BEC re-equilibrates and part of the BEC, once again, overlaps with the negative scattering region and a new soliton is released. This process repeats until the BEC is depleted to such an extent that no further solitons can be created. Rodas-Verde *et al.* were able to vary the rate at which solitons were emitted and also the total number of emitted solitons. In principle, a pulsed soliton laser could be created if a method for continuously refilling the BEC reservoir could be developed. Another example of a pulsed soliton laser was demonstrated by Carr and Brand [134]. The method is similar to [135], where multiple solitons are generated via tuning of the Feshbach resonance from positive to negative values well beyond the critical value for the initial number of atoms in the condensate. However, Carr and Brand invert the the harmonic trapping such that it becomes expulsive, resulting in a train of counterpropagating solitons which form our soliton laser. This method doesn't allow for continuous emission as there is no way to refill the BEC to create more solitons.

Enhanced quantum reflection

Lee and Brand [131] have demonstrated some interesting behaviour while investigating the quantum reflection of solitons from a potential well, using a 1D mean-field approach. When the entire soliton was seen to reflect from the potential well, it was intriguing to note that part of the soliton entered the well, however, it gained a π change in phase. An argument for the enhanced quantum reflection that they observed could be that the π phase difference of the quasi-trapped cloud is enhancing the repulsion of the soliton from the well. As mentioned in section 2.2.8, Lee and Brand observed sudden switching from reflection to transmission as a function of incident velocity. An N-body approach has postulated that discontinuous jumps in reflection and transmission may be a signature of interesting quantum effects occurring that cannot be generated using a mean-field formalism [127]. However, if this near discontinuous switching were to manifest itself in an experimental scenario, it could be harnessed for velocity filtering of solitons[8].

[8] Although, the presence of uncertainty in the momentum of the soliton could lead to smearing out of this velocity filtering effect.

Suppressed collapse in an attractive BEC

The tendency of attractive condensates to collapse has typically limited solitary waves to an upper bound of the low thousands of atoms[9]. It can be a great benefit to stabilise against this collapse in order to generate larger, more visible solitary waves. There have been a number of theoretical predictions for methods that would help stabilise a solitary wave from collapse. One method is to modulate the interaction strength, while keeping its mean attractive [137–141], although this was eventually shown to not be suffient in stabilising a solitary wave [142]. The theoretical simulation of fragmented states, so called because the condensate is fragmented across multiple modes, has been shown to allow metastable states with atom numbers well above the critical collapse value [143]. It had also been postulated that condensates may be more stable to collapse when they are undergoing rotation [144], although more recently it was noted that this rotation has less of an effect on stabilising against collapse than was originally predicted [145, 146]. It is clear that this has been an active area of research over the past 10 years, however, it still remains uncertain whether we will find an experimentally viable method that stabilizes a solitary wave beyond the critical number.

2.3 Recent progress

Having now covered the fundamentals of the field of bright solitary wave research, the aim in this section is to detail some of the more pressing issues that have recently been investigated in the field, with the hope that many of the theoretical results presented here could eventually be applied to a solitary wave experiment.

2.3.1 Soliton interferometry and interactions with barriers

Atoms can be modelled as both particles and waves. They possess many intriguing properties for use in experiments that would have originally been

[9] Although, more recently there have been indications of much larger atom numbers in a solitary wave of ^{7}Li [136].

limited to waves, such as diffraction [147] and interferometry [148], opening up the fascinating world of atom optics [149]. Very soon after the production of the first BEC, an early experiment demonstrated that two condensates could be shown to be coherent with one another and manifest interference fringes [19] by releasing them from a double well potential. It has been noted, however, that it is extremely difficult to obtain long lived phase coherence between separate Bose–Einstein condensates [150] due to the interatomic interactions typically observed in a BEC. Later experiments continued to use the double well potential method [151–153], with some of these implemented on an atom chip. By exploiting a Feshbach resonance, resulting in a weakly interacting condensate, another experiment was able to strongly reduce the interaction induced decoherence [154].

Contrary to what we have already stated, one recent experiment actually demonstrated the benefits of exploiting nonlinearity (interactions) in atom interferometry [155] and another has given glimpses of the possibilities of solitary wave interferometry [156]. It is clear that theoretically exploring potential applications of solitary waves for use in interferometric measurements could lead to some interesting predictions.

Outside the realm of interferometry, the study of soliton interactions with attractive or repulsive barriers is interesting in its own right, with outcomes such as resonant trapping [157], regimes of wave-like and particle-like behaviour [158] and elastic scattering in the N-body formalism [159].

Solitary wave interferometry

The first step in achieving interferometry of solitary waves is to investigate the methods of producing two separate but coherent solitary waves. The most commonly suggested method is to make use of a narrow potential barrier in order to split a single soliton into two separate solitons, converting centre of mass kinetic energy into interaction energy [126, 136, 158]. Other methods of coherently splitting a solitary wave include applying a density modulation by exploiting a second internal atomic state [160] and also by utilising only the interatomic interactions via a Feshbach resonance [135].

Billam *et al.* propose an experiment that may be crucial in determining the validity of the GPE in describing the dynamics of experimentally observed

solitary waves [160]. They simulated multiple binary solitary wave collisions in varied trap anisotropies and with variable relative phases. The number of collisions for which these binary solitary waves remained solitonlike was recorded and a strong oscillatory dependence on trap anisotropy, as well as relative phase, was observed. They stated that the presence of these oscillatory dependencies in experimental data would indicate the sufficiency of the GPE description of solitary waves, resulting in an important step towards solitary wave interferometry experiments [160].

The study of the splitting and recombination of high energy solitons[10] on a delta function potential and gaussian barrier was undertaken by Helm *et al.* [161] in a 1D GPE framework. They concluded that nonlinearity introduces a skew, enhancing the phase sensitivity of their interferometer, in the transmitted and reflected components of two colliding solitons with varying relative phase. A key result from an earlier publication [162] was also presented, that determines the regimes in which a reflected or transmitted soliton is formed,

$$A_{\mathrm{T}} = \max\left(0, 2\left|t\left(v\right)\right| - 1\right) \quad \text{and} \quad A_{\mathrm{R}} = \max\left(0, 2\left|r\left(v\right)\right| - 1\right), \tag{2.33}$$

where A_{T} and A_{R} are the amplitudes of the transmitted and reflected solitons, while $|t(v)|$ and $|r(v)|$ are the magnitudes of the amplitudes of the transmitted and reflected components for plane waves in linear quantum mechanics and are given by,

$$|t(v)| = \sqrt{\frac{v^2}{v^2 + v_{\mathrm{B}}^2}} \quad \text{and} \quad |r(v)| = \sqrt{\frac{v_{\mathrm{B}}^2}{v^2 + v_{\mathrm{B}}^2}}, \tag{2.34}$$

where v is the velocity of the plane wave (or soliton) and $v_{\mathrm{B}} = \sqrt{2V_{\max}/m}$ is the classical velocity required for a particle of mass m to travel over a barrier of height $V_{\max}$. When $A_{\mathrm{T}} = 0$ or $A_{\mathrm{R}} = 0$, the transmitted or reflected component does not manifest a soliton, instead only radiation will be observed [161].

Martin *et al.* have undertaken an in-depth study [126] of a recent experiment where solitary waves are split on a barrier [156], in an attempt to investigate

[10] Such that there is sufficient kinetic energy to transfer into the interaction energy required to produce two solitons.

whether solitary waves will be a highly sensitive tool for measuring small fluctuations in a force such as gravity. Within the framework of the 1D GPE, the results look exceptionally promising, with a sharp change in the transmitted or reflected components, as a function of relative phase, for certain strengths of nonlinearity and barrier widths. Unfortunately, when the model is extended beyond the mean-field (in 1D), atom number fluctuations have been shown to severely degrade the performance of the solitary wave interferometer [126].

Cuevas *et al.* have also analysed [136] the same experiment [156], undertaken using the 1D and 3D GPE. They also noted a loss of sensitivity of the interferometry apparatus due to the nonlinearity, although they observed that this effect could be countered by the presence of a narrower barrier (1 μm instead of 4.5 μm). They noted the importance of studying deviations from the mean-field analysis in 3D, which will be a challenging undertaking.

One of the potentially most straightforward methods of generating multiple coherent solitary waves is via Feshbach-resonance tuning, as described by Michinel *et al.* [135]. They propose placing a strongly repulsive BEC in a shallow optical dipole trap and then switching the interactions from repulsive to attractive[11] leading to controllable solitary wave formation via modulational instability [163]. The expression that they determined for the number of emitted solitons via this method is,

$$N_{\text{emitted}} \approx 2\left[\frac{c_1\sqrt{|g_2|\,N}\left(c_2\sqrt{g_1 N}-\tilde{L}\right)}{(g_1 N)^{1/4}}\right], \tag{2.35}$$

where $c_1 = 0.22$ and $c_2 = 2.49$ are coefficients determined from fitting, N is the number of atoms in the initial repulsive condensate, $\tilde{L}$ characterises the initial size of the condensate and is scaled by the radial harmonic length $a_r = \sqrt{\hbar/(m\omega_r)}$ and g_1 and g_2 are the initial and final nonlinear interaction strengths respectively, where $g = 2a_s/a_r$ and a_s is the s-wave scattering length in S.I. units.

[11] They also suggest a spatially varying scattering length much like [133] as another possible method for generating multiple solitons, although this is less practical.

Solitary wave interactions with barriers

While splitting is currently most commonly associated with potential interferometry experiments, a recent paper by Ernst and Brand [157] studied the resonant trapping resulting from the collision of a soliton with a square potential well in the framework of the 1D GPE. They state that the process by which this nonlinear trapping occurs is dependent on resonant transfer between the soliton and bound states in the potential well and radiation was also found to play a part. They also claim that solitons could be used to probe bound states of an unknown localised potential that are inaccessible in a linear regime (scattering a single atom). A key result from this paper is that the linear expression for transmission through a square well of width L [164],

$$T_{\text{lin}}\left(v_{\text{B}}\right)=\left[1+\frac{v_{\text{B}}^{4}}{4v^{2}\left(v^{2}+v_{\text{B}}^{2}\right)}\sin^{2}\left(\frac{mL}{\hbar}\sqrt{v^{2}+v_{\text{B}}^{2}}\right)\right]^{-1}, \tag{2.36}$$

where v_{B} is the velocity required to escape the well, provides an upper bound to the transmission curve for a soliton incident on the same potential, with the curves approaching each other in the high velocity limit.

One method of trapping that they describe is via radiation loss, which, due to energy conservation, reduces the centre of mass kinetic energy of the soliton, resulting in trapping. Another aspect observed by Ernst and Brand was the temporary trapping (time delay) of a soliton, before reemission as a reflected or transmitted component, that appears to be similar to the temporary trapping of a linear wavepacket. Al-Marzoug *et al.* [165] also demonstrate this time delay effect for a single soliton and soliton molecule incident upon a reflectionless potential [166] (see (2.39) and (2.40)). This method has the benefit of negligible losses via radiation ($> 99\%$ of the soliton remains).

2.3.2 Soliton superpositions and entanglement

Superpositions and entanglement are phenomena at the heart of quantum mechanics and quantum computing [167]. Quantum computers could offer a wide array of potential benefits including quantum cryptography [168], factorising semiprime numbers in polynomial time [169], significantly speeding up the search of unsorted databases [170] and in general simulating the phys-

ical world around us [171]. Being able to create quantum superpositions is at the crux of quantum computing and much research has been focused on attempting to create superpositions with large particles (even living organisms) [172–177] and over relatively large distances [178–185].

BECs and bright solitary matter-waves offer the potential to form nonlocal quantum superpositions with mesoscopic objects and research has been flourishing in this area recently [120–123, 125, 132, 186–188]. A beyond-mean-field approach must be undertaken in the theoretical study of quantum superpositions of solitary waves (see section 2.2.8). The two most important aspects, if one wishes to implement an experiment that generates entangled solitary waves, are how to generate the entanglement and how to detect it. It is these aspects that we will draw out of the recent research.

Generating nonlocal quantum superpositions

The three key methods that have been studied recently for the generation of quantum superposition states of solitary waves are solitons scattering off a barrier [121, 122, 188], being threaded by a barrier [186] and collisions between two initially separated indistinguishable [120] and distinguishable [132] solitons.

It is possible to generate Schrödinger kitten states if the kinetic energy of the incoming soliton incident on a barrier is low but not sufficiently low enough to guarantee elastic scattering, as in the case of Streltsov *et al.* [121]. As in the case of Weiss and Castin [122] and Gertjerenken and Weiss [188], if one moves into the elastic scattering regime (see (2.31)), it is possible to create 'NOON' states (see (2.32)) by scattering off a potential barrier that is approximately equal in height to the kinetic energy of the incoming soliton.

Streltsov *et al.* [186] use a method of threading the soliton with a Gaussian barrier to create nonlocal quantum superpositions. This method created very clean Schrödinger kitten states that, as they demonstrated, were just not accessible within the GPE framework. The speed of the propagating solitons were seen to be dependent on the width of the barrier and $\approx 50:50$ superpositions could be generated even if the barrier was offset by 10% of the cloud size.

The work of Lewenstein *et al.* [120] demonstrated a proof of principle that it is possible for entanglement to occur between two initially uncorrelated solitons. One interesting effect that they noted was that if the incoming solitons had a relative phase that was completely uncertain, the result of a collision would be partial phase localisation. Gertjerenken *et al.* [132] present the proposal for an experimental scenario where entanglement is produced between two distinguishable bright solitons of ^{85}Rb and ^{133}Cs. The two solitons are intitially well separated in a harmonic trap and are then released. When the solitons collide with each other Gertjerenken *et al.* demonstrate a scenario where a Bell state is formed by observing the correlation between the two solitons.

Detecting nonlocal quantum superpositions

If one wishes to determine whether a nonlocal quantum superposition has been formed in any of the above scenarios, there are two key steps. The first step is to ensure that at each experimental run, the entire soliton can be found to either reflect or transmit, averaging out, over multiple runs, with the expected probability. This step gives the first indication that a Schrödinger cat state is formed. The final step, which confirms that a coherent superposition has indeed formed, is discussed in [122, 132, 188], where fringes are observed in the centre of mass wavefunction. Just observing the density distribution of the the soliton leads to severe smearing out of any fringes [188]. So, how does one measure the centre of mass wavefunction? Much like through the textbook double slit experiment, one photon, or in our case, one experimental run, is not sufficient for observing this fringe pattern. Instead we need multiple experimental runs, while plotting the centre of mass of the soliton at the point of recombination of the wavepackets. With appropriate binning and enough experimental runs, if a nonlocal superposition has been formed, one will observe a fringe pattern or another signature discussed in [127]. In order to maintain a quantum superposition over an entire trap oscillation, it is important to minimise the uncertainty in the generated atom number (as has been presented in [189]) and ensure particle losses do not occur, as this would lead to decoherence.

2.3.3 Soliton molecules and trains

When placed in close proximity, it has been shown that the interaction between two solitons varies sinusoidally with phase and decays exponentially with separation [104]. Experiments have been able to create multiple bright solitary matter-waves in close proximity and study their interactions (see section 2.2.6). While many papers have cited a π phase difference as the reason for stable multiple solitary wave interactions in the GPE framework, more recently groups have demonstrated that in 1D repulsive dynamics can occur solely due to going beyond mean-field interactions [119, 124, 190], regardless of the relative phase. Research studying the formation, stability and dynamics of two-soliton and many-soliton molecules has also been of increasing interest recently [105, 165, 191–195].

Fragmented states in soliton trains

In 2008 Streltsov *et al.* [190] introduced the concept of *fragmentons* to the physics vocabulary. Unlike coherent GPE solitons, which are only able to occupy a single state, the density of fragmentons, which can only be created in a many-body framework, is approximately evenly spread over more than one state. The simplest form, if only two states are accessible, is a 50:50 spread of condensate density between two states. They highlighted that fragmented states are *always* energetically more favourable than any coherent GPE two-soliton solutions. Introducing an excitation to an initial soliton, by mismatching the intial soliton shape from the expected solution for a given attraction, led to very different behaviour in the mean-field and many-body simulations. For slight perturbations breathing could be observed for both the mean-field and many-body cases. As the perturbation increased, the mean-field and many-body cases became increasingly divergent, eventually leading to the case where the initial soliton splits into two counterpropagating, stable wavepackets. During the process of splitting the system becomes fragmented, indicating behaviour that could not be observed in mean-field analysis.

The previous work has been followed by a later paper [124], investigating loss of coherence in soliton trains, with its main focus on binary soliton collisions. Similar to the previous paper, the authors demonstrated that mean-field and many-body approaches provided very different outcomes of binary soliton collisions. For both 0- and π-phase differences the interactions between the solitons are *always* repulsive in the many-body formalism, in direct opposition to the results obtained via mean-field methods. It would appear that the repulsion is somehow derived from the fact that a fragmented state is formed. For well separated wavepackets, Streltsov *et al.* provide an analytical formula for the asymptotic force between two wavepackets[12],

$$F = -\frac{4e^{-2\gamma x_0}\gamma^2}{3N}\left(n_1 - n_2\right)\left[\lambda_0\left(N-1\right)\left(\gamma x_0 - 2\right) + 4\gamma^2 x_0 - 5\gamma\right], \qquad (2.37)$$

where all quantities are dimensionless and λ_0 is the interparticle interaction strength, γ is inversely proportional to the width of the wavepackets[13], N is the total number of atoms, n_1 and n_2 are the populations of the two possible states, where $n_1 + n_2 = N$, and $2x_0$ is the separation of the wavepackets. One interesting aspect to note here is that if one substitutes the most fragmented state ($n_1 = n_2 = 50\%$) into (2.37), the result is $F = 0$. However, the system is seen to deviate from this asymptotic result when the fragmentons become close enough to one another. They also observed that if the attraction is kept constant ($\lambda_0 N = \text{const}$) and the number of atoms is increased the lifetime of the coherent soliton train, before it transforms into a fragmenton, decreases roughly quadratically[14]. For ^{7}Li this predicted lifetime is around an order of magnitude smaller than the length of an experimental run.

The presence of repulsive interactions in a beyond mean-field soliton, regardless of phase, was also noted in [119] in 1D simulations. In 3D, with the addition of quantum noise, they observed the opposite of what might be expected; the presence of quantum noise actually reduces the lifetime of solitary waves undergoing binary collisions.

[12] See supplementary material for [124].
[13] Where the initial form of the soliton is $\operatorname{sech}(\gamma x)$.
[14] See supplementary material for [124].

Soliton molecules

As derived by Gordon [104], the interaction between two solitons decays exponentially with separation and oscillates sinusoidally with phase,

$$\begin{aligned} \ddot{x}(t) &= -4\exp\left[-2x(t)\right]\cos\left[2\phi(t)\right] \\ \ddot{\phi}(t) &= 4\exp\left[-2x(t)\right]\sin\left[2\phi(t)\right], \end{aligned} \tag{2.38}$$

where $2x(t)$ is the separation of the solitons and $2\phi(t)$ is their relative phase. When solitons are in-phase and initially attract one another, the relative phase of these solitons varies with time (see (2.38)), such that if they are travelling slow enough they will eventually repel each other and, following that, attract each other. This process can repeat, resulting in the formation of a soliton molecule [192]; although this molecule is very unstable due to it having no binding energy, therefore small perturbations can lead to the break up of this molecule [193]. In 2005 optical soliton molecules were observed in a dispersion-managed fibre [196], however, matter-wave soliton molecules remain elusive, although this hasn't prevented a continued theoretical interest.

Khawaja studied the stability and dynamics of two-soliton molecules [105], developing an expression for the force between two solitons with arbitrary densities, centre of mass speeds and separation, generalising Gordon's expression, which was limited to slow collisions between almost identical solitons in the limit of large separations [105]. Stability of the molecule when interacting with a hard wall, finite barrier and another soliton was also investigated. This work was followed by [191], where the formation of soliton molecules was investigated. The authors demonstrated that molecules could only be formed when the initial force between two solitons is attractive and that this force varies periodically with the initial soliton position.

Al-Marsoug *et al.* [165] studied the scattering of a single soliton and two soliton molecules by a reflectionless potential well [166] of the form,

$$V(x) = -\frac{V_0}{\cosh^2(\alpha x)}, \tag{2.39}$$

where V_0 is the depth of the well and α determines the width of the well. In the linear regime the textbook result [197] for the transmission of a

wavepacket through this potential is,

$$T = \frac{\sinh^2(\pi m v/\hbar\alpha)}{\sinh^2(\pi m v/\hbar\alpha) + \cos^2\left(\frac{\pi}{2}\sqrt{1+\frac{8mV_0}{\hbar^2\alpha^2}}\right)}. \tag{2.40}$$

The interesting thing to note is that when $V_0 = n(n-1)\hbar^2\alpha^2/2m$, where n is a positive integer, the transmission of the wavepacket becomes $T = 1$, regardless of its speed, v. Al-Marsoug *et al.* noted that this is not the case for a nonlinear wavepacket or molecule, observing full reflection for some low velocities in both cases. A later paper [192] explored the experimental viability of generating soliton molecules by simulating a recent solitary wave splitting experiment [136, 156]. As zero velocity has been stated as a requirement for the formation of soliton molecules, the authors suggest that after splitting of a solitary wave has occurred on a barrier in a harmonic potential, at the turning point of the solitary waves, the confining axial potential and barrier could be turned off, to ensure an initial two stationary solitary wave state. Using this condition as a starting point, they then derive the form of the potential between two solitons as a function of interaction strength, density, initial phase difference and initial separation. The interaction has the form of a Morse potential [198], clearly showing regions where bound molecular states can occur.

2.3.4 Suppressed collapse of solitons and metastable states

In section 2.2.7 we discussed why, in the homogeneous regime, an attractive condensate can only be stable in 1D and why it is necessary to introduce an external trapping potential to stabilise the condensate in 2D and 3D. Later in section 2.2.9 we saw some methods that had been suggested to suppress collapse in higher dimensions. Research in this area has continued more recently [199–201].

Within the many-body formalism Tsatsos *et al.* [199] have shown that it is possible for metastable states to form beyond the expected critical number if the bosons are in a ground state with angular momentum $L \neq 0$. Abdullaev *et al.* [200] suggested that imparting orbital angular momentum on an elliptically shaped cloud, essentially causing it to spin, should greatly suppress

collapse, even in the mean-field. They state that increasing the ellipticity of the mode and its speed of rotation will further suppress any collapse.

A novel suggestion for countering the inevitable attraction at small cloud sizes, R, in the 3D trapping geometry has been suggested by Parker *et al.* [201]. By introducing repulsive p-wave interactions it is possible to counter the attractive s-wave interactions, resulting in a global minimum in the energy that does not approach $-\infty$. For 3D this takes (2.24) and transforms it into,

$$E_{\text{tot}} \sim \frac{C_{\text{KE}}}{R^2} - \frac{C_{\text{IE3}}}{R^3} + \frac{C_{\text{IE5}}}{R^5} + C_{\text{PE}}R^2, \tag{2.41}$$

where the $1/R^5$ contribution is due to the p-wave interaction and C_x are prefactors that could potentially be tuned to vary the stability of the system. In order to provide this p-wave interaction, they suggest introducing a fermionic isotope, such as ^{40}K, to a bosonic cloud of ^{87}Rb. Parker *et al.* then derive specific expressions (see (4), (6) and (8) of [201]) for the total energy contributed due to boson-boson, fermion-fermion and boson-fermion interactions, which has the form of (2.41). The collapse instability can be entirely removed and the resulting Bose-Fermi soliton can be robust against collapse with a large atom number. Tunability of such a mixture may prove difficult, as one does not possess a mechanism that can independently tune the scattering length of each mixture, using a magnetic Feshbach resonance. However, if one can find a Bose-Fermi mixture where both species exhibit Feshbach resonances around the same magnetic field, it may be possible to have some control of the energy landscape in order to create an appropriate global minimum for $R < \infty$.

2.3.5 Quantum and mean-field behaviour

Bright solitary matter-waves are an ideal candidate to probe the quantum/classical crossover, as they are relatively large objects that have the potential to display quantum behaviour, typically associated with a single atom, and classical, particle-like behaviour. With the great interest in whether a mean-field approach is sufficient to explain the behaviour of solitary waves observed in the laboratory, or whether an N-body formalism is necessary (see section 2.2.8), this section will focus on parameter regimes where we might expect to see either, or both situations.

Often, in the case that $N \to \infty$ and a single state is macroscopically occupied, a mean-field formalism is sufficient to explain the observed dynamics. However, at which value of N does mean-field analysis break down? For some scenarios it has been shown that for $N \approx 3$ the quantum and classical results display only a modest discrepancy [117]. Others have shown how very quantum signatures, such as entangled states, can be observed in systems with as many as 100 atoms (see section 2.3.2).

Three recent papers have investigated, in great detail, the mean-field [202] and quantum regimes [128] and the difference between both regimes [127].

Using a variational method, Billam *et al.* [202] studied regimes in which a Gaussian or soliton ansatz could describe the profile of a harmonically trapped cloud depending on the interaction strength and axial trapping frequency in 1D and with the addition of trap anisotropy in 3D. One of the key results of this paper is a pair of coupled equations that can be used to determine the radial and axial lengths of a cloud in a harmonic trap relative to the 1D soliton length and the harmonic length. It is essentially measuring how much the radial and axial directions couple together. The benefit of this is that one can determine how soliton-like a cloud will be in a given trap geometry with a particular interaction strength. These coupled equations are as follows,

$$k_s = \left(\frac{6\kappa\gamma\ell_s}{6\kappa\gamma\ell_s - 1} \right)^{1/4}, \tag{2.42}$$

and

$$\ell_s = \frac{\left[\chi\left(\gamma k_s^{-4}\right)\right]^{1/2} k_s^{2/3}}{2^{11/6}\left(\pi\gamma\right)^{2/3}} \left\{ \left[\left(\frac{2}{\chi\left(\gamma k_s^{-4}\right)} \right)^{3/2} - 1 \right]^{1/2} - 1 \right\}, \tag{2.43}$$

where $0 \leq (1/k_s) \leq 1$ quantifies the radial size of the cloud relative to the radial harmonic length, $a_r = \sqrt{\hbar/m\omega_r}$, $0 \leq l_s \leq 1$ quantifies the axial length of the cloud relative to the soliton length, $a_s = \hbar/(2m\omega_r|a|N)$ [15], $\kappa = \omega_r/\omega_x$,

[15] The real radial and axial lengths are simply a_r/k_s and $\ell_s a_s$ respectively.

$\gamma = (a_s/a_x)^2$, where a_x is the axial harmonic length and χ is given by,

$$\chi(\gamma) = \left[1 + \left(1 + \frac{1024\pi^2\gamma^2}{27}\right)^{1/2}\right]^{1/3} + \left[1 - \left(1 + \frac{1024\pi^2\gamma^2}{27}\right)^{1/2}\right]^{1/3}. \tag{2.44}$$

For a given κ and γ, the values for ℓ_s and k_s can be determined via an iterative method. Simply placing $k_s = 1$ into (2.43) and then placing the calculated value of ℓ_s into (2.42) and repeating the process will lead to a convergence in their values. One can explore this κ and γ parameter space and look for where $\ell_s \to 1$, to determine how soliton-like a given solution is.

Comparing these calculated lengths to other lengths relevant to the cloud, or an experimental setup, will help us to determine parameter regimes where quantum or classical behaviour will be observed. For example, Holdaway *et al.* [128] separate out the centre of mass coordinate from the internal motion of a cloud, resulting in a centre of mass wavefunction (see (2.28)) with a size,

$$\sigma_{\mathrm{CoM}} = 1/\sqrt{\gamma N}. \tag{2.45}$$

Comparing ℓ_s with σ_{CoM} can give a good indication where to expect to observe quantum or classical behaviour. For example, if $\ell_s \gg \sigma_{\mathrm{CoM}}$, any non-localisation in the centre of mass, a very quantum behaviour, would not be possible to observe. Instead, if $\ell_s \ll \sigma_{\mathrm{CoM}}$, quantum superposition states should be more readily observable in an experiment.

The same analysis can be applied when a barrier is introduced to an experiment. If σ_{bar} is the width of a barrier and $\sigma_{\mathrm{bar}} \gg \ell_s$, one would expect to observe classical particle-like behaviour from the solitary wave—either it entirely reflects, or entirely transmits, depending on whether its centre-of-mass kinetic energy is sufficient to travel over the potential. Narrowing the barrier to the point where $\sigma_{\mathrm{bar}} \ll \ell_s$ should result in the observation of more wave-like behaviour from the soliton; introducing the possibility of splitting to our experimental scenario.

Gertjerenken *et al.* [127] undertook a detailed analysis of quantum verses mean-field behaviour in the low centre-of-mass kinetic energy regime (see much of section 2.2.8). They stated that a possible method for determining parameter regimes where quantum superpositions could be formed is to run

a standard GPE simulation of a particular scenario and look for a discontinuity in the reflection probability, as the centre-of-mass kinetic energy is varied. These discontinuities can be interpreted as regions where quantum superpositions may be forming on the N-body level.

2.3.6 Quantum reflection from a surface

In 2009 Cornish *et al.* [29] proposed the use of solitary matter-waves to probe atom surface interactions via quantum reflection. They cited a number of benefits of using solitary waves in comparison with a standard repulsive or non-interacting BEC (for a comparison see [65] and [203]); these included very precise low-velocity control and the ability to accurately measure reflection probabilities—both due to the non-dispersive nature of solitary waves. They presented the regime where one would expect to observe significant quantum reflection, known as *the badlands* elsewhere [204]. They state that if a particle with a local wavevector $k = \sqrt{k_\infty^2 - 2mV(x)/\hbar^2}$ changes by more than k over a distance of $1/k$, significant quantum reflection is expected. k_∞ is the wavevector of the particle far from the potential, $V(x)$. This boundary can be expressed as,

$$\frac{1}{k}\left|\frac{dk}{dx}\right| = k. \tag{2.46}$$

Expressing this in a slightly different form allows for straightforward calculations of the boundary beyond which significant quantum reflection should be expected,

$$\frac{m}{\hbar^2}\frac{1}{k^3}\left|\frac{dV(x)}{dx}\right| \equiv \mathcal{B}_{\mathrm{ad}} = 1. \tag{2.47}$$

To date the author is not aware of any experiments that have probed solitary wave–surface interactions, although this is one of the main goals of this experiment (see section 1.3.4). However, recent experiments, including our own, have probed the interactions between ultracold atoms and a dielectric surface [67, 77, 78] and a carbon nanotube [205], while another has studied the ad- and desorption of Rb atoms on a gold nanofilm [206].

In [67], the authors observe classical reflection of an ultracold cloud of ^{87}Rb atoms from a combined evanescent wave and unknown surface potential, V_{SF}. Through tuning of the power of the laser generating the evanescent wave potential it is possible to create a barrier, as shown in figure 1.1. As

long as the evanescent potential is known, it is possible to determine the unknown potential by measuring the classical critical velocity of the cloud at a given laser power, thus measuring the height of the barrier. Two equations allow the calculation of this unknown potential,

$$x_B\left(P\right) = -\frac{x_0}{2}\ln\left(\frac{1}{C_0}\frac{dE_B}{dP}\right), \tag{2.48}$$

and

$$E_B = V_{\mathrm{SF}}\left(x_B\right) + C_0 P \exp\left(-2\frac{x_B}{x_0}\right), \tag{2.49}$$

where x_B is the position of the barrier, which is essentially calculated from the gradient of the barrier height, E_B, as a function of laser power, P, while C_0 is a constant and x_0 is the decay length [207].

A recent publication by Judd *et al.* [208] found that quantum reflection could be increased above 90% by using thin dielectric films, thus reducing the Casimir-Polder potential. They also suggest a novel use for a graphene monolayer; a surface from which to quantum reflect that has the advantages of straightforward removal of adsorbed atoms, via current annealing; and as resistance of the monolayer changes when atoms are adsorbed, it would be possible to monitor the quantum reflection of atoms in real-time in a non-invasive way, without having to use destructive imaging techniques.

2.4 Experimentally observable phenomena using solitary waves

The purpose of this section is to summarise the theory and recent work that has been presented already in this chapter. The resulting table should provide quick access to experiments and relevant equations that it may be possible to explore with our apparatus. We will provide a simple grade to indicate whether it is possible to undertake such experiments with the current apparatus (*), with the addition of new equipment or a slight change of the apparatus (**) or whether a redesign or rebuild of the apparatus would be necessary (***). Note that these grades do not relate to the difficulty in performing the experiment, or the likelihood of success.

Experiment summary	Additional equipment and notes	Equations and references	Grade
BEC collapse in different trapping geometries	None	(2.25), [26, 55, 72, 103, 112, 114–116]	*
Investigate multiple solitary wave formation	None	(2.25, 2.35), [27, 56, 107, 108, 133, 134, 163]	*
Determine resolution of current imaging system	None	(2.42, 2.43, 2.44), [202]	*
Quantum reflection from a potential well	None	(2.36, 2.46, 2.47), [131, 157]	*
Generate counterpropagating solitary waves through Feshbach tuning	None	(2.35), [135, 163]	*
Investigate solitary wave profile in different trapping geometries	Very high resolution imaging system	(2.42, 2.43, 2.44), [202]	*/**
Create a soliton interferometer	Blue detuned laser, a laser to modulate BEC density or tuning of Feshbach resonance and a laser to imprint phase	(2.23, 2.33, 2.34), [57, 58, 110, 126, 135, 136, 158, 160, 161]	*[135]/**
Investigate trapping in a potential well	None/Very high resolution imaging system	(2.36), [157, 165]	*/**
Quantum reflection from a surface	None/Introduce thin surface material (eg. graphene)	(2.46, 2.47), [29, 204, 208]	*/***
Calculate unknown surface potential from classical solitary wave reflection	Blue detuned laser and access to prism to generate evanescent wave	(2.48, 2.49), [67, 207]	**
Entangle two solitary waves	Very high resolution imaging system, no losses and $N \sim 100$	(2.27, 2.30, 2.31, 2.32), [120–122, 127, 132, 186, 188]	**
Observe uncertainty in solitary wave centre of mass	Very high resolution imaging system and N very low	(2.28, 2.29, 2.45), [128]	**
Create a solitary wave laser	Very small Feshbach coil or expulsive potential	[133, 134]	**
Split solitary wave on a narrow repulsive barrier	Blue detuned laser	(2.33, 2.34, 2.46, 2.47), [126, 136, 158, 161]	**
Form solitary wave molecules	A weak harmonic potential that can be switched off and a barrier to split on	(2.38), [104, 105, 191, 192]	**
Suppress collapse of attractive condensate	Boson-Fermion mixture or rotating BEC	(2.24, 2.25, 2.41), [199–201]	**/***

Table 2.1: Possible experiments to be undertaken after this thesis. Provided are a description of the experiment, any extra equipment required or relevant information, relevant equations and references and a grade indicating how much the experimental apparatus must be adapted (None: *, Minor: **, Major: ***).

2.5 Calculations

In this section we aim to explore the parameter regimes that are before us when investigating various aspects of the phenomena mentioned above. We will indicate how plausible it is that we will be able to achieve certain experimental goals that are listed in table 2.1.

2.5.1 Quantum reflection from a potential well and barrier

While the analysis contained within this section is based on the assumption that we are observing a plane wave, it can also be applied to a soliton, with the condition that its kinetic energy is well defined. This can also be thought of as being in the regime where the size of the soliton is larger than that of the potential.

The potential well

Earlier we discussed the conditions required to observe a strong quantum reflection signal (see (2.46) and (2.47)). Using (2.46) and (2.47) we will plot $\mathcal{B}_{\mathrm{ad}}$ for a soliton released off-centre in a harmonic trap, heading towards a gaussian potential well placed at the centre of the trap. The gaussian well is created by inserting a red detuned light-sheet perpendicular to the direction of the waveguide confining the soliton. The $1/e^2$ radius (waist) of the light-sheet perpendicular to the soliton propagation is 260 μm (see section 7.5.1), such that the intensity of the light-sheet is approximately even along the radial direction of the waveguide. The waist along the direction of propagation of the soliton is varied. All investigations in this section focus on ^{85}Rb. In figure 2.3 we fix the frequency of the harmonic trap to $\omega = 2\pi \times 1.00$ Hz and the initial offset of the soliton to $x_I = 100$ μm, which corresponds to a kinetic energy of $k_{\mathrm{B}} \times 2.0$ nK and velocity of 0.63 mm s^{-1} at the trap centre. The beam power and wavelength of the light-sheet is $P = 10$ mW and $\lambda = 852$ nm respectively. In figure 2.3 (b) there is the additional constraint of the $1/e^2$ radius of the light-sheet along the soliton propagation direction being 3 μm.

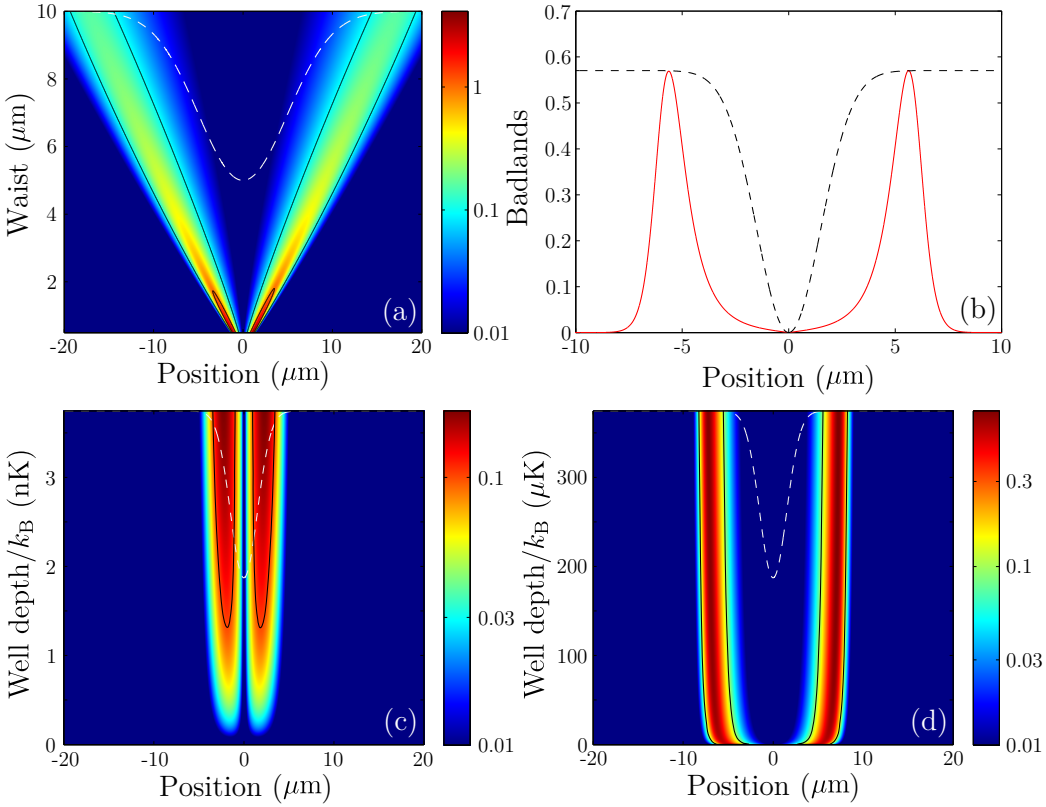

Figure 2.3: The effect of altering the width and depth of a gaussian potential well on quantum reflection. Significant quantum reflection is expected to occur when $\mathcal{B}_{\rm ad} > 1$ (see (2.47)). A ^{85}Rb soliton is released 100 μm from the centre of a harmonic trap with trap frequency, $\omega = 2\pi\times 1.00$ Hz, and accelerates towards a gaussian potential well (a $P = 10$ mW, $\lambda = 852$ nm light-sheet with waist, $w_y = 260$ μm perpendicular to the soliton motion) located at the centre of the trap. (a) $\mathcal{B}_{\rm ad}$ (quantified by the colour map) is given as a function of the $1/e^2$ radius (waist) of the well in the direction of soliton motion and position of soliton after its release. The inner contour is at $\mathcal{B}_{\rm ad} = 1$ and the outer contour at $\mathcal{B}_{\rm ad} = 0.1$. The dashed white line indicates the shape of a 10 μm potential well. (b) Red solid line: $\mathcal{B}_{\rm ad}$ for a soliton incident on a well of waist 3 μm. Black dashed line: The potential due to the well. Counterintuitively, the peak of $\mathcal{B}_{\rm ad}$ occurs well away from the steepest gradient in the potential. (c) $\mathcal{B}_{\rm ad}$ (quantified by the colour map) is given as a function of the depth of the well and position of soliton after its release. The maximum well depth corresponds to $P = 10$ μW. The dashed white line indicates the shape of a 3 μm potential well. The contour is at $\mathcal{B}_{\rm ad} = 0.1$. When the well depth is comparable to the kinetic energy of the incoming soliton (KE $\sim$ 2 nK), the greatest value of $\mathcal{B}_{\rm ad}$ can be found at the steepest part of the potential. (d) $\mathcal{B}_{\rm ad}$ (quantified by the colour map) is given as a function of the depth of the well and position of soliton after its release. The maximum trap depth corresponds to $P = 1$ W. The dashed white line indicates the shape of a 3 μm potential well. The contour is at $\mathcal{B}_{\rm ad} = 0.1$. When the well depth is much larger than the kinetic energy of the incoming soliton, the greatest value of $\mathcal{B}_{\rm ad}$ moves to the wings of the well, due to the $1/k^3$ dependence of (2.47). The maximum value of $\mathcal{B}_{\rm ad}$ is very insensitive to the depth of the well.

For a given waist, far away from the potential, $\mathcal{B}_{\text{ad}}$ has a very low value due the change in potential being minimal. As the soliton approaches the well, $\mathcal{B}_{\text{ad}}$ rapidly increases, reaching a maximum before becoming zero at the centre of the well, due to the gradient being zero. $\mathcal{B}_{\text{ad}}$ is symmetric due to the symmetry of the well. Counterintuitively, the location of the $\mathcal{B}_{\text{ad}}$ maximum is separate from the steepest gradient in the potential. This is due to the fact that $\mathcal{B}_{\text{ad}}$ is dependent on both the wavevector of the soliton and the gradient of the potential. In the region of steepest gradient the wavevector has become much larger due to the increase in kinetic energy from the well. This increase in kinetic energy counters any benefit of a steep change in potential. As a result, the peak in $\mathcal{B}_{\text{ad}}$ is found outside the region in which the soliton gains a significant amount of kinetic energy, due to the well (see white dashed line of figure 2.3 (a)). Two contours are shown in figure 2.3 (a); the inner contour is for $\mathcal{B}_{\text{ad}} = 1$ (the region where we expect to observe significant quantum reflection) and the outer contour is for $\mathcal{B}_{\text{ad}} = 0.1$. In order to observe significant quantum reflection with the parameters chosen, we must produce a beam with a waist < 2 μm, which will be challenging. For clarity, figure 2.3 (b) shows a single cut of figure 2.3 (a) at a fixed waist of 3 μm. The solid red line shows the value of $\mathcal{B}_{\text{ad}}$ as a function of soliton position after release 100 μm from the trap centre. The offset of the $\mathcal{B}_{\text{ad}}$ peak from the peak in the potential (black dashed line) gradient is even more clear here.

The dependence of $\mathcal{B}_{\text{ad}}$ as a function of well depth is given in figure 2.3 (c) and (d). Panel (c) shows that when the depth of the well is comparable to the incoming kinetic energy of the soliton, the peak in $\mathcal{B}_{\text{ad}}$ is found at the steepest part of the potential. This can be understood as being due to the well not imparting a significant amount of kinetic energy to the soliton. The $1/k^3$ dependence of (2.47) doesn't increase by a large amount as the soliton traverses the potential. Therefore, the change in $1/k^3$ is significantly less than the change in the gradient of the potential, resulting in the potential governing where the peak value of $\mathcal{B}_{\text{ad}}$ occurs. Panel (d) gives a very different regime where the position of the $\mathcal{B}_{\text{ad}}$ peak has moved out to the wings of the potential. The reason for this is that the depth of the well is approximately *five orders of magnitude* larger than the incoming kinetic energy of the soliton. Now the change in $1/k^3$ becomes the dominant factor, cancelling out any benefit in having a steep potential. One other important aspect to note

is that, beyond the point where the well depth is comparable to the kinetic energy of the incoming soliton, the maximum value of $\mathcal{B}_{\rm ad}$ is very insensitive to the depth of the well.

In order to improve the characterisation of regions where quantum reflection is likely to occur, figure 2.4 is provided. For the two plots contained within this figure we give the maximum of $\mathcal{B}_{\rm ad}$ for a particular set of parameters. One example would be the peak of figure 2.3 (b). This maximum is investigated as a function of light-sheet (well) waist, soliton initial position and trap frequency. In each of the plots two contours are given, with the inner (lower) indicating a $\mathcal{B}_{\rm ad}$ maximum of 1 and the outer (higher) indicating a $\mathcal{B}_{\rm ad}$ maximum of 0.1.

In figure 2.4 (a) we have fixed $P = 10$ mW, $\lambda = 852$ nm and $\omega = 2\pi \times 1.00$ Hz and varied the waist of the light-sheet and initial offset of the soliton from the centre of the trap. In order to reach a region of high probability of quantum reflection we require $\mathcal{B}_{\rm ad} > 1$ which is given as a contour stretching from ($w_x = 2$ μm, $x_I = 0.1$ mm) to ($w_x = 0.5$ μm, $x_I = 0.4$ mm). There is a strong dependence of the $\mathcal{B}_{\rm ad}$ maximum on both the waist and initial position. In figure 2.4 (b) we vary the frequency of the harmonic trap and

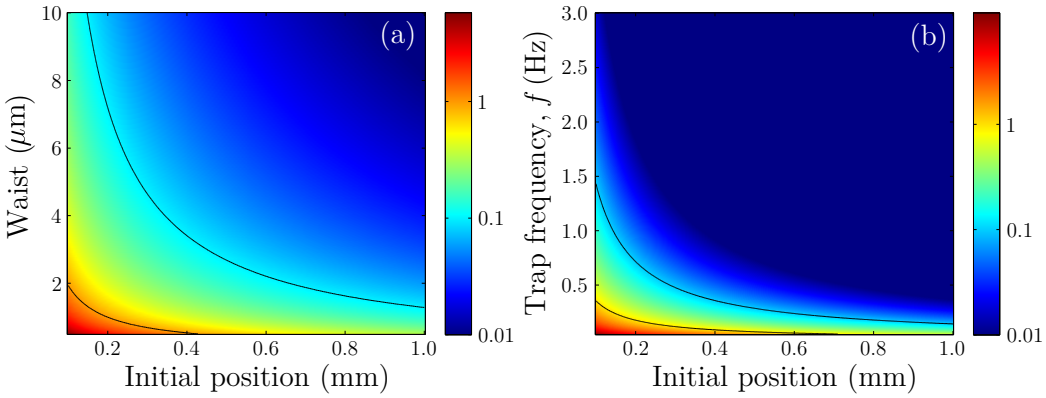

Figure 2.4: The likelihood of quantum reflection from a gaussian potential well as a function of a variety of parameters. Significant quantum reflection is expected to occur when $\mathcal{B}_{\rm ad} > 1$ (see (2.47)). A ^{85}Rb soliton is released off-centre from a harmonic trap and accelerates towards a gaussian potential well (a light sheet with waist 260 μm perpendicular to the soliton motion) located at the centre of the trap. The colour map quantifies $\mathcal{B}_{\rm ad}$. The inner contour is at $\mathcal{B}_{\rm ad} = 1$ and the outer contour at $\mathcal{B}_{\rm ad} = 0.1$. (a) The maximum value of $\mathcal{B}_{\rm ad}$ (the peak of figure 2.3 (b)) as a function of the $1/e^2$ radius (waist) of the barrier and initial offset of the soliton. $P = 10$ mW, $\lambda = 852$ nm and $\omega = 2\pi \times 1.00$ Hz. (b) The maximum value of $\mathcal{B}_{\rm ad}$ as a function of trap frequency f, where $\omega = 2\pi f$, and initial offset of soliton. $\lambda = 852$ nm, barrier waist is 3 μm and $P = 10$ mW.

the initial offset of the soliton, while fixing $\lambda = 852$ nm, $w_x = 3$ μm and $P = 10$ mW. In order to achieve a high likelihood of quantum reflection we must be within the contour stretching from ($\omega = 2\pi \times 0.4$ Hz, $x_I = 0.1$ mm) to ($\omega = 2\pi \times 0.05$ Hz, $x_I = 0.7$ mm).

The potential barrier

We now repeat a similar set of calculations for a $\lambda = 532$ nm potential barrier and will see that the parameter space, or $\mathcal{B}_{\text{ad}}$, in this circumstance is very different to a potential well. A potential well possesses no classical turning point, regardless of depth, resulting in a badlands function that is always real. In contrast to this, a potential barrier possesses a classical turning point when its height is greater than the kinetic energy of the incoming soliton. Therefore, this causes k to become complex (see (2.47) and the text above), which means that the classical turning point has been reached, resulting in quantum and classical reflection becoming indistinguishable from one another.

Figure 2.5 (a) gives the dependence of $\mathcal{B}_{\text{ad}}$ (the colour map) on the barrier waist and position of an incoming soliton for an initial soliton offset of $x_I = 0.1$ mm in a harmonic trap with frequency $\omega = 2\pi \times 1.00$ Hz, with the barrier at the minimum of the harmonic trap. $\mathcal{B}_{\text{ad}}$ remains symmetric about the barrier, however, the position of the maximum is much closer to the peak of the barrier than in the case of the potential well (see figure 2.3). Contours are, once again, given at $\mathcal{B}_{\text{ad}} = 1$ (inner contour) and $\mathcal{B}_{\text{ad}} = 0.1$ (outer contour). The white dashed line shows the profile of a gaussian barrier with a $1/e^2$ radius of 3 μm.

The stark difference between the most likely position of reflection (the maximum in $\mathcal{B}_{\text{ad}}$) in a potential barrier and well is clearly seen when comparing figure 2.5 (b) with figure 2.3 (b). The peak in $\mathcal{B}_{\text{ad}}$ is very close to the centre for a barrier, but extends much further out in the well. This is because the barrier has the effect of slowing down a soliton, aiding the likelihood of reflection, whereas the potential well accelerates the soliton towards its centre, reducing the likelihood of reflection. The profile of a 3 μm barrier is given by the dashed line in figure 2.5 (b).

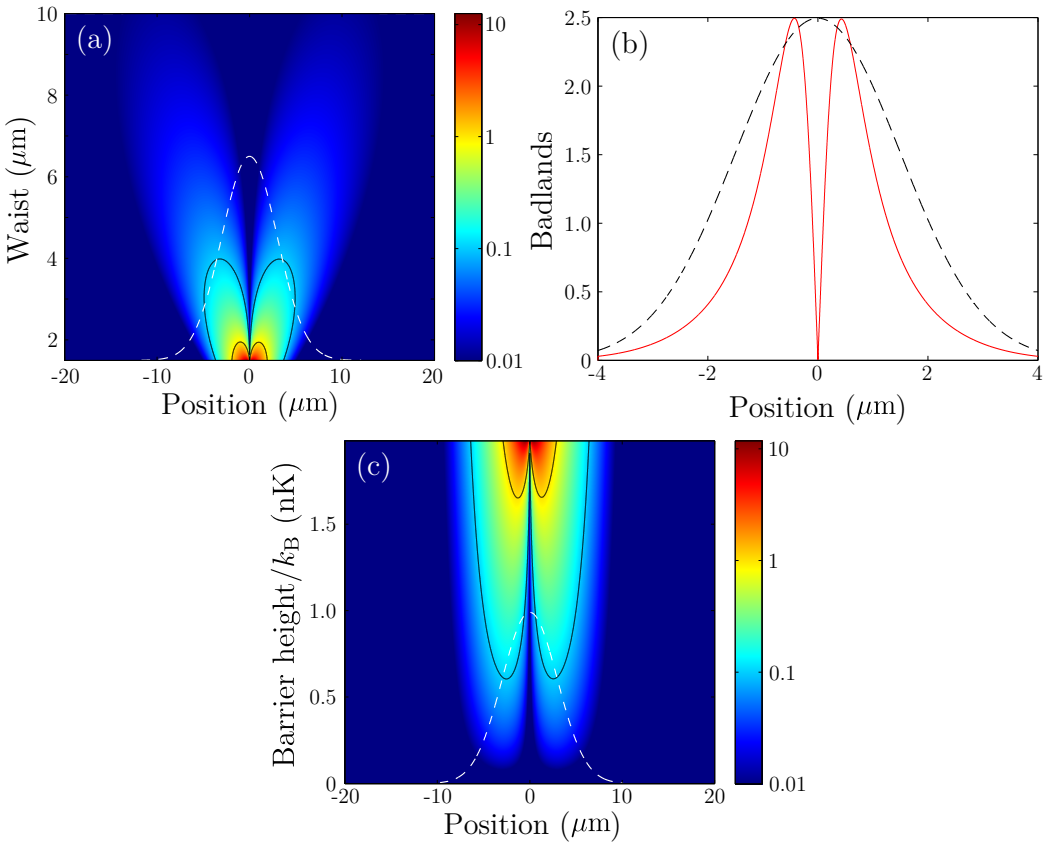

Figure 2.5: The effect of altering the width and height of a repulsive barrier on quantum reflection. The colour map gives the value of $\mathcal{B}_{\rm ad}$. Contours are given at $\mathcal{B}_{\rm ad} = 1$ (inner contour) and $\mathcal{B}_{\rm ad} = 0.1$ (outer contour). The dashed line gives the profile of a barrier with a $1/e^2$ radius of 3 μm. The initial offset of the soliton is kept constant at $x_I = 0.1$ mm and the wavelength of the light sheet forming the barrier is $\lambda = 532$ nm. (a) $\mathcal{B}_{\rm ad}$ as a function of barrier waist and soliton position for a light sheet with a power of $P = 21$ μW. The maximum of $\mathcal{B}_{\rm ad}$ remains close to the peak of the barrier. (b) $\mathcal{B}_{\rm ad}$ as a function of soliton position for $P = 40$ μW and $w_x = 3$ μm. (c) $\mathcal{B}_{\rm ad}$ as a function of barrier height and soliton position for a light sheet with a waist of $w_x = 3$ μm. Beyond a barrier height of 2 nK the soliton classically reflects and $\mathcal{B}_{\rm ad}$ becomes complex (see main text).

In figure 2.5 (c) we observe the effect of increasing the barrier height for a soliton with a constant initial offset of $x_I = 0.1$ mm in a harmonic trap with frequency $\omega = 2\pi \times 1.00$ Hz. The maximum value of $\mathcal{B}_{\rm ad}$ remains close to the peak of the barrier and rapidly approaches very high values close to the classical turning point, where the height is $\sim k_{\rm B} \times 2$ nK. Contours are given at $\mathcal{B}_{\rm ad} = 1$ (inner contour) and $\mathcal{B}_{\rm ad} = 0.1$ (outer contour). In the case of a barrier, a small initial offset of the soliton is not necessarily beneficial, unlike the case of a well. Having a small offset ($x_I = 0.1$ mm) results in the need for very low barrier heights ($\sim k_{\rm B} \times 2$ nK) in order to possibly observe quantum

reflection, as we must not increase the barrier height beyond the classical turning point for the soliton. Therefore, greater initial positions would be beneficial as we would not need to stabilize the height of the barrier to such a small value. An additional complication is that the region over which $\mathcal{B}_{\mathrm{ad}} > 1$ is extremely close to the classical turning point, making it potentially very difficult to distinguish between classical and quantum reflection. This problem does not manifest itself for a potential well as it does not possess a classical turning point. This narrow region of high quantum reflection probability is even more apparent in figure 2.6.

The dependence of the maximum $\mathcal{B}_{\mathrm{ad}}$ as a function of barrier waist and soliton initial position are given in figure 2.6 (a), for $\lambda = 532$ nm, $P = 4$ mW and $\omega = 2\pi \times 1.00$ Hz. The region where quantum reflection is likely to occur ($\mathcal{B}_{\mathrm{ad}} > 1$) is very narrow, resulting in the need for precise and stable control over the experimental parameters; otherwise, it will become impossible to distinguish between quantum reflection and classical reflection. This figure demonstrates that for a potential barrier it is possible to observe quantum reflection over a large range of soliton initial positions by varying the waist (or height) of the barrier. This is much more difficult to achieve for the potential well (see figure 2.3).

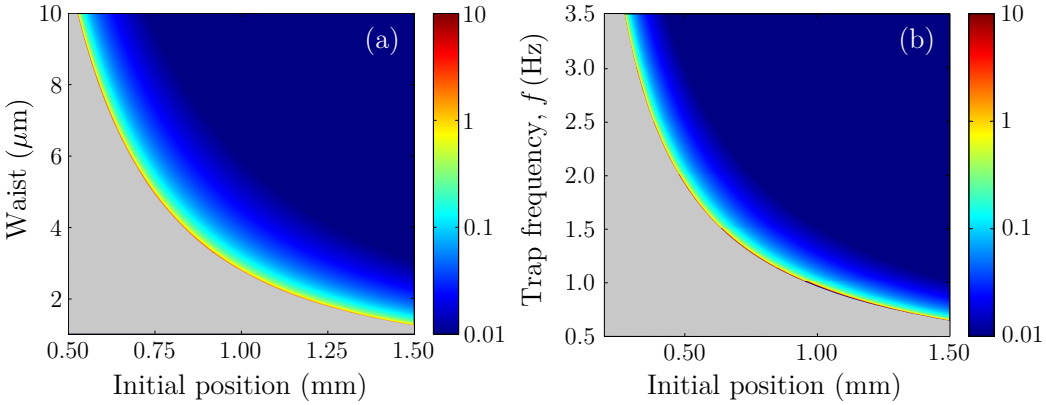

Figure 2.6: The likelihood of quantum reflection from a gaussian potential barrier as a function of a variety of parameters. During these calculations the following quantities are kept constant; $\lambda = 532$ nm and $P = 4$ mW. Note the narrow region over which $\mathcal{B}_{\mathrm{ad}} > 1$ in both of these plots. The greyed out regions are where the soliton reaches a classical turning point and $\mathcal{B}_{\mathrm{ad}}$ becomes complex. (a) The maximum of $\mathcal{B}_{\mathrm{ad}}$ as a function of barrier waist and soliton initial position for $\omega = 2\pi \times 1.00$ Hz. (b) The maximum of $\mathcal{B}_{\mathrm{ad}}$ as a function of trap frequency and soliton initial position for $w_x = 3$ μm.

The same analysis is undertaken in figure 2.6 (b) for variable trap frequency and soliton initial position, where $\lambda = 532$ nm, $P = 4$ mW and $w_x = 3$ μm. The similar appearance of this figure to (a) shows how flexible the $\mathcal{B}_{\text{ad}}$ parameter space is for producing high reflection probabilities with a potential barrier, with the caveat that the parameters are precisely known and kept stable.

Comparing the potential well and barrier

In order to truly demonstrate the similarities and stark differences between a soliton interaction with a potential well and barrier, we present figure 2.7, where the position and value of the peak in $\mathcal{B}_{\text{ad}}$ is given for a potential well and barrier as a function barrier height or well depth.

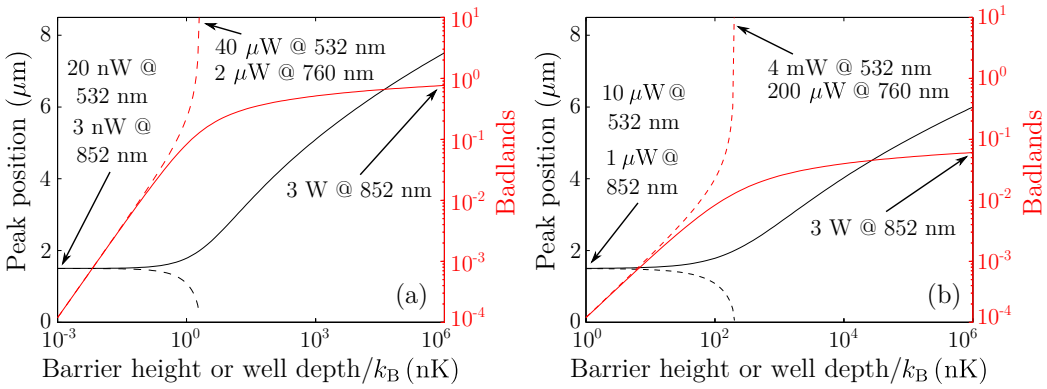

Figure 2.7: The position and value of the badlands peak as a function of barrier height and well depth. Red solid line: The maximum value of $\mathcal{B}_{\text{ad}}$ for the potential well. Red dashed line: The maximum value of $\mathcal{B}_{\text{ad}}$ for the potential barrier. Black solid line: The position of the maximum $\mathcal{B}_{\text{ad}}$ value for the potential well. Black dashed line: The position of the maximum $\mathcal{B}_{\text{ad}}$ value for the potential barrier. $\lambda = 532$ nm for the barrier and $\lambda = 852$ nm for the well, although powers are also given for a barrier at $\lambda = 760$ nm. The other quantities that are kept constant are $w_x = 3$ μm and $\omega = 2\pi \times 1.00$ Hz. Key powers at different wavelengths, that correspond to particular barrier heights or well depths are given in the figures. (a) $\mathcal{B}_{\text{ad}}$ peak position and $\mathcal{B}_{\text{ad}}$ as a function of barrier height and well depth for $x_I = 0.1$ mm. (b) $\mathcal{B}_{\text{ad}}$ peak position and $\mathcal{B}_{\text{ad}}$ as a function of barrier height and well depth for $x_I = 1$ mm.

In figure 2.7 (a) the dependence of the $\mathcal{B}_{\text{ad}}$ peak position and value on the barrier height and well depth are given. For very low heights ($< k_{\text{B}} \times 0.1$ nK, which is ~ 5 % of the soliton kinetic energy) it is impossible to distinguish the difference between a barrier and a well. Both peak positions and $\mathcal{B}_{\text{ad}}$ values are almost exactly the same. This can be understood by referring to

(2.47). As $\mathcal{B}_{\text{ad}}$ is inversely proportional to $1/k^3$, if the depth or height of the potential is minimal in comparison with the soliton velocity, k just becomes approximately equal to the wavevector of the incoming soliton. k is barely perturbed by the presence of the shallow potential. $\mathcal{B}_{\text{ad}}$ is still proportional to the magnitude of the potential gradient, which is exactly the same for a potential barrier or well with the same profile. Therefore, for a soliton with the same incoming kinetic energy, a barrier and well will approach the same value of $\mathcal{B}_{\text{ad}}$ and peak position for potentials that don't significantly perturb the soliton wavevector.

As the height (depth) of a barrier (well) becomes comparable to the incident kinetic energy of the soliton, the barrier (well) increasingly perturbs the soliton wavevector and the two cases dramatically diverge. The increase in kinetic energy due to the well has a negative impact on the value of $\mathcal{B}_{\text{ad}}$, as it levels off, approaching an asymptotic limit. This is directly linked to the $1/k^3$ dependence of $\mathcal{B}_{\text{ad}}$. Conversely, for a barrier the value of $\mathcal{B}_{\text{ad}}$ rapidly increases, due to the reduction of the soliton kinetic energy, significantly increasing the $1/k^3$ term in (2.47). As stated earlier, $\mathcal{B}_{\text{ad}}$ becomes complex beyond the classical turning point, which is being asymptotically approached by the barrier curves (red and black dashed lines) in figure 2.7 (a).

Another difference between the well and barrier is that as the height or depth of the potential increases, the $\mathcal{B}_{\text{ad}}$ peak approaches the centre of the barrier, whereas it approaches the wings of the well. For a small initial soliton offset ($x_I = 0.1$ mm in figure 2.7 (a)), the classical turning point is at very low laser powers—40 μW at $\lambda = 532$ nm or 2 μW at $\lambda = 760$ nm. Achieving stable quantum reflection from a barrier will be difficult in this regime, however, the $\mathcal{B}_{\text{ad}}$ curve for the well, is significantly more gentle, approaching $\mathcal{B}_{\text{ad}} \sim 1$. Therefore, it can be concluded that small initial soliton offsets are beneficial for potential wells but prove difficult for barriers.

The previous point is reinforced when observing the behaviour in figure 2.7 (b). The initial offset is now $x_I = 1$ mm and no other parameters are changed. The asymptotic limit of $\mathcal{B}_{\text{ad}}$ is significantly reduced for the well, due to the increased kinetic energy of the soliton having an adverse effect on the $1/k^3$ dependence of $\mathcal{B}_{\text{ad}}$. The barrier, however, does not suffer from the increased soliton kinetic energy. It is simply a matter of increasing the height of the barrier such that the soliton, once again, becomes close to the classical

turning point. As can be seen in (b), a rapid change in peak position and value can be seen near the turning point, although, as expected, the required barrier height to reach this point has increased when compared with (a). The classical turning point is reached around 4 mW at $\lambda = 532$ nm or 200 μW at $\lambda = 760$ nm. These values are much more reasonable to stabilise in an experimental scenario, allowing it to be concluded that releasing the soliton a reasonable distance from the barrier ($x_I \sim 1$ mm) is beneficial for an interaction with a barrier, but not for a soliton interaction with a potential well.

One final conclusion that can be drawn from this analysis is that continuing to increase the depth of a potential well does *not* make it significantly more likely that quantum reflection will manifest itself. Instead, it is essential that the waist of the well is as narrow as possible. Conversely, finely tuning of the height of a potential barrier has a significant effect on the likelihood of observing quantum reflection, with a less stringent requirement of barrier width (see figure 2.6 (a)). However, one unfortunate difficulty in this scenario can be distinguishing between quantum and classical reflection.

2.5.2 Solitary wave size and imaging

As we will discover in section 3.2.1, our imaging system has a finite resolution that is fundamentally limited by diffraction. In addition to this, our lenses introduce aberrations which further decrease the resolution of our imaging system. Finally, if the object we are imaging has a size of the order of a few pixels, the discretisation from the CCD also introduces a further notable decrease in the resolution.

We will now attempt to calculate a lower bound for the measured size of a solitary wave using our imaging system. The reason that this is a lower bound, is that we have been unable to determine the extent to which aberrations, due to our lens system, limit our resolution[16]. Therefore we will only account for diffraction and discretisation.

Using (3.15), we later determine that the resolution of our horizontal imaging system is $R = 3.8$ μm. Approximating the Airy pattern that forms when a

[16]We have made every effort to use high quality imaging lenses, in order to reduce the effect of aberrations to as small a value as possible.

beam with $\lambda = 780$ nm (our imaging beam) is focussed to a spot, by a gaussian with a root mean square radius of $\sigma_{\text{diff}} = 3.8/2 = 1.9$ μm allows us to determine the resulting imaged size of a solitary wave by convolving the solitary wave profile (also approximated with a gaussian) with the diffraction limited profile. Using the three-dimensional variational methods discussed in section 2.3.5 we predict the root mean square radius of the solitary wave to be $\sigma_{\text{sw:ax}} = 2.3$ μm axially and $\sigma_{\text{sw:rad}} = 2.0$ μm radially. The convolution of two gaussians with widths σ_A and σ_B results in a new gaussian with $\sigma_C^2 = \sigma_A^2 + \sigma_B^2$. Therefore, the diffraction limited axial and radial sizes become,

$$\sigma_{\text{tot:ax}} = \sqrt{\sigma_{\text{diff}}^2 + \sigma_{\text{sw:ax}}^2} = 3.0 \ \mu\text{m}, \quad \sigma_{\text{tot:rad}} = \sqrt{\sigma_{\text{diff}}^2 + \sigma_{\text{sw:rad}}^2} = 2.7 \ \mu\text{m}. \tag{2.50}$$

Beyond the above values, aberrations with the lenses in the imaging system will increase the minimum measureable sizes. However, we will not discuss this here due to there currently being an absence of this data for our imaging system (see above). The final notable source of error is the discretisation of the images, which increases the size of the smallest resolvable object. An analysis of how the level of noise and width of cloud affects the ability to fit the resulting image is presented below.

For simplicity, a one-dimensional gaussian cloud is generated, with form

$$\text{OD}_{\text{1D}}(x) = \exp\left(-\frac{x^2}{2\sigma_{\text{cloud}}^2}\right), \tag{2.51}$$

where $\text{OD}_{\text{1D}}(x)$ is the optical depth (amplitude) of the cloud at a given position. In order to present this analysis in its most general form, the peak optical depth of (2.51) is scaled to 1. The optical depth is then sampled at regular discrete intervals which correspond to individual pixels of a CCD. In addition to this, random noise, $\text{OD}_{\text{noise}}(x)$, is introduced to the distribution in order to present a more realistic comparison to an experimental scenario. The level of noise will be described as the fractional mean noise (FMN). A FMN of 0.1 corresponds to isotropic random noise with range $-0.1 \leq \text{OD}_{\text{noise}}(x) \leq 0.1$ relative to the peak optical depth of 1, which can be expressed more generally as $-\text{FMN} \leq \text{OD}_{\text{noise}}(x) \leq \text{FMN}$. Finally, for figures 2.8 and 2.9 the resulting plots have a total optical depth OD_{tot} which

can be expressed as

$$\mathrm{OD}_{\mathrm{tot}}(x) = \mathrm{OD}_{\mathrm{1D}}(x) + \mathrm{OD}_{\mathrm{noise}}(x). \tag{2.52}$$

An example of how the level of noise affects the ability to resolve a moderately sized cloud ($\sigma_{\mathrm{cloud}} = 10$ px) is given in figure 2.8. The solid red line represents the scaled gaussian, $\mathrm{OD}_{\mathrm{1D}}$, prior to the addition of any noise. The dashed blue line represents the gaussian fit to $\mathrm{OD}_{\mathrm{tot}}(x)$.

In figure 2.8 (a), a discretised gaussian can be seen with FMN = 0. Both the original curve (solid red line) and the curve fitted to the discretised data (dashed blue line) are seen to overlap. Negligible information has been lost in the process of discretisation. This is not the case when noise is introduced to the picture. Panels (b-f) show the same cloud with varying levels of noise; (b) FMN = 0.1, (c) FMN = 0.2, (d) FMN = 0.3, (e) FMN = 0.5 and (f) FMN = 1.0. It can be seen that in each of these examples the original curve and fitted curve are both very similar, but not exactly the same. The addition of noise has removed information from the discretised curve. However, it is perhaps surprising that when the mean level of noise is the same as the peak optical depth (FMN = 1.0) the fitted curve still bears a close resemblance to the original curve. The width of the gaussian is such

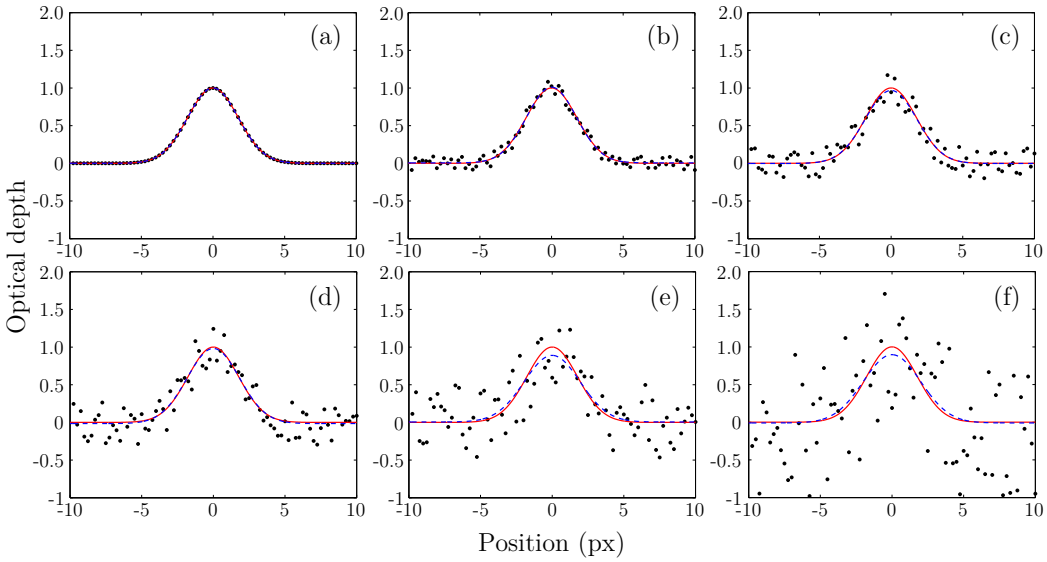

Figure 2.8: The effect of random noise on the ability to fit to a discretised gaussian with a root mean square radius of 10 px. Black points: $\mathrm{OD}_{\mathrm{tot}}(x)$. Red solid line: $\mathrm{OD}_{\mathrm{1D}}(x)$. Blue dashed line: Gaussian fit to $\mathrm{OD}_{\mathrm{tot}}(x)$. The fractional mean noise is (a) 0, (b) 0.1, (c) 0.2, (d) 0.3, (e) 0.5 and (f) 1.0.

that a region at the bottom middle of panel (f) can be observed to have no data points present. If no peak was present it would be highly unlikely to find no data points over such a broad region, therefore, the fitting algorithm finds the data masked by the high level of noise. Another way in which to think of this is that essentially redundancy is built into such a wide cloud, with many pixels describing its profile. If one pixel is shifted up due to the random noise, it is likely that another nearby will be shifted down, compensating for the original shift. The result is that the fitting algorithm can find a path describing the profile of the original cloud, almost hidden amongst the noise.

An important point to note is that while true optical depth is a quantity that cannot be negative, the quantity shown in figures 2.8 and 2.9 is the *inferred* optical depth. Three different images (absorption, probe and background—see section 3.2.1) are combined to reach the inferred optical depth. In between the absorption and probe images minor vibrations in the apparatus can direct the laser light along a slightly different path. The result of this is a mismatch between the absorption and probe images, resulting in the possibility of more power being measured in the probe image than is expected.

As the width of the cloud decreases, the number of pixels describing its profile also decreases, resulting in a reduction in redundancy. Therefore, when the width of the gaussian becomes comparable to the size of a pixel, this redundancy becomes negligible. Figure 2.9 demonstrates this effect, showing a similar study to above but for a gaussian with $\sigma_{\text{cloud}} = 0.75$ px.

Once again, panel (a) shows excellent agreement between the original curve and the fit. With so few discretised points describing the gaussian profile, the values of the points in its wings are critical in allowing the algorithm to find the correct parameters for the fitted gaussian. The moment any noise is introduced, the data in the wings becomes significantly less useful and eventually the gaussian is indistinguishable from from the background noise (see transition from (b) to (f) in figure 2.9). The algorithm simply fits a very wide gaussian ($\sigma \gg 1$) though the data and it becomes impossible to extract sensible a width.

In order to quantify the limits imposed by discretisation, with the addition of random noise, figure 2.10 was created. In panel (a), the fractional difference between the fitted and original cloud widths are given for different values of FMN, as a function of σ_{cloud}. For FMN > 0.1 we observe very sudden changes

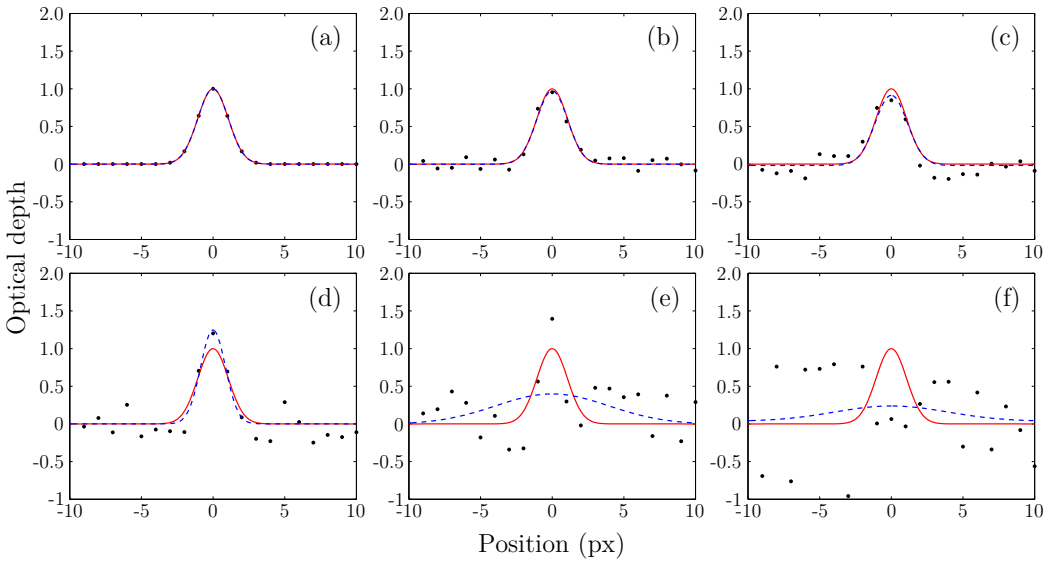

Figure 2.9: The effect of random noise on the ability to fit to a discretised gaussian with a root mean square radius of 0.75 px. Black points: $\mathrm{OD}_{\mathrm{tot}}(x)$. Red solid line: $\mathrm{OD}_{\mathrm{1D}}(x)$. Blue dashed line: Gaussian fit to $\mathrm{OD}_{\mathrm{tot}}(x)$. The fractional mean noise is (a) 0, (b) 0.1, (c) 0.2, (d) 0.3, (e) 0.5 and (f) 1.0.

from accurate fitting to an inability to fit as σ_{cloud} is reduced. The y-axis of (a) has been truncated at 1, as the sudden switching results in $\sigma_{\mathrm{fit}} \gg \sigma_{\mathrm{cloud}}$, indicating an unusable fit. The general trend is that as the FMN is reduced it is possible to resolve smaller and smaller clouds that would have been masked by greater levels of noise. The limit of this is FMN = 0, which results in effectively no error in the fitted curve down to $\sigma_{\mathrm{cloud}} = 0.3$ px, and most likely continuing well below this value. This sudden switching behaviour is not present at FMN < 0.1. Instead, a general trend of $\sigma_{\mathrm{fit}} < \sigma_{\mathrm{cloud}}$ begins to appear at $\sigma_{\mathrm{cloud}} \sim 0.5$ px. This can be understood as occurring due to loss of data in the wings of the gaussian from the addition of noise. This loss of data in the wings means that the fitting algorithm only has a very small number of data points from which to determine the cloud width. With discretisation and lack of data in the wings, the result is that the fitting algorithm underestimates the width of the cloud (see figure 2.9 (d) for a particular example).

In figure 2.10 (b) the minimum resolvable cloud size is given as a function of the fractional mean noise. The data demonstrates the expected trend of increasing FMN resulting in the minimum resolvable cloud size also increasing. In other words, as the noise level increases, we must introduce more

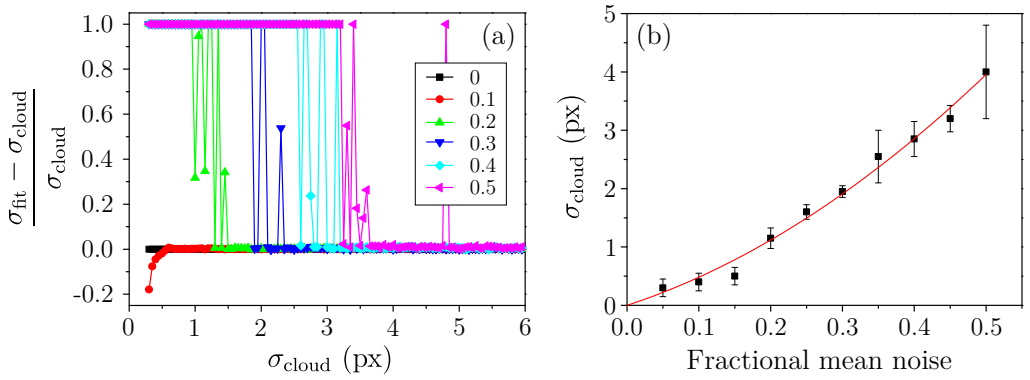

Figure 2.10: Determining the minimum cloud radius that can be measured for a given mean amplitude of random noise. (a) The fractional difference between the original cloud width and fitted cloud width as a function of the original cloud width and fractional mean noise (FMN). The key gives the FMN for the different curves. The y-axis is truncated at 1 due to it becoming exceptionally large when the algorithm can no longer fit the cloud (see figure 2.9 (e-f) for an example). Note that in the majority of cases the fitting becomes poor very suddenly, switching rather than following a general trend. At lower noise levels, the general trend is to initially reduce the size of the fitted sigma (see the red line/circles). (b) The minimum resolvable cloud size as a function of fractional mean noise. A phenomenological quadratic fit provides straightforward access to relevant quantities. For a function of form $\sigma_{\text{cloud}} = A \times \text{FMN} + B \times \text{FMN}^2$, the fitted parameters are $A = 4.0(6)$ and $B = 7(2)$.

redundancy[17] to compensate. A quadratic phenomenological fit of the form $\sigma_{\text{cloud}} = A \times \text{FMN} + B \times \text{FMN}^2$ is provided to allow for efficient calculations to be undertaken. As a result of the fitting, the parameters are $A = 4.0(6)$ and $B = 7(2)$.

The typical mean experimental noise lies in the range $0.05 \leq \text{OD} \leq 0.1$ and the typical peak optical depth of a measured cloud is in the range $0.2 \leq \text{OD} \leq 1.8$. The solitons observed in section 6.7.1, have an optical depth $\sim$ 0.4. The value of the resulting maximum fractional mean noise is $\text{FMN} = 0.1/0.4 = 0.25$, giving a maximum resolvable cloud size of $\sigma_{\text{cloud}} = 1.4(5)$ px, using the fit to figure 2.10 (b). For measured optical depths of 0.2, the maximum resolvable cloud size becomes $\sigma_{\text{cloud}} = 4(1)$ px and for clouds with a measured peak optical depth of 1.8, the maximum resolvable cloud size reduces to $\sigma_{\text{cloud}} = 0.24(8)$ px.

From this brief analysis it is clear that in some of our experimental scenarios it should be possible to resolve clouds with a root mean square radius that

[17] More densely packed discretised data points over the cloud profile.

is below 1 pixel. This is surprising, due to the fact that in section 6.7.1 we measure solitary waves with a sizes of ~ 2 px, when they should be ~ 0.5 px. The conclusion that can be drawn from this is that aberrations in the lens are the most likely source of the increased size of the measured solitary wave, rather than the process of discretisation.

2.5.3 Solitary wave profile

As a final analysis we will investigate the profile of a solitary wave in a variety of different three dimensional trap geometries through the solution of (2.43). The experimental parameters that are required to produce solitary waves that are very similar to their one-dimensional counterparts will be provided. The extent to which a three-dimensional solitary wave is similar to its one-dimensional counterpart will be refered to as how *solitonlike* it is. Finally, comparisons will be provided between the solitary waves produced by a variety of groups, focussing on how solitonlike these manifestations were.

Using expressions and methods provided by Billam *et al.* [202] (see section 2.3.5), we provide the axial variational parameter ℓ_s as a function of κ, the dimensionless ratio of trap frequencies, and γ in figure 2.11. The position of experimental manifestations of solitary waves in this parameter space are also given in the figure. The accompanying table 2.2 gives the experimental parameters used to calculate κ and γ for these manifestations.

Experiment	Mass (a.m.u.)	ω_x (Hz)	ω_r (Hz)	N	a (a_0)
Rice (2002) [27]	7	$2\pi \times 4$	$2\pi \times 800$	5000	-3
JILA (2006) [56]	85	$2\pi \times 7$	$2\pi \times 17.5$	1500	-11
Durham (2012) [80]	85	$2\pi \times 1.17$	$2\pi \times 22.4$	2500	-12

Table 2.2: The experimental parameters that were used to calculate κ and γ in order to plot the points in figure 2.11. Mass is given in atomic mass units (a.m.u.), where 1 a.m.u. $= 1.66 \times 10^{-27}$ kg.

The outer contour of figure 2.11 gives where $\ell_s = 0.9$ and the inner contour gives where $\ell_s = 0.99$. ℓ_s effectively describes how solitonlike a three-dimensional solitary wave is, with values of ℓ_s close to 1 being highly solitonlike. The smaller the value of ℓ_s, the more the axial solitary wave length has been pulled inwards in comparison with its one-dimensional equivalent. All experimental manifestations of solitary waves can be seen to have been generally near to the point of collapse. The experiments at Rice University

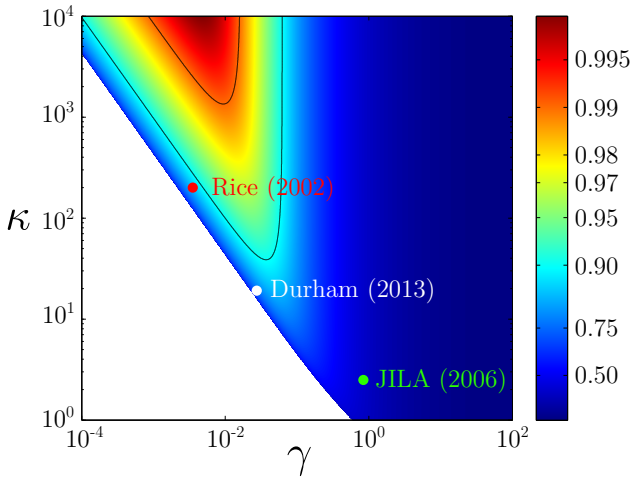

Figure 2.11: The variational axial parameter ℓ_s as a function of κ and γ (see section 2.3.5). The colour map quantifies the value of ℓ_s and is provided on a logarithmic scale. The outer contour is where $\ell_s = 0.9$ and the inner contour where $\ell_s = 0.99$. The white region is where it is not possible to form a solitary wave as the parameters lead to its collapse and the expulsion of atoms. Values of ℓ_s are plotted for past and current solitary wave experiments. Note that the ENS experiment [28] could not be plotted as the calculation is only valid for confining harmonic potentials.

were closest to achieving a highly solitonlike manifestation, with $\ell_s \sim 0.9$. It is clear from figure 2.11, that if one wishes to form solitonlike solitary waves ($\ell_s > 0.9$) it is necessary to have $\kappa \gtrsim 40$, which has already been demonstrated by one group, as shown in the figure. To achieve $\ell_s > 0.99$, we must be even more stringent, requiring $\kappa \gtrsim 2000$. This extreme trap anistropy is much more difficult to achieve experimentally, needing either an optical lattice or a very weak focus (waist $> 300\ \mu$m). The downside of a weak focus is that the axial trap frequency is of the order of mHz, which doesn't help with observing interesting solitary wave dynamics.

In section 2.5.2 we discussed the potential difficulties in resolving solitary waves manifested in our experiment. Rather than attempting to continue improving our imaging system, another possibility would be to increase the size of the solitary wave. In soliton units, the axial profile of the solitary wave is maximised when $\ell_s = 1$, therefore if we want to achieve a reasonable axial length it is recommended that $\ell_s > 0.9$ and, as a result, $\kappa \gtrsim 40$. The absolute solitary wave axial length is $\ell_s a_s$, where $a_s = \hbar/(2m\omega_r|a|N)$ (see section 2.3.5). Therefore, it is also necessary to maximise a_s by reducing the scattering length a or the atom number N. In order to maintain a reasonable optical depth, it is recommended that the scattering length is

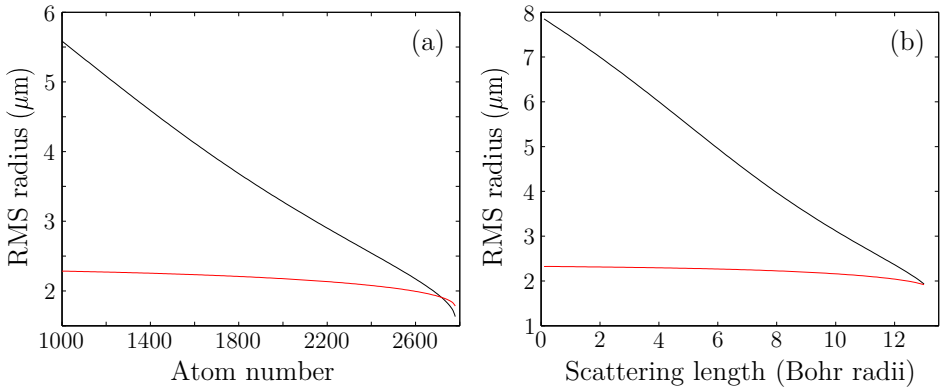

Figure 2.12: The axial (black line) and radial (red line) root mean square radius of a solitary wave, trapped in a quasi-one-dimensional waveguide, as a function of (a) atom number and (b) s-wave scattering length. The variational method presented in section 2.3.5 has been used to obtain these sizes. The following parameters are kept constant in both plots: $\omega_x = 2\pi \times 1.00$ Hz, $\omega_r = 2\pi \times 22.0$ Hz and $m = 1.41 \times 10^{-25}$ kg. (a) Root mean square radius as a function of atom number for $a = -12\ a_0$. (a) Root mean square radius as a function of s-wave scattering length for $N = 2500$.

the parameter that is reduced. Doing so could potentially lead to solitary waves that span many pixels, allowing for more solitary wave detail being resolvable. Figure 2.12 gives the absolute sizes of a solitary wave, in the axial and radial directions, trapped in the waveguide described in chapter 6, by using the variational method presented in section 2.3.5.

2.6 Conclusion

In this chapter we have discussed the necessary soliton and solitary wave background and theory to understand the motivation behind this experiment and its results. Recent theoretical progress has also been presented with the focus on predicting and understanding experimental results. An experimental outlook was also provided, noting the difficulty in achieving certain scenarios using our current apparatus. Finally, theoretical analysis was undertaken in three key areas of experimental interest, namely, quantum reflection, solitary wave size and solitary wave profile.

Part II

Experimental details

Chapter 3

Overview of experimental apparatus and routines

Comprehensive descriptions of our experimental apparatus have already been provided in a variety of forms elsewhere [69, 72, 78]. Therefore, in this chapter we will only provide a brief summary of the apparatus, routines and diagnostics used in the day to day running of the experiment.

3.1 Experimental apparatus

3.1.1 Overview of Apparatus

Our experimental apparatus is split into two main sections. Both of these sections perform different functions and are also physically separated—each on its own table. One table prepares the majority of the laser light for the experiment, which is briefly discussed in section 3.1.2, which is then sent via optical fibres to the second table, housing the the vacuum system. It is this second table that we will present in this section (see figure 3.1).

The vacuum system is split into two sections; the magneto-optical trap (MOT) chamber and the science cell. These sections are connected through a differential pumping stage, which allows relatively high pressures in the MOT chamber, for fast loading of atoms, while providing an environment that enables long lifetimes in the science cell. Once atoms are captured in the MOT, they are transferred into a magnetic quadrupole trap mounted on

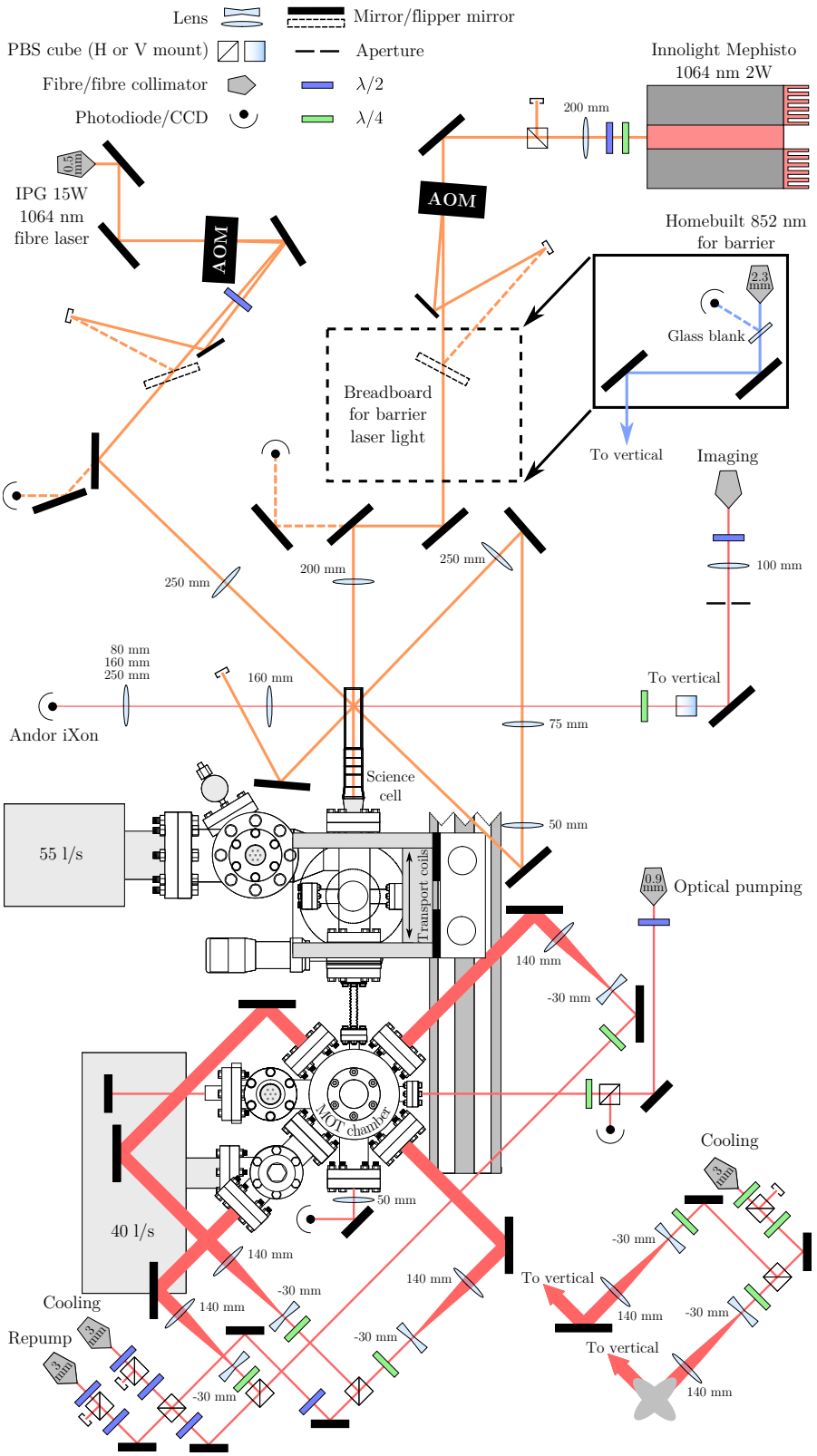

Figure 3.1: The complete experimental apparatus on the table containing the vacuum chamber. The $1/e^2$ radii of the collimated beams emerging from the fibre collimators are contained within their symbol.

a translation stage (Parker 404XR), which we refer to as the transport coils. The transport coils physically move from being centred on the MOT chamber to being centred on the science cell, transporting the low-field-seeking $F = 2$, $m_F = -2$ ^{85}Rb ($F = 1$, $m_F = -1$ ^{87}Rb) atoms along with them. Before the atoms reach the science cell, they are transported over an obstacle (see section 3.1.3), via a bias field, which provides isolation of the science cell from any stray hot atoms that could be travelling from the MOT chamber. Once the atoms reach the science cell, they are in a region of the vacuum system with excellent optical access. This reduces the restrictions on the placement of imaging, dipole trap and any other required laser beams.

3.1.2 Laser system

Our laser table houses two Toptica DL100 lasers with an additional Toptica BoosTA tapered amplifier (see table 3.1), which increases the power of the beam that will be used in the MOT, allowing a greater MOT beam diameter to be used. All light that is utilised for spectroscopy, cooling, repumping, optical pumping and imaging is derived from these three lasers. Table 3.2 lists the transitions and detunings relative to these transitions for the derived laser light.

In order to stabilise the frequency of the DL100 lasers we exploit two different methods of spectroscopy. For the laser providing the cooling light we use modulation transfer spectroscopy [209]; locking -230 MHz from the ^{85}Rb D_2 ($5^2S_{1/2} \rightarrow 5^2P_{3/2}$) $F = 3 \rightarrow F' = 4$ transition. The repump laser is locked -230 MHz from the ^{85}Rb D_2 $F = 2 \rightarrow F' = 3$ transition, using frequency modulation spectroscopy [210]. This -230 MHz detuning from the relevant transitions has been chosen as it allows the greatest flexibility in the range of frequencies that our acousto-optic modulators (AOMs) are able to access. Using AOMs in our optical setup has the added benefit of fast on–off switching times for our beams. We investigate the merging of clouds of ^{85}Rb and ^{87}Rb in chapter 5. The relevant transitions for ^{87}Rb in these investigations are the cooling, D_2 $F = 2 \rightarrow F' = 3$, and repump, D_2 $F = 1 \rightarrow F' = 2$.

Laser	Wavelength	Linewidth	Power	Application
Toptica DL100	780 nm	< 100 kHz	< 150 mW	Deriving cooling, spectroscopy and probe light
Toptica DL100	780 nm	< 100 kHz	< 150 mW	Deriving repump and spectroscopy light
Toptica BoosTA	780 nm	See master	< 1 W	Increasing power of cooling light
IPG YLR LP-SF	1064 nm	≈ 100 kHz	< 15 W	Crossed dipole trap light
Innolight Mephisto	1064 nm	≈ 1 kHz	< 2 W	Waveguide light
Homebuilt (SDL-5411 diode)	852 nm	< 1 MHz	< 100 mW	Barrier light
Homebuilt (EYP-RWE-0790-04000)	750-790 nm	< 1 MHz	< 100 mW	Single mode diode for evanescent wave light
Homebuilt (Intense 1020 diode)	765 nm	≈ 2 nm	< 2 W	Multi mode diode for evanescent wave light

Table 3.1: List of lasers used in the experiment.

	^{85}Rb		^{87}Rb	
	Transition	Detuning (MHz)	Transition	Detuning (MHz)
Spectroscopy	$F = 3 \rightarrow F' = 4$	0.0 ± 0.1	$F = 2 \rightarrow F' = 3$	0.0 ± 0.1
Spectroscopy	$F = 2 \rightarrow F' = 3$	0.0 ± 0.1	$F = 1 \rightarrow F' = 2$	0.0 ± 0.1
MOT	$F = 3 \rightarrow F' = 4$	-15.0 ± 0.1	$F = 2 \rightarrow F' = 3$	-15.0 ± 0.1
CMOT	$F = 3 \rightarrow F' = 4$	-35.0 ± 0.1	$F = 2 \rightarrow F' = 3$	-30.0 ± 0.1
Molasses	$F = 3 \rightarrow F' = 4$	-90.0 ± 0.1	$F = 2 \rightarrow F' = 3$	-50.0 ± 0.1
Probe	$F = 3 \rightarrow F' = 4$	3.2 ± 0.1	$F = 2 \rightarrow F' = 3$	4.3 ± 0.1
Repump	$F = 2 \rightarrow F' = 3$	0.0 ± 0.1	$F = 1 \rightarrow F' = 2$	0.0 ± 0.1
Optical pumping	$F = 2 \rightarrow F' = 2$	0.0 ± 0.1	$F = 1 \rightarrow F' = 1$	0.0 ± 0.1

Table 3.2: The laser frequencies used in this experiment with their detunings relative to their respective transition. Note that the ^{87}Rb detunings are given for when the ^{85}Rb–^{87}Rb merging experiments were undertaken.

The detunings of the laser beams during the cooling stages in the MOT chamber are provided in table 3.2. While we will not discuss the mechanics of the MOT, as these have been presented elsewhere in great detail [211], for contextual reasons we will, however, touch on the very basics of our initial experimental routine. There are three key stages in the initial cooling process; the MOT, where we trap around 1×10^9 atoms in ≈ 25 s; the compressed-MOT (CMOT), where for 20 ms we actually reduce the quadrupole trap gradient[1] from 10 G cm^{-1} to 5 G cm^{-1}, reduce the intensity of the repump light and increase the detuning of the cooling light, which cools the sample due to the reduced atom–photon scattering rate; and the molasses stage, where for 15 ms there is no longer a quadrupole gradient and the cooling light detuning is increased again to further cool the atomic sample.

Following this process of cooling, atoms are optically pumped into the $F = 2, m_F = -2$ state, transferred into a magnetic quadrupole trap formed by the transport coils and transported through the vacuum chamber to the science cell.

3.1.3 The obstacle

Our apparatus contains a prism, which we have called *the obstacle*, that is positioned where the transport coils are centred in figure 3.1. There are two main reasons for placing an obstacle in the path of the atomic cloud as it is transported through the vacuum chamber. Firstly, the obstacle blocks the path of stray hot atoms, preventing them from reaching the UHV science cell end of the chamber and secondly, it is a safe and effective method of coupling out high power dipole trap beams that are directed through the back of the prism in our science cell. We can turn the obstacle into a 'gate' by placing coils outside of the vacuum chamber, around the obstacle, in the Helmholtz configuration, thus producing a bias field of 216 G that shifts atoms contained in the quadrupole transport coils 1.2 cm vertically over the obstacle. The acceleration felt by the atoms due to the displacement around the obstacle (≈ 4 m s^{-2}) is very low in comparison with the acceleration due

[1] The original point of the CMOT was to provide a transient increase in atomic density in order to be able to potentially aid in the production of a BEC and also to improve the loading of a cloud of atoms from the MOT into a magnetic trap [212]. Our use of this term is really a misnomer.

to their confinement by the transport coils ($\approx 40\ \mathrm{m\,s^{-2}}$), therefore transport around the obstacle doesn't significantly heat the cloud.

3.1.4 The prism

A super-polished Dove prism has been placed at the far end of the science cell for the purpose of observing soliton–surface interactions in the long term. We have, however, already observed evaporation via atom–surface interactions, utilising the prism [77]. If a blue detuned laser beam undergoes total internal reflection by the prism, it results in a repulsive evanescent potential, which can compete with the atom surface interactions, producing a localised barrier to any atoms approaching the surface. Details of the work undertaken towards this goal are presented in chapter 8.

3.1.5 Magnetic trapping

For a detailed list of the coils used to generate magnetic fields in this experiment, see appendix A of [69]. We will cover the details of only the coils relevant to magnetic trapping, in this section. All coil pairs that we use for trapping are loosely in the anti-Helmholtz configuration[2], forming a magnetic quadrupole trap. An atom with a magnetic dipole moment in the presence of a magnetic field, B, will align itself with that field. The change in energy that the atom undergoes, in the weak field regime, is linear and expressed as [213]

$$\Delta E = m_F g_F \mu_\mathrm{B} B, \tag{3.1}$$

where m_F is the atom's magnetic sub-level, g_F is the hyperfine Landé g-factor and μ_B is the Bohr magneton. In a magnetic trap the resulting potential that the atom sees is,

$$U(\mathbf{r}) = m_F g_F \mu_\mathrm{B} \left|B(\mathbf{r})\right|. \tag{3.2}$$

The presence of $|B(\mathbf{r})|$, as opposed to just $B(\mathbf{r})$, is due to the magnetic moment of the atom constantly aligning itself with the field (adiabatic following). If we have an expression for a potential, it is straightforward to

[2]Where, in this definition, we refer to anti-Helmholtz as two coils whose currents oppose each other.

express the force on an atom by the simple relation, $F_{\text{atom}}(\mathbf{r}) = -\nabla U(\mathbf{r})$, resulting in,

$$F_{\text{atom}}(\mathbf{r}) = -m_F g_F \mu_{\text{B}} \nabla \left|B(\mathbf{r})\right| . \tag{3.3}$$

The form of the magnetic field is $|B(x, y, z)| = C\sqrt{x^2 + y^2 + 4z^2}$, for a quadrupole trap, with z being in the axial direction of the coil pair and C being a constant quantifying the gradient of the field. When we discuss the quadrupole traps in this experiment we refer to their gradients as the relevant parameter. The magnetic field near the zero of the trap (at the centre of the coil pair) is linear in form, radially symmetric and the axial gradient is twice that of the radial direction. It is this axial gradient, dB_z/dz, that we refer to, unless stated otherwise.

The vacuum chamber contains a 5 mm and 6 mm aperture, which limits the size of the cloud that can be transported through to the science cell. To ensure that there is minimal loss, while maintaining a power that our cooling system can dissipate[3], we choose a gradient of 180 $\text{G}\,\text{cm}^{-1}$. Increasing the gradient to 240 $\text{G}\,\text{cm}^{-1}$ would only increase the atom number by 10%, while pushing our cooling system to the limit [69]. The transport coils travel 51 cm in 2 s from the MOT chamber to the science cell. Once the science cell has been reached, the transport gradient is ramped down to zero in 0.5 s, while a fixed quadrupole trap is ramped up to 180 $\text{G}\,\text{cm}^{-1}$. Once the atoms have been transferred to the fixed quadrupole trap, the transport coils are rapidly moved back to the MOT chamber. At this point RF evaporation is undertaken in the trap to cool the atoms (see [72] and section 6.4.1 for details) before loading an optical dipole trap to continue the evaporation to degeneracy.

3.1.6 Optical trapping

The field at the centre of a magnetic quadrupole trap is zero. The longer that an atom spends in this region, the more time that the atom does not observe a magnetic field to align itself with, resulting in a greater likelihood of its spin flipping from a trapable low-field-seeking state to an untrappable high-field-seeking state. This loss mechanism is known as a Majorana loss

[3]Each of our high current coils has a hole bored in the centre, through which cold water flows, dissipating the heat that the coil generates.

and its rate increases as the temperature of a cloud decreases (see (6.9)) and section (6.2.2)) [214]. To combat this loss, which results in a lifetime of 1 s at 30 μK in a 180 G cm^{-1} trap, the atoms are transferred into an optical dipole trap.

We refer the reader to the detailed description of optical dipole traps given elsewhere [207] and, for brevity, will not cover this here. Instead we will briefly give an overview of the optical dipole traps used in our experiment (see table 3.1). There are two key traps in our experiment, the first is a crossed-dipole trap, in which the second half of the evaporation to degeneracy is undertaken, and the second is a single-beam waveguide, in which we form and propagate our solitary waves.

The crossed-dipole trap is formed from a single Gaussian beam, produced by a 1064 nm IPG YLR LP-SF 15 W fibre laser, that is focussed to ≈ 130 μm and recycled in a bow tie arrangement, as shown in figure 3.1. Once the ultracold cloud of ^{85}Rb is loaded into the crossed-dipole trap, evaporation is simply undertaken by reducing the depth of the trap (reducing the power of the laser). Optimising this direct evaporation trajectory[4] is not straightforward with ^{85}Rb for a number of reasons (see section 6.2). At ≈ 250 mW we reach degeneracy and transfer to the waveguide (1064 nm Innolight Mephisto), which provides an approximate 1D trapping geometry ($\omega_r \approx 2\pi \times 25$ Hz and $\omega_z = 2\pi \times 1.17$ Hz[5]). Further details of the waveguide will be provided in chapter 7.

3.2 Experimental diagnostics

In order to interpret the data that we obtain in this experiment it is essential that appropriate experimental diagnostics are utilised. There are three main diagnostics that we use; absorption imaging, magnetic field calibration through trap loss and parametric heating, to measure trap frequencies. The first of these allows us to calculate almost everything we need to know about

[4]More recently, groups evaporating ^{85}Rb have not undertaken direct evaporation, but instead use a technique known as *sympathetic cooling* where a different species that is easier to cool—such as ^{87}Rb [215]—is used as a thermal bath, resulting in larger condensates [216, 217].

[5]The optical only axial trapping frequency is actually $\omega_z \approx 2\pi \times 0.1$ Hz. The bulk of the trapping along the axial direction is provided by a magnetic field generated by a combination of our static quadupole coils and a bias field. For more details see chapter 7.

a cloud of atoms, such as atom number, width, temperature and phase space density, and can be used to infer quantities such as trap frequencies. As direct evaporation to BEC in ^{85}Rb is field critical and the formation of solitary waves is even more sensitive on the magnetic field, a very precise calibration of the magnetic field is necessary. We also need to understand our trap geometry and, therefore, often use parametric heating (see section 3.2.3) to obtain this information. We briefly detail below these three important diagnostics.

3.2.1 Absorption imaging

A thorough description of absorption imaging has been given elsewhere [218, 219], hence, we will only cover the relevant results that will be referred to later in this thesis. The core quantity that we determine is the optical depth as a function of position. When we shine resonant light onto our sample of atoms, the amount of this light that remains after travelling through the cloud is expressed as

$$I(x,z) = I_0 \exp\left[-\mathrm{OD}(x,z)\right], \tag{3.4}$$

where I_0 is the intensity of the light incident on the cloud. The method used to determine this optical depth is to take three separate images on the camera. The first measures the intensity of light incident on the CCD when atoms are present (I_{atoms}), absorbing the resonant light, effectively casting a shadow on the camera. The second measures the intensity of the light without any atoms present to absorb it (I_{probe}). The final image measures any background light that is incident on the CCD (I_{back}). From (3.4) it can be seen that if we know these intensities, the expression becomes

$$\mathrm{OD}(x,z) = \ln\left(\frac{I_{\mathrm{probe}} - I_{\mathrm{back}}}{I_{\mathrm{atoms}} - I_{\mathrm{back}}}\right). \tag{3.5}$$

We use software developed in-house in MATLAB to analyse our images (see section 4.6.1). When analysing our images we can use two different methods to determine the total number of atoms from the spread of optical depths in a single image.

The amount of light absorbed by a cloud of atoms can be expressed as [218]

$$\frac{dI}{dy} = -n(x, y, z)\sigma I(x, z), \tag{3.6}$$

where $n(x, y, z)$ is the density of the cloud and σ is the scattering cross-section, expressed as [219]

$$\sigma = \frac{\sigma_0}{1 + I/I_{\text{sat}} + 4\left(\Delta/\Gamma\right)^2}, \tag{3.7}$$

where $\sigma_0 = 3\lambda^2/2\pi$ for a two level atom [218] with transition at wavelength λ, I is the intensity of the light, I_{sat} is the saturation intensity, as defined in [213], and Δ is the detuning from the transition with linewidth Γ.

By making the approximation that our clouds have a small optical depth, we can treat I/I_{sat} as a constant and perform a simple integration of (3.6),

$$\int_{I_0}^{I} \frac{dI}{I(x, z)} = -\sigma \int_{-\infty}^{\infty} n(x, y, z)dy \quad \Rightarrow \quad \ln\left(\frac{I(x, z)}{I_0}\right) = -\sigma n(x, z), \tag{3.8}$$

by expressing the density in the imaging (y) direction as a normalised Gaussian. Noting our definition of optical depth in (3.4), we can express $n(x, z)$ in terms of the optical depth,

$$n(x, z) = \frac{\text{OD}(x, z)}{\sigma}. \tag{3.9}$$

Calculating atom number

Integrating (3.9) over all space gives the total number of atoms. Therefore it can be seen for an image,

$$N = \frac{\text{px}^2}{\sigma} \sum_{\text{row, col}} \text{OD}_{\text{row, col}}, \tag{3.10}$$

where $\text{OD}_{\text{row, col}}$ is the optical depth measured for a pixel in a particular row and column and px^2 is the area that a single pixel in the image represents. This expression can be particularly useful for determining the total number of atoms if the cloud is non-Gaussian in shape. An alternative expression for the total atom number can be obtained by assuming that we are imaging a

cloud that has a Gaussian profile,

$$n(x,z) = \frac{N}{2\pi\sigma_x\sigma_z}\exp\left(-\frac{x^2}{2\sigma_x^2} - \frac{z^2}{2\sigma_z^2}\right), \tag{3.11}$$

where $\sigma_{x,z}$ are the root mean square radii of the cloud. By substituting (3.11) into (3.9) and determining the optical depth at the centre of the cloud $(x, z = 0)$, $\mathrm{OD}_{\mathrm{peak}}$, we have a simple expression for the total atom number solely dependent on $\sigma_{x,z}$ and $\mathrm{OD}_{\mathrm{peak}}$, calculated from a fit to the cloud,

$$N = \frac{2\pi}{\sigma}\sigma_x\sigma_z\mathrm{OD}_{\mathrm{peak}}. \tag{3.12}$$

We can now determine how *Gaussian* our cloud is by comparing the numbers calculated via (3.12) and (3.10).

Calculating the temperature

In order to determine other thermodynamic quantities, such as peak density and phase space density, it is necessary for us to calculate the temperature of our cloud. We release a cloud from a harmonic trap and allow ballistic expansion to occur for a time τ. This results in a single shot that is generally used to determine the temperature.

The width of the cloud after it has expanded for a time τ is [72, 218, 219]

$$\sigma_{x,z}(\tau) = \sqrt{\sigma_{x,z}^2(0) + \omega_{x,z}^2\tau^2\sigma_{x,z}^2(0)} = \sigma_{x,z}(0)\sqrt{1+\omega_{x,z}^2\tau^2}, \tag{3.13}$$

where $\sigma_{x,z}(0)$ is the equilibrium width of the cloud in the trap. If we know $\omega_{x,z}$, $\sigma_{x,z}(\tau)$ and τ we can calculate the temperature, $T_{x,z}$, of the cloud from the equilibrium width,

$$T_{x,z} = \frac{m\omega_{x,z}^2\sigma_{x,z}^2(0)}{k_{\mathrm{B}}}. \tag{3.14}$$

From (3.14) it can be seen that one is not required to expand a cloud to calculate its temperature—the width can be measured in-trap. The reason for expansion is two-fold; firstly, the optical depth of a cloud in-trap is typically very high, such that the measured optical depth would become truncated and the width would be overestimated; secondly, at colder temperatures the cloud is typically very small, such that accurately determining its width in-

trap becomes more difficult. Hence, expansion of the cloud solves both of these issues by increasing its width and reducing its optical depth.

The resolution and magnification of our imaging system

In figure 3.1 we can see a variety of lens combinations that we use for our horizontal imaging system that result in magnifications of $\times 0.5$ ($f_1 = 160$ mm, $f_2 = 80$ mm), $\times 1$ ($f_1 = 160$ mm, $f_2 = 160$ mm) and $\times 1.5$ ($f_1 = 160$ mm, $f_2 = 250$ mm). With a pixel dimension of 8 μm for our camera, this results in predicted resolutions of 16 μm, 8 μm and 5.3 μm respectively for each lens combination. While the scaled size of our pixels may be as small as 5.3 μm, our imaging resolution is actually limited by aberrations in our optics and, fundamentally, the diffraction limit of our lens and wavelength of imaging light combination. This diffraction limit actually governs the smallest size that we can resolve with our imaging system and is expressed as

$$R = 1.22\frac{f\lambda}{D} = 1.22\lambda(\mathrm{NA}), \tag{3.15}$$

where f is the lens focal length, D is the lens diameter, λ is the wavelength of the imaging light and NA is the numerical aperture of the lens (NA $= f/D$). For our horizontal imaging system we have $f_1 = 160$ mm, $D = 40$ mm and $\lambda = 780$ nm, resulting in $R = 3.8$ μm. As this is the fundamental diffraction limit of our horizontal imaging system, it can be seen that increasing the magnification would not be beneficial. Instead we have introduced imaging in the vertical direction, which allows us to observe the shape and dynamics of a cloud in a previously unobserved direction (for more details of the vertical imaging system, see chapter 7). The parameters of our vertical imaging system are $f_1 = 18$ mm, $D = 20$ mm and $\lambda = 780$ nm, resulting in $R = 0.86$ μm. This new resolution limit should allow us to achieve straightforwardly pixel sizes of around 2 μm, or smaller, without being limited by diffraction.

3.2.2 Magnetic field calibration

If we wish to form solitary waves, it is essential to have precise control and characterisation of our magnetic fields. In ^{85}Rb, around 165.75 G ($a = 0$), beyond the 155 G Feshbach resonance, the scattering length, a, varies as $\Delta a/\Delta B = -40\ a_0/\mathrm{G}$ (see section 6.4.2). Therefore, if we want to know our scattering length to within 1 a_0, we must be able to determine our magnetic field to within 25 mG. Our method utilises Stern–Gerlach spectroscopy.

We apply a brief pulse (of order 10 ms) of radio-frequency (RF) electromagnetic field perpendicular to the magnetic field controlling the scattering length of ^{85}Rb. The effect of this is to drive transitions of $\Delta m_F = 1$ when $E_{\Delta m_F=1} = hf_{\mathrm{RF}}$, where $E_{\Delta m_F=1}$ is the energy between adjacent magnetic sub-levels and f_{RF} is the frequency of the RF field.

We look for one of two signatures as a result of the above; both of which require a magnetic field gradient to be present in the gravitational direction. If the optical dipole trap is deep enough to counteract gravity, we look for the presence of multiple clouds that form due to multiple m_F levels being populated and trapped. From (3.3) it can be seen that different magnetic sub-levels will experience a different force in a magnetic field gradient, which causes this separation. When we approach degeneracy, the optical dipole trap can become so weak that it can no longer counteract gravity on its own; instead the presence of the magnetic field gradient can be exploited to counteract the effects of gravity, resulting in a levitated trap, typically for only one of the magnetic sub-levels in ^{85}Rb. In order to determine the gradient required to levitate an atom subject to gravity, it is possible to equate (3.3) with the gravitational force, resulting in,

$$\left|\frac{\partial B}{\partial z}\right| = \frac{mg}{m_F g_F \mu_{\mathrm{B}}}, \tag{3.16}$$

where g is the acceleration due to gravity. If a ^{85}Rb atom starts in the $F = 2$, $m_F = -2$ state, once atoms are transferred to the adjacent sub-level ($m_F = -1$), the force counteracting gravity is halved and this often becomes insufficient to maintain the trapping potential. The result is atom loss from the trap and this is the second signature that we generally look for when calibrating the magnetic field across a condensate.

3.2.3 Parametric heating

There are a number of methods that can be used to deduce the trap frequencies of a harmonic trap[6]. One can offset a cold cloud and watch the centre of mass oscillate in the trap for multiple periods—this is how we determine the axial and radial waveguide frequencies in section 6.6.3; induce breathing modes in a condensate (see section 6.5.1) or undertake parametric heating of the cloud.

Parametric heating is a method of pumping energy into a cloud of atoms by periodically varying a particular parameter of the trap, in our case trap depth (laser power) and, as a result, trap frequency. Varying the trap depth modulates the frequency of the trap, and the rate at which the frequency is modulated will determine whether energy is efficiently pumped into the cloud or not. This process is analogous to a child on a swing—choosing an appropriate instance and rate at which to move her legs forward and backward will affect whether the swing travels higher, slows down or nothing changes.

For a cloud of atoms trapped in a finite depth harmonic trap, the result of parametric heating is an increase in temperature and also, potentially, atom loss—we typically look for loss of atoms. This increase in energy is seen to occur when the laser power is modulated at approximately twice the frequency of the trap [220].

3.3 Conclusion

In this chapter we have presented a brief overview of the key experimental apparatus relevant to this thesis, including our prism—a surface from which to reflect a solitary wave, details of magnetic and optical trapping and a variety of experimental diagnostics. These diagnostics were absorption imaging, magnetic field calibration and parametric heating. We encourage the reader to use this chapter as a reference for the remainder of the thesis.

[6]The Gaussian optical dipole trap, in which we later form a BEC (see chapter 6), can be approximated by a harmonic potential near the bottom of the trap.

Chapter 4

Development of experimental control and analysis software

4.1 Introduction

When deciding the necessary features in a control system for an experiment there are a number of typical questions. These are:

1. Does the experiment require an automated system?
2. What proportion of the experiment requires synchronisation?
3. What temporal resolution is needed?
4. How many digital and analogue devices need to be controlled?

Quite often it may be the case that an experimentalist does not require an automated control system, if the results they wish to obtain do not require strict timing or have a timing on the order of seconds or minutes. This can be a desirable solution as it does not require potentially learning a new programming language and designing and developing a new control system. However, in the case that timing is of paramount importance, one can then determine the extent to which synchronisation is required.

When deciding how to synchronise different parts of the experiment, one must first decide how control of all areas of the experiment will be undertaken. Users of the system must ask themselves whether just digital control

is required or whether other methods of control such as analogue outputs and General Purpose Interface Bus (GPIB) would be used. If the former is the case, then complex synchronisation does not typically need to be discussed, unless a large number of digital channels (> 32) are required. It would then be advisable to try to find a single card with a sufficient number of channels to run an experiment (eg. [221]), as opposed to running multiple cards with fewer digital outputs. This may become particularly difficult if you require more than 160 configurable digital channels. As we do not require more than this number of channels in our experiment, we will not discuss possible solutions to this problem here.

If analogue and digital control of an experiment is required, the user has the option of either purchasing two separate cards, like those mentioned in section 4.3, or to find a card that that has both (see section 4.4.2). The former may be a cheaper option, if synchronisation of analogue and digital channels is not required. However, if it is needed, it would be strongly recommended that the latter option be chosen due to the ease of implementing synchronisation.

As the author is currently unaware of any single card that offers digital, analogue and GPIB outputs, it is not straightforward to implement a comprehensively synchronised system for all three aspects of control. Therefore, GPIB can be semi-synchronised as is discussed in section 4.4.4.

Finally, the temporal resolution required from the outputs is critical in deciding what to purchase for the control system and also how the control program is written. If > 1 ms resolution is sufficient, then the control can be completely undertaken through the operating system with individual steps determined by control loops in LabVIEW. However, if < 1 ms resolution is required, the performance of the operating system will start to become detrimental to experimental control. In most cases the program will not respond in the time that the user has specified and the routine will be delayed. It is now necessary for routines to be run directly from the card, bypassing the operating system entirely. Hardware timing is far more reliable than software timing, as you do not have an operating system juggling a number of tasks while running the experimental cycle. This is often very restrictive on the routines that can be run, as highlighted by the inefficiency of the old system in section 4.3. However, solutions can be found with reconfigurable chips that allow greater flexibility in the programming of routines (see section 4.4.2).

4.2 Creating and visualising experimental routines

As the number of channels that the system uses to control devices increases, the ability to keep track of what an individual channel is doing, at a certain step in the experimental routine, becomes increasingly difficult. With several channels it may be sufficient just to have a list of changes at each step in the routine, however, even at this point it can be very hard to see the bigger picture and take note of the state of a channel in relation to another. One method of dealing with this problem is to create an idealised timing diagram. An example of one of these for a 'MOT load and image' routine is shown in Fig. 4.1.

In an idealised timing diagram, the time at which every relevant channel should trigger [1] is shown. Only digital channels are given in this particular idealised timing diagram, however, these diagrams could also be extended to include analogue and GPIB channels. In order to ensure that the diagram is as intuitive to interpret as possible it is wise to group similar channels together, such as channels that occur at similar times in a routine (eg. MOT shutter, MOT beam) or those which control devices of a similar type (eg. MOT shutter, repump shutter).

Once the channel order has been determined, the channels can then be stacked on top of each other in the diagram and individual steps in the routine can be determined. From this point the user can decide which devices need to trigger simultaneously, for a given step, and which require their own step. If the length of each step has been finalised and will not be altered, then the length of each step could also be included in the diagram.

Presenting the user with such an idealised timing diagram that can be updated live would generally be a desirable quality of a control program. However, this can seem over-the-top for sections of the routine that have been developed and tested comprehensively, as the user should not need to see them.

[1] Not including device delays, as these can be taken account of later.

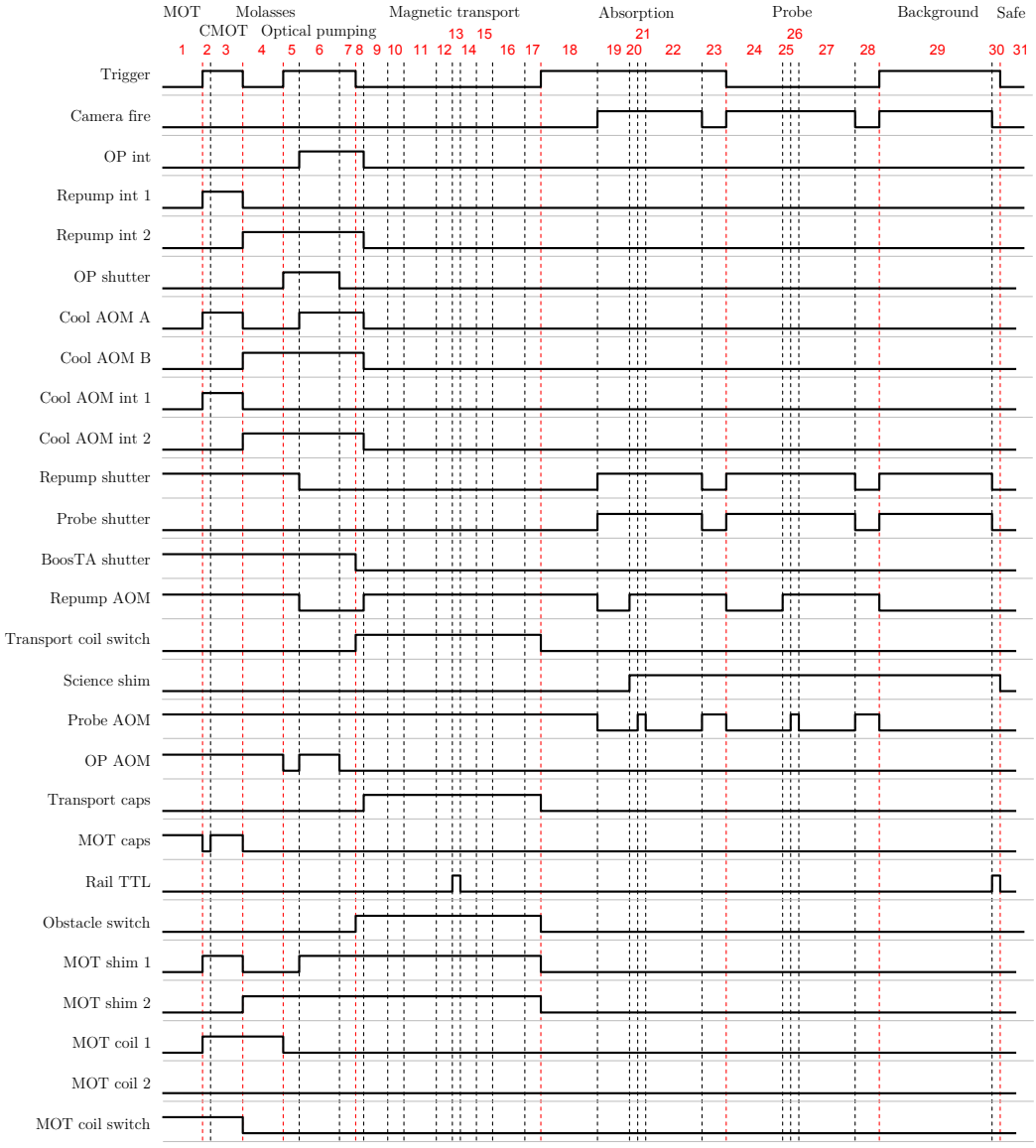

Figure 4.1: An example of an idealised timing diagram showing the state of individual digital channels for steps in a 'MOT load and image' routine. Vertical dashed lines separate individual steps in the routine and red lines indicate the different sections of the routine.

4.3 The original system (pre-2009)

Our original control system consisted of two PCI cards—a PCI-6533 (PCI-DIO-32HS) [222] and a PCI-6713 [223], both of which were developed by National Instruments. The PCI-6533 contained 32 digital channels, configurable as outputs or inputs, while the PCI-6713 contained 8 configurable digital channels and 8 analogue outputs. A program written in LabVIEW would communicate with experimental devices via the outputs and inputs of these cards.

To control the timings of the experiment, a matrix would be created in LabVIEW, like the one given in Fig. 4.2. Individual columns of the matrix represented a 1 μs temporal step and rows corresponded to a digital output that controlled the switching of a device, such as an acousto-optic modulator (AOM). This temporal step was fixed at 1 μs, therefore, if 1 ms passed without a single change in the state of the matrix, 1000 identical steps would be generated, which is clearly very inefficient, but necessary for the card.

The matrix was hidden from view in the *block diagram* in LabVIEW. Instead, the user would be presented with a *front panel* control, as shown in Fig. 4.3,

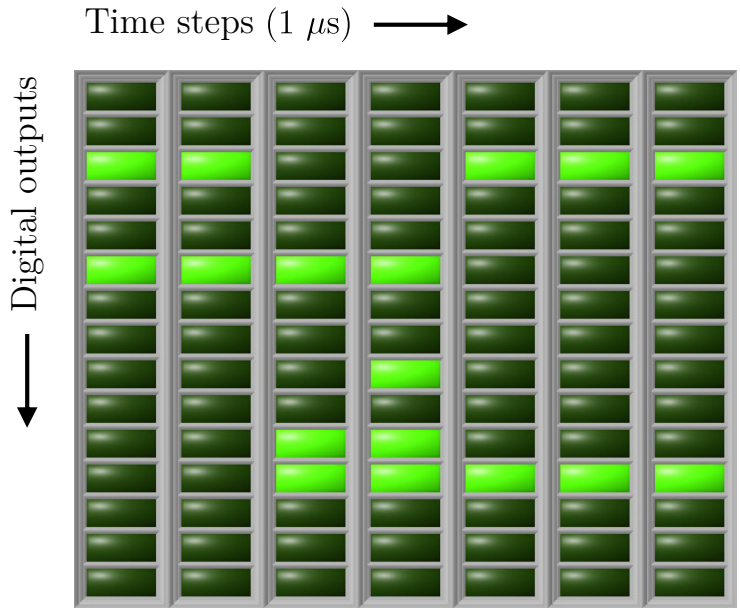

Figure 4.2: A matrix representing how an experimental routine is stored in LabVIEW in the original control software. Note that the size of the time steps was fixed at 1 μs, leading to inefficiency if long sections of the routine contained no changes.

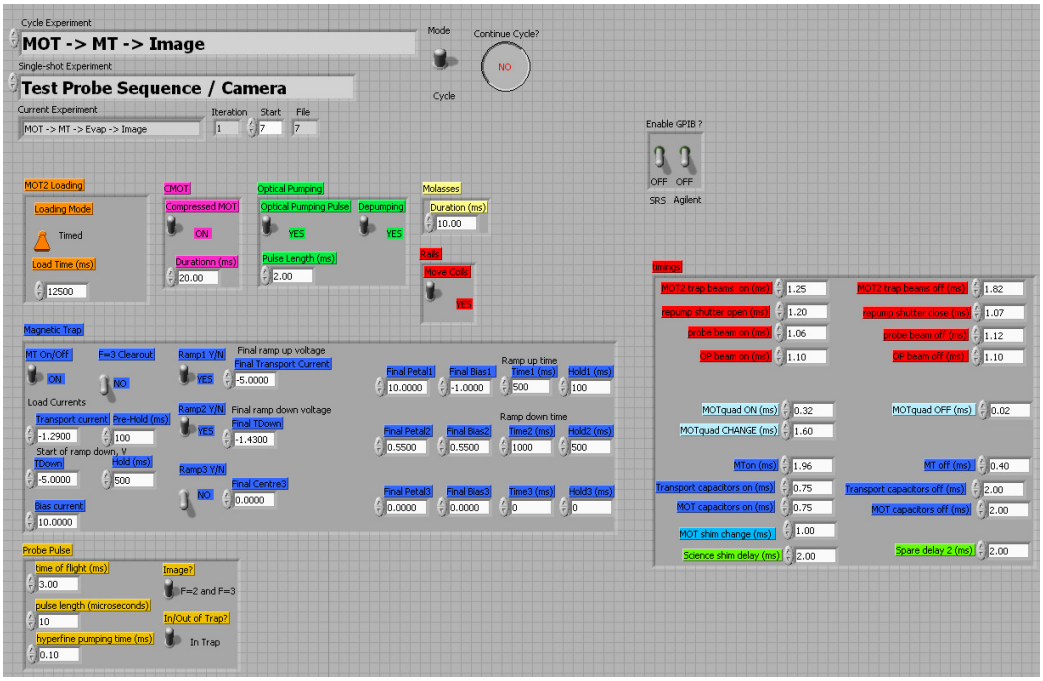

Figure 4.3: The LabVIEW front panel of our old experimental control system. Delays would be entered here, but routines were hidden away from view in the block diagram.

that allowed delays to be entered to take account of the length of time a device would take to respond to a trigger. Bringing this matrix to the foreground would achieve our goal to show an idealised timing diagram to the user as they are operating the program. This was one major reason to redesign the original control software.

Analogue and digital channels were treated independently, due to them being spread over two different PCI cards. This meant that it would be very difficult to create a system where analogue and digital channels could be simultaneously controlled and are synchronised. It would be necessary for both of the cards to be in constant communication with one another so that they could correct for any differences between their clock rates. As a compromise, analogue control was undertaken outside of the digital routine. For example, if a ramp of the current through a coil had to be undertaken, all digital communication would be stopped while the ramp was executed. Once complete, digital communication would continue with no analogue device control. Due to the difficulty of synchronisation and restriction of device control in this system, we decided to make use of control hardware containing a field programmable gate array.

4.4 The FPGA control system (2009-2013)

The development of the control software began in 2009 with inherited LabVIEW code [224] that was adapted and improved over the period of a few months. The sections below detail this development.

4.4.1 Field programmable gate arrays

When an integrated circuit is manufactured it is common for it to be no longer physically configurable. These application-specific integrated circuits (ASICs) perform particular tasks and are limited to the use for which they have been originally designed. While beneficial for inclusion in mass production of devices such as PCs, televisions and mobile phones [225], if a person requires hardware control of a system that is constantly evolving, then such a device would be impractical and very expensive to constantly remanufacture.

As our experiment is one which is constantly evolving, an ASIC was not the appropriate solution for our hardware control. Instead we chose to use a field programmable gate array (FPGA). An FPGA is a reconfigurable chip containing a vast array of logic gates. A schematic of such a device is given in Fig. 4.4.

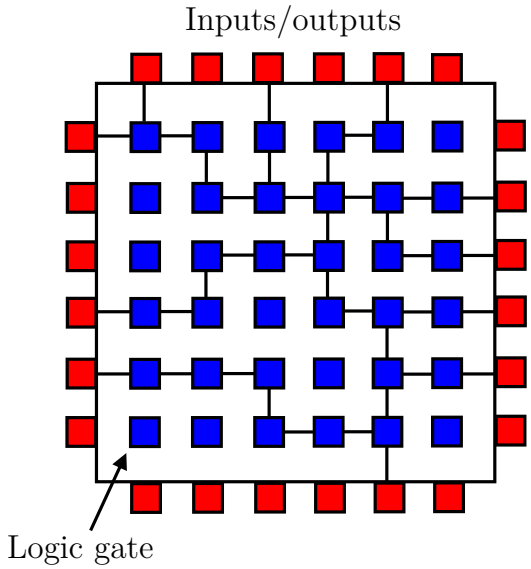

Figure 4.4: A schematic showing the configuration of gates and input/output connectors on a field programmable gate array. The array of gates allows the FGPA to process tasks in parallel by physically reconfiguring connectors between inputs/outputs and gates on the chip.

The first commercial FPGA was developed in 1985 by Xilinx [226]. In the late 80s FPGAs contained thousands of reconfigurable logic gates, however, by 2011 Xilinx were announcing the shipment of an FPGA with 20 million gates [227]. Due to such a vast array of interconnected logic gates on the chip, and the fact that connections are reconfigurable, tasks can be run in parallel, therefore enabling more efficient processing.

4.4.2 LabVIEW FPGA

Control of the FPGA via LabVIEW occurs through a virtual instrument (VI) that reconfigures the FPGA to perform the task that the user requires. This is the most important virtual instrument in the entire code as it controls how efficiently an FPGA program runs. The advantage of using LabVIEW to configure the FPGA is that the user is not required to know very complex programming languages such as VHDL (Very-high-speed integrated circuits Hardware Description Language), resulting in a broader user base and faster time to produce FPGA programs.

The single cycle timed loop (SCTL)

Arguably one of the most useful functions within LabVIEW FPGA for efficiently speeding up a program is the single-cycle timed loop (SCTL). It allows functions that would usually take multiple cycles of the card, to execute within a single-cycle. It reconfigures the card in such a way as to allow the tasks to be executed in parallel. Fig. 4.5 demonstrates an example of a simple case.

If a given function took 10 cycles to process, one would instantly achieve an increase in execution rate of a factor of 10, by simply placing such a function into an SCTL. There are, however, a number of limitations on the LabVIEW functions that can be placed within an SCTL. Some of these are quite fundamental, such as divide, quotient and remainder, for loop and square root. For a more detailed list see [229]. Solving the speed issue can sometimes generate new problems such as having to find elaborate methods of performing the fundamental, but disallowed, functions with those accepted by SCTLs.

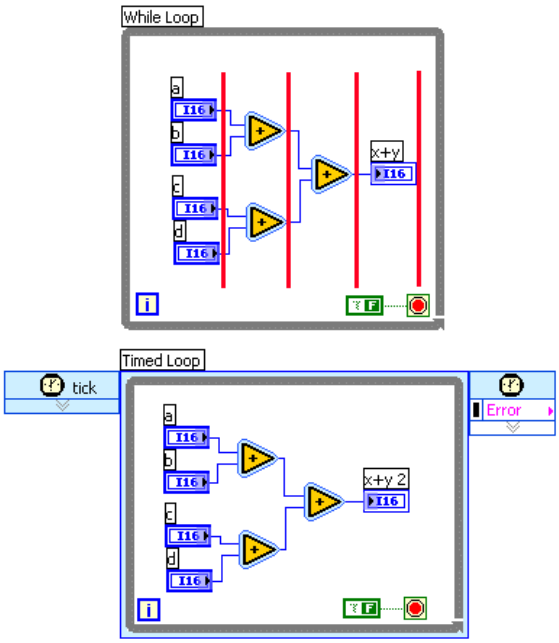

Figure 4.5: From [228]. A single-cycle timed loop (SCTL) can significantly increase the execution speed of a program by exploiting the parallel processing abilities of an FPGA. Tasks that would usually take more than one cycle of the card, where one cycle is denoted by the columns separated by red vertical lines, can be entirely executed in one cycle within an SCTL.

4.4.3 Experimental control software

There were a number of features that we desired for the new control program:

- Idealised timing diagrams directly viewed and controlled by the user.
- Synchronised analogue and digital channels.
- A large (50+) number of digital channels.
- Digital precision to 1 μs and analogue precision to 10 μs.

Testing of the system was undertaken and it has now been implemented for everyday use in the experiment for the past three years. It is worth noting that during this time there has been minimal downtime due to control software or hardware failure. A view of the front panel which the user interacts with is shown in Fig. 4.6.

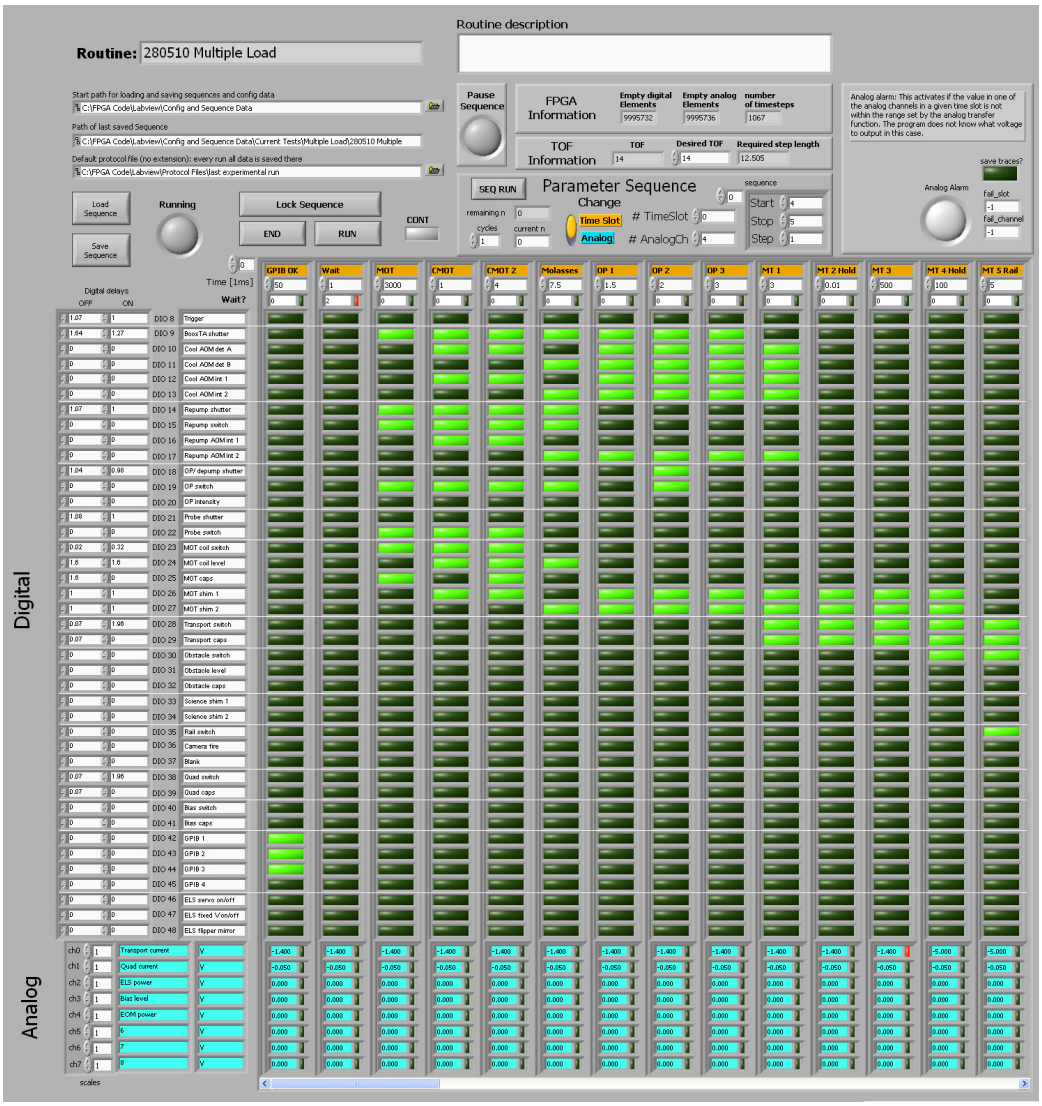

Figure 4.6: The LabVIEW front panel that is used to control all experiments in the soliton project.

Similarly to figure 4.2, the user is presented with a matrix where the states of channels can be adjusted for any given step in an experimental routine. In figure 4.6 40 digital channels are shown on the front panel, however, over the past three years this has gradually expanded and has a limit of 88.

For each of the digital channels an 'on' and 'off' delay can be stipulated. This takes account of the length of time a given device will take to respond to a trigger. A sub VI in the block diagram takes these delays and ensures channels that contain a delay will be triggered early by the specified amount. Names can be given to an individual time step, for clarity, and below this the user enters the length of the step in ms to a resolution of 0.001 ms.

For time steps larger than 0.002 ms analogue channels can be triggered, with the FPGA card providing a total of 8 analogue outputs and 8 analogue inputs. In the current configuration the 8 analogue outputs are in use and this number cannot be expanded. The solution for this—involving a redesign of the program architecture—is discussed in section 4.5. Currently none of the analogue inputs are used for direct feedback, however, they allow the flexibility of automating other aspects of the experiment. An example of this would be loading a MOT for a variable amount of time up to a given atom number, with the analogue input taking a feed from a photodiode measuring MOT fluorescence.

Also present on the front panel is a row entitled 'Wait?'. This was an addition to the inherited code, which allows the program to wait for an external trigger. This was a necessity for a number of different aspects of the experiment, for example, when a trigger is sent to the rails to move the transport coils the program must wait until the rails reach the science cell, after which point the routine can continue. This can account for variable timings between experimental runs and doesn't require the user to manually synchronise these parts of the experiment.

Communication between the FPGA card and the front panel is undertaken via direct memory access (DMA) and a data structure known as a FIFO (first in first out). A FIFO is effectively a queue of data stored in memory, accessed in the order it was placed there by the FPGA card via DMA. Using DMA the FPGA card can directly access this data, bypassing the CPU. This prevents there being any reliance on the state of the operating system during a routine, which is beneficial for program stability.

4.4.4 GPIB control

The initial problem that we had with synchronisation once again made a reappearance with the requirement of integrating GPIB with our new control system. Due to the lack of a single card with everything we required, we needed to use a separate GPIB card to control our power supplies and external function generators. Our solution to the synchronisation problem was to install the card on an entirely different PC. Communication between the FPGA PC and GPIB PC was undertaken via fast digital outputs and inputs present on both computers. Four digital channels on the FPGA PC were assigned to communicate with the GPIB PC and the state of these channels dictated which GPIB routine would be executed, as seen in Fig. 4.7.

During any GPIB control the FPGA PC waits for confirmation of completion of the GPIB routine. This ensures that no synchronisation errors can occur by not attempting to synchronise the FPGA and GPIB routines. Once the GPIB routine is complete, the FPGA PC continues with the rest of its routine until another GPIB command needs to be sent. This system could be called *semi-synchronised* due to the fact that GPIB commands are executed at particular points in the routine, but during GPIB control nothing else is run. In contrast to our system, if we attempted to run a 1 minute experiment with independent FPGA and GPIB routines, it could be quite possible that the GPIB routine is more than a few seconds out of sync with the FPGA routine by the end of the experiment. This could have drastic consequences on the condition of field effect transistors (FETs) if power supply voltages were changed too late in the routine.

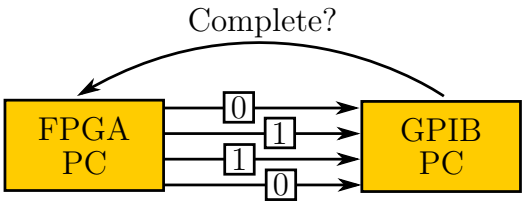

Figure 4.7: The method of communication between the FPGA PC and GPIB PC during an experimental routine. Four digital channels are assigned on the FPGA PC in order to control the GPIB routines that are run, depending on the state of these four channels. The FPGA PC waits until the GPIB routine has been completed, then it continues to run.

4.5 Development of the new control software (2013-)

While the system is now stable and reliable, having been used almost daily for the past three years, we intend to improve the functionality of the program. The aim is to develop a very flexible, entirely new, control system that will function for up to 10 years for at least three different experiments. It would be preferable that the user requires very little knowledge of LabVIEW for running and creating new routines within the control software.

4.5.1 Limitations of the first FPGA system

The architecture of the inherited, and subsequently developed, FPGA code restricted development of certain areas of the program, which resulted in the full array of features of the FPGA card not being utilised. The following is a list of these limitations:

- Digital outputs limited to 88.
- Digital inputs limited to 8.
- Analogue outputs limited to 8.
- Analogue inputs not utilised to create a feedback loop.
- Second PC required for GPIB control.

Beyond these fundamental hardware limitations there are a number of significant improvements that need to made to the software. The main aim of the software improvement is to fix the hardware limitations—through a complete overhaul of the program architecture—and to increase clarity for the user and future developers.

4.5.2 Requirements of the new system

In section 4.5.1 we discussed the limitations of the first FPGA program developed for the soliton project. Taking account of these observations, we created a list of requirements for the new system:

- Increase number of digital outputs and inputs.
- Increase number of analogue outputs.
- Utilise 8 analogue inputs for feedback during routines and long term monitoring.
- Integrate GPIB control onto the FPGA machine.
- Editing of LabVIEW code should be kept at a minimum for the user.
- Program architecture and code should be intuitive to follow.

The following section will discuss some of the key developments that have enabled the above requirements to be met.

4.5.3 Introducing new hardware

In order to increase the number of digital inputs, outputs and analogue outputs simultaneously, it was necessary to introduce a new piece of hardware to the system—the NI-9151 R-Series Expansion Chassis [230]. This chassis allows one of the three ports on the FPGA card—which would normally provide 40 digital channels—to be converted into an additional four C-Series ports. There is a wide array of physical modules [231] that can be attached to each of these ports, providing digital and analogue inputs and outputs. We have chosen to add one NI-9403—providing 32 digital channels—and one NI-9264—providing 16 analogue outputs—with the option of connecting one more of each of these to the expansion chassis at a later date [232, 233]. The addition of this new piece of hardware addresses the first three requirements listed in section 4.5.2.

4.5.4 Developing a new architecture

When adapting the original LabVIEW FPGA code it became apparent how critical the architecture of a control system becomes, particularly when dealing with something of this scale. On first glance, and second glance, the block diagram of the old FPGA control system is very difficult to interpret (eg. see figure 4.10) and delving deeper into other subroutines only makes this worse. As a result of this, when more features are added to this code it becomes increasingly cumbersome and difficult to understand.

The aim of the new FPGA system was to determine in advance all the features that it currently needed to possess, while building a structure for the program that was modular. This would make the initial build of the program logical and tidy, however, if any new features needed to be added, this would no longer be difficult due to the modular nature of the program. New features could essentially be *bolted on* to the original program, conforming to the architecture, therefore maintaining a clear and intuitive block diagram (eg. see figure 4.11). Two key features strongly encouraging modularity and readability, that are exploited in the new FPGA code, are given below.

The producer/consumer design pattern

It quickly became clear that in order to create an architecture that promoted readability and ease of expansion, while maintaining a responsive user interface, it was necessary to utilise the producer/consumer design pattern. This particular design pattern contains two while loops—the producer loop and the consumer loop. The producer loop generates data that is placed into a queue. If the queue becomes full it will wait until a space is free before placing any more data into the queue. The consumer loop independently reads data, saved by the producer loop, from the queue and performs an action, often dependent on the data it has read. There are significant benefits of employing this structure to process commands from a graphical user interface (GUI) and these are described below.

In this program the producer loop contains an event structure. This structure awaits an event, typically produced by the user, such as a mouse click on a button. The name of the event and any relevant data is then passed to the queue. Following this, the structure awaits another event produced by the

user. The consumer loop contains a case structure which executes a particular function depending on the specific event generated. If one did not employ a producer/consumer design pattern, typically a user would have to wait for the function to complete its execution until another event could be generated. If the function is slow ($\gtrsim$ 200 ms), it can make the graphical user interface appear sluggish. Instead, using the producer/consumer design pattern it is possible to continue generating events, placing data into a queue, while a function is being executed. Once the execution is complete, the consumer loop will begin executing the next function.

The producer/consumer design pattern (with event structure and case structure) is also modular as new events and cases can very easily be added. Future additions will always have to conform to this structure ensuring continued clarity in the block diagram. An example of the producer/consumer design pattern can be seen in figure 4.8.

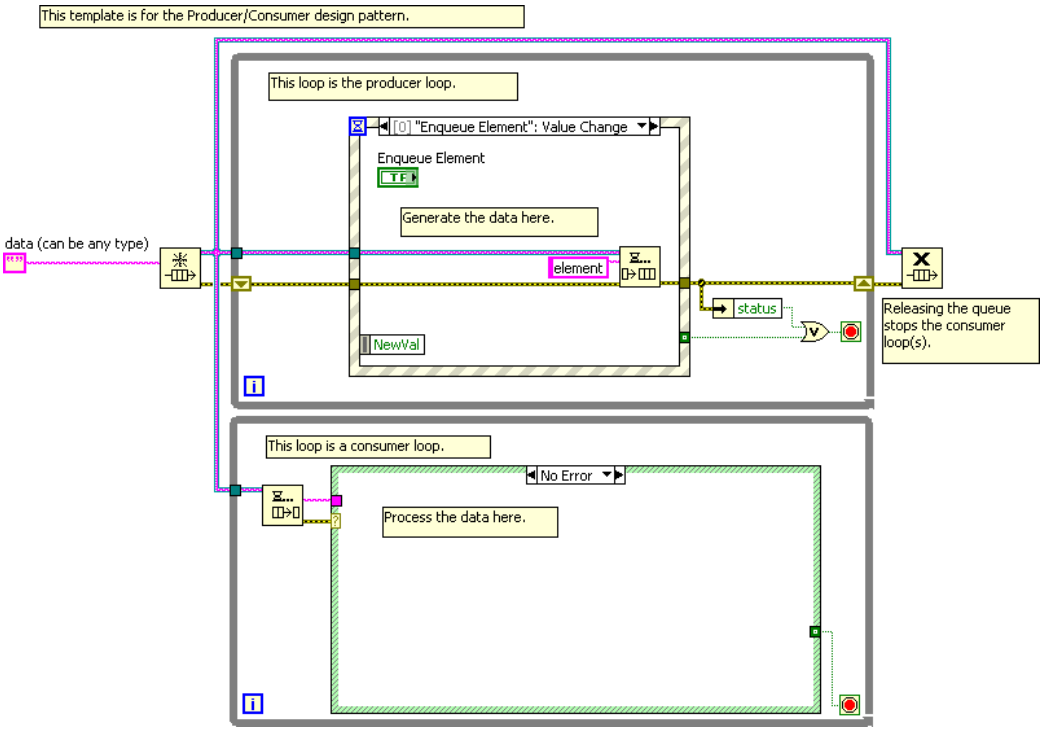

Figure 4.8: The producer/consumer design pattern template as created by LabVIEW. Two separate while loops are present. One while loop—the producer—awaits a user event, such as a mouse click on a button, and then puts the event into a queue. The event is read from the queue by the other while loop—the consumer—which independently processes the result of the user event, such as starting the experimental sequence. This structure allows the user to create events (*i.e.* click buttons) as fast as they desire, without any event being lost due to the result of the event being a slow process.

The action engine

If one wishes to store data that can be accessed anywhere within a control program, global variables are good candidates. These remove any necessity for wiring this data from its source to every other place that it is used in the program. For this reason global variables can increase the clarity of a program's structure. A specific type of global variable that is more flexible is the action engine, which is a more general type of functional global variable [234]. The action engine allows data to be stored, accessed and manipulated in any way that the programmer desires. Similarly to the producer/consumer design pattern, the action engine is modular in structure, allowing additional actions to be created with ease, without affecting code that is already using the engine. It achieves this goal by, once again, making use of case structures to determine the particular action to execute. A simple example of an action engine with three commands—*Initialize*, *Read* and *Write*—is shown in figure 4.9.

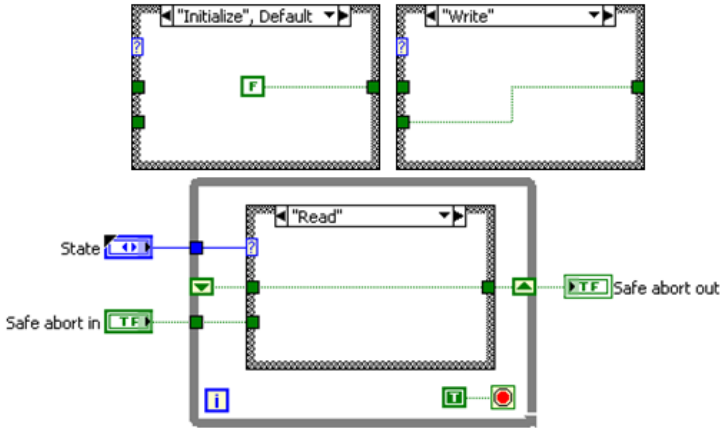

Figure 4.9: An example of an action engine. An action engine is created by placing a conditional loop inside a while loop containing a shift register. The presence of the shift register stores data in computer memory, which can then be modified or read out by any other part of the program. Additional commands can be set for the action engine, allowing the manipulation of the stored data.

The entire control program is built around action engines with a variety of different functions and data types, ranging from the simple to the quite complex. Throughout the process of building the program it has been very easy to introduce new features due to the structure of the action engine.

Comparisons of the old and new block diagrams

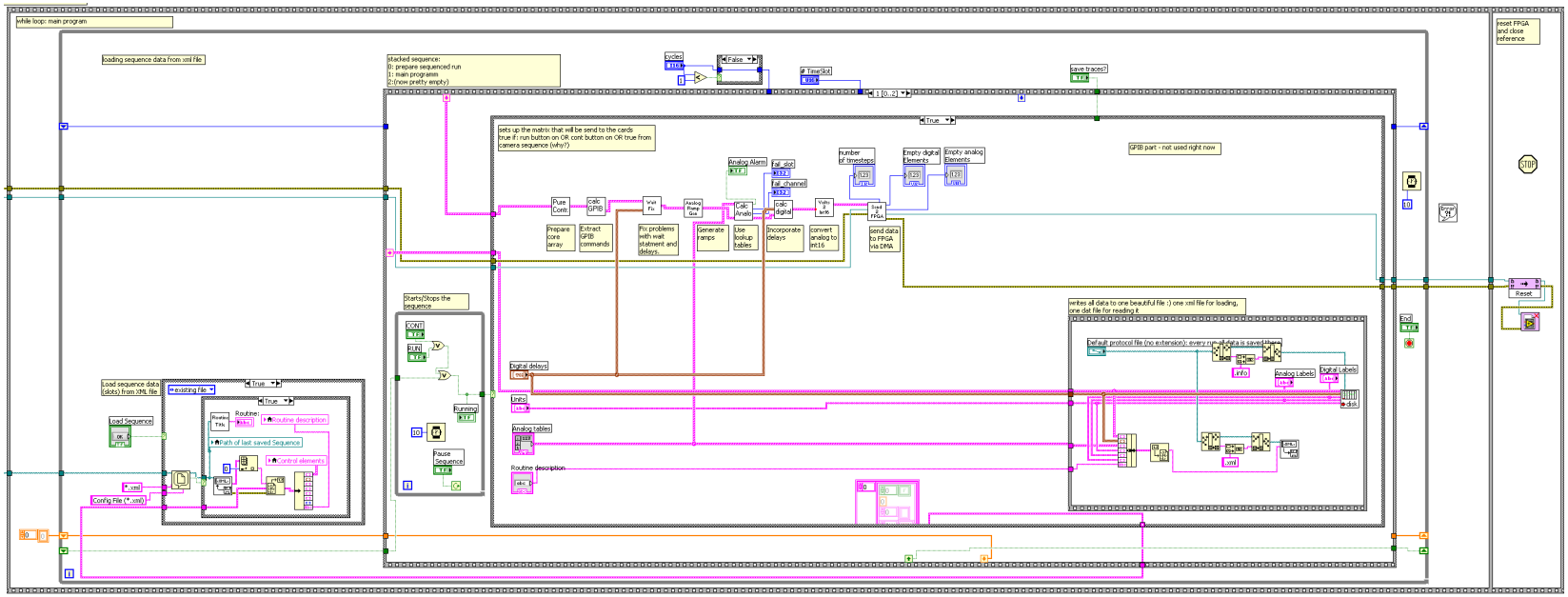

Figure 4.10: The architecture of the old FPGA system (2009-2013). This relies on a while loop that is constantly running, checking for the command to begin executing the routine. Routine data is stored in the front panel array, which can be difficult to access elsewhere in the program. SubVIs are used, but in an irregular fashion and the block diagram is signficantly larger than our computer monitor can display. All of this makes the old system difficult to understand, edit and expand.

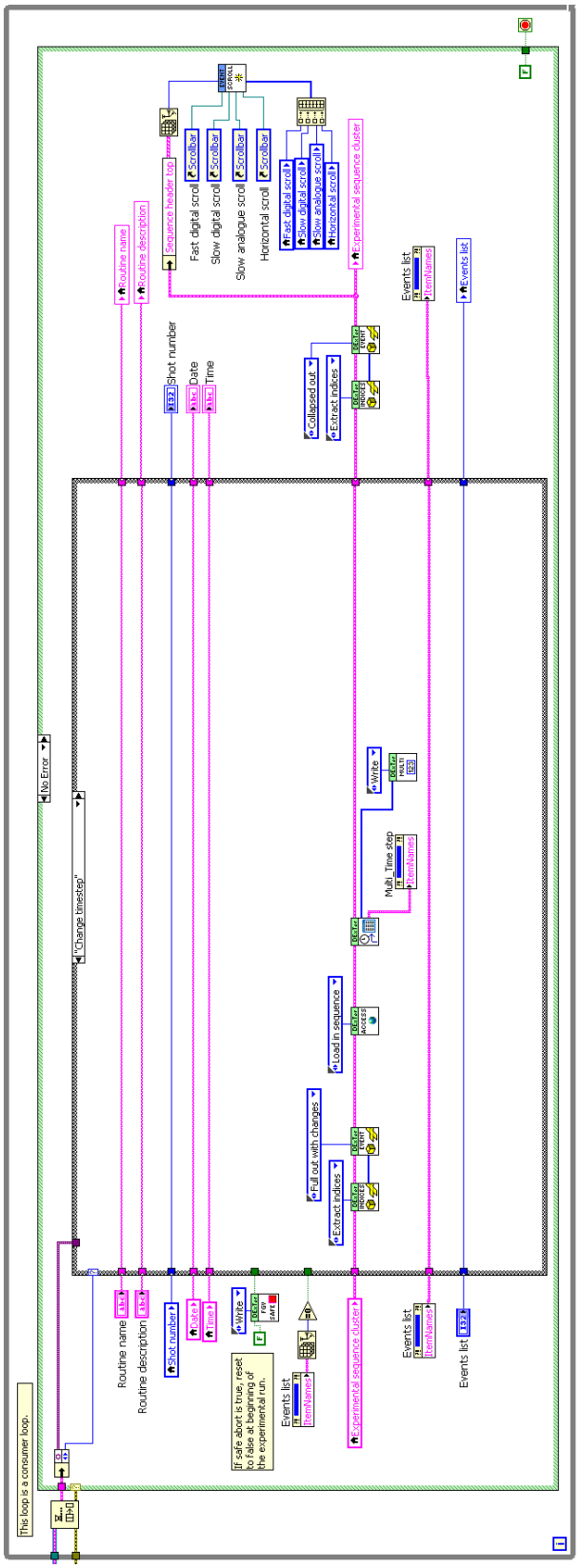

Figure 4.11: The architecture of the new FPGA system (2013-). This system uses a producer/consumer architecture. The program awaits user actions, such as mouse clicks, and then executes the necessary function. A while loop is not constantly running, using CPU time, and different modules can be easily created and viewed through the different states in a case structure. Fundamental code is buried away in small self-contained modules, which are then put together to undertake the complex tasks of the program.

4.5.5 Improving the user experience

The old FPGA user interface (see figure 4.6) suffered from a number of downsides that we aimed to improve in this iteration. The most obvious downside was its scale. The front panel was larger, both horizontally and vertically, than the monitors that were used in the lab, the number of visible channels was very large and many sections of routines that would never be changed were shown to the user. The aim of the new front panel was threefold; to keep the front panel to the width of the monitor on which it would be displayed, to reduce the number of channels on display to the user at any given moment and to allow sections of an experimental routine to be hidden, on demand, by the user. An image of the front panel can be seen in figure 4.12.

A few additional features of the program, integrated into the front panel are listed below:

- The ability to create and save *events*, which then join together to form entire routines.
- *Events* can be reordered.
- A batch of routines can be run using the *multi-run* feature, changing one parameter each run.
- Due to new hardware, the channels are now separated into *fast digital*, *fast analogue*, *slow digital* and *slow analogue*.
- Labelling and visibility of analogue and digital triggers are improved.
- GPIB functionality is clearly integrated into the front panel.
- Time can be defined as μs, ms or s.

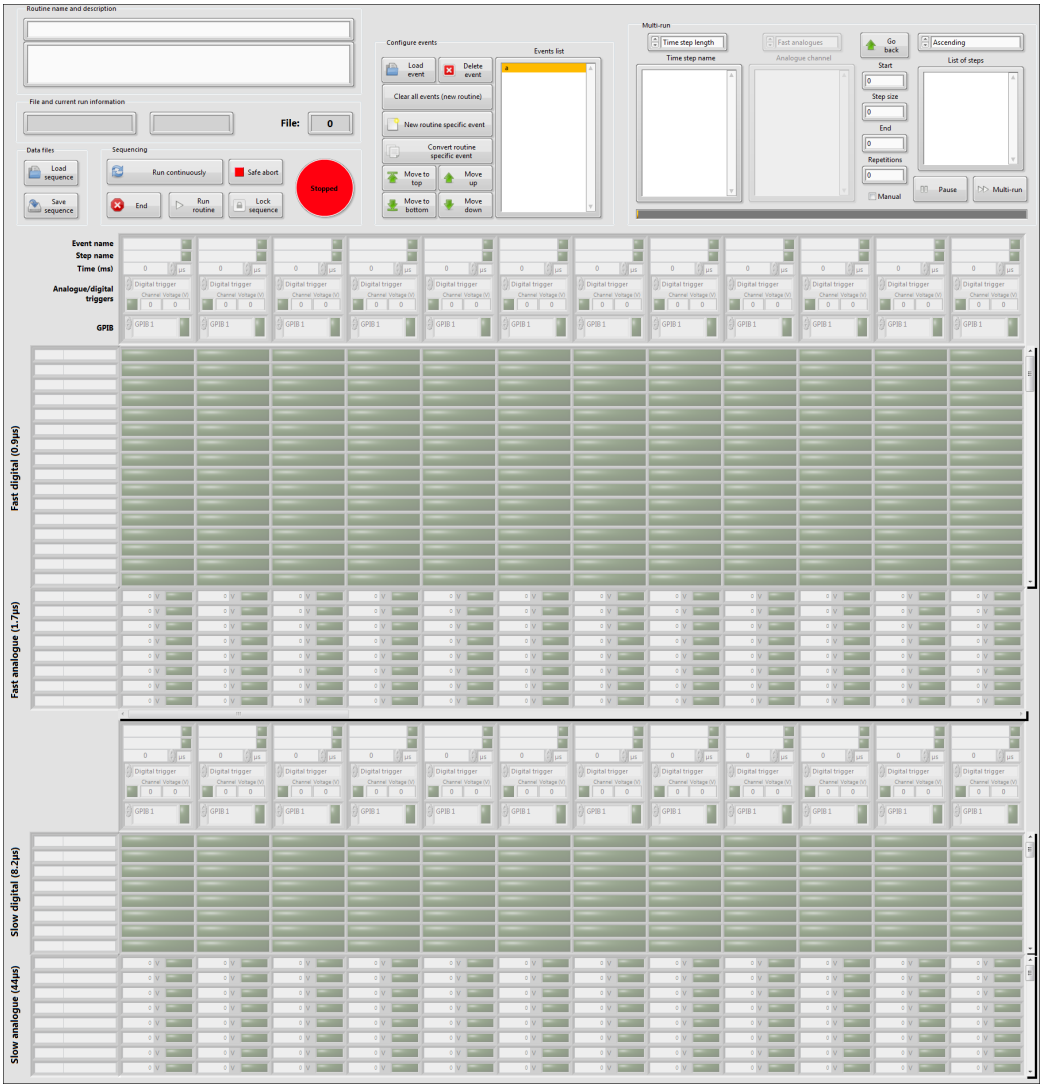

Figure 4.12: The user interface of the new FPGA control system. It has been designed such that all the critical controls and indicators can be seen simultaneously on a widescreen monitor with a resolution of 1920×1080. The user only has to scroll up and down to see other controls, unlike the required side scrolling with the old user interface.

4.6 Experimental analysis

In this section we will discuss the two key pieces of software that we have developed as part of our investigation into the formation and dynamics of solitary waves. Both programs have been created in the MATLAB programming language within the GUIDE environment [235].

4.6.1 Imaging software

The software that we use to analyse our absorption images (see section 3.2.1) was originally created in Oxford in 1998 by Gerald Hechenblaikner. The purpose of the software is to take the three images (absorption, probe and background) obtained via an Andor iXon camera, combine them to calculate the optical depth, display, fit and output the properties of a cloud. Details of its initial iteration on a project in Durham and its use for dual species can be found elsewhere [219]. Since the image analysis program came to Durham it has undergone many interations. The latest iteration, undertaken during the project described in this thesis, resulted in a number of improvements. The first of these was a new graphical user interface (GUI) created within the GUIDE environment in MATLAB. The rationale behind this was to convert the program into a form that is more straightforward to edit for future users and to arrange objects on the GUI in an intuitive way. The latest GUI can be seen in figure 4.13.

Another useful addition to the program is the ability to easily export graphs as a vector format image (PDF) and as a comma separated variable (CSV) data file. The most critical addition to the program was the ability to fit bimodal two-dimensional data. An example of where this is very important is when we reach degeneracy. Typically one may want to create a very pure condensate, however, in many of our shots we have observed the presence of a thermal fraction. If one does not incorporate a bimodal fitting algorithm, the width of the condensate will typically be overestimated—biased by the thermal fraction. We undertake a least-squares 11 parameter free fitting

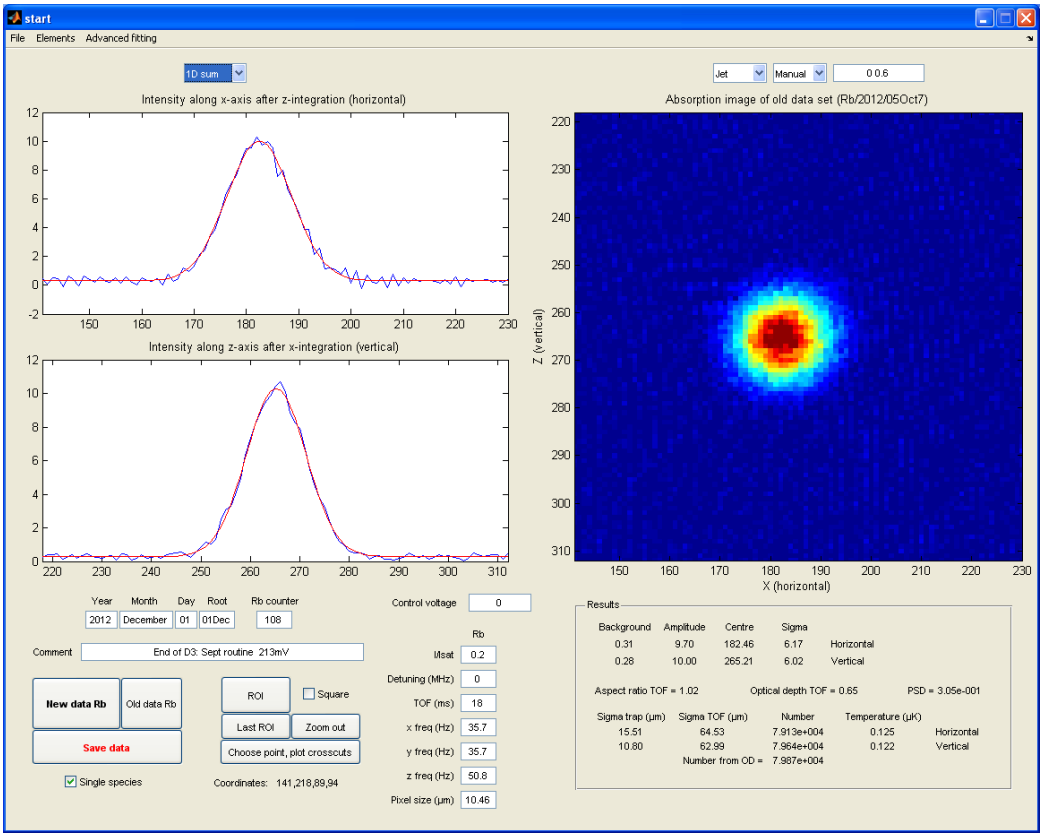

Figure 4.13: The user interface of the image analysis program.

routine described by

$$\begin{aligned} \mathrm{OD} = \mathrm{OD}_{\mathrm{back}} + \mathrm{OD}_{\mathrm{b}} \exp\left(-\frac{(x-x_{0\mathrm{b}})^2}{2\sigma_{x\mathrm{b}}^2} - \frac{(y-y_{0\mathrm{b}})^2}{2\sigma_{y\mathrm{b}}^2}\right) \\ + \mathrm{OD}_{\mathrm{t}} \exp\left(-\frac{(x-x_{0\mathrm{t}})^2}{2\sigma_{x\mathrm{t}}^2} - \frac{(y-y_{0\mathrm{t}})^2}{2\sigma_{y\mathrm{t}}^2}\right), \end{aligned} \tag{4.1}$$

where $\mathrm{OD}_{\mathrm{back}}$ is the background contribution to the optical depth[2], OD_{b} and OD_{t} are the BEC and thermal contributions to the total optical depth, OD, respectively, $x_{0\mathrm{b}}$, $y_{0\mathrm{b}}$, $x_{0\mathrm{t}}$, $y_{0\mathrm{t}}$ are the BEC and thermal, axial and radial, centres respectively and $\sigma_{x\mathrm{b}}$, $\sigma_{y\mathrm{b}}$, $\sigma_{x\mathrm{t}}$, $\sigma_{y\mathrm{t}}$ are the BEC and thermal, axial and radial, RMS radii respectively. It is important to note that correlations among the 11 parameters are not taken account of when uncertainties, in the extracted parameters, are quoted. We do not use the Thomas-Fermi approximation because we typically study our condensates at $a \sim 0$. Having a fit with 11 parameters leaves a lot of room for potential unphysical fits,

[2]This should be very close to zero.

due to the algorithm getting stuck in local minima of such a large parameter space. To compensate for this, we undertake the following procedure,

1. Fit a single 2D Gaussian to the bimodal data.
2. Extract the background, peak optical depth, x and y RMS widths and the x and y centres.
3. Make $\mathrm{OD}_{\mathrm{back}}$ the same as the background and OD_{b} and OD_{t} half of the peak optical depth.
4. Make $x_{0\mathrm{b}}$ and $x_{0\mathrm{t}}$ equal to the x centre.
5. Make $y_{0\mathrm{b}}$ and $y_{0\mathrm{t}}$ equal to the y centre.
6. Make $\sigma_{x\mathrm{b}} = (x \text{ RMS width}) \times 0.5$ and $\sigma_{x\mathrm{t}} = (x \text{ RMS width}) \times 1.5$.
7. Make $\sigma_{y\mathrm{b}} = (y \text{ RMS width}) \times 0.5$ and $\sigma_{y\mathrm{t}} = (y \text{ RMS width}) \times 1.5$.

Reducing the BEC width and enlarging the thermal width assumes that the cloud has been released from a trap and the interatomic interactions are relatively weak, such that the thermal fraction expands quicker than the condensate. Remarkably, using the above procedure the algorithm has generally been able to fit 2D bimodal distributions, undertaking a minimisation in 11 parameter space. We have found that occasionally the multiplication factors in steps (6) and (7) need to be altered to achieve a reasonable fit. An example of a bimodal fit to a solitary wave with a thermal pedestal is shown in figure 4.14.

4.6.2 Dipole trap simulator

It is essential to understand the form of the potential that our atoms are trapped in, when we are cooling to degeneracy. To aid with our understanding we have chosen to model the potential with a piece of software written in MATLAB. Originally created by Pauline Trouve, the intention of this software was to model the combined potential as a result of magnetic fields generated by a variety of coils in our experiment and optical forces from a dipole trap. This software can report important trap parameters, such as frequencies, centre positions and depths. The original software modelled a

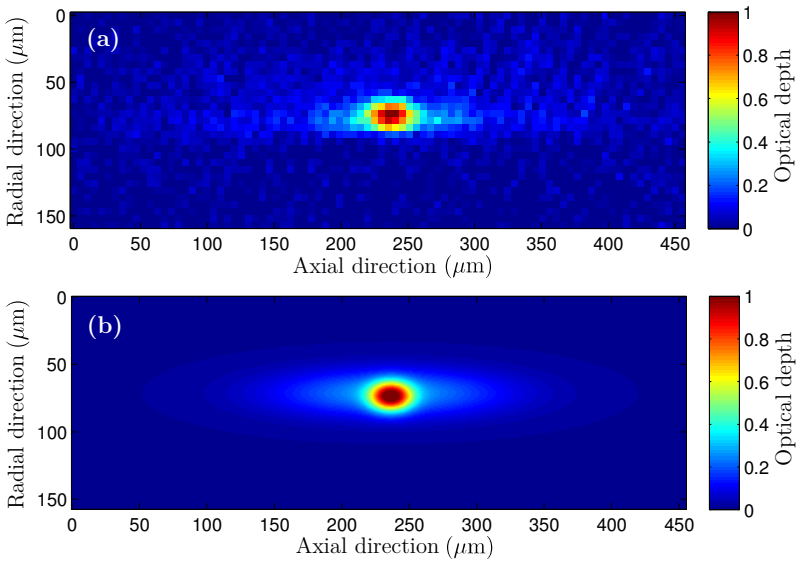

Figure 4.14: An example of fitting a bimodal distribution to a solitary wave. (a) A real image of a bimodal distribution, containing a solitary wave and thermal pedestal, obtained via absorption imaging. (b) The two-dimensional bimodal fit using (4.1) to the data in (a).

dipole trap created by a single beam or the intersection of two beams with the addition of a pair of coils creating a trapping potential and another pair of coils creating a bias field. This initial instance of the program was a success and helped with the characterisation of our early dipole traps. As the experiment became more complicated, it was clear that further additions to the program were required. Early corrections and improvements were made by Steve Hopkins, followed by a combination of Steve Hopkins and the author and the latest improvements have been solely undertaken by the author. We shall discuss the author's contribution below.

Similarly to the imaging analysis software (see section 4.6.1), the first major improvement was to make the entire program more readable, through identification of repeated code that could be implemented as a subroutine, and a significant improvement to the user interface, by separating the configuration screen from the results screen. The entire interface was rebuilt using MATLABs GUIDE GUI programming environment. An example of the new configuration GUI can be seen in figure 4.15, while the results GUI can be seen in figure 4.16.

An additional feature to this new iteration was a vast array of export features, examples of which can be seen in figure 4.17 (a), accessable via right-clicking

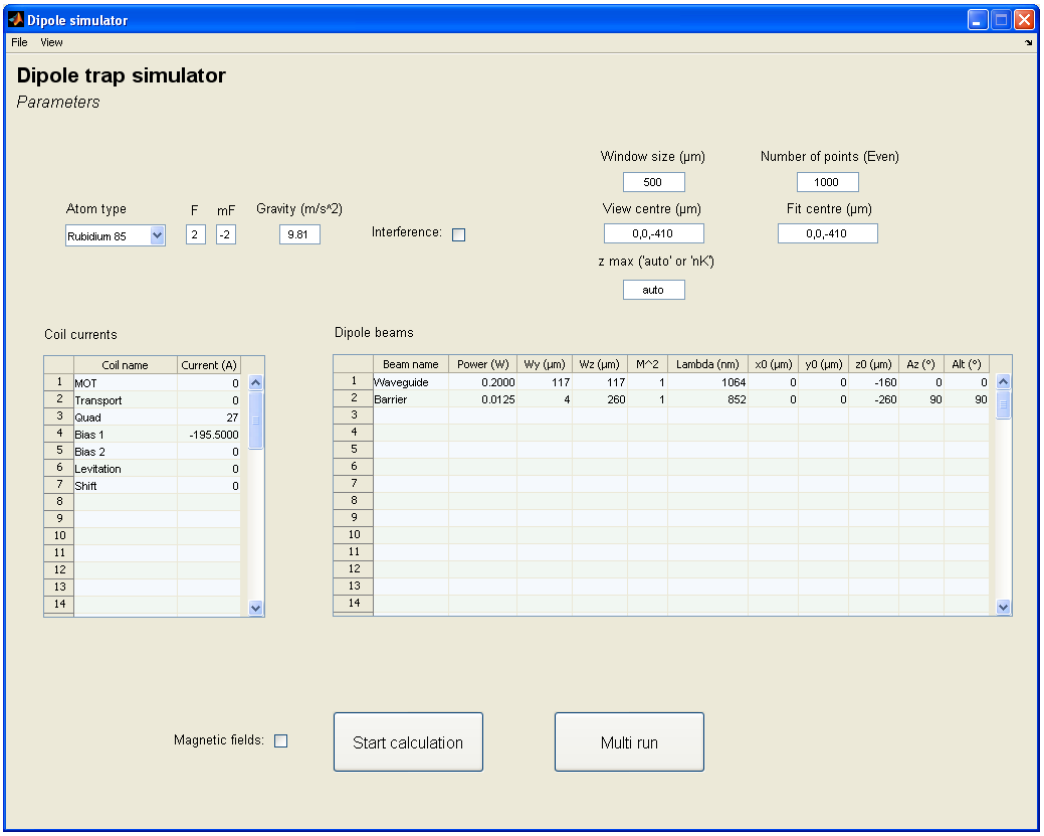

Figure 4.15: The user interface of the dipole trap simulator.

on a graph or via the `File` menu. A complete list of the exportable formats is given below,

1. Export all: Exports all graphs as a PDF and CSV file and trap parameters, such as trap depth and frequency, as a CSV file.

2. Export graph data: Exports all graphs as CSV, Excel 2003 or Excel 2007 formats.

3. Export graphs: Exports all graphs as EPS, PDF or PNG files.

4. Export data: Exports parameters as CSV, Excel 2003 or Excel 2007 formats.

5. Individual export: Bitmap - BMP, JPG, TIFF, PNG; Vector - EMF, EPS, PDF; Data - CSV, Excel 2003, Excel 2007.

6. Isolate graph: 2D and 1D plots can be opened in a new window as a different type of graph. These graphs are; 1D - Line and scatter; 2D - Con-

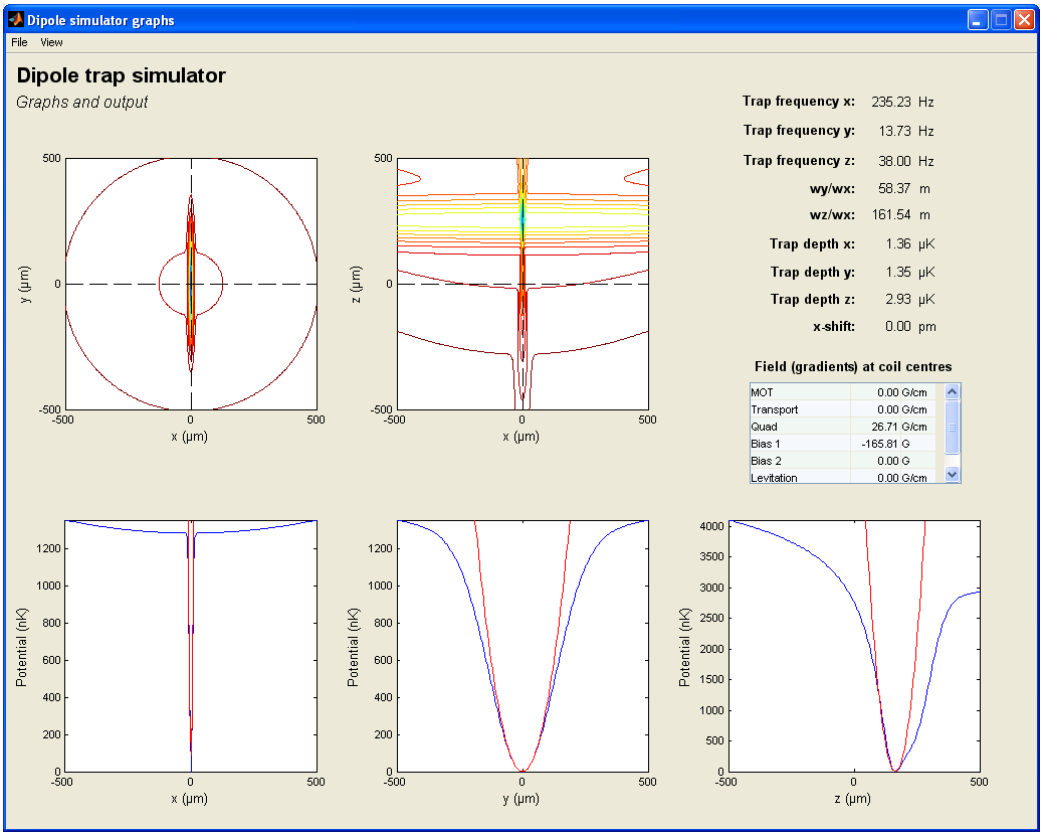

Figure 4.16: The results panel of the dipole trap simulator.

tour, Contour (Filled), Contour (3D), Image, Mesh, Mesh/Contour, Surface, Suface/Contour.

In the original iteration of the program, if one wanted to see how a parameter, such as trap frequency, changed as a function of beam power, position or any other physical property of a beam or coil, it was necessary to step the physical property manually and record the parameter for each run of the program. A new addition added by the author was the option of a batch routine, known as a multi-run, where the user would decide the beginning and end values of a physical property and the number of steps to take. The resulting data is plotted and can be saved. The original program was very slow to generate 2D potentials larger than 150×150 points, due to the Biot-Savart law being solved by integration. A significant increase in speed (around three orders of magnitude) was obtained by solving the Biot-savart law via elliptic integrals [236, 237].

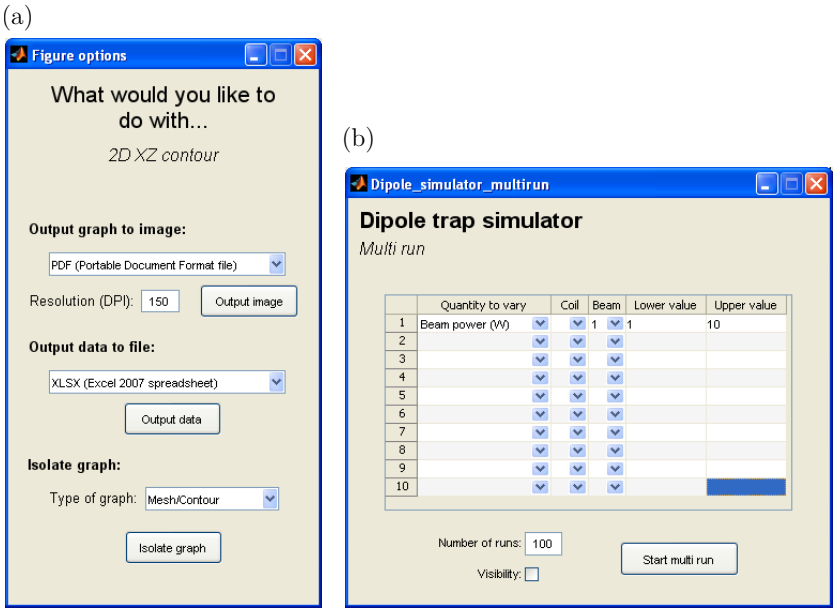

Figure 4.17: The (a) export and (b) multi-run features in the dipole trap simulator.

Below is a list of features of the program, now available mostly due to additions by the author,

1. Models the potential generated by up to 50 coil pairs (easily extendable to greater numbers) that can be rotated by 90 degrees into the vertical or horizontal planes.

2. Models the potential generated by up to 100 laser beams (easily extendable to greater numbers) that can be rotated by any arbitrary angle in three dimensions.

3. Beam parameters are very flexible, with variable powers, waists, M^2, λ, waist positions and orientations.

4. The waist of a laser beam can be independently altered in such a way as to create elliptical beams, to model a light sheet.

5. Coil parameters are hidden away but can be accessed via a simple menu selection. Types of coil pairs are very flexible, with variable sizes, separations, orientations and geometries (square or circular).

6. Potentials can currently be modelled for ^{87}Rb, ^{85}Rb and ^{133}Cs.

4.7 Error analysis

Good analysis of experimental uncertainties is essential to ensure that theoretical models, being tested against experimental data, can be verified or discounted. It is also very important in order to obtain bounds of values extracted via fitting, such as frequencies, amplitudes or centres. Generally throughout this thesis uncertainties have been extracted via a chi-squared (χ^2) minimisation, as described in detail in [238], using the graphing software *Origin*. The author strongly recommends that the option to `Scale Errors with sqrt(reduced chi^2)` is turned off when fitting using *Origin*. Beyond this it is still essential to check the magnitude of the errors and, using a common sense approach, decide whether they have been significantly underestimated or overestimated. Where this has occurred within *Origin*, the author has undertaken a manual χ^2 minimisation using *Microsoft Excel* or *MATLAB*.

4.8 Conclusion

In this chapter we have discussed the evolution and creation of a complex LabVIEW based experimental control system, utilising a field programmable gate array (FPGA). The latter part of this chapter has focussed on the experimental analysis and theoretical modelling software that is in daily use in the Durham experiment.

Part III

Experiments with ultracold atoms

Chapter 5

Magnetic merging of ultracold atomic gases of ^{85}Rb and ^{87}Rb

This chapter is based on the following publication:

S. Händel, T. P. Wiles, A. L. Marchant, S. A. Hopkins, C. S. Adams, and S. L. Cornish, *Magnetic merging of ultracold atomic gases of ^{85}Rb and ^{87}Rb*, Phys. Rev. A **83**, 053633 (2011).

'We report the magnetic merging of ultracold atomic gases of ^{85}Rb and ^{87}Rb by the controlled overlap of two initially spatially-separated magnetic traps. We present a detailed analysis of the combined magnetic field potential as the two traps are brought together, which predicts a clear optimum trajectory for the merging. We verify this prediction experimentally using ^{85}Rb and find that the final atom number in the merged trap is maximized with minimal heating by following the predicted optimum trajectory. Using the magnetic merging approach allows us to create variable ratio isotopic Rb mixtures with a single laser cooling setup by simply storing one isotope in a magnetic trap before jumping the laser frequencies to the transitions necessary to laser cool the second isotope.'

5.1 Introduction

5.1.1 Mixtures of atomic gases

The production of mixtures of two or more ultracold atomic gases [239–250] provides access to a diverse range of exciting new phenomena [251–256]. Many of these phenomena result from the fact that the component species in the mixture can have notably different intrinsic properties, such as different spins, masses, collision cross sections, optical polarisabilities and quantum statistics. Atomic mixtures have also come to prominence in the production of ultracold heteronuclear molecules [257] through magneto-association [258, 259] and/or optical association [260]. Indeed the recent production of ultracold molecules in the rovibrational ground state [261–266] from ultracold atomic gases brings the realm of dipolar molecular quantum gases [267] within reach. As well as possessing the above intrinsic interest, mixtures play an important technical role in the sympathetic cooling of 'difficult' bosonic species such as ^{85}Rb [217, 248] and ^{41}K [268] and all fermions [269] owing to the suppression of s-wave scattering for fermions. However, the realisation of some mixtures can be challenging due to detrimental light assisted inelastic collisions between the two species [270, 271].

5.1.2 Features of a ^{85}Rb and ^{87}Rb mixture

A mixture of ^{85}Rb and ^{87}Rb has several attractive features for quantum gas studies. There exist two interspecies Feshbach resonances [272] suitable for the production of heteronuclear molecules [216]. The interspecies elastic cross-section is favourable for sympathetic cooling of ^{85}Rb [272], initially demonstrated in 2001 [215] and later used to reach quantum degeneracy by two groups [217, 248]. The broad intraspecies Feshbach resonance in ^{85}Rb has been extensively used to control the atomic interactions in a Bose-Einstein condensate [15], permitting the study of the collapse of a condensate [26, 55] and the formation of bright matter-wave solitons [56], as well as enabling the investigation of phase separation in a dual–species ^{85}Rb – ^{87}Rb condensate [248].

5.1.3 Experimental scheme

In this chapter we report a novel scheme to prepare ultracold mixtures using two magnetic traps which are controllably merged to combine the two atomic gases. The scheme has general applicability in that any pair of magnetically trappable species could be merged. However the merging of two initially separated trapping potentials is non-trivial and the bulk of this chapter is devoted to a detailed theoretical and experimental study of this process. In particular, we provide for the first time a detailed analysis of the combined magnetic field potential during the merging process which highlights the optimum merging trajectory. This analysis significantly extends the previous experimental study [273] and should have general applicability for any similar trap-merging experiments. We convincingly demonstrate the validity of our analysis with a specific example, the merging of ultracold atomic gases of ^{85}Rb and ^{87}Rb.

The overall sequence of our experiment is as follows. Ultracold atoms are collected from a background vapour in a magneto-optical trap (MOT), loaded into a magnetic quadrupole trap (trap 1) and transported [274, 275] from the MOT chamber to a UHV glass cell using a motorised translation stage (Fig. 5.1(a)). The atoms are then transferred into a static quadrupole trap (trap 2) and trap 1 is moved back to the MOT chamber. At the same time the laser frequencies are jumped to the transitions necessary to laser cool the second isotope. A second sample of atoms is collected and again transported to the UHV cell where the two traps are controllably merged. Hence we are able to realise the production of a mixture of the two Rb isotopes by magnetic merging with only a single laser cooling setup.

Table 5.1 summarises the parameters of the coils used in the experiment to generate the two quadrupole traps.

5.1.4 Structure of the chapter

The structure of the chapter is as follows. In section 5.2 we describe the calculations of the magnetic potential which lead to the prediction of an optimum merging trajectory. The experimental apparatus used has already been presented in section 3.1. In section 5.3 we describe experiments that test the predictions of our magnetic potential analysis, and verify that the predicted

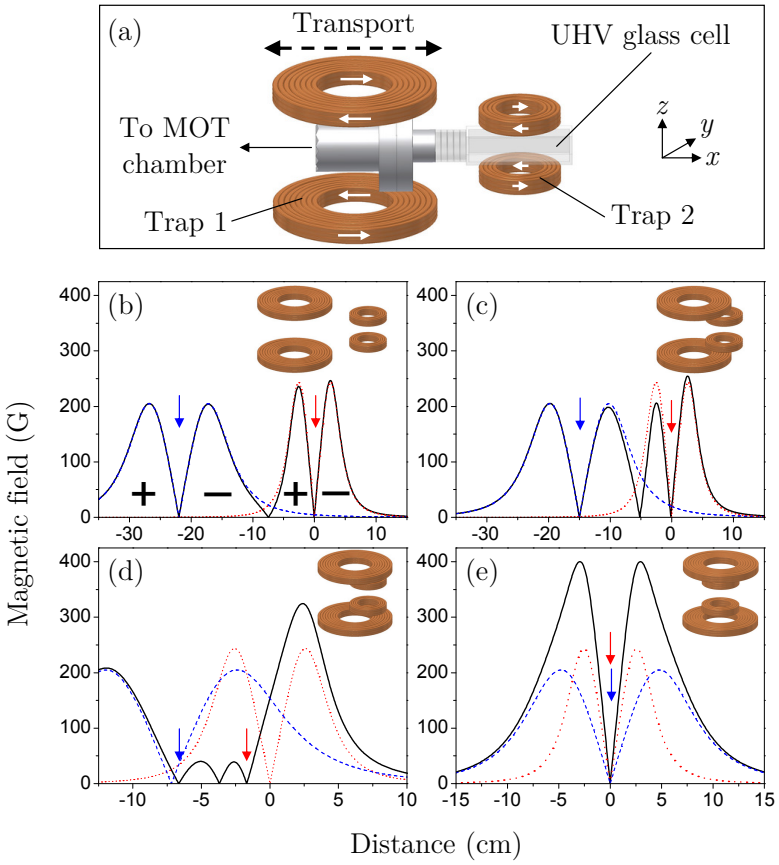

Figure 5.1: (a) Schematic of the experiment. A cloud of ultracold atoms is transported from the MOT chamber in a quadrupole trap (trap 1) mounted on a motorised translation stage. Trap 1 reaches the UHV glass cell and the cloud is transferred into the static quadrupole trap (trap 2). Trap 1 then returns to the MOT chamber, collects a second cloud and is merged with the static trap. (b)-(e) The magnitude of the magnetic field along the x-axis for trap 1 (dashed/blue), trap 2 (dotted/red) and the sum (solid/black) for different separations of the coils. (b) Separation 22.5 cm: Two separate quadrupole traps. The signs (+/-) indicate the direction of the field. (c) Separation 15 cm: As trap 1 approaches trap 2 an additional quadrupole-like zero is created where the dotted/red and the dashed/blue curves cross and the opposing signs of the field cause cancellation. The two inner barriers in the magnetic potential prevent the atoms entering the central trap. (d) Separation 7.5 cm: The height of the inner barriers is significantly reduced as the separation of the traps is decreased. However, the atoms are still confined in the two outer traps. Note the gradient ratio has been adjusted between (c) and (d) to maintain two inner barriers of the same height. (e) Separation 0 cm: Once merging is complete, both traps are overlapped to create a single quadrupole trap.

	Trap 1	Trap 2
Number of turns N	3×8	3×3
Tubing dimensions (mm × mm)	4.0×4.0	3.5×3.5
Inner separation (cm)	8.6(1)	3.7(1)
Outer separation (cm)	11.1(1)	5.9(1)
Inner radius (cm)	3.0(1)	2.2(1)
Outer radius (cm)	6.5(1)	3.4(1)
Equivalent coil separation (cm)	10.4(1)	4.7(1)
Equivalent coil radius (cm)	4.9(1)	2.7(1)
Axial field gradient ($\mathrm{G\,cm^{-1}\,A^{-1}}$)	0.606(1)	0.974(1)
Field maximum ($\mathrm{G\,A^{-1}}$)	1.004	0.961

Table 5.1: Parameters of the 'physical' and 'equivalent' coils used to generate quadrupole traps 1 and 2. All the coils are wound from square cross-section copper tubing. The axial field gradient and the field maximum apply to the pair of coils in each case.

optimum trajectory maximises the final atom number in the merged trap with minimal heating of the gas. Finally we demonstrate merging of variable proportions of the two different isotopes of rubidium.

5.2 Theory

5.2.1 Calculating the magnetic fields

The magnetic traps employed in the experiment are simple quadrupole traps generated using two circular coils in which the currents flow in opposite directions. The resulting magnetic field increases linearly in all directions from a field zero located on-axis midway between the coils. The traps are characterised by their axial field gradient, which is twice the radial gradient. Due to adiabatic following, the magnetic potential, U_{mag}, experienced by an atom is proportional to the magnitude of the field, *i.e.* $U_{\mathrm{mag}} = m_{\mathrm{F}} g_{\mathrm{F}} \mu_{\mathrm{B}} |B|$ [276], where m_{F} is the magnetic sub-level, g_{F} is the Landé g-factor and μ_{B} is the Bohr magneton. However, as the two traps merge the magnetic fields add vectorially so that the local direction of the magnetic field is also important. The potential that results from the interference of the two magnetic fields as the traps merge depends sensitively on the field generated by each coil. Consequently, to understand the merging process we calculate the combined magnetic potential resulting from both quadrupole traps as the distance between them is varied.

The magnetic field generated by each coil is calculated by numerical integration of the Biot–Savart law

$$\mathbf{B} = \int \frac{\mu_0 I'}{4\pi} \frac{\mathrm{d}\mathbf{l} \times \mathbf{r}}{|\mathbf{r}|^3}, \tag{5.1}$$

where μ_0 is the permeability of free space, I' is the current through the coil, $\mathrm{d}\mathbf{l}$ is an infinitesimally small element of the coil and $\mathbf{r}$ is the vector from the element $\mathrm{d}\mathbf{l}$ to the point in space where the magnetic field is to be calculated. The total magnetic field is then found by summing the contributions from each coil. In the experiment the real coils are wound from multiple turns of square cross-section copper tubing with the dimensions summarised in table 5.1. For simplicity, the coils are approximated by 'equivalent coils' consisting of a single turn of infinitesimal thickness and carrying a current of $I' = N \cdot I$, where N is the number of turns of the real coil and I is the current in the real coil. The radii and separations of the 'equivalent coils' were found by matching the calculated first and third spatial derivatives to the measured values for the real coils. Comparing the measured and calculated magnetic fields results in a normalised RMS deviation of $\approx 1\%$ over the range of interest, confirming the validity of this approximation.

5.2.2 Analysing the magnetic fields in one, two and three dimensions

We performed the calculation of the combined magnetic potential on a three-dimensional grid spanning both traps (see section 5.2.5 for a visualisation of the 3D potential). From this grid we generated one-dimensional cuts, two-dimensional contours and three-dimensional isosurfaces of this potential. A preliminary analysis revealed that the essential details of the merging process could be extracted from the simpler one-dimensional cuts of the combined magnetic potential along the line joining the two trap centers. Examples of such one-dimensional cuts are shown in Fig. 5.1(b-e), where the magnetic field due to traps 1 and 2 and the combined magnetic field are indicated by the dashed blue, dotted red and solid black lines respectively.

5.2.3 Understanding the merging process

For a given set of coils the form of the combined magnetic potential depends critically on two parameters; the separation of the two trap centers and the ratio of the axial magnetic field gradients at each trap center (trap 2/trap 1), henceforth referred to as the 'gradient ratio'. Our insight is that successful merging requires that we follow the idealised merging scenario shown in Fig. 5.1(b-e) in which the inner barriers of the magnetic potential that separate the two traps are maintained at equal heights throughout the merging. We stress that this is not usually the case when two magnetic quadrupole traps are simply moved towards each other and requires that the gradient ratio (and therefore the currents in each coil) be adjusted as the trap centers approach each other.

5.2.4 Detailed analysis of merging

To fully explore the merging process a set of ≈ 1000 one-dimensional plots of combined magnetic potential was generated for varying trap separations and gradient ratios. To condense this grid of plots into a more useful form we identified regions where qualitatively similar behavior was present in the combined magnetic potential, such as the presence of three field zeros or the existence of a single merged trap. These regions are shown in Fig. 5.2(a) as a function of trap center separation and gradient ratio. Each merging event has a unique trajectory through this 'potential map', traveling from left to right on the figure. Examples of four individual points in Fig. 5.2(a) are shown in Fig. 5.2(b-e) in order to demonstrate how the combined magnetic potential changes with respect to gradient ratio for a fixed trap separation.

Understanding the potential map is fundamental to understanding the merging process, therefore, we will now discuss in detail the regions highlighted in Fig. 5.2(a). Regions with differing Roman numerals identify different qualitative behavior in the combined magnetic potential. In region **I** the combined magnetic potential exhibits three field zeros separated by two potential barriers (Fig. 5.2(b) and (c)). Separating this region into two parts is the dashed line, along which the barriers are of equal height (Fig. 5.2(b)). The barrier height along this line is shown, as a function of separation, in the inset of Fig. 5.2(a). Either side of the dashed line the barriers are asymmetric and

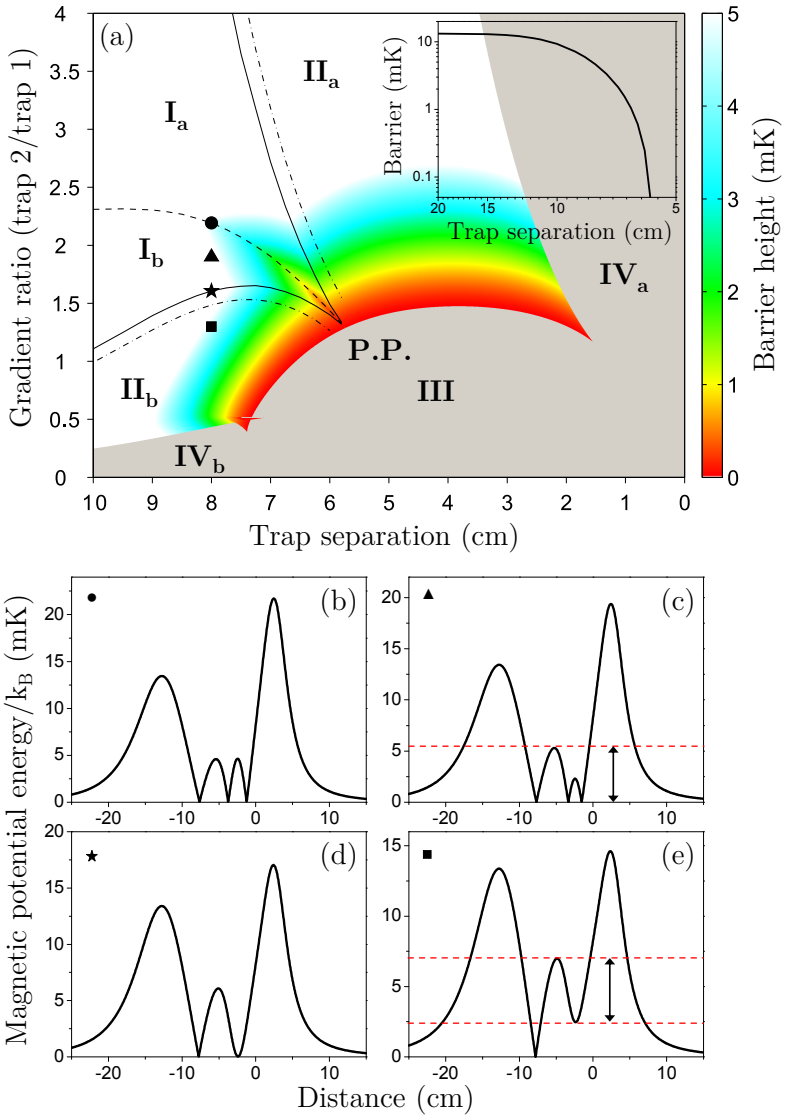

Figure 5.2: (a) Combined magnetic potential as a function of gradient ratio (trap 2/trap 1) and trap separation for ^{85}Rb ($F = 2, m_F = -2$), where the axial field gradient of trap 1 is $180\,\mathrm{G\,cm^{-1}}$. The dashed black line indicates where the two inner potential barriers are maintained at an equal height and the inset of (a) shows how this barrier height changes as a function of the trap separation. The solid/black lines show the trajectories where two zeros have merged and the resulting single minimum is about to lift up. The upper (lower) dot-dashed line represents where the trap 1 (trap 2) minimum is lifted to 1 mK. (b-e) show the combined potentials along the transport axis for the points marked in (a). Dashed red lines in (c) and (e) indicate the relevant barrier heights plotted in (a) as a colour variation in mK for regions **I** and **II**, respectively. The 'pinch point' referred to in the main text is labeled as '**P.P.**'.

smaller on the side of trap 1 ($\mathbf{I}_a$) or trap 2 ($\mathbf{I}_b$) (Fig. 5.2(c)). In region **II** there are only two field minima and one barrier as the central field zero and either trap 1 ($\mathbf{II}_a$) or trap 2 ($\mathbf{II}_b$) have combined (Fig. 5.2(d) and (e)). The solid black lines mark the boundary between regions **I** and **II** (Fig. 5.2(d)). As we venture further into region **II** the magnetic field of the combined minimum becomes non-zero and increases in magnitude as we move further from the solid line (Fig. 5.2(e)). The dot-dashed lines indicate where this minimum has been lifted to a potential of 1 mK. Note that all potential energies presented in this analysis refer to ^{85}Rb ($F = 2, m_F = -2$) and an axial field gradient of trap 1 equal to $180\,\mathrm{G\,cm^{-1}}$.

The optimum merging strategy is to avoid the raised minima that occur in region **II** as the raised potential could heat the cloud. Consequently the optimal 'merging channel' is given by the boundaries of region **I**, where two intermediate barriers and three magnetic field zeros continue to be maintained. The three lines guiding the channel converge and lead into region **III** at the 'pinch point' (indicated in Fig. 5.2(a) as **P.P.**). In region **III** (and region **IV**) traps 1 and 2 have merged into a single trap. As an aside, we note that the conveyor-like shifting of such single, merged traps operating permanently in region **III** has previously been demonstrated to great effect for the magnetic transport of ultracold atoms [274, 277]; however those experiments did not involve true merging in the sense employed in this work. In this simple picture we identify optimal trajectories as those which broadly follow the dashed line in region **I** passing through the merging channel and entering region **III** at the pinch point, thereby avoiding the raised minima in region **II**.

The colour map

The colour map in Fig. 5.2(a) represents the relevant barrier height and can be used to assess the extent of merging between the two atom clouds with finite energy. While the merging process is not adiabatic, to give some indication of the kinetic energy of atoms in the traps with respect to the inner barrier heights, we will treat the clouds as being in thermal equilibrium in the following analysis. We assume a temperature of $250\,\mu$K for a gas confined in a trap with an axial field gradient of $180\,\mathrm{G\,cm^{-1}}$. In region **I** the colour map indicates the maximum intermediate barrier height in mK, given by

the dashed red line in Fig. 5.2(c). Within the white area of this region no merging occurs as $< 1\,\%$ of atoms have sufficient kinetic energy to traverse potential barriers of height $> 2.75\,\mathrm{mK}$. Merging of the two traps begins to occur below a potential barrier height of $\approx 2.75\,\mathrm{mK}$, however, it is important to note that atoms from one trap may spill over the smaller barrier into the intermediate trap while the combined magnetic potential remains in region **I**. Once the trajectory reaches a barrier height of $1\,\mathrm{mK} \approx 50\,\%$ of atoms can traverse the inner barriers. In region **II** the colour map shows the minimum relative barrier height, given by the dashed red lines in Fig. 5.2(e). Here atoms could suffer an undesirable gain in kinetic energy during merging as they may be dropped from the lifted non-zero minimum into the trap with a field zero. Introducing finite energy broadens the merging channel because individual traps can be lifted if the kinetic energy that results from dropping the atoms into the second trap is small in comparison with the initial thermal energy of the gas. The dot-dashed lines in Fig. 5.2(a) give an indication of this broadening for a tolerance of the trap lifting up to 1 mK.

5.2.5 Analysing the optimal merging trajectory in 3D

Earlier (see section 5.2.2) we argued that to understand the merging process it was only necessary to study the trap properties in the direction of transport. It is, however, instructive to study a couple of extreme examples of the merging dynamics in 3D. Figure 5.3 gives two examples of merging scenarios.

In panels (a-g) trap 1 is stepped towards trap 2, while the gradient ratio follows the optimal trajectory, given by the dashed line in figure 5.2 (a). In (a) the 1 mK isosurface (red blob) of trap 2 can be seen at the far right of the panel, while trap 1 remains beyond the limits of the panel at the far left. The larger isosurface in the middle of panel (a) surrounds the middle field zero, formed in between the two traps (see figure 5.2 (b-c)), and initially contains no atoms. As trap 1 is brought closer to trap 2 the middle isosurface starts to sag, due to gravity, and comes in contact with the science cell (see (c)), however, no atoms are lost as the outer traps have not yet merged with the central trap. By the time trap 1 merges with the central trap, there is no contact with the science cell (see (d)), therefore any loss will be minimal. All three traps merge into one single elongated trap in (e), hence, the two clouds have now merged. Eventually trap 1 becomes centred on trap 2 and

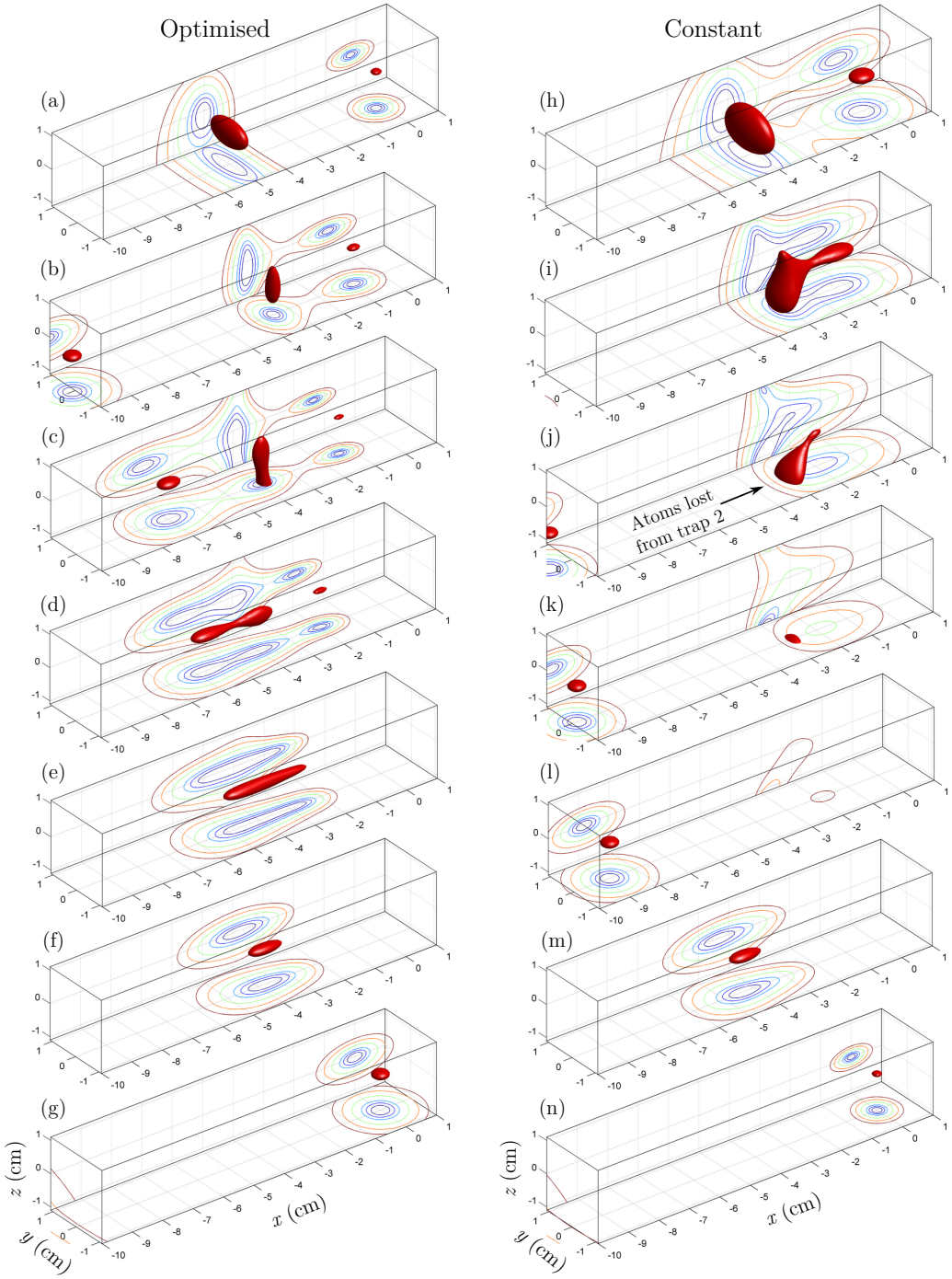

Figure 5.3: Analysis of two different merging strategies in 3D. The 3D potential observed by the atoms, with isosurfaces (red blobs) at 1 mK and contours at 1 mK, 1.5 mK, 2 mK, 3 mK, 4 mK and 5 mK shown in the x-y and x-z plane. The axes correspond to x: transport, y: imaging and z: gravitational. The border of each image gives the approximate size of our science cell. (a-g) The optimised merging trajectory, following the dashed line in figure 5.2 (a). (h-n) Unsuccesful merging at a constant gradient ratio of 0.78. See the main text for analysis.

the atoms have merged and reached their final destination (see (g)).

In panels (h-n) the same merging process occurs as (a-g), except that instead of following the optimal trajectory, we keep the gradient ratio constant at a value of 0.78. Following a straight line at 0.78 on figure 5.2 (a) it can be seen that we are well outside the optimal merging trajectory. The weaker trap 2 results in a larger 1 mK isosurface in (h) when compared with (a). (b-c) show how trap 2 merges with the central trap, which subsequently ploughs into the base of the science cell, removing all of the atoms that were originally present in trap 2. In (k-n) trap 1 can be seen approaching trap 2, however, as the atoms in trap 2 have sagged significantly, due to gravity, trap 1 continues on its journey to a final position centred on trap 2. In this scenario all the atoms from trap 2 have been lost while almost all of the atoms in trap 1 have remained.

5.2.6 Test scenarios to confirm the validity of the model

In order to confirm the validity of the above analysis we identify two trajectories on figure 5.2(a) that we test experimentally in section 5.3. The first of these trajectories is maintaining a constant gradient ratio during merging (see figure 5.4). We predict that for high or low gradient ratios atoms will only be maintained from the dominant trap and expect that poor merging will occur for intermediate ratios due to these not following the optimal trajectory. For our second trajectory we aim to maintain a gradient ratio that follows the dashed line on figure 5.2(a). Since merging only begins to occur below a barrier height of $\approx 2.75\,\mathrm{mK}$ in region **I**, we choose a trajectory consisting of a constant gradient ratio followed by a ramp downward tangential to the dashed line below $\approx 2.75\,\mathrm{mK}$ (see figure 5.6(a) inset). We expect to observe optimal merging following such trajectories.

5.3 Experimental results

To test the predictions based upon the potential map in figure 5.2(a), we initially performed a series of merging experiments with ^{85}Rb atoms confined in both traps (sections 5.3.1-5.3.3). Subsequently we demonstrate the merging of two different isotopes of rubidium (section 5.3.4).

5.3.1 Merging with fixed field gradients

Our initial aim was to investigate the first trajectory identified in section 5.2.6; that is whether merging could be achieved for a fixed value of the gradient ratio. To test this we confined the atoms initially in either trap 1 or trap 2 and then merged the two traps with a velocity of $5\,\mathrm{cm\,s^{-1}}$ for a range of constant gradient ratios. In both cases the second trap was initially empty. The results of these simple experiments are shown in figure 5.4. Throughout the chapter the measured atom number is scaled to the maximum number loaded into each trap before merging. For the results shown in figure 5.4, this corresponded to $(5.3\pm0.3)\times10^8$ for trap 1 and $(7.0\pm0.4)\times10^8$ for trap 2. The regions above and below the dashed/blue lines identify the gradient ratios where $< 10\,\%$ of the atoms are lost from either trap during

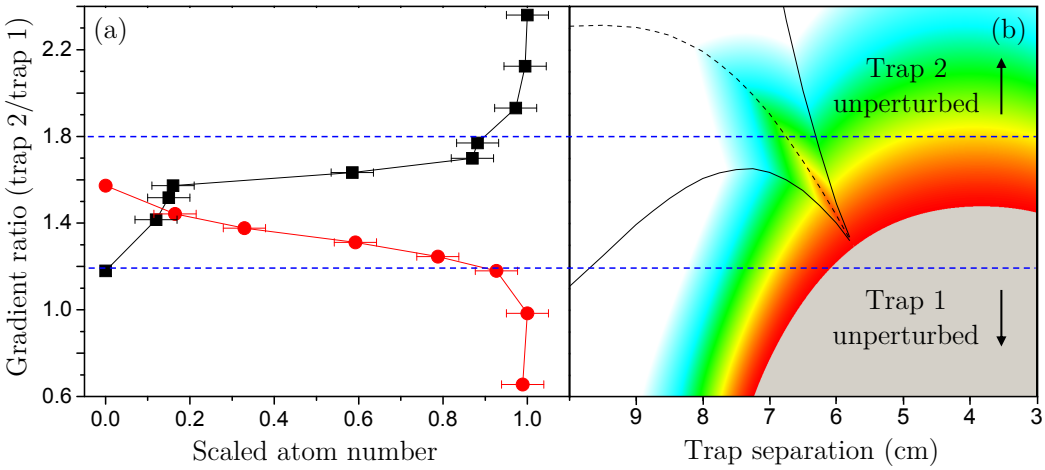

Figure 5.4: (a) Scaled atom number after merging as a function of the fixed gradient ratio of the two traps. The atoms are initially confined either in trap 2 (black squares) or in trap 1 (red circles). In both cases the second trap is initially empty. The dashed blue lines indicate the gradient ratios for each trap where 10 % of the atoms are lost during a merge event. These lines are also shown in the potential map in (b) to highlight the regions where either trap 1 or trap 2 is largely unperturbed by the presence of the other trap.

the merging process and these lines are also indicated on the potential map. Henceforth, we shall refer to the dominant trap in each of these regions as being 'unperturbed'. As predicted in section 5.2, at high gradient ratios trap 2 dominates trap 1. Evidence of this can be seen in figure 5.4(a) where atoms from the weaker trap 1 fail to enter the stronger trap 2. The converse can be seen for low gradient ratios. Also, as predicted, there is a smooth transition between the two unperturbed regions. However, the merging here is highly inefficient. For example, at a gradient ratio of ≈ 1.5, where the atom number is equal for both traps, only $\approx 15\,\%$ of the atoms are retained from each of the traps.

5.3.2 Merging with ramped field gradients

In order to discover whether successful merging could be achieved by following the narrow merging channel of region **I**, we employed a linear ramp of the gradient ratio during the merging as depicted in figure 5.5. In this scenario the gradient in trap 1 is held constant at $160\,\mathrm{G\,cm^{-1}}$ as it is moved towards the static trap 2. At a separation of 10 cm, where the traps are far from the merging region (see figure 5.2(a)), the reference trigger from the hardware controlling the motorised translation stage is sent to our control system. After trap 1 has traveled a variable distance beyond this reference point, which we refer to as the 'ramp start distance', the gradient of trap 2 is linearly decreased from the initial $320\,\mathrm{G\,cm^{-1}}$ to zero over a variable time. In order for the data to be comparable to figure 5.2(a) we relate the time taken for this linear ramp to the distance that the trap separation has decreased in this time and define it as 'ramp length'. The velocity of trap 1 is altered from the transport setting ($26\,\mathrm{cm\,s^{-1}}$) to a new variable velocity before the merging begins, as depicted in figure 5.5. By varying the ramp start distance and the ramp length we are able to explore the potential map in figure 5.2(a), searching for the optimum merging trajectory.

In a first set of experiments, we fixed the ramp length and varied the ramp start distance, thus translating the ramp horizontally (w.r.t to figure 5.2(a) and figure 5.5) across the merging channel and the pinch point. For each experiment the merging was performed three times; firstly with the atoms in trap 1, then with the atoms in trap 2 and finally with the atoms loaded into both traps. The results in figure 5.6(a) are for a ramp length of 3 cm,

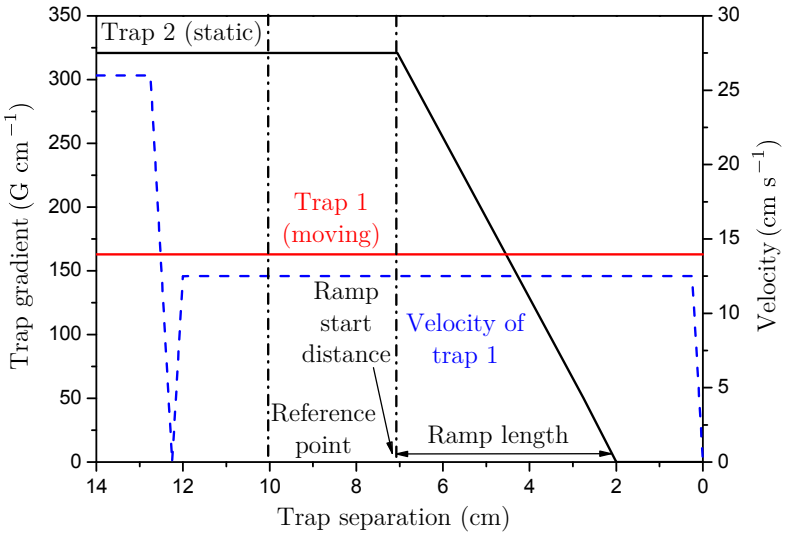

Figure 5.5: Typical evolution profiles of the gradients and velocities of the quadrupole traps during merging. The gradient of trap 1 (lower solid red line) remains constant, whilst the gradient of trap 2 (upper solid black line) is decreased during the merging process. The dashed blue line shows the velocity profile of trap 1, which decreases from the transport setting to a new variable velocity before the merging begins.

merging speed of 12.5 cm s^{-1} and initial atom number of 1.5×10^8. The left hand side of this figure corresponds to an experiment where effectively trap 2 is turned off before trap 1 arrives, and accordingly all the atoms initially in trap 1 remain. The right hand side of the figure corresponds to an experiment where trap 1 and trap 2 are effectively merged with a constant gradient ratio (equal to 2 in this case). In this limit, therefore, the results are consistent with the experiment presented in figure 5.4, with the majority of the atoms initially in trap 2 remaining. In the central region of the figure a mixture of atoms from trap 1 and trap 2 remain in the merged trap. The solid blue line in the inset of figure 5.6(a) depicts the ramp given by the circled data point, which clearly follows the identified merging channel, passing very close to the pinch point. In this case, highly improved merging is observed for an optimum ramp start distance of 6.7 ± 0.1 cm when compared to the fixed gradient case shown in figure 5.4.

We then repeated this experiment for several ramp lengths, with the aim of confirming the existence of the pinch point. In each case we were able to identify an optimum ramp start distance for the given ramp length by requiring that approximately equal numbers of atoms were transferred from each trap into the final merged trap. Strikingly, within experimental error,

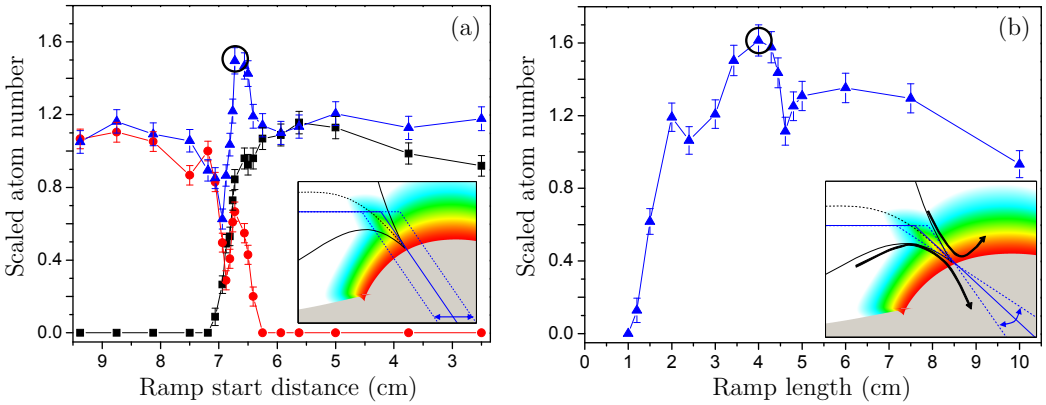

Figure 5.6: Optimising the merging process through measurements of the scaled atom number following the merging as a function of the ramp parameters. In (a) we vary the ramp start position, for a ramp length of 3.0 cm, translating the ramp across the pinch point and in (b) we vary the ramp length *i.e.* the angle of the trajectory through the pinch point. Data are shown for atoms initially in trap 2 (black squares), trap 1 (red circles) and both traps (blue triangles). The solid blue lines in the insets indicate the ramps circled in each figure, while the dotted blue lines indicate the variation of the ramp in each experiment. The results of a large number of experimentally tested ramps are summarised in the inset of (b) with the single-headed curved black arrows indicating where the merged atom number is $\approx 50\,\%$ of that seen for the optimal trajectory.

the optimum ramps intersect and we identify an experimental pinch point of (trap separation, gradient ratio) $= (5.8 \pm 0.1\,\text{cm}, 1.4 \pm 0.1)$. This is in remarkably good agreement with the theoretically determined pinch point of (5.76 cm, 1.30). Moreover, closer examination of this data highlights that the most successful merging occurs for trajectories that follow the merging channel. These results therefore confirm our predictions that the optimum merging trajectory will follow the merging channel and will pass through the narrow pinch point.

5.3.3 Optimising the merging trajectory

To test the dependence of the merging on the slope of the trajectory, we performed a second set of experiments in which the ramp length was varied whilst the ramp start distance was adjusted to ensure that the trajectory still passed through the experimentally determined pinch point, effectively swiveling around this point (see double headed arrow in figure 5.6(b) inset). Traps 1 and 2 were again loaded with equal numbers of atoms and the combined atom number after merging was measured. The results are plotted in

figure 5.6(b), identifying an optimum ramp length of (4.0 ± 0.5) cm through the experimentally determined pinch point. This merging trajectory through the potential map is entirely consistent with our theoretical predictions in section 5.2 and there is excellent agreement between the slope of the trajectory and the gradient of the dashed line in figure 5.2(a) in the vicinity of the pinch point (see solid blue line in inset of figure 5.6(b)). Note, however, the uncertainty in the optimum ramp length, due to the broad peak seen in figure 5.6(b), is an indication of the presence of a broadened merging channel.

Having established the optimum merging trajectory for the experimentally determined pinch point, we carried out many more runs varying the trajectory around this optimum in order to estimate the size and width of the merging channel. The results are summarised in the inset of figure 5.6(b). The black single-headed curved arrows indicate trajectories where the merged atom number is half of the number obtained along the optimum trajectory. As theoretically predicted in section 5.2, the channel narrows into the crucial pinch point and then opens wide once merging is achieved, with the black single-headed arrows confirming the broadening of the pinch point due to the finite temperature of the atoms.

In a further experiment, we also varied the velocity of trap 1 during the merging for this optimum ramp length. This showed that, within the exper-

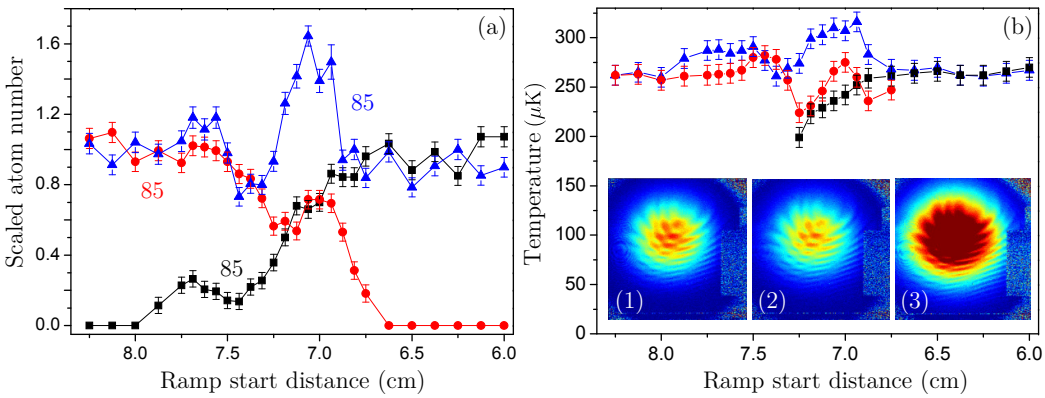

Figure 5.7: Detailed results of the merging for ^{85}Rb. Scaled atom number (a) and temperature (b) following the merging (for atoms initially in trap 2 (black squares), trap 1 (red circles) and both traps (blue triangles)) as a function of the ramp start distance for a fixed ramp length of 4.0 cm, initial gradient ratio of 2 and a merging speed of 12.5 cm s^{-1}. The inset in (b) shows false colour absorption images of the atomic cloud following merging (for atoms initially in (1) trap 1, (2) trap 2 and (3) both traps). Both traps contained a maximum number of 3.5×10^8 atoms.

imental uncertainties, the maximum achievable atom number is independent of the speed with which the two traps merge up to $12.5\,\mathrm{cm\,s^{-1}}$. For higher speeds the number of atoms remaining in trap 1 falls off quickly towards zero.

Using the optimum ramp length determined from figure 5.6(b), we made a detailed measurement of the atom number and the temperature for the merged cloud as a function of the ramp start distance for ^{85}Rb in both traps (see figure 5.7). The results indicate that a merge of $\approx 75\,\%$ of the atoms from each trap was possible giving $\approx 150\,\%$ of the number achieved in a single load. In addition, we do not observe any significant heating, with the final merged clouds having typical temperatures of $\approx 300\,\mu$K to be compared with the temperatures of the initial clouds of $\approx 260\,\mu$K.

5.3.4 Merging ^{85}Rb and ^{87}Rb

In a final experiment, we demonstrated the merging of the two different rubidium isotopes as shown in figure 5.8 by simply using the optimum ramp length determined for ^{85}Rb. Throughout this experiment, we ensured that the number of ^{87}Rb atoms in trap 1 prior to the merging was the same as the number of ^{85}Rb present in trap 2. In this case we were only able to achieve an equal merge of $\approx 40\,\%$ from each isotope, primarily due to poorer transfer of ^{87}Rb into the combined trap. We believe this is due to a technical limitation whereby we were unable to completely compensate for the smaller magnetic moment of ^{87}Rb ($\mu_{87} = 3/4 \times \mu_{85}$). To regain the same trap stiffness as for ^{85}Rb the magnetic field gradient has to increase by 4/3, however, this was not possible due to the current limit of the power supply to the coils. We note that for sympathetic cooling it is desirable to start with a high ratio of refrigerant species to the species to be cooled *e.g.* > 30:1 (^{87}Rb:^{85}Rb) [216, 217]. Hence, despite this poorer merging efficiency, we are able to create suitable conditions for sympathetic cooling of ^{85}Rb with ^{87}Rb, either by choosing the appropriate ramp start distance or by simply loading less ^{85}Rb into trap 2. Specifically we have loaded 1.5×10^8 ^{87}Rb atoms with 5×10^7 ^{85}Rb atoms at a temperature of $\approx 200\,\mu$K, enabling straightforward access to similar starting conditions to experiments that employ separate laser cooling setups for each isotope [216, 217].

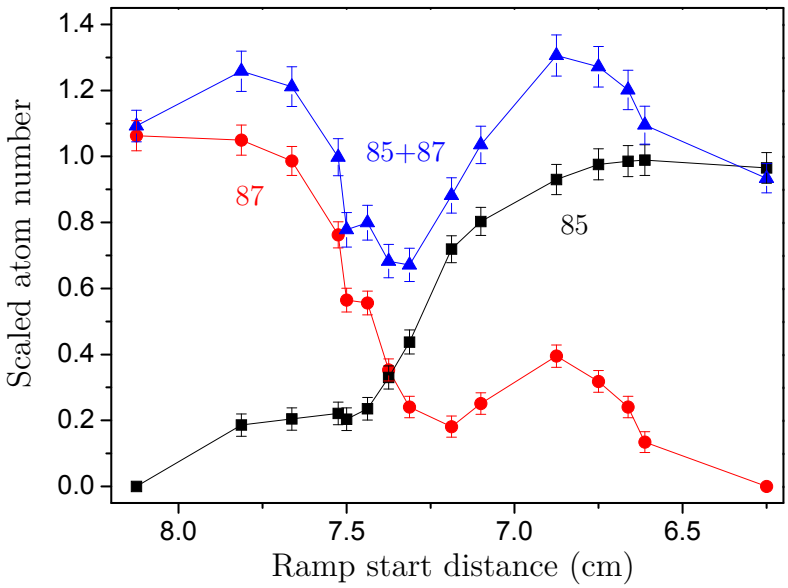

Figure 5.8: Merging of the two rubidium isotopes, using the optimum ramp length and merging speed determined in the ^{85}Rb experiments. Scaled atom number is shown as a function of the ramp start distance. ^{85}Rb is held initially in trap 2 and then merged with ^{87}Rb in trap 1.

5.4 Discussion

Before concluding we mention two more points of interest regarding our experimental results. Firstly, all the experiments described have been repeated at least twice over several months and the detailed structure seen in the merging plots of figures 5.6 (a), 5.7 (a) and 5.8 is reproducible. We believe this is related to the dynamics of the atoms as they cross the magnetic potential barriers outlined in our analysis in section II. This demonstrates the need for precise control and synchronisation of the transport mechanism with the gradient ramps in order to achieve reproducible merging. Secondly, despite our best effort to obtain merging of $\approx 100\,\%$ of the atoms from each trap, we were only able to achieve $\approx 75\,\%$ of each ^{85}Rb cloud. A possible explanation is that more energetic atoms in the cloud are colliding with the surface of our vacuum chamber. However, we have repeated the merging with initial cloud temperatures of $\approx 260\,\mu$K and $\approx 70\,\mu$K and saw no improvement in the merging percentage for the colder atoms. An alternative explanation is that we experience enhanced Majorana losses as the intermediate trap barriers are reduced to zero during the merging. The extent of the region of magnetic field where Majorana losses will occur again depends sensitively on the exact trajectory through the potential map and this fact may also contribute to

the detailed structure seen in the merging plots.

In general, the technique of magnetic merging we have described allows the merging of any two magnetically trappable species and is not limited to the case of an isotopic mixture. It offers an advantage whenever two atom clouds cannot be laser-cooled in the same trap, for instance it circumvents the problem of detrimental light-assisted collisions that occur in some two species magneto-optical traps [270, 271]. Such collisions often severely limit the achievable range of atom numbers (and their ratios) in the MOT. We believe that as experiments in the field become ever more complex and sophisticated, techniques such as magnetic merging will become essential to access new physics in these rich systems. The merging process can in principle be repeated several times allowing the generation of even more complex mixtures comprising three [242] or more species. This could greatly extend the range of possible physics in mixture experiments. Also our analysis of the merging process is extendable to other trap geometries and may therefore be of interest to the atom chip community.

Modern BEC experiments with differentially pumped vacuum chambers tend to fall into two camps, those employing a push beam with a double MOT system or Zeeman slower to collect atoms separately from the ultra-high vacuum science chamber, or those employing a magnetic transport system to achieve the same separation of collection and science zones. The latter method offers the advantages of very long lifetimes in the science cell combined with excellent optical access owing to the lack of MOT optics. Certainly in these magnetic transport systems it is a relatively simple matter to implement the magnetic merging that we have described as it is primarily a matter of synchronising the magnetic-field-generating currents with the pre-existing coil motion.

In our specific case of ^{85}Rb and ^{87}Rb we were able to use just one laser cooling system (*i.e.* a cooling laser and a repumping laser with associated AOMs, optics and fibers) to load each isotope at separate times before magnetic merging. This considerable simplification allowed stable and reproducible loading of the number of atoms of each isotope over a large range from zero to 5×10^8 for each species and the ratio of the atomic numbers can be further tailored reproducibly during the merging process. The technique allows equal ratio mixtures to be realised which is often difficult in two species MOTs.

5.5 Conclusion

In conclusion, we have demonstrated the magnetic merging of two ultracold atomic gases by the controlled overlap of two initially well-separated magnetic quadrupole traps. We have shown that a simple 1D analysis of the combined magnetic field potential as the two traps are brought together is sufficient to identify and understand the region where merging occurs, and leads to a clear prediction of the optimum trajectory for the merging. We have verified this prediction experimentally using ^{85}Rb and found that the final atom number in the merged trap is maximised with minimal heating by following the predicted optimum trajectory. We believe that optimal merging trajectories could be determined for any specific coil geometries and sizes by following a similar methodology. We have used the merging technique to multiply load atoms into a single magnetic quadrupole trap. Whilst this did not produce an increase in phase space density, the accumulation of atoms in a single trap can be beneficial for subsequent evaporative cooling. Finally we have used the magnetic merging to create controlled variable ratio atomic mixtures of the two isotopes of rubidium into a single quadrupole trap with a simple laser system for laser cooling each isotope sequentially.

Chapter 6

Evaporation of ^{85}Rb to BEC and the formation of solitary waves

6.1 Introduction

In this chapter we will discuss the experimental route that we have taken to achieve Bose-Einsten condensation in ^{85}Rb via direct evaporation and some of the challenges that have been observed in the process. We also present experiments that demonstrate the tunable nature of a ^{85}Rb condensate and the resulting formation of solitary waves in an optical waveguide.

6.2 ^{85}Rb and ^{87}Rb: How two neutrons can make all the difference

Our journey towards forming solitary waves out of ^{85}Rb begins with creating a BEC. We must first understand the potential challenges that will become manifest when evaporation towards BEC is undertaken. These challenges vary greatly between isotopes and ^{85}Rb is a particularly difficult isotope to condense for two reasons, which are presented below. If ^{85}Rb is such a difficult isotope to condense, while ^{87}Rb is significantly more straightforward, why focus our efforts on condensing such a difficult species? If we wish to

create a solitary wave from this BEC, it is necessary to have excellent control over the scattering length of the particles, which requires a method of tuning the scattering length. We use a wide (10.7 G wide at 155 G) Feshbach resonance in ^{85}Rb [115, 278] to achieve this, which makes this isotope an ideal candidate to study solitary waves, even though it is very difficult to condense. While, in comparison, ^{87}Rb is much easier to condense, the widest Feshbach resonance that has been discovered in this isotope is only 0.2 G wide and at a high field (1007 G) [279], which would result in very poor control of the scattering length of ^{87}Rb.

There are two factors that one must take account of to determine if efficient evaporation of a cloud of atoms is going to occur; the rate of elastic collisions and the rate of inelastic collisions. Elastic collisions rethermalise the cloud when hot atoms are lost from the trap, the result of which is the reduction in temperature and a possible increase in phase space density of the cloud. Competing against the elastic collisions are the inelastic collisions[1], which remove atoms from the trap that on average have less than the mean energy of an atom in the cloud. The resulting effect of this is to heat the cloud, decreasing its phase space density. The ratio of elastic to inelastic collision rates ($\Gamma_{\rm el}/\Gamma_{\rm in}$) will become an important quantity to consider in our evaporation to BEC and will govern the amount of time we spend evaporating.

6.2.1 Elastic scattering cross-section

The rate of elastic collisions in our cloud of atoms is given by [280]

$$\Gamma_{\rm el} = \langle n \rangle \, \sigma \, \langle v_R \rangle \,, \tag{6.1}$$

where $\langle n \rangle$ is the mean density of the cloud, σ is the elastic scattering cross-section and $\langle v_R \rangle$ is the mean relative speed of the trapped atoms and is given by [281]

$$\langle v_R \rangle = \left(\frac{16 k_{\rm B} T}{m \pi} \right)^{1/2} . \tag{6.2}$$

Both $\langle v_R \rangle$ and $\langle n \rangle$ are essentially independent of the isotope of rubidium

[1] An example of this is the process that forms molecules in the trap, causing three-body loss.

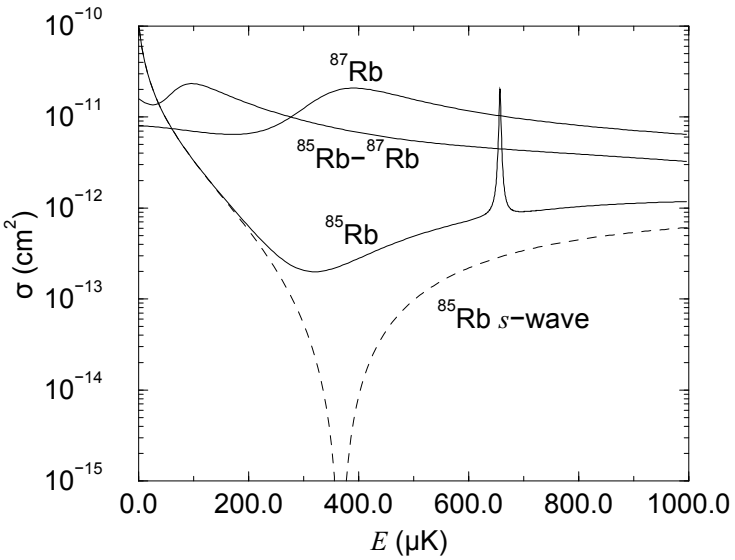

Figure 6.1: The elastic scattering cross-section for collisions between the rubidium isotopes. The minimum in the s-wave partial cross section at 375 μK causes a significant decrease in the total cross section for ^{85}Rb. From [282].

we are working with[2]. The same cannot be said for σ, as this is strongly isotope and collision energy dependent, with variations over orders of magnitude [282]. Figure 6.1 shows the scale of variation in the elastic scattering cross-section for different rubidium isotopes and collision energies.

For collision energies above 100 μK it can be clearly seen that σ is significantly smaller for ^{85}Rb–^{85}Rb collisions in comparison with ^{87}Rb–^{87}Rb or ^{85}Rb–^{87}Rb collisions. At its lowest point—around 300 μK—$\sigma_{^{87}\mathrm{Rb}} \sim 50\sigma_{^{85}\mathrm{Rb}}$. We start our evaporation at $T \sim 300$ μK and collision energy is dependent on the mean relative velocity,

$$\langle E_{\mathrm{col}} \rangle = \frac{1}{2} m \langle v_R \rangle^2 = \frac{8 k_{\mathrm{B}} T}{\pi}. \tag{6.3}$$

Substituting $T \sim 300$ μK into (6.3) gives $\langle E_{\mathrm{col}} \rangle \sim 760$ μK. As we evaporate our cloud, the cross-section becomes smaller and smaller until $T \sim 120$ μK, where the elastic collision rate has reached its most inefficient point. Throughout this process, our evaporation is a lot less efficient than if we were using ^{87}Rb. The result of this inefficiency is an increase in the rethermalisation time, resulting in the need for longer evaporation times. Unfortunately, due to inelastic losses, this means we are actually throwing away more atoms

[2]With the exception of a small factor of $\sqrt{85/87}$ due to the mass being present in $\langle v_R \rangle$.

in order to achieve the same phase space density in ^{85}Rb. Eventually, at $T \sim 40$ μK, when we are about to load the optical dipole trap, the cross-sections of different isotope collisions become comparable. We now, however, have another effect to contend with!

6.2.2 Inelastic losses

In ^{85}Rb not only do we have problems with the elastic scattering rate but also the addition of very high inelastic collision rates. Inelastic collisions are those which heat the cloud due to losses of particles with lower than the mean energy. These loss mechanisms have to be continuously fought against during the entire evaporative cooling process if you want to reach BEC. One particular method is described in section 6.4.2. The three typical loss mechanisms that are experienced by a cloud of atoms during evaporative cooling are shown in Fig. 6.2.

The first of these, two-body dipolar relaxation, occurs when two particles in the cloud collide, causing their spins to flip to an untrapped state and its rate is described by

$$\Gamma_{2B} = -K_2 \langle n \rangle . \tag{6.4}$$

It is important to note that the two-body decay constant, K_2, for ^{85}Rb is orders of magnitude larger than in ^{87}Rb, which contributes to the difficulty in evaporative cooling [218, 272],

$$K_2\left(^{85}\mathrm{Rb}\right) = 3 \times 10^{-14}\ \mathrm{cm^3\,s^{-1}}, \qquad K_2\left(^{87}\mathrm{Rb}\right) \approx 10^{-18}\ \mathrm{cm^3\,s^{-1}}. \tag{6.5}$$

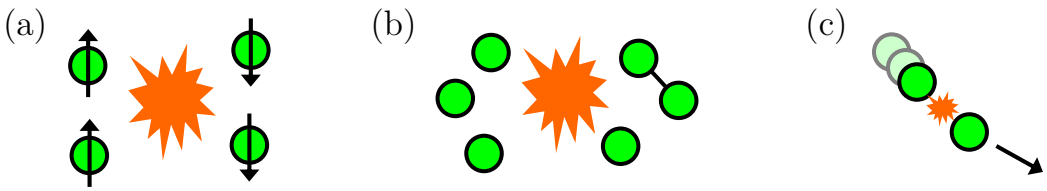

Figure 6.2: The three main loss mechanisms during evaporative cooling are: (a) two-body dipolar relaxation, where two atoms collide and their spins are flipped and are no longer trapped, (b) three-body recombination, where three atoms collide, forming a molecule, which is lost from the trap and (c) background collisions, where a hot atom from outside the cloud collides with an atom in the cloud, transferring kinetic energy, leading to loss of the atom.

Due to its dependence on the square of the density of the cloud, three-body recombination becomes increasingly prevalent as we approach BEC. This is where three particles collide causing the formation of a molecule, which is no longer trapped, with a rate given by

$$\Gamma_{3\mathrm{B}} = -K_3 \left\langle n^2 \right\rangle . \tag{6.6}$$

The three-body decay constant K_3 has been shown to scale with the scattering length as a^4 [283–285]. We also find that the three-body decay constant is around three orders of magnitude larger in ^{85}Rb than ^{87}Rb [218, 286],

$$K_3\left(^{85}\mathrm{Rb}\right) = 5 - 10 \times 10^{-25}\ \mathrm{cm}^6\,\mathrm{s}^{-1}, \qquad K_3\left(^{87}\mathrm{Rb}\right) = 4 \times 10^{-29}\ \mathrm{cm}^6\,\mathrm{s}^{-1}. \tag{6.7}$$

It is important to note that both K_2 and K_3 are dependent on the scattering length of an atom [287–289], and therefore dependent on the magnetic field across a cloud of ^{85}Rb atoms. Therefore, the values of K_2 and K_3 can be changed by orders of magnitude around a Feshbach resonance [79, 116, 290, 291].

The final general loss mechanism is through collisions with high energy background particles in the vacuum, which is independent of the isotope that we are cooling. These particles have not been cooled, hence, they have much greater energy than atoms in the cloud. These collisions will cause an evaporatively cooled atom to be kicked out of the trap due to conservation of momentum. The lifetime due to background collisions, τ_{Back}, is a quantity that is measured for a particular vacuum system and can then be converted to a rate,

$$\Gamma_{\mathrm{Back}} = \frac{1}{\tau_{\mathrm{Back}}}. \tag{6.8}$$

While the first three can be applied to any generic trap, there is a further loss mechanism that occurs within a trap containing a magnetic field zero, such as a quadrupole trap, and these are Majorana spin-flips. The flip of spin to an untrapped state can occur while the atom travels close to the field zero. The rate at which Majorana spin-flips occur in a quadrupole trap has

been calculated as [214]

$$\Gamma_{\mathrm{Maj}} = 1.85\frac{\hbar}{m}\left(\frac{m_F g_f \mu_{\mathrm{B}}}{k_{\mathrm{B}}T}\frac{\partial B}{\partial r}\right)^2. \tag{6.9}$$

When atoms are being stored in a dipole trap, the scattering of photons can also lead to heating of the atom cloud; the rate of which can be quantified by (13) in [207].

6.3 Methods of condensing ^{85}Rb

When we choose to attempt the condensation of a difficult species, like ^{85}Rb, we have two routes that can achieve degeneracy, each of which has its pros and cons. Both of these routes use evaporative cooling as their workhorse, but the species which is cooled differs. Figure 6.3 shows a schematic of evaporative cooling in quadrupole and dipole traps. We shall discuss the routes and elaborate on the relevant issues below.

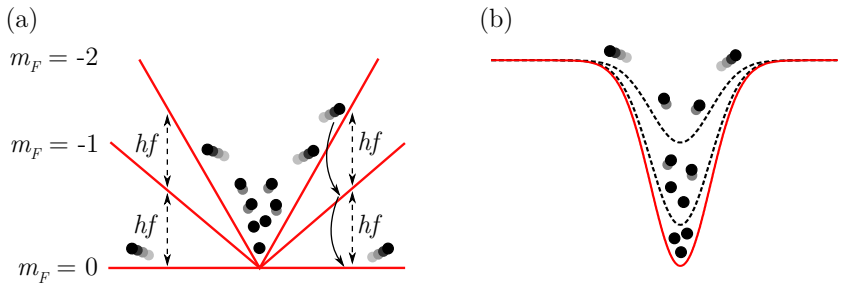

Figure 6.3: Two typical schemes of evaporative cooling. In (a) a radio frequency 'knife' is applied to a magnetic quadrupole trap to remove atoms above a chosen energy level, by flipping their spin. The application of an rf-field reduces the energy gap between adjacent magnetic sub-levels, resulting in a degeneracy between the sub-levels for high energy atoms. These high energy atoms eventually reach magnetically untrappable states, allowing evaporation to occur. In (b) the depth of an optical dipole trap is reduced to allow high energy atoms to escape while continuing to trap lower energy atoms, thus reducing the temperature.

6.3.1 Direct evaporation

The simplest method to use in our attempt to reach degeneracy is direct evaporation, in which our trap only contains one species—in our case ^{85}Rb.

What we mean by direct evaporation is the cooling of an atomic species by the gradual removal of atoms, of that species, that have an energy that is greater than the mean energy of an atom in the cloud. As a result of this, the cloud rethermalises and cools and this has been the standard way to achieve Bose–Einstein condensation since the method was first presented in this context [292, 293].

If we can efficiently evaporate our species, direct evaporation is the clear method to use, as we maintain the simplicity of only needing one laser system for the isotope that we are evaporating. The complication arises when a species is particularly inefficient to condense, like ^{85}Rb. In this circumstance it is necessary for the experimentalist to decide whether simplicity in the apparatus trumps the difficulty of achieving degeneracy. One downside is that the final atom number in the condensate will typically be very low, due to the high inelastic collision rates throughout the entire process. Direct evaporation was the method used to reach degeneracy for the first time in ^{85}Rb [15], achieving atom numbers of around 10^4 in a pure condensate.

6.3.2 Sympathetic cooling

It may be important to have as many atoms in a BEC as possible. In this case sympathetic cooling can be undertaken at the expense of a more complex experimental apparatus (*e.g.* see [294]). Sympathetic cooling uses an evaporatively efficient species to act as a thermal bath in which to cool a 'difficult' species via elastic collisions. As can be seen in figure 6.1, the elastic scattering cross-section for ^{85}Rb–^{87}Rb collisions is around an order of magnitude greater at the start of the evaporation process than for ^{85}Rb–^{85}Rb collisions. This results in an increased collision rate, which means that we can undertake evaporation rapidly, reducing the impact of inelastic losses.

Since the first demonstration of sympathetic cooling between ^{85}Rb and ^{87}Rb [215] there have been two groups that have created a BEC via this method [217, 248]. By combining a small cloud of ^{85}Rb atoms and a much larger cloud of ^{87}Rb atoms[3], the ^{87}Rb atoms could be preferrably evaporated away with minimal loss to the ^{85}Rb atoms. The resulting BECs have had atom numbers as high as 8×10^4 [248] and 10^5 [116].

[3] In the case of [216, 248], the ratio ^{85}Rb:^{87}Rb at the start of evaporation was as high as 1:300.

A separate laser system for each species is not essential in order to undertake sympathetic cooling, as we have demonstrated in chapter 5. All that is needed is a method with an end result of a mixture of ^{85}Rb and ^{87}Rb. If merging was undertaken to achieve this goal, the amount of experimental apparatus used would be significantly reduced, however this method is still more complicated than undertaking direct evaporation.

6.3.3 The chosen method of this experiment

Weighing up the pros and cons of the two above methods, we have chosen the more simplistic experimental setup and undertake direct evaporation, at the expense of smaller atom numbers. However, we will demonstrate in the following sections that through careful optimisation of our evaporation trajectory, it is possible to achieve atom numbers as great as 5×10^4 in a BEC in our experiment via direct evaporation.

6.4 Condensing ^{85}Rb through direct evaporation

Our typical route to degeneracy when we initially formed a ^{85}Rb condensate can be seen in table 6.1. This table summarises how the atom number, cloud temperature and phase space density changes throughout our experimental routine.

Stage	Number	Temperature	PSD
Transfer to static quadrupole trap	3.5×10^8	300 μK	5×10^{-8}
End of RF evaporation	3.5×10^7	42 μK	5×10^{-5}
Transfer to crossed-dipole trap	5.5×10^6	14 μK	2×10^{-3}
Evaporation at low bias field	1.8×10^6	3 μK	1×10^{-2}
Ramp bias field to 170 G	8.7×10^5	2 μK	2×10^{-2}
Evaporation at 175 G	2.5×10^5	150 nK	0.7
Evaporation to BEC at 161 G	$\approx 5 \times 10^4$	$\approx$ 15 nK	> 2.61

Table 6.1: The route to degeneracy in ^{85}Rb. These were the parameters oberserved for the initial period of BEC formation, relating to [79]. The exact routine used in this period differs slightly from the routine presented in table 6.2.

The main points to note in our experimental routine are that we load 3.5×10^8 atoms at 300 μK into the static quadrupole trap in the science cell; the load-

ing of the crossed-dipole trap increases the phase space density of the cloud by nearly two orders of magnitude due to rapid initial evaporation; we evaporate at $\sim$ 175 G for as long as we are able as the losses are minimised at this field, but the interactions are attractive; and we ramp the field from $\sim$ 175 G to $\sim$ 161 G to continue with slightly less efficient evaporation to degeneracy at a repulsive, stable, scattering length. This final relatively efficient evaporation field region was originally discovered in the first experiment that condensed ^{85}Rb [15].

Table 6.1 gives the cloud parameters that we achieved when we first observed condensation of ^{85}Rb [79] (see red circles in figure 6.4). The majority of data presented in the rest of this section has been obtained six months after the initial observation, with some significant differences, such as a reduced atom number in the BEC ($N \sim 5 \times 10^3$). Careful optimisation has not resulted in the discovery of the reason why the atom number has reduced by an order of magnitude. While this situation may not seem optimal, it has not prevented us studying the dynamics of solitary waves as $N_{\mathrm{cr}} \sim 3000$ for our trap parameters, therefore, we have sufficient atom numbers to be able to create single solitary waves close to the critical number.

Figure 6.4 shows the evaporation trajectory originally undertaken in [79] (red circles), while the most recent evaporation trajectory is shown underneath (black squares). We will discuss in more detail each stage of this evaporation process and will regularly refer back to figure 6.4 in the process.

6.4.1 Quadrupole trap

Our evaporative journey begins in the science cell with our atoms contained in the static quadrupole trap. At this point we have a cloud of atoms with $N \sim 3.5 \times 10^8$ and $T \sim 300$ μK, resulting in a phase space density more than seven orders of magnitude away from degeneracy. The gradient of the quadrupole trap is 180 G cm^{-1} throughout this entire process. The cloud must be cooled and this is undertaken via radio-frequency (RF) evaporation. In figure 6.3 (a) we see a schematic of RF evaporation occurring in a magnetic quadrupole trap. We apply an RF-field with a frequency f, resulting in a total energy of $E_{\mathrm{RF}} = hf$ imparted to the atoms in the quadrupole trap. In exactly the same way as the Majorana mechanism, it is possible for an atom

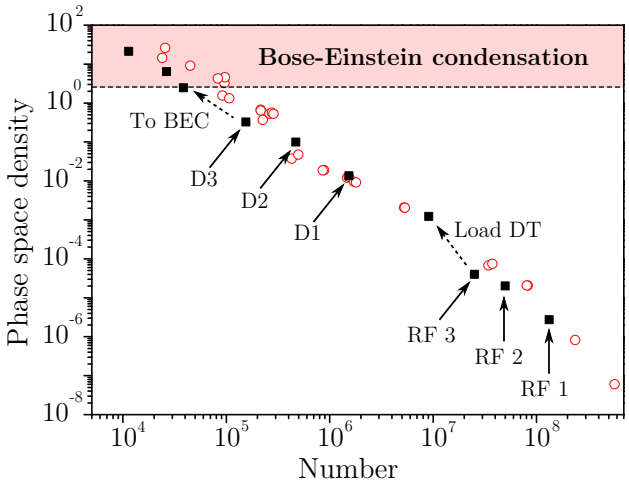

Figure 6.4: The evaporation trajectory to BEC in ^{85}Rb. Red circles: The original trajectory taken in the first period of forming a ^{85}Rb BEC. Black squares: The current trajectory, which shows a reduced atom number in our BEC, which optimisation has not been able to correct for (see section 6.4.4).

to flip into a different degenerate magnetic sub-level if it spends a suffiently long time in that region. In other words, we essentially need our atom to have reached close to its turning point in the trap, such that almost all its kinetic energy has been converted into potential energy. The total energy, E_{tot}, of one of these atoms in the trap is now expressed by (3.1). At this moment we want the atom to have suffient energy to be able to transfer into the adjacent magnetic sub-level, which can be expressed as

$$hf = \Delta m_F g_F \mu_{\text{B}} B, \tag{6.10}$$

where $\Delta m_F = 1$. Rearranging (3.1) in terms of E_{tot} results in

$$B = \frac{E_{\text{tot}}}{m_F g_F \mu_{\text{B}}}. \tag{6.11}$$

Remembering that $\Delta m_F = 1$, substituting (6.11) into (6.10) gives the energy at which atoms are removed from the trap in terms of the RF-energy imparted to them,

$$E_{\text{tot}} = |m_F|\, hf. \tag{6.12}$$

Placing typical values into (6.12) ($m_F = -2$ and $f = 25$ MHz) results in $E_{\text{tot}} = 2.4$ mK, which means that if our cloud is at 300 μK, we are removing atoms at $8k_{\text{B}}T$. The energy surface at which we are removing atoms is

described by the evaporation parameter η, where the energy is given by $\eta k_{\mathrm{B}} T$. Therefore evaporation in our quadrupole trap occurs at $\eta \sim 8$.

We undertake three RF ramps, aiming to halve the temperature of our cloud at each stage. At each of these stages we aim to maximise the efficiency of evaporation, by removing as few atoms as we are able while reaching as high a phase space density as possible. The parameters that we can tune are the initial, f_i, and final, f_f, value of frequency and the time to spend ramping between these values. The first ramp that we undertake is $f_i = 25$ MHz to $f_f = 7$ MHz in 20 s, which takes us to the point *RF 1* in figure 6.4. *RF 2* follows with a ramp of $f_i = 7$ MHz to $f_f = 4$ MHz in 5 s and, finally, *RF 3* completes the process with a ramp of $f_i = 4$ MHz to $f_f = 2.4$ MHz in 1 s. The final atom number and temperature at the end of the RF evaporation is $N \sim 2.5 \times 10^7$ and $T \sim 40$ μK. Majorana losses become too significant beyond this temperature, therefore, we need to transfer our atoms into a trap that does not contain a magnetic field zero—the crossed dipole trap.

6.4.2 The importance of the Feshbach resonance

The origin of a Feshbach resonance is described in detail elsewhere [259], therefore, we will not cover this again here. Instead, we must focus on the important role that the ^{85}Rb 155 G Feshbach resonance plays in achieving a BEC. The presence of a Feshbach resonance in an atomic species allows the tuning of its scattering length, over many orders of magnitude, by varying the magnetic field across a cloud. The functional form of the resonance is [259]

$$a(B) = a_{\mathrm{bg}} \left(1 - \frac{\Delta}{B - B_0}\right), \tag{6.13}$$

where a_{bg} is the scattering length far from the resonance, while Δ and B_0 are the width and position of the resonance respectively. The values of the parameters for the Feshbach resonance that we use to condense and form solitary waves are [115] $a_{\mathrm{bg}} = -443(3)\ a_0$, $B_0 = 155.041(18)$ G and $\Delta = 10.71(2)$ G. Using these parameters we can plot the scattering length against applied magnetic field around this resonance, resulting in figure 6.5.

By placing ourselves to the right of the Feshbach resonance ($B > 155$ G), we are in a region where the scattering length of our atoms can be varied

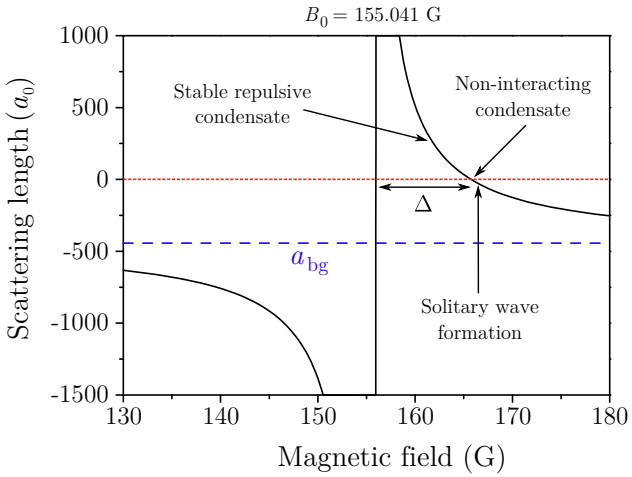

Figure 6.5: The ^{85}Rb 155 G Feshbach resonance. This broad Feshbach resonance ($\Delta = 10.71$ G) has been the workhorse for forming a ^{85}Rb BEC and solitary waves for more than ten years. For $B > 155.041$ G we are in the region where we can form stable repulsive condensates, non-interacting condensates and form solitary waves.

continuously over many orders of magnitude, from strongly repulsive to very-weakly-interacting to strongly attractive. It is this continuous variation, with a zero crossing, that allows us to have precise control over the interatomic interactions of our atoms, allowing the formation of stable condensates in the repulsive region or solitary waves in the weakly attractive region. The precision of the scattering length is dependent on the stability of our magnetic field and the gradient at the zero crossing. Differentiating (6.13) we obtain,

$$\frac{da}{dB} = a_{\rm bg}\frac{\Delta}{(B - B_0)^2}. \tag{6.14}$$

By definition, around $a = 0$ the magnetic field is $B \approx B_0 + \Delta$, resulting in,

$$\frac{da}{dB} \approx \frac{a_{\rm bg}}{\Delta}. \tag{6.15}$$

Putting the values of $a_{\rm bg}$ and Δ into (6.15) we obtain $da/dB \approx -40\ a_0$/G. The other isotope where solitary waves have been created is ^{7}Li and its very broad Feshbach resonance, used to create solitary waves, has a gradient that significantly increases stability in the scattering length around the field zero ($da/dB \approx 0.13\ a_0$/G) [295]. While this increased stability may be beneficial in creating solitary waves, below we will demonstrate that 40 a_0/G is perfectly adequate to allow the formation of stable solitary waves.

6.4.3 Crossed dipole trap

The experimental routine from the point of loading the dipole trap to the creation of a ^{85}Rb BEC is given in table 6.2. We give the gradient of the static quadrupole trap, the bias field and the power of the crossed dipole trap beam. These are the key parameters that govern if we will form a BEC.

Action	Time	Quad (G cm^{-1})	Bias (G)	Dipole (W)
Quad ramp	0.5 s	180 $\rightarrow$ 21.5	0	10
Hold	0.1 s	21.5	0	10
Dipole ramp 1	5 s	21.5	0	10 $\rightarrow$ 2.7
Bias ramp	50 ms	21.5	0 $\rightarrow$ 175	2.7
Dipole ramp 2	1 s	21.5	175	2.7 $\rightarrow$ 1.7
Dipole ramp 3	3 s	21.5	175	1.7 $\rightarrow$ 0.7
Bias ramp	10 ms	21.5	175 $\rightarrow$ 161	0.7
Quad ramp	0.1 s	21.5 $\rightarrow$ 26.5	161	0.7
Dipole ramp 4	6 s	26.5	161	0.7 $\rightarrow$ 0.3
Hold and reach BEC	2 s	26.5	161	0.3

Table 6.2: The experimental sequence used to reach degeneracy in ^{85}Rb. The time for each evaporation stage and the values of the static quadrupole trap gradient (Quad), bias field (Bias) and crossed dipole trap power (Dipole) throughout the evaporation to BEC are given.

In the process of transferring the cloud from the magnetic quadrupole trap into the crossed optical dipole trap we lose around 75% of our atoms, but gain a factor of 25 in phase space density, due to rapid evaporation and a tighter trap. This corresponds to an evaporation efficiency of 2, as quantified in (6.16). Following the loading of the dipole trap, the gradient of the quadrupole trap is ramped from 180 G cm^{-1} to $\sim$ 21.5 G cm^{-1}, just below levitation against gravity, in 0.5 s. We hold the atoms in the new trap, without any further purturbations, for 0.1 s, to allow them to equilibrate, before begining the first ramp of the dipole trap.

We make our initial ramp of the dipole trap power from 10 W to 2.7 W, reducing the depth of the trap by around a factor of four. This reduces the atom number by approximately a factor of 10, however, this increases the phase space density by approximately the same factor, due to the decrease in temperature. At the end of the first dipole ramp we choose to ramp the bias field from 0 G to 175 G, on the other side of the Feshbach resonance. This serves two purposes; optimising the ratio of elastic to inelastic collision rates (see section 6.4.3) and changing from the hybrid to the levitated trap config-

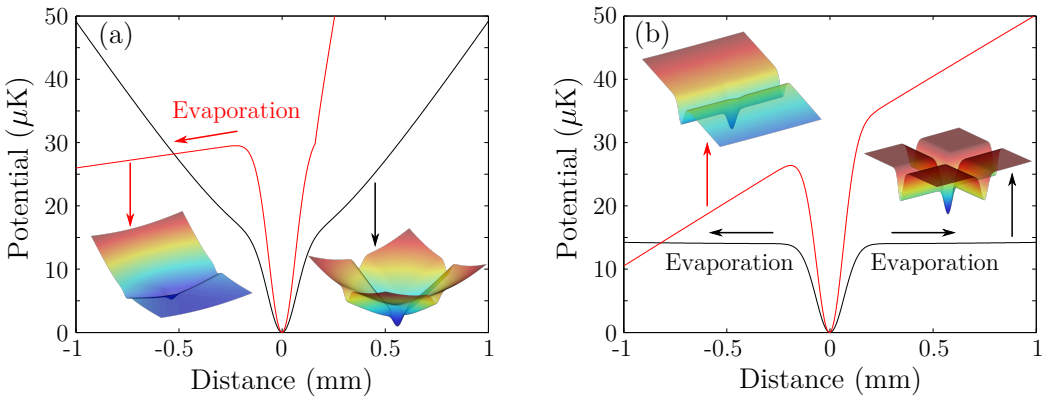

Figure 6.6: The hybrid and levitated trap configurations at the end of dipole ramp 1 (see table 6.2). Surface plots give the two-dimensional potential along the vertical and horizontal directions. (a) The hybrid configuration, where the quadrupole trap is on at 21.5 G cm^{-1}, no bias field is present and the dipole trap power is 2.7 W. Evaporation occurs along the vertical direction (red line), due to gravity, as the quadrupole trap keeps atoms confined in the horizontal direction (black line). (b) The levitated configuration, the same as (a) except with an applied bias field of 175 G, which moves the quadrupole trap zero far away for the crossed dipole trap centre. There is now negligible confinement in the horizontal direction, leading to evaporation along the beams, instead of the vertical direction.

uration (see figure 6.6) [72, 79]. The dipole trap lies ~ 160 μm below the zero of the quadrupole trap, which results in the horizontal (black line) and vertical (red line) potentials shown in figure 6.6 (a), with the insets showing the the 2D potential surface along the horizontal and vertical directions. Evaporation occurs along one side of the vertical direction, with atoms spilling out of the trap, due to the quadrupole field gradient not quite cancelling gravity. On the other side a very steep gradient can be seen, due to the quadrupole gradient summing with gravity resulting in a force approximately twice that of gravity. Along the horizontal direction the quadrupole trap keeps any high energy atoms in the cloud from escaping along that direction.

The application of a moderate bias field (~ 175 G) significantly changes the picture (see figure 6.6 (b)). The effect of this is to shift the magnetic field zero far away, resulting in negligible magnetic trapping along the horizontal direction[4] and a magnetic potential in the vertical direction that partially cancels the gravitational field. Evaporation now occurs along the horizontal direction, due to the lack of any notable confining magnetic potential.

[4]This trapping is only negligible when our cloud is relatively hot. We will find in section 6.7.1 that this weak trapping ($\omega_x \sim 2\pi \times 1.17$ Hz) is essential to observing the propagation of a solitary wave along an optical waveguide.

Investigating the evaporation parameter

Earlier we introduced the evaporation parameter, η, which quantifies the energy of the atoms that are evaporated from a particular trap. This can be thought of as the energy at which the Maxwell-Boltzman distribution is truncated. The energy at which the distribution is truncated varies depending on the geometry of the trap in which evaporation is occurring. When we were investigating the condensation of ^{87}Rb we quantified the evaporation parameter for three different types of trap[5]; the hybrid and levitated, which we have met already, and the pure crossed dipole trap, for which no magnetic trapping is present. Figure 6.7 shows the result of this analysis.

The method of determining the evaporation parameter was to transfer a cloud of atoms into the crossed dipole trap, at a variety of different beam powers. In each case the cloud was allowed to rethermalise with this new trap and its temperature was measured. The temperature data was scaled by a factor of η to fit to the trap depth data obtained using our dipole trap simulator and the gradient of the data was not altered. For the hybrid trap, evaporation occurs in the vertical direction, with $\eta = 12.6 \pm 0.5$. Contrasting this, in the levitated trap evaporation now occurs preferably along the beams in the horizontal direction, with $\eta = 9.8 \pm 0.5$. Finally, very interesting evaporative behaviour occurs in the pure trap, where the type of evaporation changes from the horizontal direction, with the evaporation parameter transitioning between $\eta = 11.0 \pm 0.5$ at low powers to $\eta = 8.7 \pm 0.5$ at higher powers. The transition between these two values occurs in the region bounded by the two thick lines in figure 6.7. The reason for this transition in the pure trap is because initially gravity has very little effect on reducing the trap depth in the vertical direction at high powers, however, as the power of the beam is reduced, the trap depth also reduces and gravity has a greater effect, causing the trap to disappear completely below 1 W.

The value of the evaporation parameter is determined by the heating rate in the trap. In the ideal scenario, where there was no heating of the cloud in the trap, the only way to maintain equilibrium would be for no evaporation to also occur. In other words, in a system with no mechanism for heating $\eta \to \infty$. As the heating rate increases, the value of η must decrease, balancing

[5]Note that this is the only section of this chapter in which we investigate ^{87}Rb. However, the same principle should also apply to ^{85}Rb.

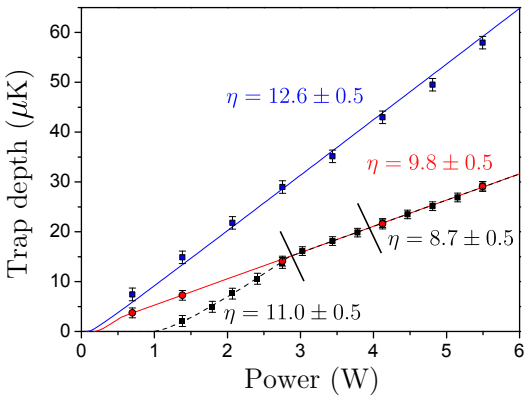

Figure 6.7: The effect of trap geometry on the evaporation parameter. A ^{87}Rb cloud was transferred into the crossed dipole trap and allowed to rethermalise with the trap at a variety of different powers. The data points are experimentally obtained and are scaled by a variable η to the trap depth calculated using the dipole simulator (see section 4.6.2). The evaporation parameter for each type of evaporation is given. In the hybrid trap (blue line/squares), evaporation always occurs along the vertical direction, as the application of a magnetic field gradient confines atoms in the horizontal direction. In the levitated trap (red line/circles) evaporation always occurs along the horizontal direction, as when gravity has been compensated for the trap will always be more shallow horizontally. Interesting behaviour can be seen in the pure trap (black dashed line/squares); initially evaporation occurs along the horizontal direction with it switching rapidly to the vertical direction as the tilting of the trap, due to gravity, has a greater effect on the shallower trap. Points in the intermediate regime of the pure trap (between the two thick lines) transition from one value of η to the other.

this heating rate with an increased cooling rate. Therefore, a trap with a lower value of η must be causing a greater heating rate of the cloud, in order to maintain equilibrium. From figure 6.7, greater heating rates appear to occur in the horizontal direction. The reason for this is most likely because it is more difficult for atoms to actually escape this way. There is still weak trapping over a long distance, which can slow the escaping atoms and turn them around to smash back into the cloud, encouraging mechanisms for heating. Along the vertical direction any atoms that escape the trap are lost forever, as the background potential, due to gravity, accelerates the atoms away from the trap, providing more efficient evaporation.

Balancing inelastic losses and rethermalisation

Throughout the rest of the evaporation to BEC we are very careful to be as efficient as possible. We quantify the efficiency as

$$\text{Efficiency} = -\log_{10}\left(\frac{\text{PSD}_\text{f}/\text{PSD}_\text{i}}{N_\text{f}/N_\text{i}}\right), \tag{6.16}$$

where $\text{PSD}_{\text{f,i}}$ are the final and initial phase space densities either side of one evaporation stage and $N_{\text{f,i}}$ are the final and initial atom numbers during the same stage. This is what we plot in figure 6.8 (a).

As our cloud cools, the density increases, resulting in increased two- and three-body loss rates. As discussed earlier (see section 6.2.2), the magnitude of the loss rates in ^{85}Rb make it a very difficult species to condense. Our method of gaining an upper hand is to exploit the 155 G Feshbach resonance to tune the ratio of elastic to inelastic collisions. Building on the previous work by another group [290], we studied the efficiency of evaporation as a function of magnetic field. As one scans the field from 160-200 G it is known [290] that there is a minimum in the elastic scattering rate at 167 G, while the minimum in the inelastic collision rate is offset at 175 G. This offset is advantagous to us, because if we tune our magnetic field to 175 G, we place ourselves in a region where we can undertake relatively efficient evaporation. The efficiency of evaporation as a function of magnetic field can be seen in figure 6.8 (a), which was undertaken as work contributing to [72] and [79]. Counterintuitively, the evaporation is least efficient very close to the minimum in the three-body loss rate (see figure 6.8 (d)). This is due to the minimum in the elastic scattering rate, as the effective size of our atoms becomes very small (see figure 6.8 (c)). Rethermalisation is critical if we want to evaporatively cool a sample of atoms, and the rate at which rethermalisation occurs close to $a = 0$ is very slow ($\Gamma_\text{el} \sim 10^{-3}$ s^{-1} [290]), therefore as we attempt to evaporate our sample, we instead just chop away hot atoms without the cloud having the oppotunity to cool (see figure 6.8 (b)). Just beyond $a \sim 0$ at $B > 175$ G we find significantly more efficient evaporation due to the increase in the elastic scattering rate ($\Gamma_\text{el} \sim 10^{-1}$ s^{-1} [290]) while the inelastic collision rate still remains close to its minimum.

In order to extract a three-body loss coefficient at a particular magnetic field we placed a cloud of atoms at $T \sim 1$ μK into a deep trap (more than 20

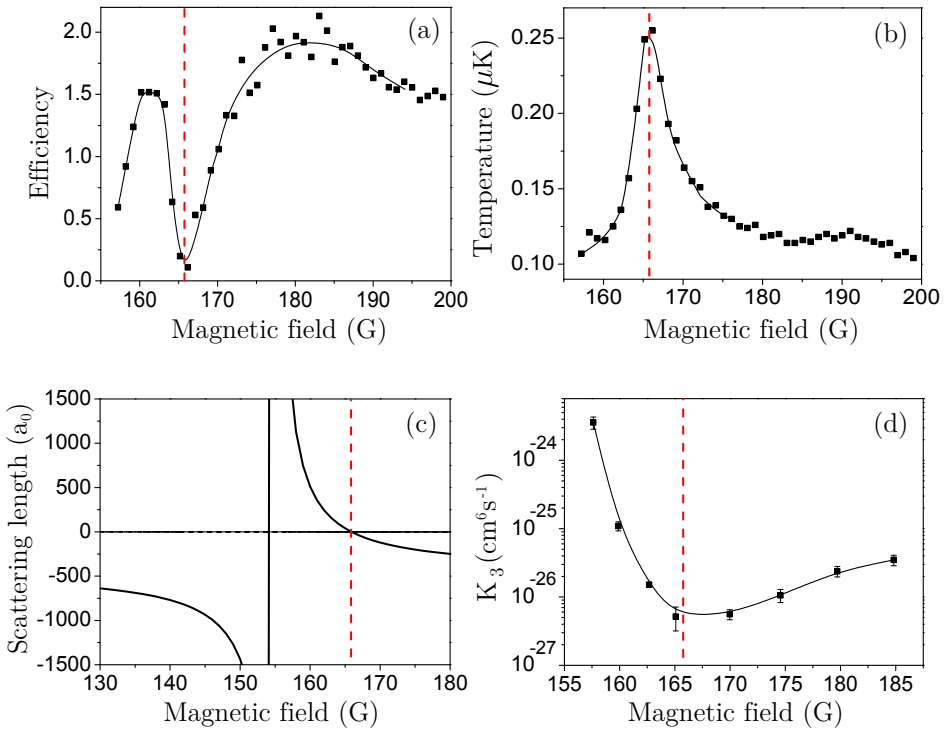

Figure 6.8: The effect of the Feshbach resonance on evaporation efficiency. The red dashed line gives the position of $a = 0$. (a) Efficiency, defined in (6.16), during an evaporation ramp to BEC. Evaporating at $B > 175$ G increases efficiency, before the field must be switched to 161 G to form a stable repulsive BEC. (b) The inefficiency in (a) is due to the cloud's inability to rethermalise and cool. The peak in temperature coincides with $a \sim 0$. (c) The scattering length of ^{85}Rb around the 155 G Feshbach resonance. (d) The variation in the three-body loss coefficient for ^{85}Rb near the 155 G Feshbach resonance. The minimum in K_3 occurs very close to $a = 0$ but is suffiently far away to be able to exploit during evaporation to increase efficiency. From [72].

times the cloud temperature). The atom loss and heating of the cloud was observed and a pair of coupled differential equations were fitted to the atom number and temperature data. These equations are [296]

$$\frac{dN}{dt} = -\alpha N - \gamma \frac{N^3}{T^3} \quad \text{and} \quad \frac{dT}{dt} = \gamma \frac{N^2}{T^3} \frac{(T + T_h)}{3}, \tag{6.17}$$

where α is the background loss rate, $\gamma = K_3(m\overline{\omega}^2/2\pi k_\mathrm{B})^3/\sqrt{27}$, with $\overline{\omega}$ being the geometric mean of the trap frequencies, and T_h is the heating associated with the loss of one atom via three-body recombination. Both two- and three-body loss occurs in the cloud, however, they can be very difficult to distinguish through fitting [290]. Therefore, rather than add even more parameters to fit, we determined that as the density in the trap at

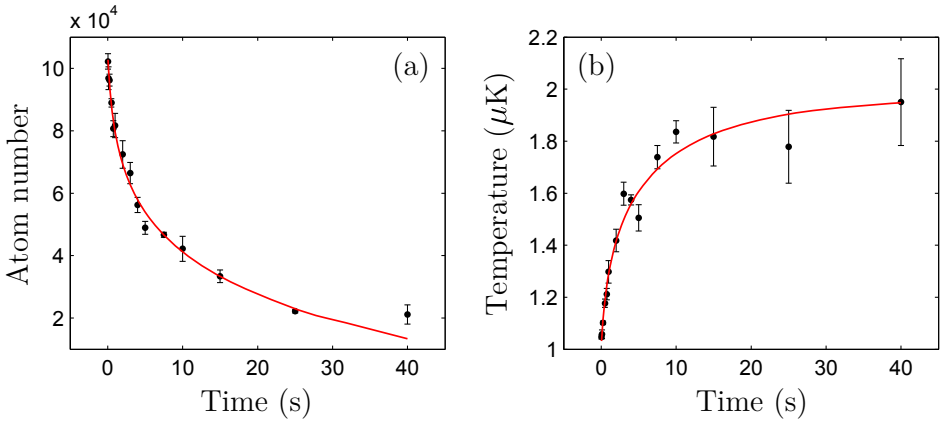

Figure 6.9: Extracting the three-body loss coefficient. A cloud at initially $T = 1.0(1)$ μK and $N_0 = 1.1(1) \times 10^5$ is placed in a trap of depth ~ 25 μK and allowed to heat up. The magnetic field across the cloud is 159.89 G (535 a_0). Through this heating process K_3 is extracted via (6.17). (a) The atom number remaining in the trap as a function of time held in the trap. (b) The temperature of the cloud in the trap as a function of time held in the trap. For this set of data $K_3 = 1.0(1) \times 10^{-25}$ cm^6 s^{-1}.

1 μK is relatively high, the three-body loss rate dominates. As a result we neglected the two-body mechanism in the coupled fitting equations. Figure 6.9 gives example fits to number (a) and temperature (b) at 159.89 G (535 a_0) where $K_3 = 1.0(1) \times 10^{-25}$ cm^6 s^{-1}. For more information see [72].

6.4.4 Reaching Bose–Einstein condensation

Two more ramps of the dipole trap power are undertaken at $B \sim 175$ G, further evaporating the cloud, resulting in a cloud with $N \sim 1.5 \times 10^5$ and a phase space density of ~ 0.3. These are the last steps before we take the final route to BEC.

Following the three ramps of the dipole trap power that we have undertaken, we are now very close to producing a ^{85}Rb condensate. However, we must first tune our interactions to be repulsive, rather than attractive, which is the current configuration. If we did not do this we would be unable to form a stable BEC. The change of sign of the scattering length is undertaken in a 10 ms ramp of the bias field from $\sim$ 175 G to $\sim$ 161 G. This places us in a region where evaporation is slightly less efficient (from figure 6.8, ~ 1.5 instead of ~ 1.8) and the efficiency is significantly more sensitive to the exact magnetic field that we apply across the cloud (see figure 6.8 (a)), however, we are now able to form a stable BEC.

One final step is undertaken before the last ramp of the dipole trap power—an increase in the quadrupole trap gradient to compensate for the 15% decrease in the magnetic moment of a ^{85}Rb atom due to the application of a moderate bias field. If we did not increase the the quadrupole trap gradient, as we reduce the power of the dipole trap beams, we would very quickly lose our trapping in the vertical direction, as we are well below levitating against gravity (see figure 6.6 (b)). By increasing the gradient, we levitate the trap in the vertical direction, leading to an approximately flat background in the potential and a more stable configuration in which to form a BEC.

We are now in the position to begin the final evaporation stages towards BEC. The final ramp of the dipole trap power is from 0.7 W to 0.3 W in 6 s, which cools our cloud significantly, however we have found that in order to efficiently form a BEC, it is then necessary to hold the trap—changing no parameters—for a further 2 s, in which time a BEC with $N \sim 5000$ atoms is found to form. The resulting transition from thermal cloud to condensate can be seen in figure 6.10.

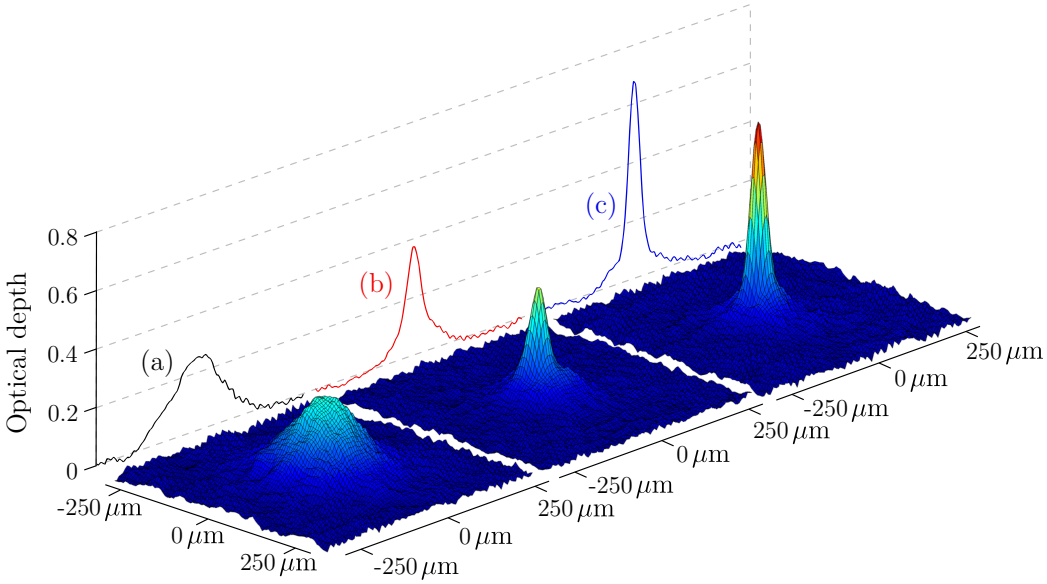

Figure 6.10: The transition to Bose–Einstein condensation. The black, red and blue lines give the one-dimensional cuts through the centre of the thermal, bimodal and pure clouds in the relevant directions. (a) The thermal cloud just before the BEC transition is reached ($N \sim 50000$, PSD ~ 2). (b) A bimodal cloud just above the BEC transition ($N \sim 20000$, PSD > 3.61). (c) A nearly pure BEC with $N \sim 7000$ and $N_{\mathrm{BEC}} \sim 5000$.

6.5 Demonstrating tunable interactions

Now that we are in possession of a BEC whose interactions we can tune, there are a number of experiments that can be undertaken to demonstrate such behaviour. The most straightforward of these is observing the time of flight expansion of a condensate, in comparison with a thermal cloud, at a variety of different values of scattering length. Breathing of the condensate can also be observed for sudden changes in the scattering length, making the cloud no longer in equilibrium with the dipole trap. Finally, collapse of the condensate can be observed, as the scattering length is tuned to negative values, leading to the formation of solitary waves.

6.5.1 Expansion and breathing mode oscillations

When we are in possession of a thermal cloud of dilute ^{85}Rb, the interaction energy is relatively low, due to the poor overlap of the individual particle wavefunctions. However, once a condensate is formed, there is significant overlap of the individual particle wavefunctions, increasing the possibility for large interaction energies. While the BEC is still trapped, large repulsive interactions can lead to the Thomas-Fermi regime, where the cloud takes the inverted shape of the trap potential (see section 2.2.4). When releasing from the trap, these strong repulsive interactions lead to a rapid expansion of the condensate, particularly in directions where the trapping potential had most strongly confined the cloud. Conversely, if $a \sim 0$ the expansion of the condensate is significantly reduced and we observe a much smaller cloud at the same expansion time. For a thermal cloud we observe negligible variation in the cloud size as a function of scattering length. Figure 6.11 (a) gives an example of this from [72], where the cloud was released and allowed to expand for 55 ms at a variety of magnetic fields. The expansion of the BEC reaches its lowest point when $a = 0$, indicated by the red dashed line. The increase in cloud size beyond $a = 0$ is due to collapse being initiated (see section 6.5.2).

By making a sudden change in the scattering length of the atoms in the BEC, it is possible to induce breathing mode oscillations, due to the sudden change to a non-equilibrium parameter regime. The width of the cloud oscillates around what would be its equilibrium width at the new scattering length.

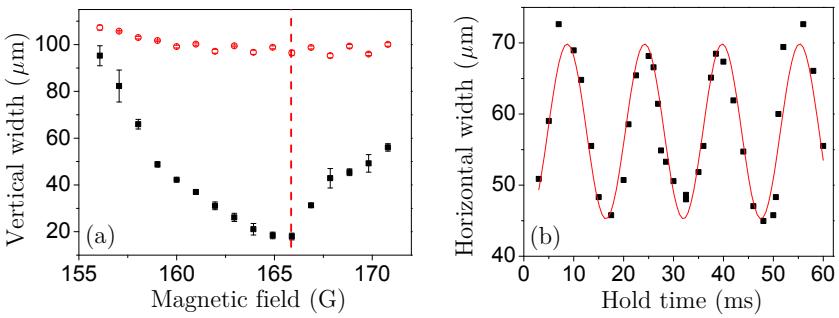

Figure 6.11: Demonstrating the tunable nature of a ^{85}Rb BEC. (a) The root mean square radius of a BEC (black squares) and a thermal cloud (red circles) 55 ms after release from the crossed dipole trap at various magnetic fields. The red dashed line indicates the position of $a = 0$. (b) Oscillations in the root mean square radius of the cloud when the scattering length is suddenly changed from $\sim 315\ a_0$ to $\sim 50\ a_0$ and held at this new scattering length. From [72].

Contrary to the breathing of a non-interacting condensate, which would oscillate at twice the trap frequency, an interacting condensate breathes at $\sqrt{5}\,\omega$ [83]. Figure 6.11 (b) gives an example of such a breathing mode oscillation from [72], where the scattering length of the atoms in the condensate was instantaneously switched from $\sim 315\ a_0$ to $\sim 50\ a_0$. It is stated in [72] that the trap frequency obtained from the data in figure 6.11 (b) is in good agreement with the expected value.

6.5.2 Collapse of a condensate

As discussed in detail earlier (see section 2.2.7), a condensate is only stable, in the homogenous regime, with attractive interactions, in a strictly one-dimensional system. This is not experimentally viable, as we are only able to create, at best, quasi-1D trapping geometries. Therefore, we introduce a trapping potential, which enables quasi-stable attractive condensates to be formed. The atom number at which collapse occurs is dependent on the scattering length of the atoms in the condensate and the trapping geometry, as seen in (2.25). In this experiment we observed the collapse of a condensate in our approximately spherical crossed dipole trap. The result was qualitatively similar to that previously observed [26, 116]. More details of this can be found in [72].

6.6 The waveguide

In this section we will discuss the addition of a single beam to our experimental apparatus, into which we transfer our BEC and subsequently form a solitary wave. For reference during this section, see the diagram of the experimental apparatus in figure 3.1.

6.6.1 The purpose and configuration of the waveguide

Our aim has been to study the formation and dynamics of solitary waves in a quasi-1D trap geometry, in order to closely mimic the ideal one-dimensional scenario often presented in theoretical simulations—the *true* soliton. With this aim in mind we introduced an Innolight Mephisto 1064 nm 2 W laser [297], which created the waveguide beam. The beam was directed through the back of our dove prism, at an angle of $\sim 45°$ relative to either of the crossed dipole beams. This beam was focussed to a waist of 117 μm and aligned with the crossed dipole trap (see the next section).

It is essential to perturb the the BEC as little as possible in the transfer from the crossed dipole trap to the waveguide, therefore we matched the radial trap frequency of the waveguide with the mean frequency of the crossed dipole trap[6] ($\omega_r \sim 2\pi \times 30$ Hz). This trap frequency corresponds to a waveguide power of 170 mW and the resulting axial trapping frequency is approximately $2\pi \times 0.1$ Hz. This is not very useful for studying the dynamics of solitary waves, as a full trap oscillation would take 10 s, however, the continued presence of the quadrupole trap with the addition of the moderate bias field leaves a $\omega_x = 2\pi \times 1.16(1)$ Hz axial trapping frequency. Section 6.7 gives further detail of the actual experimental routine undertaken to form solitary waves.

6.6.2 Alignment of the waveguide

In the process of investigating the effect of applying a variety of different bias fields, up to the 175 G that we typically apply during the *levitated* portion of the experimental routine, we discovered a novel method of quickly aligning

[6] BEC was formed in the crossed dipole trap with $\omega_{x,y} \sim 26$ Hz and $\omega_z \sim 36$ Hz.

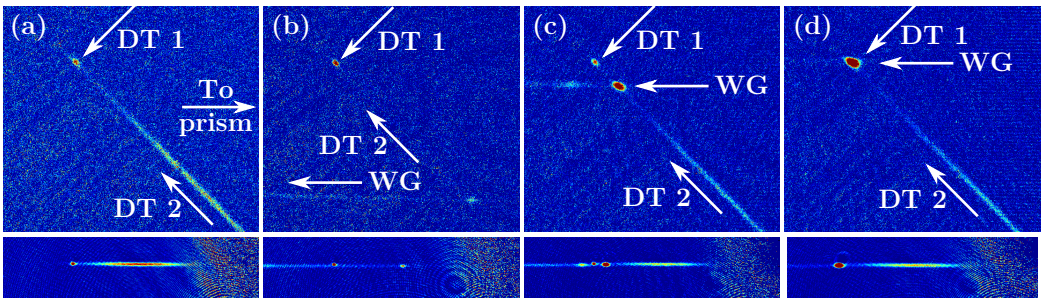

Figure 6.12: Aligning the waveguide with the crossed-dipole trap. DT 1: The incoming dipole trap beam. DT 2: The recycled dipole trap beam. WG: The waveguide. Top frames: Vertical view. Bottom frames: Horizontal view. (a) The application of a bias field of $B \sim 100$ G reduces the confinement of atoms horizontally in the trap, causing them to spread along one of the beams of the crossed dipole trap. (b) The waveguide is turned on, resulting in a new trap being formed approximately 2 mm away from the original dipole trap. (c) The waveguide is positioned closer to the original crossed dipole trap resulting in three traps being formed; one at the intersection of DT 1 and DT 2, another at the intersection of DT 1 and WG and the most prominent at the intersection of DT 2 and WG. (d) A single trap is formed once all of the beams overlap.

a new beam (the waveguide) with the initial crossed dipole trap.

Increasing the bias field from 0 G to a nonzero value moves the magnetic field zero further away from the centre of the crossed dipole trap. As discussed earlier (see section 6.4.3), the effect of this is to reduce the trapping in the horizontal direction. At 175 G this trapping became negligible, however, at intermediate bias fields[7] we found that a scenario could be created where cold atoms remained at the centre of the crossed dipole trap, while a significant number of hotter atoms were found to spread out horizontally into one of the beams (see figure 6.12 (a)). The result of this action was to reduce the problem from a scenario where we are attempting to align a beam with an object no greater than 100 μm in size, in both directions, to a scenario where the object we are aligning with has now increased in size by more than a factor of 20 in one direction. Essentially, this means that the alignment only needed to be rough in the horizontal direction and we could focus our efforts on a single parameter alignment along the vertical direction.

The remaining frames (b-d) of figure 6.12, show a new trap being formed, when the waveguide is turned on (b) at the intersection of DT 2 and WG, and the gradual alignment of the waveguide with the original crossed dipole trap (c-d).

[7] In this scenario we are no longer strictly in the hybrid or levitated regime.

6.6.3 Characterisation of the waveguide

Once we had demonstrated that the waveguide was aligned with the centre of the crossed dipole trap, we decided to load a cloud that was hotter than we would typically use. This action would allow us to profile the waveguide as this 'hot' cloud would spread out along the beam, indicating any unexpected behaviour. Any atom loss through spilling, due to gravity, should also be clearly indicated via this method. In figure 6.13 a 100 nK cloud was loaded into the trap after three dipole trap evaporation ramps were undertaken. Over 100 ms it expands from a root mean square radius of $\sim$ 25 μm to $\sim$ 400 μm. The centre of mass of the cloud can be seen to accelerate away from its initial position. This is a clear indication of the cloud being offset from the trap centre. It was important to determine the source of this offset, therefore we next investigated centre of mass oscillations in the axial and radial directions of the waveguide.

In figure 6.14 we transferred a cold thermal cloud (close to the BEC transition) into the waveguide and allowed it to oscillate for a sufficient amount of time to determine the radial and axial trap frequencies. In (a) multiple, damped oscillations of this cloud can be seen over $\sim$ 4 s. By fitting a damped sinusoidal curve to the data, an axial trap frequency of 1.16(1) Hz

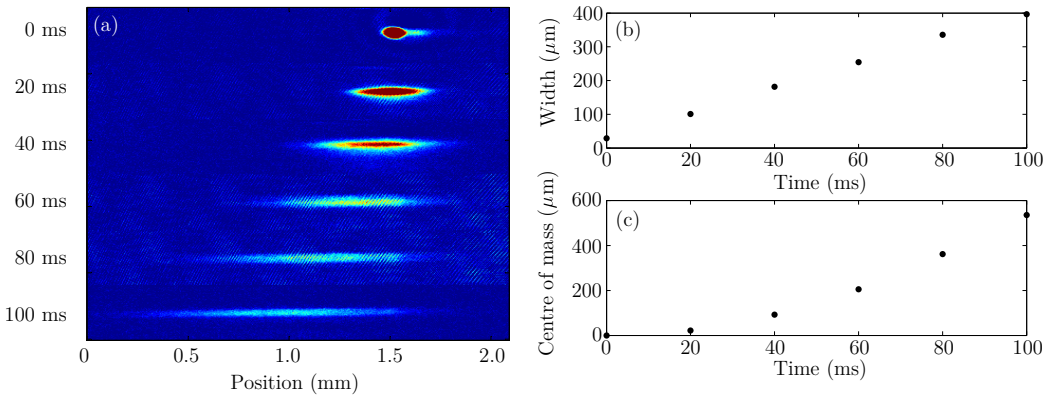

Figure 6.13: Loading a 100 nK cloud into the waveguide. Three evaporation ramps are undertaken in the crossed dipole trap, resulting in a cloud with $N \sim 1.5 \times 10^5$ at $T \sim 100$ nK. (a) This cloud is transferred into the waveguide and expands over 100 ms. (b) The root mean square radius of the cloud as a function of time after release from the crossed dipole trap. (c) The centre of mass of the cloud as a function of time after release from the crossed dipole trap. The centre of mass of the cloud can be seen to accelerate away from its original position as it is initially horizontally offset from the trap centre.

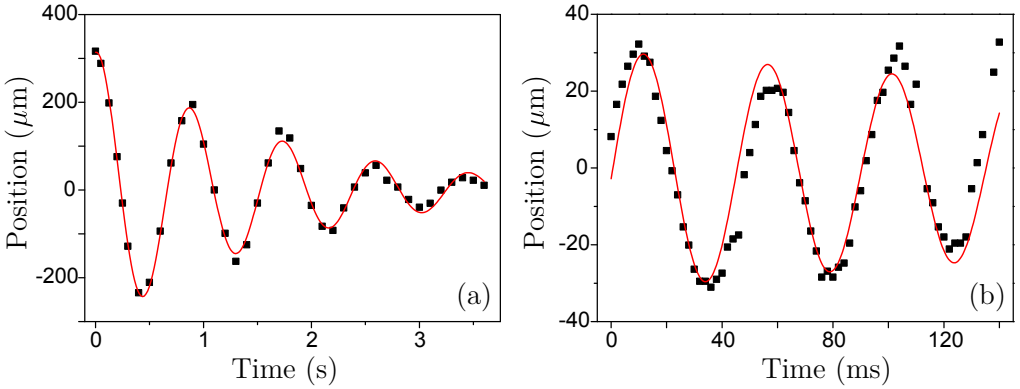

Figure 6.14: Determining the axial and radial trapping frequencies of the waveguide via centre of mass oscillations. (a) Axial trap oscillations were observed due to the offset of the magnetic trap potential centre from where a cold thermal cloud was released from the crossed dipole trap. An axial trap frequency of 1.16(1) Hz was measured and found to match the predicted trap frequency, within error. (b) The waveguide was slightly misaligned radially from the cross dipole trap in order to induce oscillations of the cold thermal cloud in the radial direction. Fitting to the resulting centre of mass oscillatons lead to a measurement of 22(1) Hz for the radial trapping frequency.

was extracted. We found good agreement with the predicted trap frequency of 1.17 Hz, using the dipole trap simulator discussed in section 4.6.2. As the axial trap frequency due solely to the waveguide was only $\sim$ 0.1 Hz, we found the main source of trapping along this direction came from the magnetic fields of the quadrupole trap and bias coils.

In figure 6.14 (b) we slightly misaligned the waveguide in the vertical direction from the crossed dipole trap. This action induced centre of mass oscillation in the radial direction of the waveguide. Through fitting of the sinusoidal oscillations observed in (b) we extracted a radial trap frequency of 22(1) Hz. There are two main factors that can affect the trap frequency in the vertical (radial) direction; the extent to which the trap is levitated against gravity (in other words, the quadrupole trap gradient) and the power of the waveguide beam. The axial and radial waveguide trap frequencies obtained by the above method were used in any later analysis undertaken in the experiment.

It is essential for any later experiments that involve solitary wave interactions with barriers that we have excellent control of the velocity of the solitary wave. The final characterisation experiment of the waveguide, shown in figure 6.15, demonstrates our ability to control the centre of mass motion of a cold cloud of atoms by applying an additional magnetic field in the axial direction of the waveguide. This provides full control over the position of the

magnetic trap centre, relative to the initial position of the cloud released from the crossed dipole trap. As the (vertically) off-axis magnetic trap provides harmonic confinement, shifting the position of the horizontal centre has a significant effect on the acceleration of the cloud. Figure 6.15 (a) shows how we are able to move the cloud in any direction that we wish or even keep it stationary, by simplying adjusting the 'shim' field of these additional magnetic coils.

As we have already determined an axial frequency of $\omega_x = 2\pi \times 1.16(1)$ Hz, we fixed this parameter and fitted a sinusoidal curve to each of the sets of data. A horizontal trap centre could therefore be determined for each of these curves and in figure 6.15 (b) we give the trap centre position as a function of the applied magnetic 'shim' field. As can be seen, by simply applying 2-8 G the trap centre can be shifted by ~ 2 mm, which would result in the cloud actually being able to explore ~ 4 mm of the waveguide potential. We extracted a trap centre position, as a function of the magnetic field, of $0.41(1)\ \mathrm{mm\,G^{-1}}$.

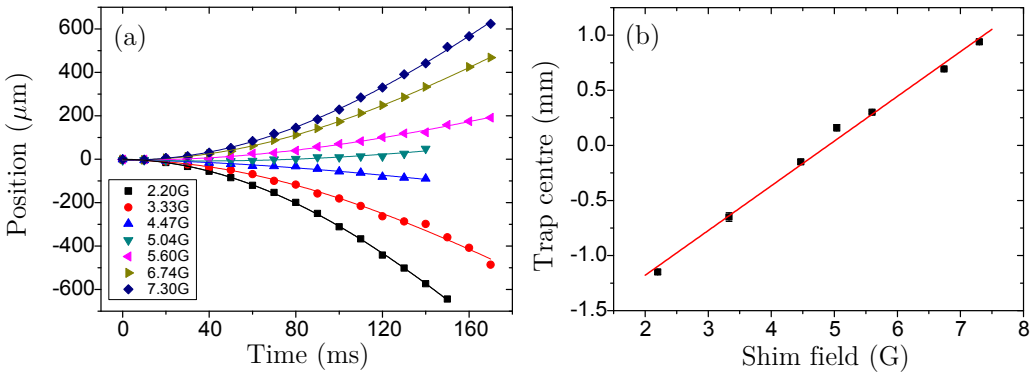

Figure 6.15: Varying the centre of mass velocity of the cloud. A variable shim field is applied along the axial direction of the waveguide, shifting the centre of the quadrupole trap in the horizontal direction. (a) The trajectories of a cold thermal cloud, close to the BEC transition, in the waveguide as a function of time after relase from the crossed dipole trap. The cloud can be moved in either direction and also be kept stationary. Gaps in the data are due to noise in the imaging being greater than the signal of the cloud. Sinusoidal fitting was undertaken, with a fixed frequency of 1.17 Hz to determine the position of the trap centre. (b) The resulting trap centre as a function of the applied shim field. The centre of the trap can be moved $0.41(1)\ \mathrm{mm\,G^{-1}}$.

6.7 The formation of solitary waves

Having demonstrated the transfer of a cloud of atoms from the crossed dipole trap into the waveguide, we have reached the point where it is our desire to form solitary waves. Our experimental sequence begins just after the final stage given in table 6.2. This route to solitary wave formation is provided in table 6.3.

Action	Time	Bias (G)	a (a_0)	DT (W)	WG (W)
Ramp to $a = 0$	50 ms	$161 \rightarrow 165.75$	$353 \rightarrow 0$	0.3	0
Hold	30 ms	165.75	0	0.3	0
WG on	Switch	165.75	0	0.3	0.17
Switch to new a	Switch	$165.75 \rightarrow 166.05$	$0 \rightarrow -12$	$0.3 \rightarrow 0$	0.17
Hold in WG	Vary	166.05	-12	0	0.17

Table 6.3: The experimental sequence used to create solitary waves in ^{85}Rb. A continuation of table 6.2. The length of each step is given, with 'switch' indicating an effectively instantaneous step and the final hold in the waveguide (WG) can vary in length depending on the experiment that is investigated. The magnetic field (Bias) and corresponding scattering length (a) are given, along with the crossed dipole trap (DT) and waveguide powers.

It is essential that we have a good grasp of the magnetic field applied to the BEC, as this controls the scattering length and, hence, the interparticle interaction strength, for which BEC formation is very sensitive to. We calibrate the magnetic fields in each experimental run via the method described in section 3.2.2. As can be seen in table 6.3, the scattering length of the BEC, before transfer into the waveguide, is $a = 0$. We quickly switch this to a new value (typically $a = -12a_0$ if we want to form a soliton) once the BEC is in the waveguide and the crossed dipole trap has been switched off. The effect of this final scattering length on the propagation of a BEC in the waveguide is shown in figure 6.16 (a). As the scattering length is reduced, the expansion rate of the BEC also reduces. When the scattering length reaches a sufficiently negative value to counteract dispersion of the cloud ($\lesssim -7\ a_0$), there is negligible expansion of the BEC and we have formed a solitary wave. In figure 6.16 (b) the root mean square radius of the thermal component of the cloud can be seen to be insensitive to the change in scattering length. This bimodal data was fitted using the algorithm and function stated in section 4.6.1.

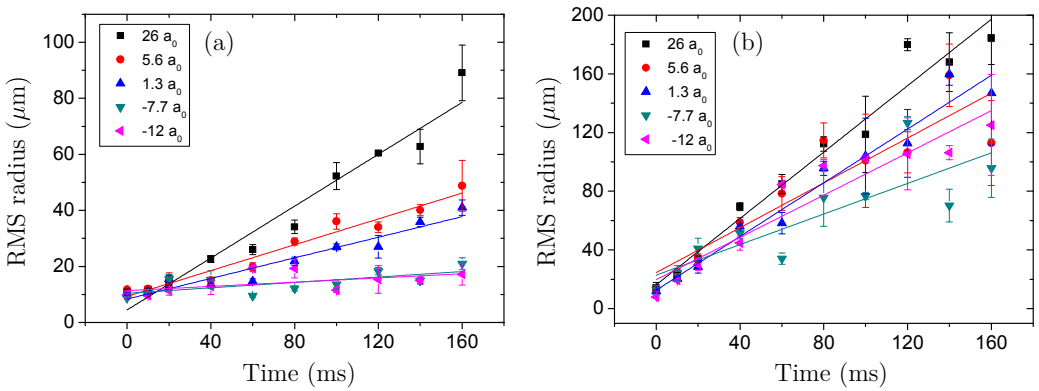

Figure 6.16: The expansion of a condensate in an optical waveguide as a function of scattering length. (a) The root mean square radius of the BEC component in the waveguide. A non-dispersing wavepacket (solitary wave) is formed for $a \lesssim -7\ a_0$. (b) The root mean square radius of the thermal component of the cloud. This cloud continues to disperse, regardless of the value of a.

At $a = -12\ a_0$ the rate of expansion of the solitary wave is $0.04(2)\ \mu\text{m}\,\text{ms}^{-1}$, in comparison with $0.46(4)\ \mu\text{m}\,\text{ms}^{-1}$ at $a = 26\ a_0$. While the expansion at $a = -12\ a_0$ is not zero, within one standard deviation, there are a couple of factors that could be the cause of this. The size of the bulk of the solitary wave takes up no more than five pixels on the camera image, therefore, even small amounts of noise could have a large effect on the measured cloud width. The solitary wave may also be finding its equilibrium size in the waveguide trapping geometry, causing this slight change in width.

6.7.1 Propagation of a solitary wave in a quasi-1D waveguide

In figure 6.17 we compare the propagation of a solitary wave at $a = -12\ a_0$ (a) with that of a repulsive BEC at $a = 26\ a_0$ (b). The initial optical depth is very high (> 2) due to the tight trapping of both the BEC and the thermal component in the crossed dipole trap. In (a), once released, the thermal component expands rapidly, reducing the total optical depth. This results in a clear bimodal distribution in the propagating cloud, with an expanding thermal component and a solitary wave component that maintains its width at $\sim 10\ \mu$m for the whole data set. In comparison, in (b), when a positive scattering length of $a = 26\ a_0$ is observed, both the thermal and BEC components can be seen to expand with time, consistently reducing the total optical depth. The bimodal distribution is more difficult to distinguish due to the expansion of both components.

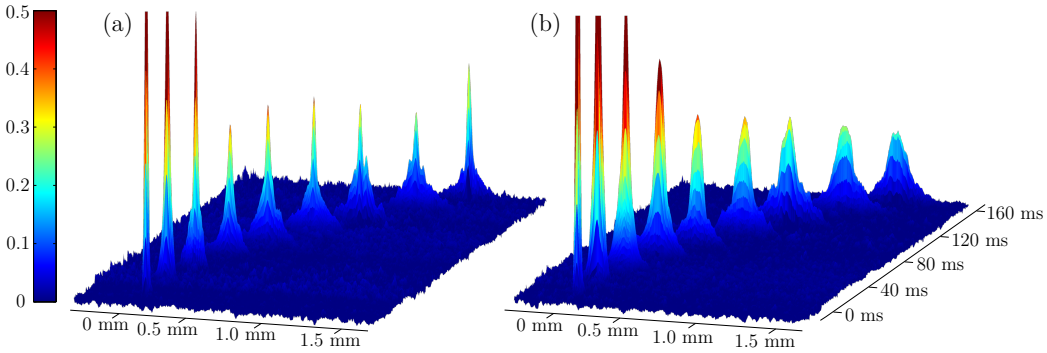

Figure 6.17: The propagation of a solitary wave and a repulsive BEC in an optical waveguide. The colour map corresponds to the optical depth of the cloud and the data is truncated at an optical depth of 0.5. (a) The propagation of a solitary wave at $a = -12\ a_0$ over 160 ms. After the release from the crossed dipole trap at 0 ms, the thermal component rapidly expands, reducing the total optical depth of the cloud. A clear bimodal distribution can be seen from $\sim$ 60 ms onwards with the solitary wave maintaining a width of $\sim$ 10 μm for the remainder of the time. (b) The propagation of a repulsive BEC at $a = 26\ a_0$. A bimodal distribution is more difficult to distinguish and the width of the cloud is seen to constantly increase.

Ideally it would have been desirable to compare the measured widths of the solitary wave observed here with the predicted values given in section 2.5.3. Unfortunately the predicted size is smaller than an individual pixel on our image, therefore, determining a profile is not possible. Instead, a diffraction limited imaging system, which we do not possess at present, may allow the experimental profile to be measured. The measured width of $\sim$ 10 μm is significantly overestimated when compared with the predicted $\sim$ 2 μm, which we believe is due to aberrations from our imaging lenses.

6.7.2 Interaction of a solitary wave with a wide repulsive barrier

Once solitary waves were being created regularly, their interaction with a wide repulsive (532 nm) barrier was studied in detail by ALM [72]. Clear particle-like behaviour was observed for the solitary wave, with either full reflection or full transmission, depending on the power of the barrier laser beam. The solitary wave presented minimal breathing during reflection from the potential, in comparison with a repulsive BEC, which is seen to breathe, increasing its width by more than a factor of two. This clearly demonstrates the advantage of using a solitary wave for cleanly probing reflection (quantum

or classical) of a cloud of atoms from a potential.

The behaviour of the solitary wave observed during this investigation was entirely classical in nature, as any form of quantum reflection would only be expected for significantly narrower barriers (see section 2.5.1).

6.8 Conclusion

In this chapter we have discussed the differences between cooling ^{85}Rb and ^{87}Rb and how we decided to undertake direct evaporation of ^{85}Rb, instead of sympathetic cooling. We concluded that it was possible to create large enough condensates of ^{85}Rb, via direct evaporation, to study and out of which to form solitary waves. We have demonstrated the tunable interactions observable around the ^{85}Rb 155 G Feshbach resonance. Finally, we presented a novel method of aligning a single beam waveguide into which we transferred our BEC, formed and propagated solitary waves.

Part IV

Towards solitary wave interactions with narrow potentials

Chapter 7

Towards solitary wave interactions with a narrow potential well

7.1 Introduction

Once solitary waves were regularly being formed, and they had been shown to interact classically with a wide potential barrier, it became clear that the next objective should be to observe manifestations of its quantum nature. There were three possible options; observe solitary wave interactions with the dielectric prism or introduce a narrow potential barrier or well formed from a blue or red detuned laser beam. Rather than attempting the difficult task of interacting the solitary wave with the prism, we decided to take a smaller step by investigating solitary wave interactions with a narrow potential well. A potential well offers the opportunity for observing the clearest quantum signal as any reflection from the well would have to be quantum in nature as the potential possesses no classical turning point. A repulsive barrier, however, can display both classical and quantum reflection and transmission (see sections 2.3.6 and 6.7.2), which makes the process of separating these effects difficult.

In this chapter we will present the preparation and characterisation of the laser beam that generates the potential well.

7.2 Possible outcomes of interactions with a potential well

The interaction between a solitary wave and an attractive potential can display rich physical behaviour. The three possible results of such an interaction are transmission, (quantum) reflection and (resonant) trapping. A schematic of this interaction can be seen in figure 7.1.

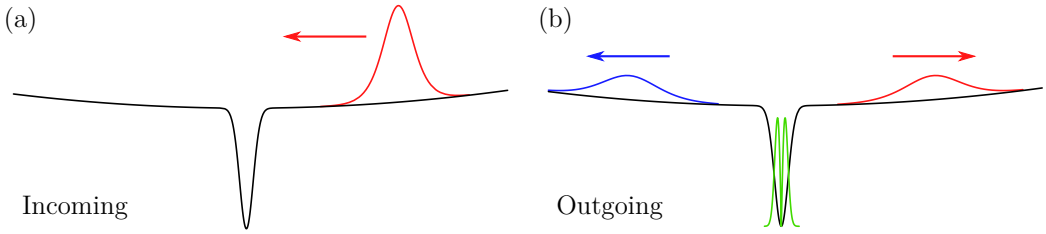

Figure 7.1: Schematic of the outcome of a solitary wave interacting with a narrow potential well. Black line: total potential observed by the atoms. (a) A solitary wave (red line) is initially offset from the centre of a weak harmonic trap and released. It accelerates towards a narrow potential well, resulting in a solitary wave–potential well interaction. (b) The result of the interaction between the solitary wave and well. Reflection (red line), transmission (blue line) and trapping (green line) can occur.

Interactions with a barrier would only result in transmission or reflection[1], which may seem simpler than the three outcomes from an interaction with a potential well, however, distinguishing quantum from classical behaviour remains the priority.

Partial, or total, quantum reflection of the solitary wave from the potential well is the result that we are aiming to observe. Achieving this requires a low momentum and a sudden change in potential (see (2.47)), therefore the two key parameters that we must minimise in order to maximise our chances of observing quantum reflection are the initial separation between solitary wave and potential well and the waist of the beam forming the well. We have already demonstrated the centre-of-mass velocity control of a cloud in figure 6.15 and in section 7.5 we will discuss how we determine the waist of the laser producing the potential well.

Observing and understanding the mechanisms for resonant trapping in solitary wave–potential well interactions would be something very interesting to

[1]There could potentially be a case where a bound state of two solitary waves forms around a barrier, however, this would be a very unlikely result of a solitary wave–barrier interaction at non-zero velocity.

explore, however, considering that we predict (see figure 2.3) that in order to have a high probability of observing quantum reflection, we need a well with waist < 2 μm, we would at best be able to observe the presence of a trapped component. To add further difficulty, resolving the density distribution of the trapped component, which arguably would be the more interesting aspect, is completely out of the question as we are aiming to make the waist of the well of order the limit of our high resolution imaging system (1.92 $\mu\mathrm{m\,px}^{-1}$). The predicted maximum proportion of trapped atoms, in comparison with the initial number in the solitary wave is $\sim 5\%$ [298], which, considering our solitary wave size is $N \sim 2500$, leaves us with a maximum of 125 trapped atoms. Observaing the presence of such a small number of atoms using our high resolution imaging system may be possible (see section 7.4.4), as this small number of atoms would be tightly confined, leading to an expected optical depth[2] of ~ 0.5.

7.3 Experimental apparatus

Further to section 3.1.1, where an overview of our experimental apparatus was given, we present an overview focussing specifically on how the laser beam generating the potential well enters the science cell. Figure 7.2 shows a schematic of the apparatus used to generate the light sheet that forms the well.

The potential well light is generated by a homebuilt laser (more details of which will be found in the thesis of MMHY), whose beam is sent through a fibre mounted to the breadboard for the potential well laser light, seen in figure 3.1. The collimated beam has a $1/e^2$ radius of 2.3 mm, with a beam sampler to pick off light for control and stabilisation of the beam power via a servo. The beam is sent towards to the cylindrical lens and is then reflected down towards the science cell, travelling through a cube which allows the potential well and vertical imaging to occur at the same time[3].

[2] This is a rough estimate from the optical depth, width and number of atoms observed in figure 7.5 (g).

[3] We eventually discovered that due to multiple reflections of the potential well beam within the cube, 852 nm light leaked onto our imaging camera, making it very difficult to image at the same time as using the potential well. In order to avoid this happening in the future, the cube will eventually be replaced by a beamsplitter not at right angles to the light.

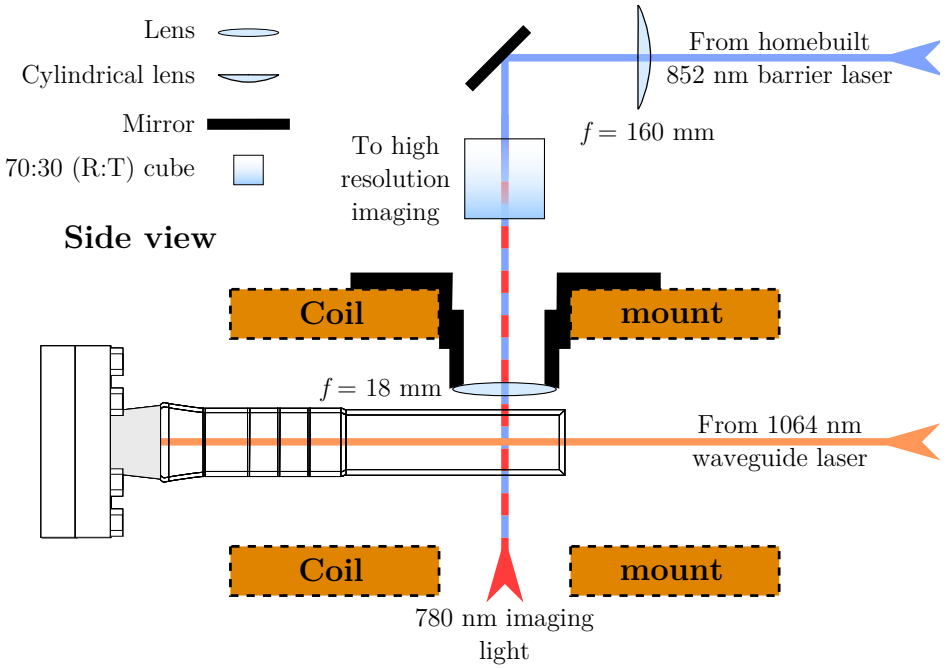

Figure 7.2: (Not to scale) Schematic of the apparatus that generates the potential well. An ~ 12 mW 852 nm Gaussian beam is formed into a light sheet using the combination of a $f = 160$ mm cylindrical lens and a $f = 18$ mm aspheric lens. The 852 nm beam intersects with the waveguide, resulting in the formation of a potential well. Counter-propagating 780 nm light allows high resolution imaging to occur, with the 70:30 (R:T) cube directing the imaging light into the page to a camera.

The one-dimensional potential (for reference see figure 7.1), along the axial direction of the waveguide, formed by the combination of potential well and waveguide is

$$U_{\mathrm{B-WG}}(x) = \frac{1}{2}m\omega_x^2 x^2 + \frac{2\alpha P}{\pi w_x w_y}\exp\left(-\frac{2x^2}{w_x^2} - \frac{2y^2}{w_y^2}\right), \tag{7.1}$$

where the first term is the broad background potential characterised by ω_x, which is the trap frequency due to the magnetic quadrupole trap ($2\pi \times 1.16$ Hz), and the second term is the potential due to the 852 nm light sheet, forming the potential well, where P is its power, α is defined by (7.15), w_x is its narrow waist (~ 2 μm) and w_y is its broader waist (~ 200 μm).

As can be seen in figure 7.2, the final lens has a very short focal length and is, therefore, placed very close to the science cell. We can see from (3.15) that the shorter the focal length of a lens, the smaller the resolvable object. In this case, for a lens with $f = 18$ mm, $D = 20$ mm and $\lambda = 852$ nm we

have a diffraction limit of $R = 0.94$ μm, which should be perfectly adequate if we aim to create a beam with $w_x \sim 2$ μm. The mount for this final lens is made from G10 and has two parts that can screw into or out of each other. The lens is glued to one part of the mount and the other part of the mount is glued to our coil mount above the science cell. Using a bespoke tool we are able to easily adjust the vertical position of the lens, which (de)focusses the imaging beam and shifts the waist of the well.

7.4 Aligning the potential well with the waveguide

Having learned from the process of aligning the waveguide with the crossed-dipole trap, in this section we present the procedure through which we aligned the potential well with the waveguide.

7.4.1 Preparation of an elongated cloud

In section 6.6.2 we presented a novel method of reducing the difficulty in aligning the waveguide with the crossed-dipole trap. The procedure was to expand the width of the trapped cloud in one of the directions. By applying a moderate bias field in the hybrid trap (see figure 6.6) we reduced the horizontal confinement due to the magnetic trapping potential, resulting in an elongated cloud. We applied the same principle with the waveguide. Starting with a cloud at the end of dipole ramp 1 (see table 6.2), we load straight into the waveguide, when it has a depth of ~ 10 μK. No bias field has yet been applied. At this point we increase the bias field from zero to a small non-zero value (< 20 G), such that the axial trap frequency is reduced, providing an elongated cloud. In the next section, we derive the axial trap frequency and root mean square radius of the cloud as a function of bias field.

The dependence of cloud size in a quadrupole trap as a function of bias field

An atom in a quadrupole trap sees a potential energy of the form

$$U(r,z) = C\left(r^2 + 4z^2\right)^{1/2}, \tag{7.2}$$

where $C = m_F g_f \mu_\mathrm{B} B'_r$ and r and z are the radial and axial coordinates with respect to the coils generating the magnetic field.

The dominant confining potential axially in the waveguide is provided by the radial component of the quadrupole trapping potential. The axial confinement due to the waveguide beam is negligible in comparison. As a bias field applied along the z axis is increased, the potential along the radial axis, r, becomes increasingly harmonic. In order to determine the axial width of the cloud we use a harmonic approximation. First, however, we must transform the z coordinate such that it is replaced by a quantity dependent on the bias field,

$$z = \left(\frac{B_\mathrm{shift}}{B'_z}\right), \tag{7.3}$$

where B_shift is the bias field along the z axis of the potential. The new potential can be written as

$$U(r) = C\left[r^2 + 4\left(\frac{B_\mathrm{shift}}{B'_z}\right)^2\right]^{1/2}. \tag{7.4}$$

In order to calculate the frequency of the quadrupole trapping potential off-axis, we must undertake a Taylor expansion of (7.4) and equate the second order term with the standard form of the harmonic trap potential energy. The second derivative of (7.4) is

$$U''(r) = C\left[r^2 + 4\left(\frac{B_\mathrm{shift}}{B'_z}\right)^2\right]^{-1/2} - r^2 C\left[r^2 + 4\left(\frac{B_\mathrm{shift}}{B'_z}\right)^2\right]^{-3/2}. \tag{7.5}$$

Around $r = 0$ the second term of (7.5) becomes zero and the resulting second

order term of the Taylor expansion, around $r = 0$, is

$$\frac{U''(0)}{2!}r^2 = \frac{r^2 C}{2}\left[4\left(\frac{B_{\text{shift}}}{B'_z}\right)^2\right]^{-1/2} = \frac{r^2 C B'_z}{4B_{\text{shift}}}. \tag{7.6}$$

We can now equate (7.6) with the form of the potential energy in a harmonic trap

$$\frac{1}{2}m\omega_r^2 r^2 = \frac{r^2 C B'_z}{4B_{\text{shift}}}. \tag{7.7}$$

Rearranging we obtain

$$\omega_r = \left(\frac{C B'_z}{2mB_{\text{shift}}}\right)^{1/2}. \tag{7.8}$$

We then substitute in for C, remembering that, for ^{85}Rb in this experiment, $m_F = -2$, $g_f = -1/3$ and for a quadrupole trap $B'_r = B'_z/2$,

$$\omega_r = \left(\frac{\mu_B B'^2_z}{6mB_{\text{shift}}}\right)^{1/2}. \tag{7.9}$$

The mean potential energy, in one dimension, of an atom in a cloud in thermal equilibrium with a harmonic trap can be equated with its thermal energy using the equipartition theorem,

$$\frac{1}{2}m\omega_r^2\sigma_r^2 = \frac{1}{2}k_{\text{B}}T, \tag{7.10}$$

where ω_r is the trap frequency and σ_r is the root mean square radius of the cloud. Rearranging for σ_r and substituting in for ω_r from (7.9) we obtain

$$\sigma_r = \left(\frac{6k_{\text{B}}TB_{\text{shift}}}{\mu_B B'^2_z}\right)^{1/2}. \tag{7.11}$$

Comparison of data and theory

We transfer a cloud from the crossed-dipole trap to the waveguide and allow it to equilibrate for 2.5 s at a variable bias field. We then measure the axial root mean square radius of the cloud and its temperature. In figure 7.3 (a) we compare the theoretical curve of trap frequency as a function of bias field (see (7.9)) with our measured frequency, calculated via 7.10 using

our measured axial cloud width and temperature. We see good agreement between experiment and theory.

The inset of (a) shows images of the cloud in equilibrium with the combined waveguide and magnetic potential at a variety of different bias fields. The cloud expands as the bias field increases, due to the reduction in the axial trap frequency. The centre-of-mass of the cloud is also seen to shift slightly, which we believe is due to how we centre the cloud on our viewable (imaging) area. In order to centre the cloud, an additional bias field is applied along the axial direction of the waveguide from a combination of three single coils, on one side of the science cell. As these are not coil pairs, there is notable curvature in the field emanating from these coils (particularly if the coils are slightly off-axis from the waveguide), which results in a magnetic potential that is non-trivial. The combination of this asymmetric axial bias field with the radial bias field and quadrupole trapping field results in shifting of the centre-of-mass, as observed in the figure.

In figure 7.3 (b) we give the temperature of the elongated cloud as a function of bias field, measured via cloud width in the vertical direction after a fixed time-of-flight expansion. We would expect the temperature of the cloud to be limited by the depth of the combined potential in the vertical direction

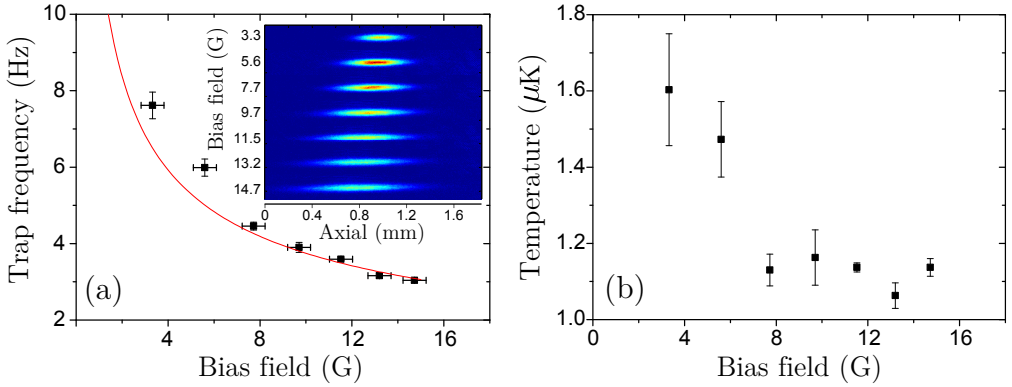

Figure 7.3: Variation of axial trap frequency, cloud profile and temperature as a function of bias field. A cloud is transferred from the crossed-dipole trap into the waveguide after dipole ramp 1. The quadrupole trap remains on at 21.5 G cm^{-1} with a variable bias field applied in the radial (vertical) direction of the waveguide. (a) The trap frequency as a function of bias field is calculated from the cloud size and temperature, using 7.10. The red line is a plot of (7.9). Inset: The cloud profile as a function of bias field, with the position in the axial direction of the waveguide quantified. (b) Variation in temperature of the equilibrated cloud in the combined waveguide and magnetic potential as a function of bias field.

(dominated by the waveguide), therefore, an increase in the bias field should not affect the measured temperature of the cloud. This is the behaviour we see above $\sim$ 8 G, however, below this value the temperature increases. The most plausible explanation of this is that a reduced bias field results in an increased axial trapping frequency, the result of which is an increase in density of the cloud. This increase in density also increases the three-body loss rates (hence the reduction in optical depth) and, therefore, the heating rate. From a previous argument (see section 6.4.3), this must mean a reduction in the evaporation parameter η, resulting in a higher temperature cloud for the same trap depth.

7.4.2 The alignment of the potential well

It was critical to ensure that the procedure for aligning the well and the high resolution imaging beam with the cloud of atoms confined in the waveguide was carefully thought through, to ensure that time was not wasted trying to find a needle in a haystack. We devised the following procedure that was very successful and enabled us to align both beams promptly (see figure 7.2):

1. Centre the probe beam on the atoms, by aligning the probe beam on the CCD with the use of no lenses, and look for absorption in the images. Aperture down the beam until it is small ($\sim$ 1 mm) and perform any minor adjustments to ensure that the beam is centred on the atoms and the CCD.

2. Place the final lens in front of the camera and focus the light onto the CCD. CAUTION: Reduce the power of the beam to a low enough value, not to damage the pixels of the CCD.

3. Overlap the potential well beam with the probe beam. This should ensure that the well is also roughly centred on the atoms.

4. Place the cylindrical lens into the potential well path, ensuring that the two beams remain overlapped.

5. Put the final lens ($f = 18$ mm) into the beam path and centre the lens on the potential well/probe beams by eye.

6. Attempt to centre atoms on the CCD, making any minor adjustments to the final lens.

7. Glue the final lens to the coil mount and adjust focus.

8. Once in focus, make minor adjustments to the well with the mirrors prior to the final lens (so that the imaging beam path is not altered) and look for the presence of the well in the images.

7.4.3 Focussing the high resolution imaging system

In figure 7.4 we show how the profile of a cloud changes as the position of the $f = 18$ mm lens was translated towards and away from the cloud. If a beam is not exactly on resonance with the atomic sample it is probing, the atoms possess an index of refraction greater than 1 [218]. The result of this is that a high density cloud of atoms, whose density varies spatially, will act as a lens for the probe beam. This causes distortions in the shape of the imaged cloud, like those seen in figure 7.4. When the distortions are minimised, the optical depth is maximised and the width of the imaged cloud is minimised we have focussed our imaging system. See [69] for a more detailed example. We chose 0.25 mm as the position where the cloud was most in focus.

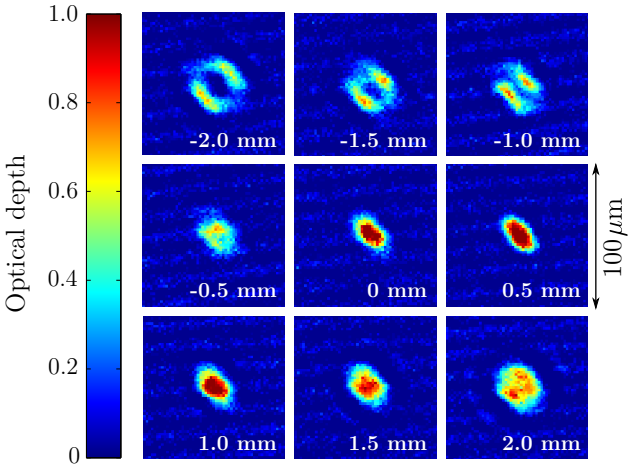

Figure 7.4: Focussing the vertical imaging system. A high density ^{85}Rb cloud, close the BEC transition is imaged in the crossed-dipole trap. Lensing affects the profile of the cloud on the images where the imaging plane is not intersecting the cloud, due to the probe beam not being exactly on resonance with the $F = 3 \rightarrow F' = 4$ transition. High optical depth and a narrow cloud is an indication of a cloud that is in focus, hence, we fixed the position of the lens at 0.25 mm after this calibration.

7.4.4 Resolution of the imaging system

Having focussed our imaging system we now attempt to quantify its limits—specifically the minimum atom number that can be imaged and the minimum cloud size that we can resolve.

The procedure that we undertake is to produce a repulsive BEC in the crossed-dipole trap ($a = 353\ a_0$) and gradually remove atoms from the BEC by lowering the depth of the trap. The resulting cloud reduces in size and the optical depth also reduces. We remove atoms from the cloud until it is no longer possible to resolve it relative to the background noise of the image. Figure 7.5 shows these clouds as an increasing number of atoms were removed from the BEC.

In figure 7.5 (g), at the limit of our high resolution imaging system, we extract an atom number $N = 150$ and root mean square radii of $\sigma_{\mathrm{ax}} = 6.2\ \mu$m and $\sigma_{\mathrm{rad}} = 3.1\ \mu$m. Therefore we concluded that the smallest resolvable atom number by this imaging system was $N = 150$ and the smallest resolvable distance was 3.1 μm, of the order of the size of a solitary wave confined in our waveguide (see section 2.5.2).

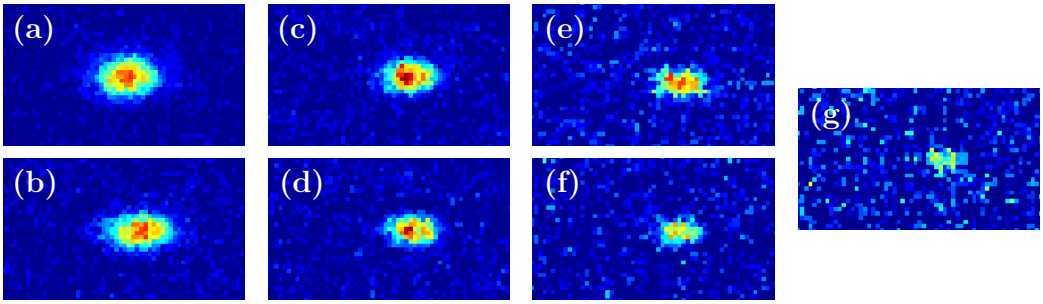

Figure 7.5: Experimentally determining the limits of the vertical imaging system. It is important to note that the images in this figure have been rotated by 45° counterclockwise, relative to figure 7.4. A repulsive BEC is confined in the crossed-dipole trap and an increasing number of atoms are allowed to escape, by the lowering of the depth of the trap from panels (a) to (g). The clouds are imaged 2 ms after release from the trap. (a) $N = 3000$, $\sigma_{\mathrm{ax}} = 10.0\ \mu$m, $\sigma_{\mathrm{rad}} = 6.4\ \mu$m and OD = 1.6. (b) $N = 2000$, $\sigma_{\mathrm{ax}} = 11.2\ \mu$m, $\sigma_{\mathrm{rad}} = 5.3\ \mu$m and OD = 1.0. (c) $N = 1500$, $\sigma_{\mathrm{ax}} = 8.6\ \mu$m, $\sigma_{\mathrm{rad}} = 4.7\ \mu$m and OD = 1.1. (d) $N = 1000$, $\sigma_{\mathrm{ax}} = 8.1\ \mu$m, $\sigma_{\mathrm{rad}} = 4.3\ \mu$m and OD = 0.8. (e) $N = 1000$, $\sigma_{\mathrm{ax}} = 9.0\ \mu$m, $\sigma_{\mathrm{rad}} = 4.0\ \mu$m and OD = 0.5. (f) $N = 400$, $\sigma_{\mathrm{ax}} = 7.5\ \mu$m, $\sigma_{\mathrm{rad}} = 3.7\ \mu$m and OD = 0.4. (g) $N = 150$, $\sigma_{\mathrm{ax}} = 6.2\ \mu$m, $\sigma_{\mathrm{rad}} = 3.1\ \mu$m and OD = 0.2.

7.5 Characterising the potential well

In order to understand the results of our future collisions with the potential well and to model the experiment theoretically, we must comprehensively characterise the beam forming the potential well. As the beam is inside the vacuum system and has a very short Rayleigh length [299] (≈ 60 μm) it is not possible to simply measure the waist of the beam and assume that it intersects with the waveguide. Instead we must use the atoms to determine the beam parameters.

As our resolution is fundamentally limited[4] to 5.23 μm px^{-1}, it is not sufficient to simply trap atoms in the well and measure the waist of the cloud, as this will be below our resolution. Instead we choose to use parametric heating to determine the size of the waist and trap frequencies of the potential well beam.

7.5.1 The geometry of the trap formed by the waveguide and potential well

Measurements of the waist of the potential well before it was placed into the experimental setup gave a $1/e^2$ radius of 4μm by 260μm. The power of the potential well beam is 15 mW at 852 nm. Assuming these values and simulating the intersection of this beam with the waveguide (200 mW at 1064 nm) results in trap frequencies of $2\pi \times 1.57$ kHz along the waveguide axis and $2\pi \times 36$ Hz (horizontally) by $2\pi \times 60$ Hz (vertically) in the radial directions of the waveguide. The tight focus of the potential well beam dominates over the axial potential of the waveguide and the magnetic potential in the same direction. Therefore the trap frequency in this direction essentially describes the potential well only. In the other directions the trap frequencies are a mix of potential well and waveguide.

While we initially thought that we would need the waveguide to be turned on, in order to aid trapping of the atoms in the potential well for parametric heating, we discovered that in a levitated geometry it was possible to trap atoms solely in the potential well. Below we compare the trap frequencies ob-

[4] Remember that we are currently unable to use our high resolution imaging system at the same time as the potential well

tained via parametric heating with those predicted earlier. We also use these frequencies to determine the waist of the light sheet forming the potential well in its two directions and the Rayleigh length.

7.5.2 Expressions for the waists and Rayleigh length of the potential well beam

The intensity of a Gaussian laser beam, in our case the potential well, can be described by

$$I = I_0 \exp\left(-\frac{2x^2}{w_x^2} - \frac{2y^2}{w_y^2}\right), \tag{7.12}$$

where w_x and w_y are the $1/e^2$ radii of the well in the x and y directions respectively and

$$I_0 = \frac{2P}{\pi w_x w_y}, \tag{7.13}$$

where P is the total power in the potential well beam. The depth of the trap, U_0, can be expressed in terms of the peak intensity, I_0, of the potential well beam

$$U_0 = \alpha I_0, \tag{7.14}$$

where

$$\alpha = -\frac{\pi c^2}{2} \sum_i \frac{D_i \Gamma_i}{\omega_i^3} \left(\frac{1}{\omega_i - \omega_\mathrm{L}} + \frac{1}{\omega_i + \omega_\mathrm{L}}\right), \tag{7.15}$$

where i is a particuar transition we are including in the sum, while $D_i = 1$ or $D_i = 2$ for a D_1 or D_2 transition, respectively, ω_i is the frequency and Γ_i is the natural linewidth of the relevant transition and ω_L is the frequency of the laser. We generally sum over the four persistent lines of Rb[5]. Oscillation frequencies, ω_x and ω_y, along the x and y directions, using a harmonic approximation, can be related to the depth or intensity of the potential well by [207]

$$\omega_x = \left(\frac{4U_0}{mw_x^2}\right)^{1/2} = \left(\frac{4\alpha I_0}{mw_x^2}\right)^{1/2} \text{ and } \omega_y = \left(\frac{4U_0}{mw_y^2}\right)^{1/2} = \left(\frac{4\alpha I_0}{mw_y^2}\right)^{1/2}. \tag{7.16}$$

[5]These are $\lambda_1 = 420.180$ nm, $\Gamma_1 = 1.8$ MHz, $\lambda_2 = 421.553$ nm, $\Gamma_2 = 1.5$ MHz, $\lambda_3 = 780.027$ nm, $\Gamma_3 = 37.0$ MHz, $\lambda_4 = 794.760$ nm and $\Gamma_4 = 34.0$ MHz [300].

By substituting (7.13) into (7.16) we get

$$\omega_x = \left(\frac{4\alpha}{mw_x^2}\frac{2P}{\pi w_x w_y}\right)^{1/2} = \left(\frac{8\alpha P}{\pi m w_x^3 w_y}\right)^{1/2}, \tag{7.17}$$

and

$$\omega_y = \left(\frac{4\alpha}{mw_y^2}\frac{2P}{\pi w_x w_y}\right)^{1/2} = \left(\frac{8\alpha P}{\pi m w_y^3 w_x}\right)^{1/2}. \tag{7.18}$$

Maintaining the definition that the Rayleigh length z_R is the distance over which the cross-sectional area of a laser beam increases by a factor of 2, we can obtain an expression for the propagation of a Gaussian light sheet,

$$w_x(z)w_y = w_x(0)w_y\left[1+\left(\frac{\sqrt{3}z}{z_R}\right)^2\right]^{1/2}. \tag{7.19}$$

It is important to note that the slightly odd addition of a factor of $\sqrt{3}$ comes from the fact that w_x varies much quicker than the almost collimated w_y, therefore, we introduce no variation in w_y. It can be seen that at $z = z_R$, the area of the light sheet is a factor of two larger, $w_x(z = z_R)w_y = 2w_x(0)w_y$. Taking a harmonic approximation along the z direction gives an expression for the trap frequency along the propagation direction of the potential well beam,

$$\omega_z = \left(\frac{6\alpha P}{\pi m w_x w_y z_R^2}\right)^{1/2}. \tag{7.20}$$

By combining and rearranging (7.17) and (7.18), we can obtain expressions for the potential well beam waists in the x,

$$w_x = \left(\frac{8\alpha P\omega_y}{\pi m\omega_x^3}\right)^{1/4}, \tag{7.21}$$

and y,

$$w_y = \left(\frac{8\alpha P\omega_x}{\pi m\omega_y^3}\right)^{1/4}, \tag{7.22}$$

directions in terms of quantities that we know or can calculate. Subsituting these expressions into (7.20) and rearranging allows us to obtain an expres-

sion for the Rayleigh length of our light sheet,

$$z_R = \frac{1}{\omega_z}\left(\frac{9\alpha P}{2\pi m}\omega_x\omega_y\right)^{1/4}. \tag{7.23}$$

We will return to these expressions, once we have measured the trap frequencies of the potential well beam in section 7.5.4.

7.5.3 Transferring atoms to the potential well

We now turn our attention to the loading of the potential well beam with atoms from the crossed-dipole trap, in order to begin the process of characterisation. In this first experiment we reduce the levitation gradient of the static quadrupole trap to a value that barely allows a trap to be formed due to the potential well beam alone. Atoms are transferred into the the potential well and fall, due to gravity. The result of the experiment is shown in figure 7.6.

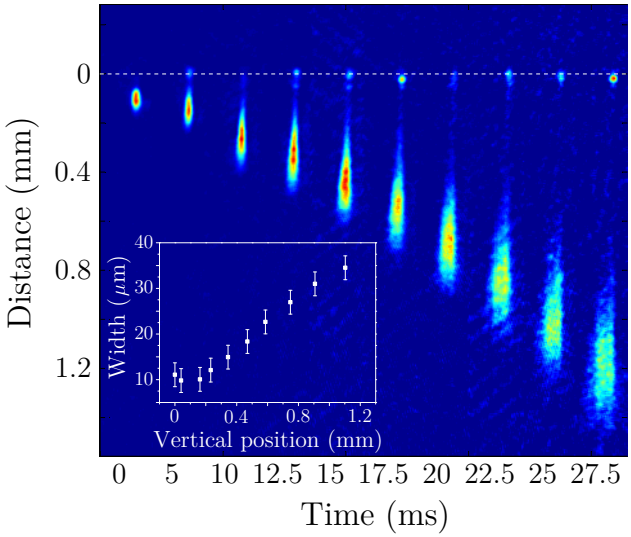

Figure 7.6: Cold atoms sampling the profile of the potential well beam. Atoms are released into the potential well after three ramps of the crossed-dipole trap power. The trap is under-levitated, resulting in the atoms falling, due to gravity. The optical depth in each image is scaled such that the maximum is 1. In the process of falling, they expand more quickly in the axial (vertical) than the radial (horizontal) direction. The lack of rapid expansion in the radial direction is due to confinement from the tight focus of the beam in this direction. The atoms are effectively sampling the profile of the beam in the radial direction. Atoms confined in a very shallow trap can be seen at the top of some of the images. Insert: Radial root mean square radius of the cloud as a function of cloud centre of mass position in the vertical direction.

As the atoms are released from the crossed-dipole trap we observe the rapid expansion of the cloud in the axial (vertical) direction, while the cloud remains confined in the radial (horizontal) direction. This confinement is due to the tight trapping in the horizontal direction, which weakens as we move away from the focus, as can be seen from (7.19). The inset of figure 7.6 shows how the horizontal root mean square radius of the cloud changes as a function of cloud centre of mass in the vertical direction. We can use this cloud radius to obtain a basic understanding of how the beam profile changes as it propagates. The beam widens in the horizontal direction as the atoms drop, with its focus somewhere above where the atoms are initially released. A very shallow trap is formed close to the focus, resulting in the trapping of $N \sim 1000$ atoms after 27.5 ms.

7.5.4 Measuring frequencies, calculating the waists and Rayleigh length of the potential well beam

The next stage of characterisation is to obtain the trap frequencies at a particular potential well beam power, resulting in the calculation of the beam waists and Rayleigh length (see (7.21), (7.22) and (7.23)). $N \sim 3000$ atoms are transferred into the potential well and parametric heating begins, by modulating the beam power at a range of frequencies, as described in section 3.2.3. An example of the remaining atom number, after 2 s of parametric heating, as a function of modulation frequency is shown in figure 7.7, for a potential well beam power of 9.9 mW. As can be seen, minimal loss is observed away from the resonance, which occurs at twice the trap frequency in the tight radial (x) direction. At around twice the trap frequency, a significant number of atoms are lost due to parametric excitation.

We also repeated this method at lower modulation frequencies in order to obtain the trap frequencies in the weak radial (y) and vertical (z) directions. The frequencies at which peak loss was observed were $\omega = 2\pi \times 4.4(1)$ kHz, $\omega = 2\pi \times 33.0(8)$ Hz and $\omega = 2\pi \times 200(5)$ Hz. Remembering that this loss occurs at twice the relevant frequency of the trap and deducing from modelling that the weakest trapping occurs along the y-axis, we obtain trap frequencies of $\omega_x = 2\pi \times 2.18(6)$ kHz, $\omega_y = 2\pi \times 16.5(5)$ Hz and $\omega_z = 2\pi \times 99(3)$ Hz.

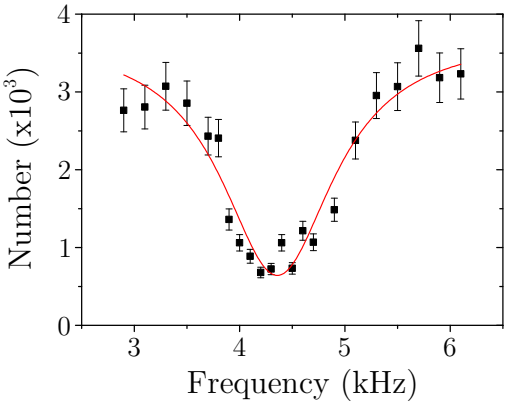

Figure 7.7: Atom loss due to parametric heating in the potential well. The power of the potential well laser is $P = 9.9$ mW. The red line is a phenomenalogical Lorentzian fit to the data, in order to obtain a centre frequency. We obtain a frequency of 4.4(1) kHz.

Substituting the measured frequencies into (7.21), (7.22) and (7.23), calculating $\alpha = 6.333 \times 10^{-36}$ J/(Wm^{-2}) for ^{85}Rb, using (7.15), and taking $\lambda = 852$ nm, we obtain trap waists of $w_x = 2.60(6)$ μm and $w_y = 343(8)$ μm and a Rayleigh length of $z_R = 50(3)$ μm. While the waist in the y direction is wider than the 260 μm we were aiming for, we have obtained a narrow waist of the order of the size of our solitary waves (see section 2.5.2), which should put us in a good position to potentially observe quantum reflection.

7.5.5 Comparing predicted trap depth with measured depth

We can place more confidence in the measured waists from the previous section through measuring the temperature of a cloud of atoms trapped in the well and comparing this temperature with the depth of the trap obtained via modelling the potential formed by a beam with the waists measured above. We expect the temperature to be approximately one tenth of the trap depth. By intersecting the waveguide with the waist of the well we are able to prevent any atoms from escaping the trap in the y or z directions. Therefore, the temperature of a cloud of atoms in the well is governed solely by evaporation along the waveguide beam.

The predicted potential trap depth was 3.24 μK, therefore we expected to measure cloud temperatures of $T \sim 0.32$ μK. Figure 7.8 shows the temperature of a cloud trapped in a the well with $P = 9.9$ mW, as measured from the

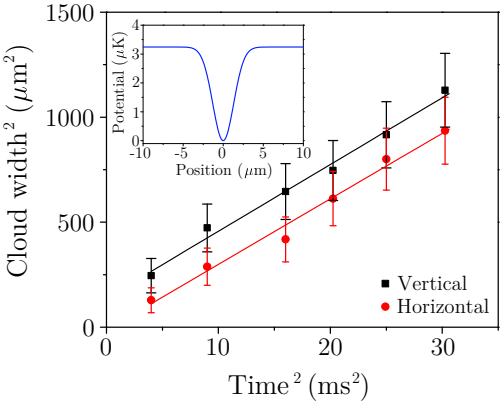

Figure 7.8: Measured temperature of a cloud trapped in the well. We can measure the temperature from the expansion of the cloud in both the horizontal and vertical directions. From the two fits (see section 3.2.1) we extract temperatures of $T_{\mathrm{V}} = 0.33(2)$ μK and $T_{\mathrm{H}} = 0.32(2)$ μK, which agree with the modelled trap depth of 3.24 μK. Inset: The profile of the potential well in the narrow direction, at its focus.

expansion in the vertical and horizontal directions. If the two temperatures agree, it shows that the cloud has equilibrated with the trap.

By plotting the square of the cloud width against the square of the time of flight, it is straightforward to obtain the temperature from the fit. By combining (3.13) and (3.14) we can see the gradient of the plot is simply $k_{\mathrm{B}}T_{V,H}/m$. We extract temperatures of $T_{\mathrm{V}} = 0.33(2)\mu$K and $T_{\mathrm{H}} = 0.32(2)$ μK, agreeing with the modelled trap depth of 3.24 μK. Therefore, the measured waists are indeed correct, within error.

7.6 Conclusion

In this chapter we have presented the preparation, alignment, loading and characterisation of a narrow potential well from which we plan to reflect a solitary wave. We have also demonstrated the focussing and determined the limits of our high resolution imaging system. We have determined that the waist of the potential well in the direction of propagation of the solitary wave is $w_x = 2.60(6)$ μm and $w_y = 343(8)$ μm along the other direction. The Rayleigh length of the beam is $z_R = 50(3)$ μm. We also indirectly measured the depth of the potential well through a measurement of the trapped cloud temperature. The measured temperatures of $T_{\mathrm{V}} = 0.33(2)$ μK and $T_{\mathrm{H}} = 0.32(2)$ μK agree with the modelled trap depth of 3.24 μK.

Chapter 8

Towards solitary wave interactions with a dielectric surface

8.1 Introduction

The major long-term aim of this experiment is to observe solitary wave–surface interactions, with the hope of witnessing quantum reflection. While this goal may prove to be a difficult feat, an initial step towards it is to probe the potential observed by atoms close to a dielectric surface by simple, classical reflection. In this chapter we will present the form of the potential observed by atoms close to a dielectric surface, combine it with a repulsive evanescent potential and quantify this resulting potential, taking particular note of the height and relative position of potential barriers formed in the process.

8.2 Atom–surface interactions

In this section we will cover the basic theory required to model the attractive potential of an atom close to a dielectric surface. In section 8.4 we combine this potential with a repulsive evanescent wave potential, generated due to the total internal reflection of a laser beam blue detuned from the dominant transitions in rubidium.

8.2.1 Length scales

The key to modelling an atom–surface potential is to understand the relevant length scales over which different factors become dominant. There are three regimes that are relevant to our study; the close, intermediate and far. It is recommended that the reader takes note of figure 8.1 during the remainder of this explanation.

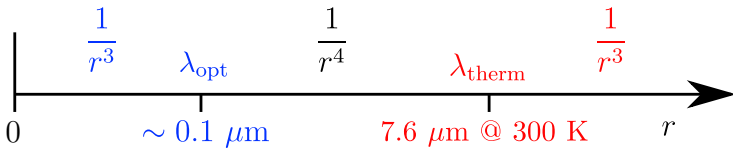

Figure 8.1: The relevant length scales for the interaction between a rubidium atom and a dielectric surface. Below λ_{opt} the potential approaches the $1/r^3$ asymptotic van der Waals–London limit, between λ_{opt} and λ_{therm} the potential follows the $1/r^4$ Casimir–Polder form and above λ_{therm} the potential returns to approaching a $1/r^3$ dependence, which is the high-temperature regime.

To distinguish between these three regimes, we have two length scales, λ_{opt} and λ_{therm}, where [301]

$$\lambda_{\text{therm}} = \frac{\hbar c}{k_{\text{B}} T}, \tag{8.1}$$

and λ_{opt} does not have a simple expression, but can be calculated using (25) from [301]. At 300 K, $\lambda_{\text{therm}} = 7.6$ μm and for Rb $\lambda_{\text{opt}} \sim 0.1$ μm. When $r \ll \lambda_{\text{opt}}$ and T is low enough (300 K in this case), we are in the van der Waals–London regime, where the potential experienced by an atom follows a $1/r^3$ form, due to instantaneous-induced dipolar interactions [302]. When $\lambda_{\text{opt}} < r < \lambda_{\text{therm}}$, the potential approaches a $1/r^4$ dependence, known as the Casimir–Polder law [303], due to retarded instantaneous-induced dipolar interactions [302]. Finally, when $r > \lambda_{\text{therm}}$, thermal fluctuations of the electromagnetic field dominate the force [301], resulting in the potential returning to an asymptotic $1/r^3$ limit.

During the remainder of this chapter we will be concerned with distances of $r < 1$ μm, therefore we are not interested in the thermal limit. In the next section we provide expressions for the potential where $r < 1$ μm.

8.2.2 Quantifying the atom–surface potential

The equations in this section are presented in a nondimensional form, in atomic units, where $m_e = e = \hbar = 4\pi\epsilon_0 = 1$, unless otherwise stated; however, all results in section 8.4 are given in S.I. units.

The potential that an atom will observe when close to a surface with a dielectric constant[1] ϵ, in our short-range limit (neglecting any effect of temperature), can be expressed as [304]

$$U_{\text{surf}}^{\text{SR}}(r,\epsilon) = -\frac{\alpha_{\text{fs}}^3}{2\pi}\int_0^\infty d\xi\, \xi^3 \alpha_{\text{pol}}(i\xi)\int_1^\infty dp\, \exp\left(-2\xi r p \alpha_{\text{fs}}\right) H(p,\epsilon), \tag{8.2}$$

where α_{fs} is the fine structure constant, $\alpha_{\text{pol}}(i\xi)$ is the non-trivial dynamic polarisability of the atom evaluated at imaginary frequencies and

$$H(p,\epsilon) = \frac{s-p}{s+p} + (1-2p^2)\frac{s-\epsilon p}{s+\epsilon p}, \tag{8.3}$$

where

$$s = \left(\epsilon - 1 + p^2\right)^{1/2}. \tag{8.4}$$

There are two important limits of (8.2)—where $r \to 0$ and $r \to \infty$—which help to simplify the expression. For $r \to 0$ we find that (8.2) is reduced to [301]

$$U_{\text{surf}}^{\text{VL}}(r,\epsilon) = -\frac{1}{4\pi r^3}\int_0^\infty \alpha_{\text{pol}}(i\xi)\frac{\epsilon-1}{\epsilon+1}d\xi, \tag{8.5}$$

where the $1/r^3$ dependence of the van der Waals–London potential can be clearly seen. For $r \to \infty$, the Casimir–Polder law, with a $1/r^4$ dependence, can be obtained [301],

$$U_{\text{surf}}^{\text{CP}}(r,\epsilon) = -\frac{3\alpha_{\text{pol:0}}}{8\pi\alpha_{\text{fs}} r^4}\frac{\epsilon-1}{\epsilon+1}\phi(\epsilon), \tag{8.6}$$

where $\alpha_{\text{pol:0}}$ is the static polarisability of the atom and $\phi(\epsilon)$ is expressed as a function in (23) of [301] and is tabulated in [305].

It is important to have an accurate expression for $\alpha_{\text{pol}}(i\xi)$, otherwise what (8.2) and (8.5) produce will be meaningless. Therefore, we use an economical

[1] ϵ is generally dependent on frequency, however, we do not make this explicit in our analysis because for fused silica (the prism) we can approximate ϵ as a constant.

and accurate method [306] where the infinite frequency integrals are replaced by sums in the following manner,

$$\int_0^\infty f(\xi)\alpha_{\rm pol}(i\xi)d\xi \quad \rightarrow \quad \sum_{k=1}^{N} w_k f(\xi_k)\alpha_{\rm pol}(i\xi_k), \tag{8.7}$$

where $f(\xi)$ is any smoothly varying function and $\alpha_{\rm pol}$ is tabulated at frequencies ξ_k, resulting in an N-point quadrature, where each term is weighted by the factor w_k. The infinite integral in (8.2) and (8.5) has been replaced by a simple sum, for which $N = 50$ in [306].

We plot the full potential and the two approximations, for Rb atoms interacting with a fused silica surface ($\epsilon = 2.123$ [305]), in figure 8.2 in units of $U \times r^3$, which allows us to see the potential approaching the asymptotic $1/r^3$ limit (a constant value on this plot) and the $1/r^4$ limit (a linear dependence on this plot).

When the full short-range potential matches the approximations in the asymptotic limit, we can be confident that (8.2) has been integrated correctly. Now that we are able to calculate the atom–surface potential, it is essential that we can accurately model the repulsive evanescent wave potential counteracting the surface potential.

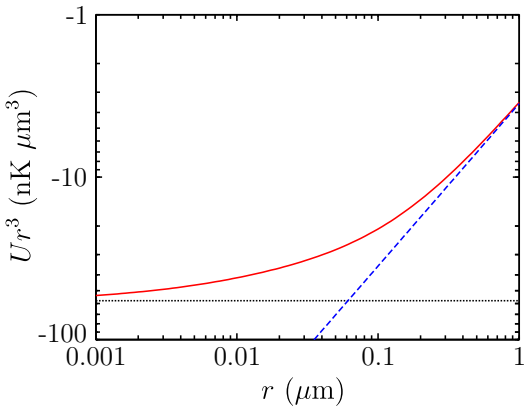

Figure 8.2: The atom–surface potential for a Rb atom approaching a fused silica surface ($\epsilon = 2.123$ [305]). The solid red line is the full potential (8.2), the dashed blue line is the Casimir–Polder potential (8.6) and the dotted black line is the van der Waals–London potential (8.5).

8.3 Producing an evanescent potential

To aid us in our understanding of the interaction between a solitary wave and a dielectric surface, with the long term aim of observing quantum reflection from the surface, we have chosen to produce an evanescent wave potential, which can be used to characterise the atom–surface potential (see section 2.3.6 and [67] for an example). Below we touch upon enough evanescent wave theory in order to demonstrate the dependence of the generated potential as a function of parameters such as beam angle, wavelength and refractive index.

8.3.1 Theory

When a beam is travelling from a medium with index of refraction n_1 into another medium with an index of refraction n_2, the coefficients of transmission can be stated as [307]

$$t_{\mathrm{TM}} = \frac{2n_1\cos(\theta_i)}{n_2\cos(\theta_i) + n_1\cos(\theta_t)} \quad \text{and} \quad t_{\mathrm{TE}} = \frac{2n_1\cos(\theta_i)}{n_1\cos(\theta_i) + n_2\cos(\theta_t)}, \tag{8.8}$$

where θ_i and θ_t are the angles of incidence and transmission respectively and TM/TE refers to the polarisation of the incoming light being transverse magnetic or transverse electric respectively. It is possible to remove any dependence on θ_t from (8.8) through Snell's law ($\sin(\theta_t) = (n_1/n_2)sin(\theta_i)$) and expressing the indices of refraction as $n = n_1/n_2$, resulting in

$$t_{\mathrm{TM}} = \frac{2n\cos(\theta_i)}{\cos(\theta_i) + n\sqrt{1 - n^2\sin^2(\theta_i)}}, \tag{8.9}$$

and

$$t_{\mathrm{TE}} = \frac{2n\cos(\theta_i)}{n\cos(\theta_i) + \sqrt{1 - n^2\sin^2(\theta_i)}}. \tag{8.10}$$

If the beam is travelling into a medium with a lower refractive index then $n_1 > n_2 \rightarrow n > 1$. As $n > 1$, at certain angles $n^2\sin^2(\theta_i) > 1$, which makes (8.9) and (8.10) complex. In this region we are beyond the critical angle and the incident beam is undergoing total internal reflection (TIR). To take

account of this, (8.9) and (8.10) can be rewritten as

$$t_{\mathrm{TM}} = \frac{2n\cos\left(\theta_i\right)}{\cos\left(\theta_i\right) + in\sqrt{n^2\sin^2\left(\theta_i\right) - 1}}, \tag{8.11}$$

and

$$t_{\mathrm{TE}} = \frac{2n\cos\left(\theta_i\right)}{n\cos\left(\theta_i\right) + i\sqrt{n^2\sin^2\left(\theta_i\right) - 1}}. \tag{8.12}$$

Finally, in order to calculate the intensity of electromagnetic field at the n_1–n_2 interface, we must find $|t_{\mathrm{TM}}|^2 \equiv T_{\mathrm{TM}}$ and $|t_{\mathrm{TE}}|^2 \equiv T_{\mathrm{TE}}$ [308],

$$T_{\mathrm{TM}} = \frac{4n^2\cos^2\left(\theta_i\right)}{\cos^2\left(\theta_i\right) + n^4\sin^2\left(\theta_i\right) - n^2} \quad \text{and} \quad T_{\mathrm{TE}} = \frac{4n^2\cos^2\left(\theta_i\right)}{n^2 - 1}. \tag{8.13}$$

In figure 8.3 we plot the dependence of these coefficients on the angle of incidence for our fused silica prism ($n = 1.45$ at $\lambda = 760$ nm [309]).

It is clear from figure 8.3 that the optimum polarisation, to achieve the largest intensity at the interface (the largest coefficient in (8.13)) depends on the angle of the incoming beam. In this experiment we are aiming to maximise the range of potentials that we can generate and, therefore, aim for $\theta_i < 45°$ and transverse magnetic polarisation.

A plane wave incident upon the interface at an angle θ_i, with a wavevector k_0 and momentum $\hbar k_0$ will undergo refraction. The component of the

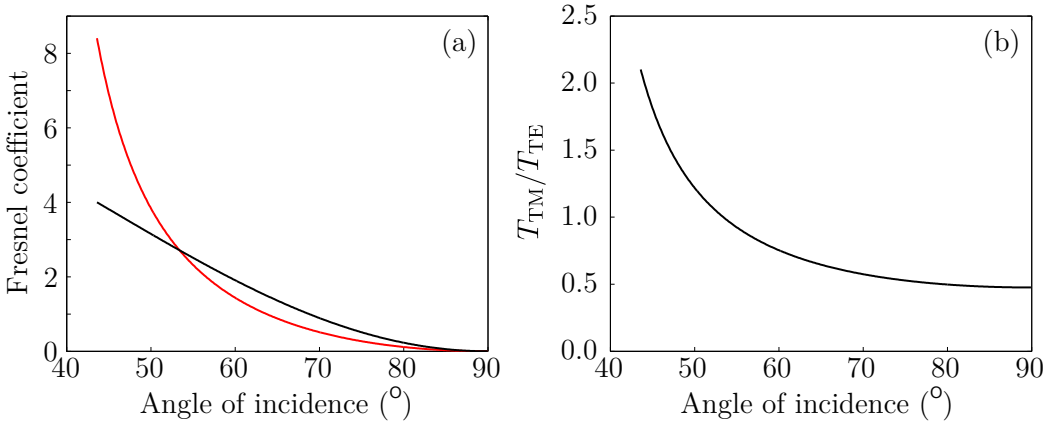

Figure 8.3: The dependence of the Fresnel coefficients on the angle of incidence. (a) Red line: The Fresnel coefficient for light of transverse magnetic polarisation (T_{TM}). Black line: The Fresnel coefficient for light of transverse electric polarisation (T_{TE}). (b) The ratio of the transverse magnetic and transverse electric coefficients.

transmitted wavevector parallel to the interface is

$$k_{\parallel t} = k_0 n \sin(\theta_i). \tag{8.14}$$

As stated above, once the critical incident angle is reached, the outgoing wavevector becomes parallel to the surface, because $n \sin(\theta_i) = 1$. However, beyond the critical angle $n \sin(\theta_i) > 1$. Here a scenario is reached where an apparent unphysical solution presents itself—$k_{\parallel t}$ is now *larger* than k_0. As $k_0^2 = k_{\parallel t}^2 + k_{\perp t}^2$, it is possible for this to continue to be true, only if $k_{\perp t} = i\kappa$, where $k_{\perp t} = k_0 \cos(\theta_t)$ and

$$\kappa = k_0 \sqrt{n^2 \sin^2(\theta_i) - 1}. \tag{8.15}$$

By substituting the resulting wavevector into the standard plane wave equation ($\mathbf{E} = \mathbf{E}_0 \exp[i(\mathbf{k}_0.\mathbf{x} - \omega t)]$) we arrive at

$$\mathbf{E}_t = \mathbf{E}_{0t} \exp[-\kappa z + i(k_0 n \sin(\theta_i)x - \omega t)], \tag{8.16}$$

where z and x are the directions perpendicular and parallel to the interface, respectively. We have arrived at an expression describing a wave that sinusoidally oscillates parallel to the interface and decays exponentially in the perpendicular direction. This is an evanescent field. The decay length perpendicular to the interface is simply $l_d = 1/\kappa$ and is plotted as a function of wavelength and incident angle in figure 8.4.

In order to calculate how the evanescent field contributes to the total potential experienced by the incoming atom, it is necessary to calculate the intensity of the evanescent field. From (8.16), taking account of the fact that the beam is gaussian, the intensity can be expressed as

$$I(x, y, z) = I_0 T_{\mathrm{TM/TE}} \exp\left(-2\frac{\cos^2(\theta_i)\, x^2 + y^2}{w^2}\right) \exp(-2\kappa z), \tag{8.17}$$

where I_0 is the intensity of the incoming beam and w is its waist. The potential can then be calculated using (7.14) and (7.15).

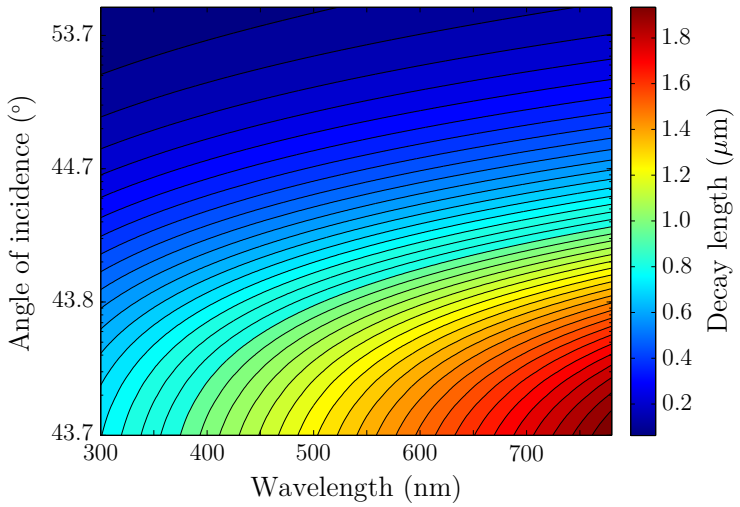

Figure 8.4: The decay length of the evanescent wave as a function of incident angle and wavelength, for $n = 1.45$.

8.3.2 Coherence length measurement

Using a known (evanescent) potential to calculate an unknown (surface) potential will only be successful if any unexpected behaviour in the known potential is minimised. One example of a behaviour that could complicate the form of the known potential is interference between the incident and reflected components of the gaussian beam. It is not clear whether this interference could be a significant problem, however, it would be extremely difficult to directly determine whether a corrugated potential, due to this interference, is present. One way to minimise the likelihood of this scenario occurring is to use a laser with a short coherence length, l_c.

The coherence length of a laser characterises the path difference beyond which minimal interference fringes are observed, between two overlapping beams derived from the same source. A detailed treatment of coherence length is presented in [307] and will only be touched upon here. A monochromatic beam will always be able to interfere when it overlaps with itself, regardless of the distance travelled in between. The same is not true for light with a spread of frequencies. Each frequency component can be treated individually, with each contributing its own interference fringes [307]. As the spacing of the fringes for each component varies slightly, eventually the phase of the interference patterns of each component will be significantly different, such that when one is dark, another is light. The result of this is significant washing out of the fringe pattern after a given distance—the coherence length.

By comparing the intensity between adjacent maxima ($I_{\max}$) and minima ($I_{\min}$) it is possible to obtain what is known as the visibility,

$$\mathcal{V} = \frac{I_{\max} - I_{\min}}{I_{\max} + I_{\min}}. \tag{8.18}$$

One can determine the coherence length by plotting a curve of visibility as a function of path difference, which will reach a minimal value at the coherence length. For a source with a top-hat-shaped spectral intensity distribution, of width Δk, the visibility curve follows a |sinc| profile[2], with its first minimum at a path difference of $2\pi/k$ [307], which is equated with the coherence length here. In the analysis below, for simplicity, it is assumed that the spectral intensity follows a top hat profile.

Experimental apparatus

We constructed a Michelson interferometer in order to observe the interference fringes created by two homebuilt lasers—one single-mode and the other multi-mode. Specifications of these lasers can be found in table 3.1. A schematic of this experimental apparatus can be seen in figure 8.5.

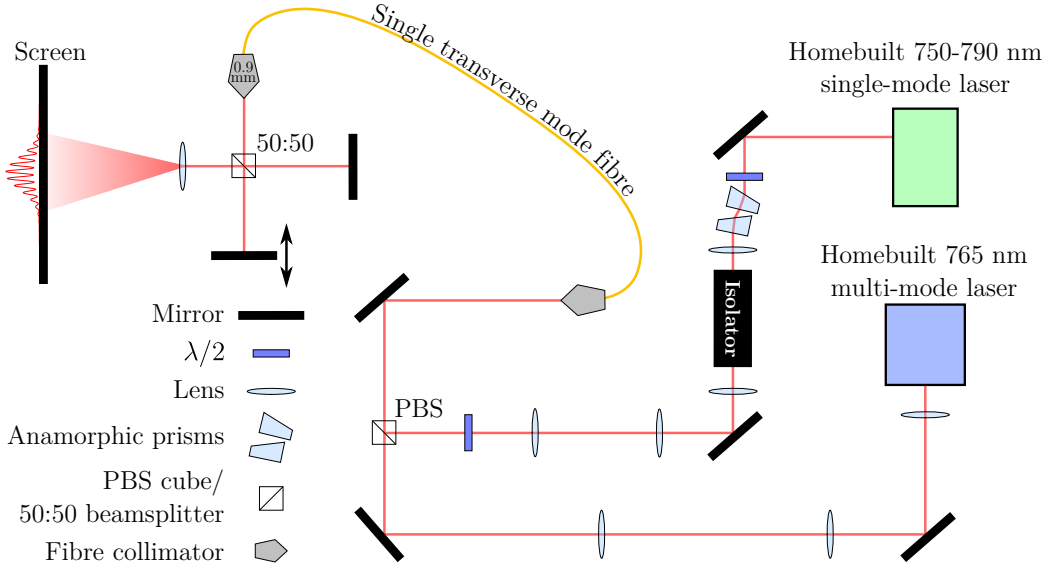

Figure 8.5: Schematic of the experimental apparatus used to measure the coherence length of the lasers that could generate an evanescent potential. One of the mirrors in the interferometer is slightly angled, resulting in fringes that are horizontally aligned.

[2] $\mathrm{sinc}(x) = \sin(x)/x$.

Measuring fringe visibility

The intensity pattern obtained due to the Michelson interferometer shown in figure 8.5 has a gaussian envelope with sinusoidal consecutive bright and dark fringes. We make the approximation that $\lambda \ll l_c$, in other words, $\mathcal{V}$ is essentially constant over one instance of a fringe pattern. With this assumption, it is possible to extract $\mathcal{V}$ from the curve by fitting the following function,

$$I(x) = I_0 \left[1 - \left(\frac{2\mathcal{V}}{1+\mathcal{V}}\right) \cos^2(kx + \phi)\right] \exp\left[-2\frac{(x-x_0)^2}{w^2}\right]. \tag{8.19}$$

As we have significantly increased the size of the beam with a lens (see figure 8.5), for the purposes of imaging, we are not interested in any of the terms in (8.19) other than extracting a value for $\mathcal{V}$, which doesn't change by expanding the beam.

We first measured the interference pattern due to the single-mode laser, as this should produce very clear fringes with $\mathcal{V} \sim 1$. All interference images were taken with a Panasonic NV DS27 camcorder set to night vision mode[3]. One of these images is shown in figure 8.6 (a) for a single-mode laser. The resulting interference pattern is very clear, with regularly spaced fringes. By integrating the column intensities of the image (a sum of the pixels in the vertical direction), we obtain the intensity distribution in figure 8.6 (b).

[3]This removes an infrared filter from the camcorder, resulting in it being very sensitive to infrared light.

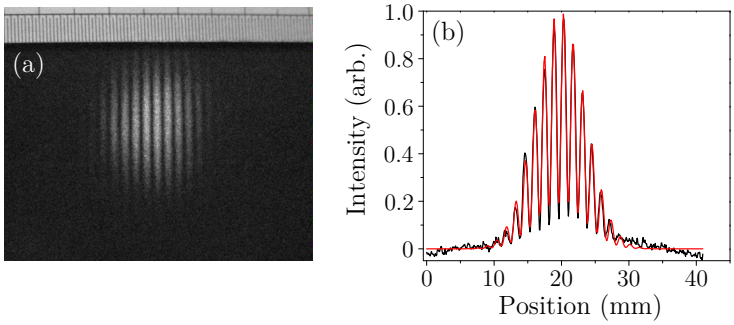

Figure 8.6: Measuring fringe visibility for the single-mode laser. (a) A camcorder image showing the intensity distribution due to an overlapping single-mode laser beam, showing clear sinusoidal fringing. (b) Summing the columns in the image results in the given distribution, with $\mathcal{V} = 0.675(8)$. We fit (8.19) to the data.

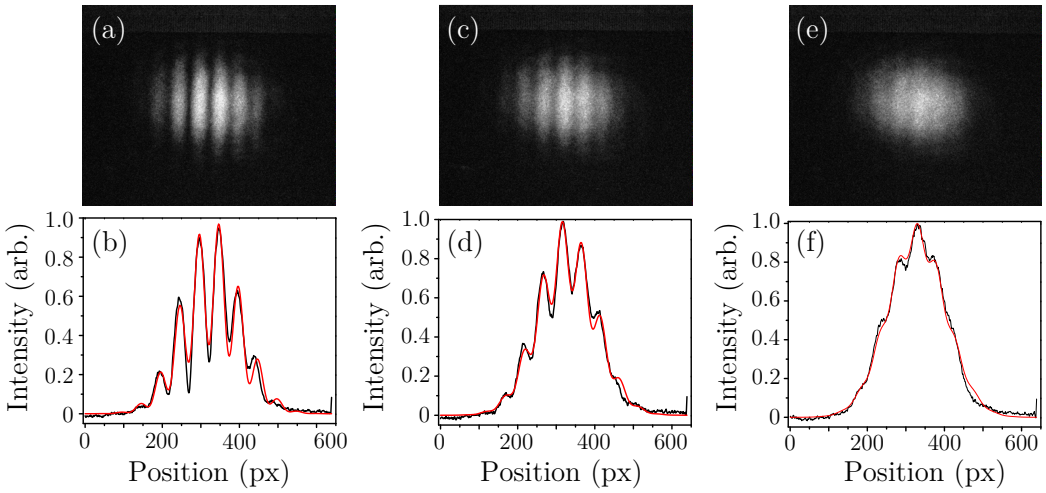

Figure 8.7: Measuring fringe visibility for the multi-mode laser. (a-b) The intensity distribution for a path difference of 0.00(5) mm. $\mathcal{V} = 0.48(5)$. (c-d) The intensity distribution for a path difference of 0.90(5) mm. $\mathcal{V} = 0.22(3)$. (e-f) The intensity distribution for a path difference of 0.70(5) mm. $\mathcal{V} = 0.07(3)$.

By fitting (8.19) to the data in figure 8.6 (b), we obtain a fringe visibility of $\mathcal{V} = 0.675(8)$, which is significantly lower than the expected value of 1. We attribute this lower value to scattered light and fringes that are not exactly vertical. This value of fringe visibility gives the signal-to-noise ratio of the measurement, setting an upper bound of what we can expect to measure for $\mathcal{V}$ with the multi-mode laser.

With the multi-mode laser we should expect to observe a strong dependence of fringe visibility with path difference. Figure 8.7 shows three expample intensity distributions for the multi-mode laser, with differing visibilities.

Fringe visibilities of $\mathcal{V} = 0.48(5)$, $\mathcal{V} = 0.22(3)$ and $\mathcal{V} = 0.07(3)$ were obtained from figure 8.7, showing the largest and smallest values of $\mathcal{V}$ during the entire investigation of the multi-mode laser.

Determining the coherence length

As stated earlier, when plotting $\mathcal{V}$ as a function of path difference we expect a pattern that has a shape not dissimilar to a |sinc| function. In an ideal scenario $\mathcal{V} = 1$ for a path difference of zero, however, we have not observed this, for reasons mentioned above. As a result, we have allowed the peak of the function to be scaled and fit to the data given in figure 8.8.

By fitting a sinc function to the curve in figure 8.8 and extracting the distance

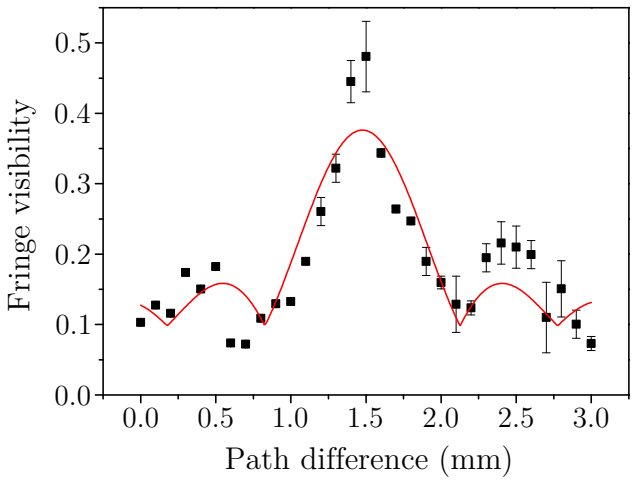

Figure 8.8: Determining the coherence length of the multi-mode laser. $\mathcal{V}$ is given as a function of path difference. The distance between the maximum and the first minimum in $\mathcal{V}$ is extracted from the fit—a variable height and frequency sinc function—and results in a measured coherence length of 0.65(3) mm.

between the peak and the first minimum, a coherence length of 0.65(3) mm is obtained. This is comparable to the 0.60(1) mm coherence length stated by the manufacturer of the diode. It should be noted, however, that although we approximate the spectral intensity distribution of the laser by a top-hat function, we find in section 8.3.3 that the distribution deviates from this ideal case.

Such a short coherence length should significantly reduce the probability of an undesireable corrugated evanescent potential being formed. However, it is unknown whether the single-mode laser would definitely produce such a potential. A disadvantage of using the multi-mode laser is that its wavelength is not tunable, as no grating is used in the setup in order that a wide spectral intensity distribution is maintained. The single-mode laser, which makes use of a grating, is widely tunable over a 40 nm range, from 750 nm to 790 nm. From figure 8.4 it is clear that being able to tune the wavelength of the laser would give a wider range of decay lengths to utilise, resulting in a greater flexibility in the evanescent barrier that could be formed.

8.3.3 Spectral intensity measurement

In section 8.3.2, it was assumed that the spectral intensity distribution of the multi-mode laser was a top hat function, in order to measure its coherence length. Here this distribution is explicitly measured, utilising a reflection

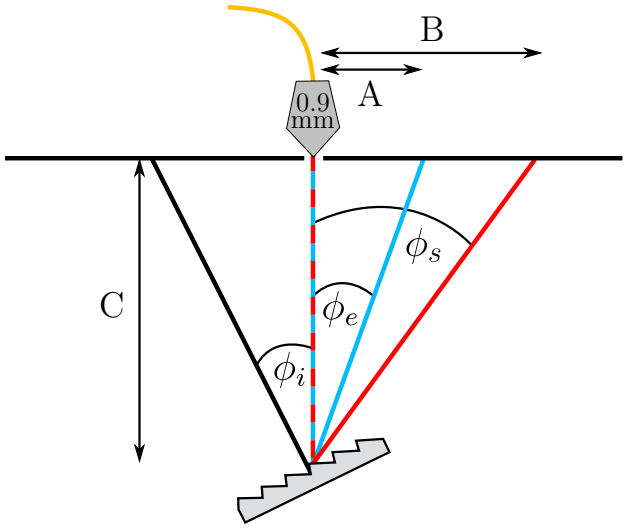

Figure 8.9: Schematic of the apparatus used to undertake a spectral intensity measurement of the beams that will be used to generate evanescent waves. Red line: The path of the tunable single-mode laser. Blue line: The path of the multi-mode laser. Black line: Indicates the direction normal to the reflection grating. Beams of different wavelengths are deflected by different angles, resulting in the separation $B - A$ of the two beams on a screen.

grating [310], and compared with that of its single-mode counterpart. The experimental apparatus and relevant parameters are shown in figure 8.9. The Michelson interferometer has been replaced by the grating, therefore, the fibre is still outcoupling both the single- and multi-mode lasers, as shown in figure 8.5. The tunable single-mode laser is represented by the red line and the multi-mode laser by the blue line. The angles given here are slightly different to those typically treated in modern textbooks[4] (*e.g.* [310]), resulting in a different, but parametrically equivalent diffraction equation below,

$$m\lambda = d\left[\sin\left(\phi_i\right) + \sin\left(\phi_r\right)\right], \tag{8.20}$$

where m is the diffraction order, $\phi_r = \phi_i + \phi_{e/s}$, ϕ_e is the deflected angle of the multi-mode laser and ϕ_s is the deflected angle of the single-mode laser. Instead of measuring ϕ_i, which is not straightforwardly accurate, we instead determine it from the deflection of a beam of known wavelength[5]. By transforming (8.20) it is possible to recast it in a more helpful form for

[4] $m\lambda = d\left[\sin\left(\phi_{\text{inc}}\right) - \sin\left(\phi_{\text{ref}}\right)\right]$, where ϕ_{inc} is the angle of incidence and ϕ_{ref} is the angle of reflection, both relative to the normal.

[5] We use a HighFinesse WS/5 Precision wavemeter to measure the wavelength of the laser.

the purpose of determining ϕ_i. Using a trignometric identity[6] (8.20) can be rewritten as

$$m\lambda_{s/e} = 2d\cos\left(\frac{\phi_{s/e}}{2}\right)\sin\left(\frac{\phi_{s/e}}{2}+\phi_i\right). \tag{8.21}$$

With $m = 1$, a simple rearrangement of 8.21 results in

$$\phi_i = \arcsin\left(\frac{\lambda_{s/e}}{2d\cos\left(\phi_{s/e}/2\right)}\right) - \frac{\phi_{s/e}}{2}. \tag{8.22}$$

Substituting $\lambda_s = 789.80(1)$ nm, $B = 116.3(1)$ mm, $C = 365(1)$ mm, $\phi_s = \arctan(B/C)$ and $d = 556$ nm[7] gives $\phi_i = 37.2(1)°$. Knowing the value of ϕ_i and taking $m = 1$ allows the calculation of λ_s and λ_e by simply measuring A and B. This distance-to-wavelength calibration is used throughout the remainder of this section to determine the spectral density profiles of the single- and multi-mode lasers.

We first investigated the broad nature of the gain medium in the multi-mode diode by setting its current to 800 mA, just above threshold (743 mA). The temperature of the diode was controlled via a thermo-electric cooler (TEC) and set to $T = 24.8$ °C. As a comparison, and to indicate the resolution of our spectrometer, we also couple the single-mode laser down the fibre. Taking the typical linewidth of a single-mode laser to be $\Gamma \sim 1$ MHz and $\lambda_c \sim 780$ nm, the linewidth can be expressed as a spread of wavelengths $\Delta\lambda$ around a central wavelength λ_c and can be calculated from

$$\Delta\lambda = c\left[\frac{\Gamma}{(c/\lambda_c)^2 - (\Gamma/2)^2}\right]. \tag{8.23}$$

The resulting spread is $\Delta\lambda \sim 2\times10^{-6}$ nm. The resolution of a grating spectrometer is expressed as [310]

$$R_{\text{spec}} = \frac{\lambda}{\lambda_0} = mN. \tag{8.24}$$

where λ_0 is the minimum resolvable wavelength and N is the number of grating lines illuminated by the laser. The grating that we use has 1800 lines/mm and the beams are coupled out from the fibre with a $1/e^2$ radius of 0.9 mm.

[6] $\sin(A)+\sin(B) = 2\sin\left(\frac{A+B}{2}\right)\cos\left(\frac{A-B}{2}\right)$ [311].
[7] The grating we use has 1800 lines/mm.

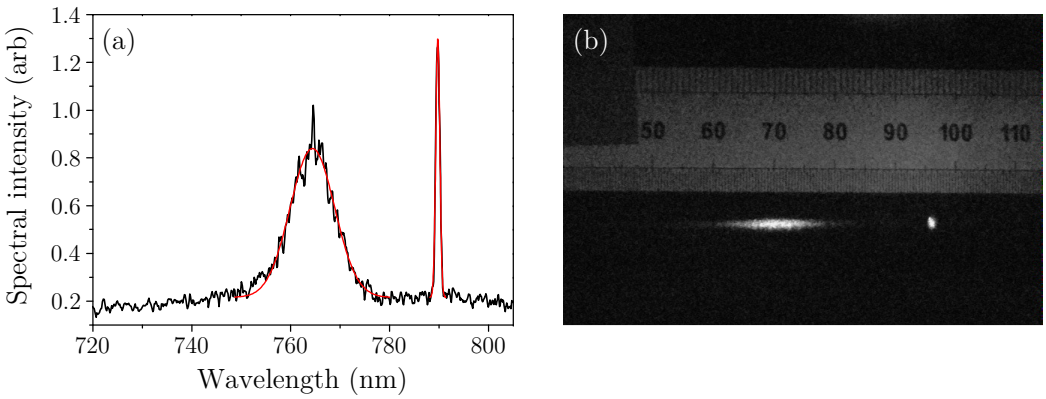

Figure 8.10: (a) The spectral intensity measurement of the multi-mode laser at $T = 24.8$ °C, with a single-mode laser at $\lambda = 789.80(1)$ nm as a reference. Columns are summed from (b) as a form of averaging to achieve this distribution. The $1/e^2$ radius of the single-mode distribution is 0.415(6) nm, resulting in a measured value of $\lambda_0 \sim 0.4$ nm. Taking this value as the error on all future measurements using the spectrometer, the multi-mode laser has a spectral intensity distribution with a $1/e^2$ radius of 4.6(4) nm. (b) A photograph of the spectrometer output on a screen.

Taking $N = 1.8 \times 1800 = 3240$, $m = 1$ and $\lambda = \lambda_c = 780$ nm results in $\lambda_0 = 0.2$ nm for a perfect reflection grating. Therefore, $\Delta\lambda \ll \lambda_0$, which means that it is impossible to resolve the spread of a single-mode laser using this spectrometer. In fact, the actual value of λ_0 is even larger than what is calculated here. In figure 8.10 we give the results of this first investigation.

The difference between the distributions of a single-mode laser and a multi-mode laser are very clear in figure 8.10, even with a measurement of the minimum resolvable wavelength of $\lambda_0 \sim 0.4$ nm. While the single-mode laser should ideally appear as a delta function, it is limited by the resolution of the spectrometer, as discussed above. The multi-mode laser displays a spread with a $1/e^2$ radius of 4.6(4) nm, close to its threshold current. Figure 8.11 shows how increasing the current to the diode reduces the spread and also gradually increases the peak wavelength of the laser.

We also varied the temperature of the diode and observed a tunable range of peak wavelengths from 763 nm to 767 nm. However, the reader is reminded that the single-mode laser presents a tunable range from 750 nm to 790 nm. Both of these lasers could potentially be used to generate an evanescent field, however, it is recommended that experiments are attempted initially with the multi-mode laser (to reduce the risk of a corrugated potential being formed). If a barrier is formed and solitary waves are seen to reflect, the single mode

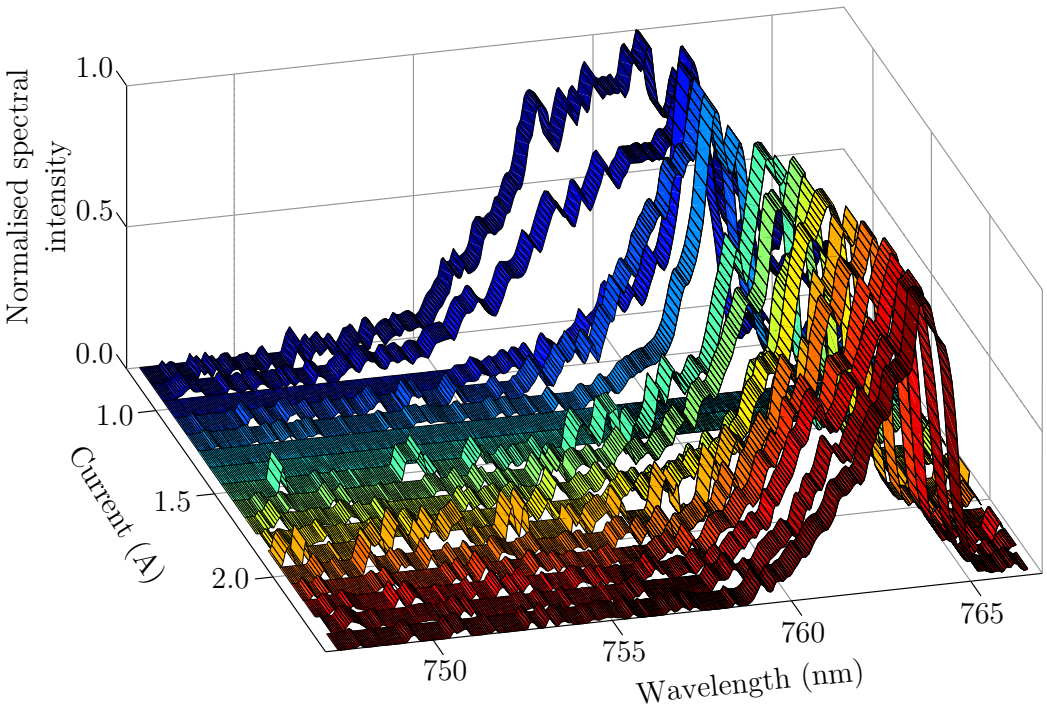

Figure 8.11: The spectral intensity of the multi-mode laser as a function of diode current. At low currents, close to the threshold current (743 mA), the laser displays a broad spectral intensity distribution, which narrows as the current increases. The peak wavelength of the distribution increases with the increasing current. At full power ($\sim$ 2 W) the $1/e^2$ radius of the distribution is $\sim$ 2 nm and centred at $\sim$ 764 nm. It has become asymmetric, quickly rising from 765 nm to 764 nm and tailing off from 764 nm to 759 nm.

laser could also be investigated, as being able to tune the wavelength adds a greater flexibility to the experimental apparatus.

8.4 Combining the evanescent and surface potentials

As a final investigation, we combine the theory of sections 8.2.2 and 8.3.1 and explore the parameter space available in our experiment in the context of all that has been discussed above. The range of available barrier heights and positions will be analysed as a function of laser power, wavelength and incident angle.

In figure 8.12 (a) the evanescent (black line), surface (green line) and combined (red line) potentials are shown as a function of distance from the sur-

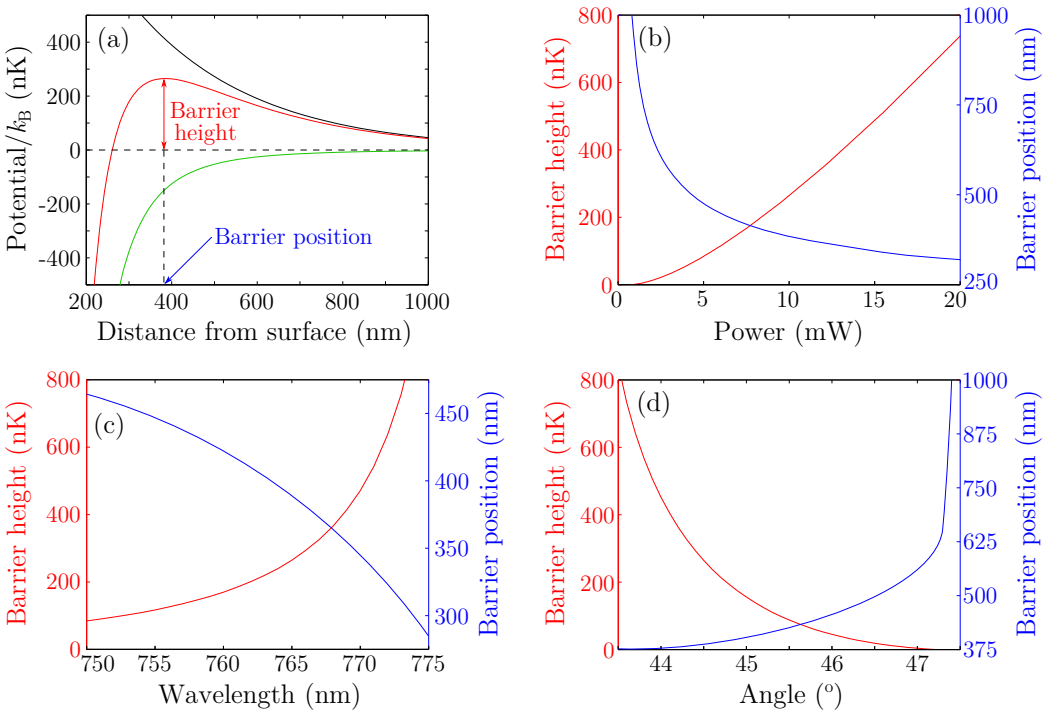

Figure 8.12: The potential formed by the combination of the atom–surface and evanescent potentials. (a) The evanescent (black line), surface (green line) and combined (red line) potentials with $\lambda = 765$ nm, $\theta_i = 44.5°$, $P = 10$ mW and $w = 200$ μm. The dependence of barrier height and barrier position on power, wavelength and angle are given in (b-d). (b) Barrier height and position as a function of laser power for $\lambda = 765$ nm, $\theta_i = 44.5°$ and $w = 200$ μm. (c) Barrier height and position as a function of laser wavelength for $\theta_i = 44.5°$, $P = 10$ mW and $w = 200$ μm. (d) Barrier height and position as a function of laser angle of incidence for $\lambda = 765$ nm, $P = 10$ mW and $w = 200$ μm.

face of the prism. For this plot $\lambda = 765$ nm, $\theta_i = 44.5°$, $P = 10$ mW and $w = 200$ μm, in order to create a fairly constant potential in the radial direction of the waveguide. The waist is kept constant at $w = 200$ μm for the remainder of this chapter. The two important quantities that are focussed on are barrier height and position. The height can be compared with the kinetic energy of an incoming solitary wave in order to predict when classical reflection is expected. The position indicates the closest distance that a solitary wave can reach, relative to the surface, and still reflect classically.

In figure 8.12 (b) the barrier height and position is given as a function of laser power where $\lambda = 765$ nm and $\theta_i = 44.5°$. For a power as small as 20 mW it is possible to create barriers that have a height in the range 0-1 μK and a position ranging from 250 nm to ~ 1 μm. Taking the axial trap frequency of the waveguide to be $\omega_x = 2\pi \times 1.16$ Hz (see section 6.6.3) and centering the

minimum at the barrier results in the following simple expression to calculate the offset p_x required to just reach the top of the barrier,

$$p_x = \sqrt{\frac{2k_{\mathrm{B}}E_{\mathrm{B}} \times 10^{-3}}{m\omega_x^2}}, \tag{8.25}$$

where E_{B} is the height of the barrier in nK and p_x is the initial offset of the solitary wave from the barrier in mm. Substituting $E_{\mathrm{B}} = 400$ nK, $m = 1.41 \times 10^{-25}$ kg and $\omega_x = 2\pi \times 1.16$ Hz into (8.25) results in $p_x = 1.2$ mm. Increasing the barrier height to 800 nK changes the position to $p_x = 1.7$ mm. Reducing the barrier height to as little as 25 nK (a power of ~ 2 mW) brings the initial position to $p_x = 0.3$ mm. From these calculations we can see that even for very low barriers, the initial position of the solitary wave is significantly larger than the width of the barrier, which is < 1 μm. The barrier width is, however, comparable to the size of the soliton itself, which is ~ 2.3 μm (see section 2.5.2). Therefore, it can be concluded that the solitary wave will have to travel a distance $> 150 \times$ its width to interact with a barrier of comparable size, repeating a similar scenario to those observed originally by John Scott Russell.

Figure 8.12 (c) gives the dependence of barrier height and position on the wavelength of the laser, indicating the potential benefits of using a widely tunable laser diode, where $\theta_i = 44.5°$ and $P = 10$ mW. The significant change in the polarisability of Rb close to 780 nm contributes to a dramatic increase in barrier height and change in position.

Finally, figure 8.12 (d) gives the dependence of barrier height and position on the angle of incidence of the laser for $\lambda = 765$ nm and $P = 10$ mW. A wide range of barrier heights and positions are accessable, however, this is confined within a small region of angles—around 3.5°. It is clear that the most important aspect to be controlled and characterised in the experiment is the angle of incidence of the laser generating the evanescent potential.

In order that a broader range of the parameter space could be explored, the height of the barrier is given as a function of power and angle of incidence in figure 8.13 (a) and power and wavelength in figure 8.13 (b). The grey areas indicate regions where no barrier is formed and the colour map gives the height of the barrier.

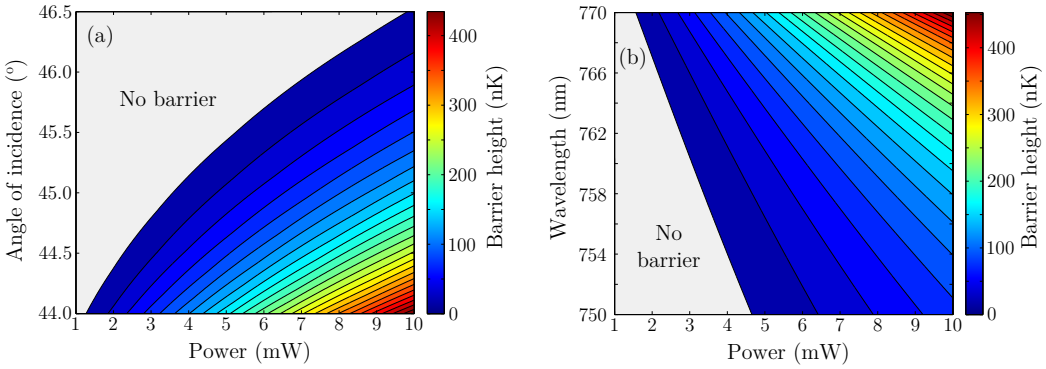

Figure 8.13: The height of the barrier formed when the varying evanescent potential is combined with the atom–surface potential in Rb. (a) Barrier height as a function of laser angle of incidence and power at $\lambda = 765$ nm. (b) Barrier height as a function of laser wavelength and power at $\theta_i = 44.5°$.

Once again, the importance of precisely choosing an angle is clear from figure 8.13 (a). Once the angle has been carefully set, it is possible to be very flexible on the power of the laser beam and still generate a barrier from which to reflect classically.

As a final point, the sharp change in potential due to the presence of the barrier may permit the observation of quantum reflection (see section 2.5.1, for an analysis of approximately similar gaussian potential barriers and wells). If classical and quantum reflection is observed from the barrier, the next stage will be to turn off the evanescent field and attempt to observe quantum reflection from the pure atom–surface potential. Observing such behaviour from a solitary wave would be a significant step in the field of atomic physics.

8.5 Conclusion

In this chapter the necessary theory was presented in order to model the combined potential due to attractive atom–surface interactions with the addition of a repulsive evanescent field. Experimental investigations were undertaken to determine the coherence length and spectral intensity distribution of a multi-mode laser diode that may be used to generate the evanescent field. Towards the end of the chapter, combined potentials were analysed in order to determine the heights and positions of barriers formed due to the atom–surface and evanescent potentials. It was shown that barriers could be generated with heights as great as 800 nK for laser powers as little as

20 mW, which corresponds to a solitary wave with offset $p_x \sim 1.7$ μm in a $\omega_x = 2\pi \times 1.16$ Hz waveguide being able to just reach the top of the barrier.

We conclude that reasonable barrier heights can be generated as long as the experimentalist is very careful in setting the angle of incidence of the evanescent laser. Once the laser has been carefully aligned, a broad parameter space is available for exploration.

Chapter 9

Conclusion

In this thesis we have demonstrated the formation and dynamics of a ^{85}Rb Bose-Einstein condensate and the subsequent solitary wave that can be formed when the interparticle interactions are tuned to be attractive.

In chapter 2 we reviewed the necessary theory to understand the formation and behaviour of an attractive BEC. We discussed the importance of trap geometry and number of spatial dimensions on the stability of an attractive condensate and gave a brief introduction to the beyond mean field approach. We also presented a review of some of the most recent theoretical results relating to the dynamics of bright solitons and solitary waves, from the perspective of an experimentalist. Finally we explored some of the expected behaviour and parameter regimes potentially observable in this experiment.

Details of the apparatus and diagnostics used in this experiment were given in chapter 3, while the development and improvement of our experimental control system—built using LabVIEW—were given in chapter 4.

Demonstration of the merging of atomic gases of ^{85}Rb and ^{87}Rb was given in chapter 5. A straightforward one-dimensional model was shown to be sufficient in explaining the reason for good or poor merging, resulting in our ability to optimise the merging process. Potential applications were shown to be the formation of multi-isotopic mixtures and the creation of the initial state required to begin sympathetic cooling.

The formation of a ^{85}Rb BEC, via direct evaporation, and a solitary wave was presented in chapter 6, with a discussion of the differences between cooling ^{85}Rb and ^{87}Rb. The importance of the 155 G ^{85}Rb Feshbach resonance was

discussed in the context of efficiently cooling towards degeneracy. Examples of experiments undertaken to demonstrate the tunable nature of a ^{85}Rb BEC were given. Following this, we presented our method for aligning and loading the one-dimensional waveguide, in which we later formed solitary waves. We presented data showing the propagation of a solitary wave, in comparison with a repulsive condensate, with a clear indication of collapse occurring. We also touched upon work undertaken towards [72] that showed the particle-like behaviour of a solitary wave incident upon a wide repulsive barrier.

In the last couple of chapters (part IV) we discussed the characterisation and preparation of equipment that we hope to eventually use to demonstrate quantum reflection of a soliton from a narrow repusive barrier (chapter 7) and from a dielectric surface (chapter 8).

9.1 Outlook

This experiment has the potential to explore a vast array of interesting solitary wave phenomena. We refer the reader to table 2.1, which lists all of these interesting phenomena, with the relevant references, which could be investigated at a later time in this experiment.

There are three key experiments that would be natural steps forward from the research undertaken during this thesis: observing quantum reflection from a narrow attractive barrier, generating counterpropagating solitary waves through Feshbach tuning and observing quantum reflection from a surface. The work undertaken in chapter 2 has contributed to the understanding of each of these phenomena and has attempted to quantify some of the expected behaviour. The experimental apparatus (chapter 3) in combination with the control hardware and software (chapter 4) has created a system for which observing the mentioned phenomena is increasingly likely. The evaporation to BEC and formation of solitary waves (chapter 6) has led to an analysis of narrow-barrier (chapter 7) and atom–surface interactions (chapter 8) antecedent to the potential future observations of quantum reflection from a barrier and surface. This thesis has provided the foundation to enable a future researcher to undertake such exciting investigations using this experimental apparatus.

Part V

Appendices and bibliography

Appendix A

Configuration of data sent to the FPGA in the new system

Data sent from the program to the FPGA card is done via a Direct Memory Access (DMA) transfer. In this program data is sent in clumps of unsigned 64-bit integers (U64). This document explains how the sequence is split up into U64 integers.

A.1 Elements and their data requirements

A lot of data must be sent to the FPGA card for each time step that the program produces. It is necessary to identify all this data and assign an appropriate number of bits to each element. Table A.1 lists this data.

A total of 13 U64 integers must be sent to the FPGA card in order to transfer all the data indentified in table A.1.

A.2 Assignment of bits

We must now assign the elements to specific bits that are sent to the FPGA card. The data is sent serially via 13 U64 integers which are repeated for each time step. The structure of the 13 U64 integers is given in the following form: [**Name, xU64**], where x is the number of the U64 grouping, and [main element name, sub-element name (bit assignment of xU64), options].

Main element name	Sub-element name	Data requirement (bits)
Time	Time unit (ms, ticks)	1
	Time	32
Trigger	Analogue/digital?	1
	Trigger?	1
	Channel	4 (upto 16 inputs)
	Voltage	16
GPIB	On/off	1
	Routine	7 (upto 128 unique GPIB routines)
Last step bit	N/A	1
Fast digital outputs	N/A	56 (56 channels)
Slow digital outputs	N/A	48 (48 channels)
Fast analogue outputs	N/A	128 (8 channels, 16-bit each)
Slow analogue outputs	N/A	512 (32 channels, 16-bit each)
Total		**808 bits ≡ 12.625 U64s**

Table A.1: Elements of data sent to the FPGA and the number of bits assigned to each element. All the data is then distributed between 13 unsigned 64-bit integers to be sent to the FPGA card via a DMA transfer. Note: The *Last step bit* is used to indicate to the FPGA when the last step has been reached and it should stop running.

1. **Header data, 1U64**
   (a) Time, Time unit (1), 0=ticks/1=ms
   (b) Time, Time (2-33)
   (c) Trigger, Analogue/Digital? (34), 0=analogue/1=digital
   (d) Trigger, Trigger? (35)
   (e) Trigger, Channel (36-39)
   (f) Trigger, Voltage (40-55)
   (g) GPIB, On/off (56)
   (h) GPIB, Routine (57-63)
   (i) Last step bit (64)
2. **Fast digital outputs, 2U64**
   (a) Fast digital outputs (1-56)
   (b) Free (57-64)
3. **Slow digital outputs, 3U64**
   (a) Slow digital outputs (1-48)
   (b) Free (49-64)

4. **Fast analogue outputs, 4U64-5U64**

   (a) Fast analogue outputs (4U64 1-64, 5U64 1-64)

5. **Slow analogue outputs, 6U64-13U64**

   (a) Slow analogue outputs (6U64 1-64, 7U64 1-64, 8U64 1-64, 9U64 1-64, 10U64 1-64, 11U64 1-64, 12U64 1-64, 13U64 1-64)

Bibliography

[1] J. F. Annett, *Superconductivity, Superfluids and Condensates* (Oxford University Press, 2004). 1

[2] S. N. Bose, *Plancks Gesetz und Lichtquantenhypothese*, Z. Phys. A **26**, 178 (1924). 1

[3] A. Einstein, *Quantentheorie des einatomigen idealen Gases*, Sitzber. Kgl. Preus. Akad. Wiss. **22**, 261 (1924).

[4] A. Einstein, *Quantentheorie des einatomigen idealen Gases*, Sitzber. Kgl. Preus. Akad. Wiss. **23**, 3 (1925). 1

[5] C. G. Townsend *et al.*, *Phase-space density in the magneto-optical trap*, Phys. Rev. A **52**, 1423 (1995). 1

[6] C. Pethick and H. Smith, *Bose-Einstein Condensates in Dilute Gases* (Cambridge University Press, 2002). 1, 2, 15

[7] M. H. Anderson, J. R. Ensher, M. R. Matthews, C. E. Wieman, and E. A. Cornell, *Observation of Bose-Einstein condensation in a dilute atomic vapor*, Science **269**, 198 (1995). 2

[8] K. B. Davis *et al.*, *Bose-Einstein condensation in a gas of sodium atoms*, Phys. Rev. Lett. **75**, 3969 (1995). 2

[9] C. C. Bradley, C. A. Sackett, J. J. Tollett, and R. G. Hulet, *Evidence of Bose-Einstein Condensation in an Atomic Gas with Attractive Interactions*, Phys. Rev. Lett. **75**, 1687 (1995). 2

[10] C. C. Bradley, C. A. Sackett, and R. G. Hulet, *Bose-Einstein Condensation of Lithium: Observation of Limited Condensate Number*, Phys. Rev. Lett. **78**, 985 (1997). 2

[11] C. C. Bradley, C. A. Sackett, J. J. Tollett, and R. G. Hulet, *Evidence of Bose-Einstein Condensation in an Atomic Gas with Attractive Interactions [Phys. Rev. Lett. 75, 1687 (1995)]*, Phys. Rev. Lett. **79**, 1170 (1997). 2

[12] D. G. Fried *et al.*, *Bose-Einstein Condensation of Atomic Hydrogen*, Phys. Rev. Lett. **81**, 3811 (1998). 2

[13] A. Robert *et al.*, *A Bose-Einstein Condensate of Metastable Atoms*, Science **292**, 461 (2001). 2

[14] G. Modugno *et al.*, *Bose-Einstein Condensation of Potassium Atoms by Sympathetic Cooling*, Science **294**, 1320 (2001). 2

[15] S. L. Cornish, N. R. Claussen, J. L. Roberts, E. A. Cornell, and C. E. Wieman, *Stable* ^{85}Rb *Bose-Einstein Condensates with Widely Tunable Interactions*, Phys. Rev. Lett. **85**, 1795 (2000). 2, 113, 139, 141

[16] M. Greiner, C. A. Regal, and D. S. Jin, *Emergence of a molecular Bose-Einstein condensate from a Fermi gas*, Nature (London) **426**, 537 (2003). 2

[17] S. Jochim *et al.*, *Bose-Einstein Condensation of Molecules*, Science **302**, 2101 (2003). 2

[18] UltraCold Atom News, *Observations: News Reports*, Accessed: 14 June 2013, URL: `http://ucan.physics.utoronto.ca/News`. 2

[19] M. R. Andrews *et al.*, *Observation of Interference Between Two Bose Condensates*, Science **275**, 637 (1997). 2, 33

[20] M. R. Matthews *et al.*, *Vortices in a Bose-Einstein Condensate*, Phys. Rev. Lett. **83**, 2498 (1999).

[21] I. Bloch, T. W. Hänsch, and T. Esslinger, *Measurement of the spatial coherence of a trapped Bose gas at the phase transition*, Nature (London) **403**, 166 (2000).

[22] K. W. Madison, F. Chevy, W. Wohlleben, and J. Dalibard, *Vortex Formation in a Stirred Bose-Einstein Condensate*, Phys. Rev. Lett. **84**, 806 (2000).

[23] J. R. Abo-Shaeer, C. Raman, J. M. Vogels, and W. Ketterle, *Observation of Vortex Lattices in Bose-Einstein Condensates*, Science **292**, 476 (2001).

[24] T. Bourdel *et al.*, *Experimental Study of the BEC-BCS Crossover Region in Lithium 6*, Phys. Rev. Lett. **93**, 050401 (2004).

[25] S. Burger *et al.*, *Dark Solitons in Bose-Einstein Condensates*, Phys. Rev. Lett. **83**, 5198 (1999). 5

[26] E. A. Donley *et al.*, *Dynamics of collapsing and exploding Bose-Einstein condensates*, Nature (London) **412**, 295 (2001). 5, 26, 48, 113, 154

[27] K. E. Strecker, G. B. Partridge, A. G. Truscott, and R. G. Hulet, *Formation and propagation of matter-wave soliton trains*, Nature (London) **417**, 150 (2002). 5, 7, 24, 48, 64

[28] L. Khaykovich *et al.*, *Formation of a Matter-Wave Bright Soliton*, Science **296**, 1290 (2002). 2, 5, 23, 65

[29] S. L. Cornish *et al.*, *Quantum reflection of bright matter-wave solitons*, Physica D **238**, 1299 (2009). 2, 9, 46, 48

[30] L. Vestergaard Hau, S. E. Harris, Z. Dutton, and C. H. Behroozi, *Light speed reduction to 17 metres per second in an ultracold atomic gas*, Nature (London) **397**, 594 (1999). 2

[31] J. M. Gerton, D. Strekalov, I. Prodan, and R. G. Hulet, *Direct observation of growth and collapse of a Bose-Einstein condensate with attractive interactions*, Nature (London) **408**, 692 (2000). 2, 26

[32] J. Scott Russell, *Report on waves*, Fourteenth meeting of the British Association for the Advancement of Science (1844). 3

[33] J. W. Miles, *The Korteweg-de Vries equation: a historical essay*, Journal of Fluid Mechanics **106**, 131 (1981). 4

[34] D. J. Korteweg and G. de Vries, *On the Change of Form of Long Waves Advancing in a Rectangular Canal, and on a New Type of Long Stationary Waves*, Phil. Mag. **39**, 422 (1895). 4

[35] E. Infeld and G. Rowlands, *Nonlinear waves, solitons and chaos* (Cambridge University Press, 1990). 4

[36] N. J. Zabusky and M. D. Kruskal, *Interaction of ''Solitons'' in a Collisionless Plasma and the Recurrence of Initial States*, Phys. Rev. Lett. **15**, 240 (1965). 4

[37] C. S. Gardner, J. M. Greene, M. D. Kruskal, and R. M. Miura, *Method for Solving the Korteweg-deVries Equation*, Phys. Rev. Lett. **19**, 1095 (1967). 4

[38] V. E. Zakharov and A. B. Shabat, *Exact Theory of Two-dimensional Self-focusing and One-dimensional Self-modulation of Waves in Nonlinear Media*, Sov. J. Exp. Theor. Phys. **34**, 62 (1972). 4

[39] A. D. Martin, C. S. Adams, and S. A. Gardiner, *Bright Matter-Wave Soliton Collisions in a Harmonic Trap: Regular and Chaotic Dynamics*, Phys. Rev. Lett. **98**, 020402 (2007). 4

[40] A. Hasegawa and F. Tappert, *Transmission of stationary nonlinear optical pulses in dispersive dielectric fibers. I. Anomalous dispersion*, Appl. Phys. Lett. **23**, 142 (1973). 5

[41] J. K. Kjems and M. Steiner, *Evidence for Soliton Modes in the One-Dimensional Ferromagnet* $CsNiF_3$, Phys. Rev. Lett. **41**, 1137 (1978). 5

[42] L. F. Mollenauer, R. H. Stolen, and J. P. Gordon, *Experimental Observation of Picosecond Pulse Narrowing and Solitons in Optical Fibers*, Phys. Rev. Lett. **45**, 1095 (1980).

[43] L. F. Mollenauer and R. H. Stolen, *The soliton laser*, Opt. Lett. **9**, 13 (1984).

[44] D. A. Kurtze and D. C. Hong, *Traffic jams, granular flow, and soliton selection*, Phys. Rev. E **52**, 218 (1995).

[45] C. Cattell, J. Crumley, J. Dombeck, J. R. Wygant, and F. S. Mozer, *Polar observations of solitary waves at the Earth's magnetopause*, Geophys. Res. Lett. **29**, 050000 (2002).

[46] K. Stasiewicz *et al.*, *Slow Magnetosonic Solitons Detected by the Cluster Spacecraft*, Phys. Rev. Lett. **90**, 085002 (2003).

[47] D. Y. Tang, L. M. Zhao, and B. Zhao, *Soliton collapse and bunched noise-like pulse generation in a passively mode-locked fiber ring laser*, Opt. Exp. **13**, 2289 (2005).

[48] T. Heimburg and A. D. Jackson, *On soliton propagation in biomembranes and nerves*, Proc. Natl. Acad. Sci. USA **102**, 9790 (2005).

[49] T. Soomere and J. Engelbrecht, *Weakly two-dimensional interaction of solitons in shallow water*, Eur. J. Mech. B Fluids **25**, 636 (2006).

[50] V. M. Pérez-García, G. F. Calvo, J. Belmonte-Beitia, D. Diego, and L. Pérez-Romasanta, *Bright solitary waves in malignant gliomas*, Phys. Rev. E **84**, 021921 (2011).

[51] M. J. Ablowitz and D. E. Baldwin, *Nonlinear shallow ocean-wave soliton interactions on flat beaches*, Phys. Rev. E **86**, 036305 (2012). 5

[52] J. Denschlag *et al.*, *Generating Solitons by Phase Engineering of a Bose-Einstein Condensate*, Science **287**, 97 (2000). 5

[53] B. P. Anderson *et al.*, *Watching Dark Solitons Decay into Vortex Rings in a Bose-Einstein Condensate*, Phys. Rev. Lett. **86**, 2926 (2001).

[54] C. Becker *et al.*, *Oscillations and interactions of dark and dark bright solitons in Bose Einstein condensates*, Nat. Phys. **4**, 496 (2008). 5

[55] J. L. Roberts *et al.*, *Controlled Collapse of a Bose-Einstein Condensate*, Phys. Rev. Lett. **86**, 4211 (2001). 5, 6, 26, 48, 113

[56] S. L. Cornish, S. T. Thompson, and C. E. Wieman, *Formation of Bright Matter-Wave Solitons during the Collapse of Attractive Bose-Einstein Condensates*, Phys. Rev. Lett. **96**, 170401 (2006). 5, 6, 7, 24, 48, 64, 113

[57] A. D. Martin, C. S. Adams, and S. A. Gardiner, *Bright solitary-matter-wave collisions in a harmonic trap: Regimes of solitonlike behavior*, Phys. Rev. A **77**, 013620 (2008). 5, 7, 24, 25, 48

[58] N. G. Parker, A. M. Martin, S. L. Cornish, and C. S. Adams, *Collisions of bright solitary matter waves*, J. Phys. B: At. Mol. Opt. Phys. **41**, 045303 (2008). 5, 7, 24, 25, 48

[59] S. L. Cornish and C. S. Adams, *Bright matter-wave solitons: formation, dynamics and quantum reflection*, Accessed: 8 January 2013, URL: `http://gow.epsrc.ac.uk/NGBOViewGrant.aspx?GrantRef=EP/F002068/1`. 6

[60] R. Eisberg and R. Resnick, *Quantum Physics of Atoms, Molecules, Solids, Nuclei, and Particles* (John Wiley & Sons, 1985). 8

[61] T. A. Pasquini *et al.*, *Atom optics with Bose Einstein condensates: quantum reflection and interferometry*, J. Phys. Conf. Ser. **19**, 139 (2005). 8

[62] A. Anderson *et al.*, *Reflection of thermal Cs atoms grazing a polished glass surface*, Phys. Rev. A **34**, 3513 (1986). 8

[63] F. Shimizu, *Specular Reflection of Very Slow Metastable Neon Atoms from a Solid Surface*, Phys. Rev. Lett. **86**, 987 (2001).

[64] H. Oberst, D. Kouznetsov, K. Shimizu, J. Fujita, and F. Shimizu, *Fresnel Diffraction Mirror for an Atomic Wave*, Phys. Rev. Lett **94**, 013203 (2005). 8

[65] T. A. Pasquini *et al.*, *Quantum Reflection from a Solid Surface at Normal Incidence*, Phys. Rev. Lett. **93**, 223201 (2004). 8, 46

[66] T. A. Pasquini *et al.*, *Low Velocity Quantum Reflection of Bose-Einstein Condensates*, Phys. Rev. Lett. **97**, 093201 (2006). 8

[67] H. Bender, P. W. Courteille, C. Marzok, C. Zimmermann, and S. Slama, *Direct Measurement of Intermediate-Range Casimir-Polder Potentials*, Phys. Rev. Lett. **104**, 083201 (2010). 8, 46, 48, 187

[68] D. M. Harber, J. M. Obrecht, J. M. McGuirk, and E. A. Cornell, *Measurement of the Casimir-Polder force through center-of-mass oscillations of a Bose-Einstein condensate*, Phys. Rev. A **72**, 033610 (2005). 8

[69] S. Händel, *Experiments on ultracold quantum gases of* ^{85}Rb *and* ^{87}Rb, PhD thesis, Durham University, 2011. 9, 68, 73, 74, 174

[70] T. P. Wiles, *Bright soliton formation and dynamics in atomic Bose-Einstein condensates*, Master's thesis, Durham University, 2009. 10

[71] S. Händel *et al.*, *Magnetic merging of ultracold atomic gases of* ^{85}Rb *and* ^{87}Rb, Phys. Rev. A **83**, 053633 (2011). 10, 11

[72] A. L. Marchant, *Formation of bright solitary matter-waves*, PhD thesis, Durham University, 2012. 10, 27, 48, 68, 74, 78, 146, 149, 150, 151, 153, 154, 162, 204

[73] S. L. Cornish and J. M. Hutson, *A Quantum Gas of Ultracold Polar Molecules*, Accessed: 27 February 2013, URL: `http://gow.epsrc.ac.uk/NGBOViewGrant.aspx?GrantRef=EP/H003363/1`. 10

[74] M. P. Köppinger, P. K. Molony, D. J. McCarron, and S. L. Cornish, *RbCs: Ultracold atomic mixtures and molecules*, Accessed: 27 February 2013, URL: `http://massey.dur.ac.uk/research/2spec/2spec.html`.

[75] E. A. Hinds *et al.*, *MMQA: MicroKelvin Molecules in a Quantum Array*, Accessed: 27 February 2013, URL: `http://gow.epsrc.ac.uk/NGBOViewGrant.aspx?GrantRef=EP/I012044/1`.

[76] K. L. Butler *et al.*, *YbCs - MicroKelvin Molecules in a Quantum Array*, Accessed: 27 February 2013, URL: `http://massey/research/YbCs/YbCs.html`. 10

[77] A. L. Marchant, S. Händel, T. P. Wiles, S. A. Hopkins, and S. L. Cornish, *Guided transport of ultracold gases of rubidium up to a room-temperature dielectric surface*, New J. Phys. **13**, 125003 (2011). 11, 46, 73

[78] S. Händel, A. L. Marchant, T. P. Wiles, S. A. Hopkins, and S. L. Cornish, *Magnetic transport apparatus for the production of ultracold atomic gases in the vicinity of a dielectric surface*, Rev. Sci. Instrum. **83**, 013105 (2012). 11, 46, 68

[79] A. L. Marchant, S. Händel, S. A. Hopkins, T. P. Wiles, and S. L. Cornish, *Bose-Einstein condensation of* ^{85}Rb *by direct evaporation in*

an optical dipole trap, Phys. Rev. A **85**, 053647 (2012). 11, 137, 140, 141, 146, 149

[80] A. L. Marchant *et al.*, *Controlled formation and reflection of a bright solitary matter-wave*, Nat. Commun. **4**, 1865 (2013). 12, 64

[81] N. P. Proukakis and B. Jackson, *PHD TUTORIAL: Finite-temperature models of Bose Einstein condensation*, J. Phys. B: At. Mol. Opt. Phys. **41**, 203002 (2008). 14, 15, 18, 19, 20

[82] N. N. Bogoliubov, *On the theory of superfluidity*, J. Phys. (USSR) **11**, 23 (1947). 15

[83] F. Dalfovo, S. Giorgini, L. P. Pitaevskii, and S. Stringari, *Theory of Bose-Einstein condensation in trapped gases*, Rev. Mod. Phys. **71**, 463 (1999). 15, 154

[84] Y. Castin, *Bose-Einstein Condensates in Atomic Gases: Simple Theoretical Results*, in *Coherent atomic matter waves*, edited by R. Kaiser, C. Westbrook, and F. David, volume 72 of *Les Houches - Ecole d'Ete de Physique Theorique*, pp. 1–136, Springer Berlin Heidelberg, 2001. 16

[85] F. S. Levin, *An Introduction to Quantum Theory* (Cambridge University Press, 2002). 18, 21

[86] E. H. Lieb, R. Seiringer, and J. Yngvason, *Justification of c-Number Substitutions in Bosonic Hamiltonians*, Phys. Rev. Lett. **94**, 080401 (2005). 19

[87] L. P. Pitaevskii, *Vortex lines in an imperfect Bose gas*, Zh. Eksp. Teor. Fiz. **40**, 646 (1961). 19

[88] E. P. Gross, *Structure of quantized vortex*, Nuovo Cimento **20**, 454 (1961). 19

[89] A. L. Fetter, *Nonuniform states of an imperfect bose gas*, Ann. Phys. **70**, 67 (1972). 19

[90] V. V. Goldman, I. F. Silvera, and A. J. Leggett, *Atomic hydrogen in an inhomogeneous magnetic field: Density profile and Bose-Einstein condensation*, Phys. Rev. B **24**, 2870 (1981).

[91] D. A. Huse and E. D. Siggia, *The density distribution of a weakly interacting bose gas in an external potential*, J. Low Temp. Phys. **46**, 137 (1982).

[92] P. Dörre, H. Haug, and D. B. Tran Thoai, *Condensate theory versus pairing theory for degenerate Bose systems*, J. Low Temp. Phys. **35**, 465 (1979).

[93] A. Griffin, *Conserving and gapless approximations for an inhomogeneous Bose gas at finite temperatures*, Phys. Rev. B **53**, 9341 (1996).

[94] D. A. W. Hutchinson *et al.*, *Gapless mean-field theory of Bose-Einstein condensates*, J. Phys. B: At. Mol. Opt. Phys. **33**, 3825 (2000).

[95] M. Rusch and K. Burnett, *Mean-field theory for excitations of trapped Bose condensates at finite temperatures*, Phys. Rev. A **59**, 3851 (1999).

[96] R. Walser, J. Williams, J. Cooper, and M. Holland, *Quantum kinetic theory for a condensed bosonic gas*, Phys. Rev. A **59**, 3878 (1999).

[97] T. R. Kirkpatrick and J. R. Dorfman, *Transport theory for a weakly interacting condensed Bose gas*, Phys. Rev. A **28**, 2576 (1983).

[98] S. A. Morgan, *A gapless theory of Bose-Einstein condensation in dilute gases at finite temperature*, J. Phys. B: At. Mol. Opt. Phys. **33**, 3847 (2000).

[99] Y. Castin and R. Dum, *Low-temperature Bose-Einstein condensates in time-dependent traps: Beyond the U(1) symmetry-breaking approach*, Phys. Rev. A **57**, 3008 (1998). 19

[100] L. P. Pitaevskii and S. Stringari, *Bose-Einstein Condensation* (Oxford University Press, 2003). 20

[101] N. G. Parker, *Numerical studies of vortices and dark solitons in atomic Bose-Einstein condensates*, PhD thesis, Durham University, 2004. 20

[102] T. P. Billam, *Bright solitary waves and non-equilibrium dynamics in atomic Bose-Einstein condensates*, PhD thesis, Durham University, 2012. 20, 21

[103] T. P. Billam, A. L. Marchant, S. L. Cornish, S. A. Gardiner, and N. G. Parker, *Bright solitary matter waves: formation, stability and interactions*, ArXiv e-prints (2012), 1209.0560. 24, 27, 48

[104] J. P. Gordon, *Interaction forces among solitons in optical fibers*, Opt. Lett. **8**, 596 (1983). 24, 39, 41, 48

[105] U. Al Khawaja, *Stability and dynamics of two-soliton molecules*, Phys. Rev. E **81**, 056603 (2010). 24, 39, 41, 48

[106] W. Li, *Directly determining the relative phase of two coherent solitary waves in attractive Bose-Einstein condensates*, ArXiv e-prints (2008), 0805.0260. 24

[107] U. Al Khawaja, H. T. Stoof, R. G. Hulet, K. E. Strecker, and G. B. Partridge, *Bright Soliton Trains of Trapped Bose-Einstein Condensates*, Phys. Rev. Lett. **89**, 200404 (2002). 24, 48

[108] L. Salasnich, A. Parola, and L. Reatto, *Modulational Instability and Complex Dynamics of Confined Matter-Wave Solitons*, Phys. Rev. Lett. **91**, 080405 (2003). 24, 48

[109] N. G. Parker, S. L. Cornish, C. S. Adams, and A. M. Martin, *Bright solitary waves and trapped solutions in Bose Einstein condensates with attractive interactions*, J. Phys. B: At. Mol. Opt. Phys. **40**, 3127 (2007). 24

[110] N. G. Parker, A. M. Martin, C. S. Adams, and S. L. Cornish, *Bright solitary waves of trapped atomic Bose-Einstein condensates*, Physica D **238**, 1456 (2009). 24, 48

[111] I. Morison, *Introduction to Astronomy and Cosmology* (Wiley, 2008). 25

[112] A. Eleftheriou and K. Huang, *Instability of a Bose-Einstein condensate with an attractive interaction*, Phys. Rev. A **61**, 043601 (2000). 26, 48

[113] P. A. Ruprecht, M. J. Holland, K. Burnett, and M. Edwards, *Time-dependent solution of the nonlinear Schrödinger equation for Bose-condensed trapped neutral atoms*, Phys. Rev. A **51**, 4704 (1995). 26

[114] A. Gammal, T. Frederico, and L. Tomio, *Critical number of atoms for attractive Bose-Einstein condensates with cylindrically symmetrical traps*, Phys. Rev. A **64**, 055602 (2001). 26, 48

[115] N. R. Claussen *et al.*, *Very-high-precision bound-state spectroscopy near a ^{85}Rb Feshbach resonance*, Phys. Rev. A **67**, 060701 (2003). 26, 134, 143

[116] P. A. Altin *et al.*, *Collapse and three-body loss in a ^{85}Rb Bose-Einstein condensate*, Phys. Rev. A **84**, 033632 (2011). 27, 48, 137, 139, 154

[117] I. E. Mazets and G. Kurizki, *How different are multiatom quantum solitons from mean-field solitons?*, Europhys. Lett. **76**, 196 (2006). 28, 44

[118] P. Calabrese and J.-S. Caux, *Dynamics of the attractive 1D Bose gas: analytical treatment from integrability*, J. Stat. Mech. Theor. Exp. **8**, 32 (2007). 28

[119] B. J. Dabrowska-Wüster, S. Wüster, and M. J. Davis, *Dynamical formation and interaction of bright solitary waves and solitons in the collapse of Bose-Einstein condensates with attractive interactions*, New J. Phys. **11**, 053017 (2009). 39, 40

[120] M. Lewenstein and B. A. Malomed, *Entanglement generation by collisions of quantum solitons in the Born approximation*, New J. Phys. **11**, 113014 (2009). 37, 38, 48

[121] A. I. Streltsov, O. E. Alon, and L. S. Cederbaum, *Scattering of an attractive Bose-Einstein condensate from a barrier: Formation of quantum superposition states*, Phys. Rev. A **80**, 043616 (2009). 37

[122] C. Weiss and Y. Castin, *Creation and Detection of a Mesoscopic Gas in a Nonlocal Quantum Superposition*, Phys. Rev. Lett. **102**, 010403 (2009). 28, 37, 38, 48

[123] G. Mazzarella, L. Salasnich, A. Parola, and F. Toigo, *Coherence and entanglement in the ground state of a bosonic Josephson junction: From macroscopic Schrödinger cat states to separable Fock states*, Phys. Rev. A **83**, 053607 (2011). 37

[124] A. I. Streltsov, O. E. Alon, and L. S. Cederbaum, *Swift Loss of Coherence of Soliton Trains in Attractive Bose-Einstein Condensates*, Phys. Rev. Lett. **106**, 240401 (2011). 39, 40

[125] J. A. Glick and L. D. Carr, *Macroscopic Quantum Tunneling of Solitons in Bose-Einstein Condensates*, ArXiv e-prints (2011), 1105.5164. 37

[126] A. D. Martin and J. Ruostekoski, *Quantum dynamics of atomic bright solitons under splitting and recollision, and implications for interferometry*, New J. Phys. **14**, 043040 (2012). 33, 34, 35, 48

[127] B. Gertjerenken, T. P. Billam, L. Khaykovich, and C. Weiss, *Scattering bright solitons: Quantum versus mean-field behavior*, Phys. Rev. A **86**, 033608 (2012). 28, 29, 30, 31, 38, 44, 45, 48

[128] D. I. H. Holdaway, C. Weiss, and S. A. Gardiner, *Quantum theory of bright matter-wave solitons in harmonic confinement*, Phys. Rev. A **85**, 053618 (2012). 28, 29, 44, 45, 48

[129] E. H. Lieb and W. Liniger, *Exact Analysis of an Interacting Bose Gas. I. The General Solution and the Ground State*, Phys. Rev. **130**, 1605 (1963). 28

[130] J. B. McGuire, *Study of Exactly Soluble One-Dimensional N-Body Problems*, J. Math. Phys. **5**, 622 (1964). 28

[131] C. Lee and J. Brand, *Enhanced quantum reflection of matter-wave solitons*, Europhys. Lett. **73**, 321 (2006). 30, 31, 48

[132] B. Gertjerenken *et al.*, *Entangling two distinguishable matter-wave bright solitons via collisions*, ArXiv e-prints (2013), 1301.0718. 30, 37, 38, 48

[133] M. I. Rodas-Verde, H. Michinel, and V. M. Pérez-García, *Controllable Soliton Emission from a Bose-Einstein Condensate*, Phys. Rev. Lett. **95**, 153903 (2005). 30, 35, 48

[134] L. D. Carr and J. Brand, *Pulsed atomic soliton laser*, Phys. Rev. A **70**, 033607 (2004). 31, 48

[135] H. Michinel, A. Paredes, M. M. Valado, and D. Feijoo, *Coherent emission of atomic soliton pairs by Feshbach-resonance tuning*, Phys. Rev. A **86**, 013620 (2012). 31, 33, 35, 48

[136] J. Cuevas, P. G. Kevrekidis, B. A. Malomed, P. Dyke, and R. G. Hulet, *Interactions of solitons with a Gaussian barrier: Splitting and recombination in quasi-1D and 3D*, ArXiv e-prints (2013), 1301.3959. 32, 33, 35, 42, 48

[137] H. Saito and M. Ueda, *Dynamically Stabilized Bright Solitons in a Two-Dimensional Bose-Einstein Condensate*, Phys. Rev. Lett. **90**, 040403 (2003). 32

[138] F. K. Abdullaev, J. G. Caputo, R. A. Kraenkel, and B. A. Malomed, *Controlling collapse in Bose-Einstein condensates by temporal modulation of the scattering length*, Phys. Rev. A **67**, 013605 (2003).

[139] S. K. Adhikari, *Stabilization of bright solitons and vortex solitons in a trapless three-dimensional Bose-Einstein condensate by temporal modulation of the scattering length*, Phys. Rev. A **69**, 063613 (2004).

[140] G. D. Montesinos, V. M. Pérez-García, and P. J. Torres, *Stabilization of solitons of the multidimensional nonlinear Schrödinger equation: matter-wave breathers*, Physica D **191**, 193 (2004).

[141] A. Itin, T. Morishita, and S. Watanabe, *Reexamination of dynamical stabilization of matter-wave solitons*, Phys. Rev. A **74**, 033613 (2006). 32

[142] V. V. Konotop and P. Pacciani, *Collapse of Solutions of the Nonlinear Schrödinger Equation with a Time-Dependent Nonlinearity: Application to Bose-Einstein Condensates*, Phys. Rev. Lett. **94**, 240405 (2005). 32

[143] L. S. Cederbaum, A. I. Streltsov, and O. E. Alon, *Fragmented Metastable States Exist in an Attractive Bose-Einstein Condensate for Atom Numbers Well above the Critical Number of the Gross-Pitaevskii Theory*, Phys. Rev. Lett. **100**, 040402 (2008). 32

[144] N. A. Jamaludin, N. G. Parker, and A. M. Martin, *Bright solitary waves of atomic Bose-Einstein condensates under rotation*, Phys. Rev. A **77**, 051603 (2008). 32

[145] N. A. Jamaludin, N. G. Parker, and A. M. Martin, *Erratum: Bright solitary waves of atomic Bose-Einstein condensates under rotation [Phys. Rev. A 77, 051603(R) (2008)]*, Phys. Rev. A **83**, 059910 (2011). 32

[146] M. C. Tsatsos, *Attractive Bose-Einstein condensates in three dimensions under rotation: Revisiting the problem of stability of the ground state in harmonic traps*, Phys. Rev. A **83**, 063615 (2011). 32

[147] D. Farias and K.-H. Rieder, *Atomic beam diffraction from solid surfaces*, Rep. Prog. Phys. **61**, 1575 (1998). 33

[148] A. D. Cronin, J. Schmiedmayer, and D. E. Pritchard, *Optics and interferometry with atoms and molecules*, Rev. Mod. Phys. **81**, 1051 (2009). 33

[149] C. S. Adams, M. Sigel, and J. Mlynek, *Atom optics*, Phys. Rep. **240**, 143 (1994). 33

[150] Y. Castin and J. Dalibard, *Relative phase of two Bose-Einstein condensates*, Phys. Rev. A **55**, 4330 (1997). 33

[151] Y. Shin *et al.*, *Atom Interferometry with Bose-Einstein Condensates in a Double-Well Potential*, Phys. Rev. Lett. **92**, 050405 (2004). 33

[152] T. Schumm *et al.*, *Matter-wave interferometry in a double well on an atom chip*, Nat. Phys. **1**, 57 (2005).

[153] Y.-J. Wang *et al.*, *Atom Michelson Interferometer on a Chip Using a Bose-Einstein Condensate*, Phys. Rev. Lett. **94**, 090405 (2005). 33

[154] M. Fattori *et al.*, *Atom Interferometry with a Weakly Interacting Bose-Einstein Condensate*, Phys. Rev. Lett. **100**, 080405 (2008). 33

[155] C. Gross, T. Zibold, E. Nicklas, J. Estève, and M. K. Oberthaler, *Nonlinear atom interferometer surpasses classical precision limit*, Nature (London) **464**, 1165 (2010). 33

[156] S. E. Pollack, D. Dries, E. J. Olson, and R. G. Hulet, *Quantum Tunneling of a Macroscopic Matter-wave Soliton*, in *APS Division of Atomic, Molecular and Optical Physics Meeting Abstracts*, p. 4001, 2010. 33, 34, 35, 42

[157] T. Ernst and J. Brand, *Resonant trapping in the transport of a matter-wave soliton through a quantum well*, Phys. Rev. A **81**, 033614 (2010). 33, 36, 48

[158] S. Damgaard Hansen, N. Nygaard, and K. Mølmer, *Scattering of matter wave solitons on localized potentials*, ArXiv e-prints (2012), 1210.1681. 33, 48

[159] C. Weiss and Y. Castin, *Elastic scattering of a quantum matter-wave bright soliton on a barrier*, J. Phys. A: Math. Theor. **45**, 455306 (2012). 33

[160] T. P. Billam, S. L. Cornish, and S. A. Gardiner, *Realizing bright-matter-wave-soliton collisions with controlled relative phase*, Phys, Rev. A **83**, 041602 (2011). 33, 34, 48

[161] J. L. Helm, T. P. Billam, and S. A. Gardiner, *Bright matter-wave soliton collisions at narrow barriers*, Phys. Rev. A **85**, 053621 (2012). 34, 48

[162] J. Holmer, J. Marzuola, and M. Zworski, *Fast Soliton Scattering by Delta Impurities*, Comm. Math. Phys. **274**, 187 (2007). 34

[163] L. D. Carr and J. Brand, *Spontaneous Soliton Formation and Modulational Instability in Bose-Einstein Condensates*, Phys. Rev. Lett. **92**, 040401 (2004). 35, 48

[164] B. H. Bransden and C. J. Joachain, *Quantum Mechanics* (Pearson, 2000). 36

[165] S. M. Al-Marzoug, S. M. Al-Amoudi, U. Al Khawaja, H. Bahlouli, and B. B. Baizakov, *Scattering of a matter-wave single soliton and a two-soliton molecule by an attractive potential*, Phys. Rev. E **83**, 026603 (2011). 36, 39, 41, 48

[166] J. Lekner, *Reflectionless eigenstates of the sech^2 potential*, Am. J. Phys. **75**, 1151 (2007). 36, 41

[167] P. Zoller *et al.*, *Quantum information processing and communication. Strategic report on current status, visions and goals for research in Europe*, Eur. Phys. J. D **36**, 203 (2005). 36

[168] N. Gisin, G. Ribordy, W. Tittel, and H. Zbinden, *Quantum cryptography*, Rev. Mod. Phys. **74**, 145 (2002). 36

[169] P. W. Shor, *Polynomial-Time Algorithms for Prime Factorization and Discrete Logarithms on a Quantum Computer*, SIAM J. Comp. **26**, 1484 (1996). 36

[170] L. K. Grover, *A fast quantum mechanical algorithm for database search*, in *Proceedings of the twenty-eighth annual ACM symposium on Theory of computing*, STOC '96, pp. 212–219, New York, NY, USA, 1996, ACM. 36

[171] R. P. Feynman, *Simulating Physics with Computers*, Int. J. Theor. Phys. **21**, 467 (1982). 37

[172] M. Arndt *et al.*, *Wave-particle duality of C_{60} molecules*, Nature (London) **401**, 680 (1999). 37

[173] J. R. Friedman, V. Patel, W. Chen, S. K. Tolpygo, and J. E. Lukens, *Quantum superposition of distinct macroscopic states*, Nature (London) **406**, 43 (2000).

[174] O. Nairz, M. Arndt, and A. Zeilinger, *Quantum interference experiments with large molecules*, Am. J. Phys. **71**, 319 (2003).

[175] O. Nairz, M. Arndt, and A. Zeilinger, *Erratum: "Quantum interference experiments with large molecules" [Am. J. Phys. 71 (4), 319-325 (2003)]*, Am. J. Phys. **71**, 1084 (2003).

[176] O. Romero-Isart, M. L. Juan, R. Quidant, and J. I. Cirac, *Toward quantum superposition of living organisms*, New J. Phys. **12**, 033015 (2010).

[177] S. Gerlich *et al.*, *Quantum interference of large organic molecules*, Nat. Commun. **2** (2011). 37

[178] J.-W. Pan, D. Bouwmeester, M. Daniell, H. Weinfurter, and A. Zeilinger, *Experimental test of quantum nonlocality in three-photon Greenberger-Horne-Zeilinger entanglement*, Nature (London) **403**, 515 (2000). 37

[179] J. M. Raimond, M. Brune, and S. Haroche, *Manipulating quantum entanglement with atoms and photons in a cavity*, Rev. Mod. Phys. **73**, 565 (2001).

[180] M. Aspelmeyer *et al.*, *Long-Distance Free-Space Distribution of Quantum Entanglement*, Science **301**, 621 (2003).

[181] C.-Z. Peng *et al.*, *Experimental Free-Space Distribution of Entangled Photon Pairs Over 13 km: Towards Satellite-Based Global Quantum Communication*, Phys. Rev. Lett. **94**, 150501 (2005).

[182] P. Neumann *et al.*, *Multipartite Entanglement Among Single Spins in Diamond*, Science **320**, 1326 (2008).

[183] K. C. Lee *et al.*, *Entangling Macroscopic Diamonds at Room Temperature*, Science **334**, 1253 (2011).

[184] J. Yin *et al.*, *Quantum teleportation and entanglement distribution over 100-kilometre free-space channels*, Nature (London) **488**, 185 (2012).

[185] J. Hofmann *et al.*, *Heralded Entanglement Between Widely Separated Atoms*, Science **337**, 72 (2012). 37

[186] A. I. Streltsov, O. E. Alon, and L. S. Cederbaum, *FAST TRACK COMMUNICATION: Efficient generation and properties of mesoscopic quantum superposition states in an attractive Bose-Einstein condensate threaded by a potential barrier*, J. Phys. B: At. Mol. Opt. Phys. **42**, 091004 (2009). 37, 48

[187] A. B. Tacla and C. M. Caves, *Entanglement-based perturbation theory for highly anisotropic Bose-Einstein condensates*, Phys. Rev. A **84**, 053606 (2011).

[188] B. Gertjerenken and C. Weiss, *Nonlocal quantum superpositions of bright matter-wave solitons and dimers*, J. Phys. B: At. Mol. Opt. Phys. **45**, 165301 (2012). 37, 38, 48

[189] C. Gross, J. Estève, M. K. Oberthaler, A. D. Martin, and J. Ruostekoski, *Local and spatially extended sub-Poisson atom-number fluctuations in optical lattices*, Phys. Rev. A **84**, 011609 (2011). 38

[190] A. I. Streltsov, O. E. Alon, and L. S. Cederbaum, *Formation and Dynamics of Many-Boson Fragmented States in One-Dimensional Attractive Ultracold Gases*, Phys. Rev. Lett. **100**, 130401 (2008). 39

[191] U. A. Khawaja, S. M. Al-Marzoug, and H. Bahlouli, *Spontaneous formation and resonant scattering of soliton molecules*, J. Phys. B: At. Mol. Opt. Phys. **44**, 115304 (2011). 39, 41, 48

[192] U. A. Khawaja and H. T. C. Stoof, *Formation of matter-wave soliton molecules*, New J. Phys. **13**, 085003 (2011). 41, 42, 48

[193] U. Al Khawaja and A. Boudjemâa, *Binding energy of soliton molecules in time-dependent harmonic potential and nonlinear interaction*, Phys. Rev. E **86**, 036606 (2012). 41

[194] K. Łakomy, R. Nath, and L. Santos, *Soliton molecules in dipolar Bose-Einstein condensates*, Phys. Rev. A **86**, 013610 (2012).

[195] U. Al Khawaja, *Interaction forces among two-dimensional bright solitons and many-soliton molecules*, Phys. Rev. E **85**, 056604 (2012). 39

[196] M. Stratmann, T. Pagel, and F. Mitschke, *Experimental Observation of Temporal Soliton Molecules*, Phys. Rev. Lett. **95**, 143902 (2005). 41

[197] L. D. Landau and E. M. Lifschitz, *Lehrbuch der Theoretischen Physik: Band III Quantenmechanik* (Berlin: Akademie-Verlag, 1966). 41

[198] P. M. Morse, *Diatomic Molecules According to the Wave Mechanics. II. Vibrational Levels*, Phys. Rev. **34**, 57 (1929). 42

[199] M. C. Tsatsos, A. I. Streltsov, O. E. Alon, and L. S. Cederbaum, *Fragmented many-body states of definite angular momentum and stability of attractive three-dimensional condensates*, Phys. Rev. A **82**, 033613 (2010). 42, 48

[200] J. Abdullaev, A. S. Desyatnikov, and E. A. Ostrovskaya, *Suppression of collapse for matter waves with orbital angular momentum*, J. Opt. **13**, 064023 (2011). 42

[201] N. G. Parker and D. A. Smith, *p-wave stabilization of three-dimensional Bose-Fermi solitons*, Phys. Rev. A **85**, 013604 (2012). 42, 43, 48

[202] T. P. Billam, S. A. Wrathmall, and S. A. Gardiner, *Variational determination of approximate bright matter-wave soliton solutions in anisotropic traps*, Phys. Rev. A **85**, 013627 (2012). 44, 48, 64

[203] R. G. Scott, A. M. Martin, T. M. Fromhold, and F. W. Sheard, *Anomalous Quantum Reflection of Bose-Einstein Condensates from a Silicon Surface: The Role of Dynamical Excitations*, Phys. Rev. Lett. **95**, 073201 (2005). 46

[204] R. Côté, B. Segev, and M. G. Raizen, *Retardation effects on quantum reflection from an evanescent-wave atomic mirror*, Phys. Rev. A **58**, 3999 (1998). 46, 48

[205] P. Schneeweiss *et al.*, *Dispersion forces between ultracold atoms and a carbon nanotube*, Nat. Nano. **7**, 515 (2012). 46

[206] C. Stehle, H. Bender, F. Jessen, C. Zimmermann, and S. Slama, *Ad- and desorption of Rb atoms on a gold nanofilm measured by surface plasmon polaritons*, New J. Phys. **12**, 083066 (2010). 46

[207] R. Grimm, M. Weidemüller, and Y. B. Ovchinnikov, *Optical Dipole Traps for Neutral Atoms*, Adv. At. Mol. Opt. Phys. **42**, 95 (2000). 47, 48, 75, 138, 177

[208] T. E. Judd, R. G. Scott, A. M. Martin, B. Kaczmarek, and T. M. Fromhold, *Quantum reflection of ultracold atoms from thin films, graphene and semiconductor heterostructures*, New J. Phys. **13**, 083020 (2011). 47, 48

[209] D. J. McCarron, S. A. King, and S. L. Cornish, *Modulation transfer spectroscopy in atomic rubidium*, Meas. Sci. Technol. **19**, 105601 (2008). 70

[210] G. C. Bjorklund, *Frequency-modulation spectroscopy: a new method for measuring weak absorptions and dispersions*, Opt. Lett. **5**, 15 (1980). 70

[211] C. J. Foot, *Atomic Physics* (Oxford University Press, 2005). 72

[212] W. Petrich, M. H. Anderson, J. R. Ensher, and E. A. Cornell, *Behavior of atoms in a compressed magneto-optical trap*, J. Opt. Soc. Am. B **11**, 1332 (1994). 72

[213] D. A. Steck, *Rubidium 85 D line data (revision 2.1.5)*, Accessed: 5 March 2013, URL: `http://steck.us/alkalidata/`. 73, 77

[214] Y. Lin, A. R. Perry, R. L. Compton, I. B. Spielman, and J. V. Porto, *Rapid production of* ^{87}Rb *Bose-Einstein condensates in a combined magnetic and optical potential*, Phys. Rev. A **79**, 063631 (2009). 75, 138

[215] I. Bloch, M. Greiner, O. Mandel, T. W. Hänsch, and T. Esslinger, *Sympathetic cooling of* ^{85}Rb *and* ^{87}Rb, Phys. Rev. A **64**, 021402 (2001). 75, 113, 139

[216] S. B. Papp and C. E. Wieman, *Observation of Heteronuclear Feshbach Molecules from a* ^{85}Rb–^{87}Rb *Gas*, Phys. Rev. Lett. **97**, 180404 (2006). 75, 113, 129, 139

[217] P. A. Altin *et al.*, ^{85}Rb *tunable-interaction Bose-Einstein condensate machine*, Rev. Sci. Instrum. **81**, 063103 (2010). 75, 113, 129, 139

[218] J. L. Roberts, *Bose-Einstein condensates with tunable atom-atom interactions: the first experiments with* ^{85}Rb *BECs*, PhD thesis, University of Colorado, 2001. 76, 77, 78, 136, 137, 174

[219] M. L. Harris, *Realisation of a cold mixture of rubidium and caesium*, PhD thesis, University of Durham, 2008. 76, 77, 78, 103

[220] S. Friebel, C. D'Andrea, J. Walz, M. Weitz, and T. W. Hänsch, CO_2-*laser optical lattice with cold rubidium atoms*, Phys. Rev. A **57**, R20 (1998). 81

[221] National Instruments, *NI PXI-7811R - R Series Digital RIO with Virtex-II 1M Gate FPGA*, Accessed: 10 January 2013, URL: http://sine.ni.com/nips/cds/view/p/lang/en/nid/13862. 83

[222] National Instruments, *NI 6533/6534 Specifications*, Accessed: 11 January 2013, URL: http://digital.ni.com/manuals.nsf/websearch/1F45100BE5806B73862570AD0058A942. 86

[223] National Instruments, *NI PCI-6713 12-Bit, 1 MS/s per Channel Analog Output Board*, Accessed: 11 January 2013, URL: http://sine.ni.com/nips/cds/view/p/lang/en/nid/10702. 86

[224] M. Gildemeister, *Private communication*, September/October 2009. 88

[225] K. Golshan, *Physical design essentials: an ASIC design implementation perspective* (Springer Science+Business Media, 2007). 88

[226] Xilinx, *Xilinx Co-Founder Ross Freeman Honored as 2009 National Inventors Hall of Fame Inductee for Invention of FPGA*, Accessed: 11 January 2013, URL: http://press.xilinx.com/phoenix.zhtml?c=212763&p=irol-newsArticle&ID=1255523&highlight. 89

[227] EE Times, *New Xilinx Virtex-7 2000T FPGA provides equivalent of 20 million ASIC gates*, Accessed: 11 January 2013, URL: http://www.eetimes.com/electronics-products/electronic-product-reviews/fpga-pld-products/4230049/New-Xilinx-Virtex-7-2000T-FPGA-provides-equivalent-of-20-million-ASIC-gates. 89

[228] National Instruments, *Using Single-Cycle Timed Loops to Optimize FPGA VIs (FPGA Module)*, Accessed: 10 January 2013, URL: http://zone.ni.com/reference/en-XX/help/371599B-01/lvfpgaconcepts/using_sctl_optimize_fpga/. 90

[229] National Instruments, *Single-Cycle Timed Loop FAQ for the LabVIEW FPGA Module*, Accessed: 10 January 2013, URL: http://digital.ni.com/public.nsf/allkb/722A9451AE4E23A586257212007DC5FD. 89

[230] National Instruments, *NI 9151 R Series Expansion Chassis for C Series I/O*, Accessed: 14 January 2013, URL: http://sine.ni.com/nips/cds/view/p/lang/en/nid/14163. 95

[231] National Instruments, *CompactRIO I/O Modules*, Accessed: 14 January 2013, URL: http://sine.ni.com/nips/cds/view/p/lang/en/nid/14147. 95

[232] National Instruments, *NI 9403 C Series 32-Ch, 5 V/TTL Bidirectional Digital I/O Module*, Accessed: 14 January 2013, URL: http://sine.ni.com/nips/cds/view/p/lang/en/nid/203490. 95

[233] National Instruments, *NI 9264 16-Channel Analog Output Module*, Accessed: 14 January 2013, URL: http://sine.ni.com/nips/cds/view/p/lang/en/nid/203424. 95

[234] National Instruments, *Community Nugget 4/08/2007 Action Engines*, Accessed: 15 January 2013, URL: http://forums.ni.com/t5/LabVIEW/Community-Nugget-4-08-2007-Action-Engines/m-p/503801. 98

[235] MathWorks, *Creating a GUI with GUIDE*, Accessed: 8 March 2013, URL: http://www.mathworks.co.uk/videos/creating-a-gui-with-guide-68979.html. 103

[236] I. G. Hughes, *Private communication*, Spring 2010. 108

[237] A. Arnold, *Preparation and Manipulation of an* ^{87}Rb *Bose-Einstein Condensate*, PhD thesis, University of Sussex, 1999. 108

[238] I. G. Hughes and T. P. A. Hase, *Measurements and their Uncertainties: A Practical Guide to Modern Error Analysis* (Oxford University Press, 2010). 110

[239] C. J. Myatt, E. A. Burt, R. W. Ghrist, E. A. Cornell, and C. E. Wieman, *Production of Two Overlapping Bose-Einstein Condensates by Sympathetic Cooling*, Phys. Rev. Lett. **78**, 586 (1997). 113

[240] J. Stenger *et al.*, *Spin domains in ground-state Bose-Einstein condensates*, Nature (London) **396**, 345 (1998).

[241] A. G. Truscott, K. E. Strecker, W. I. McAlexander, G. B. Partridge, and R. G. Hulet, *Observation of Fermi Pressure in a Gas of Trapped Atoms*, Science **291**, 2570 (2001).

[242] Z. Hadzibabic *et al.*, *Two-Species Mixture of Quantum Degenerate Bose and Fermi Gases*, Phys. Rev. Lett. **88**, 160401 (2002). 131

[243] G. Roati, F. Riboli, G. Modugno, and M. Inguscio, *Fermi-Bose Quantum Degenerate* ^{40}K-^{87}Rb *Mixture with Attractive Interaction*, Phys. Rev. Lett. **89**, 150403 (2002).

[244] G. Modugno, M. Modugno, F. Riboli, G. Roati, and M. Inguscio, *Two Atomic Species Superfluid*, Phys. Rev. Lett. **89**, 190404 (2002).

[245] C. Silber *et al.*, *Quantum-Degenerate Mixture of Fermionic Lithium and Bosonic Rubidium Gases*, Phys. Rev. Lett. **95**, 170408 (2005).

[246] M. Zaccanti *et al.*, *Control of the interaction in a Fermi-Bose mixture*, Phys. Rev. A **74**, 041605 (2006).

[247] S. Ospelkaus *et al.*, *Localization of Bosonic Atoms by Fermionic Impurities in a Three-Dimensional Optical Lattice*, Phys. Rev. Lett. **96**, 180403 (2006).

[248] S. B. Papp, J. M. Pino, and C. E. Wieman, *Tunable Miscibility in a Dual-Species Bose-Einstein Condensate*, Phys. Rev. Lett. **101**, 040402 (2008). 113, 139

[249] M. Taglieber, A.-C. Voigt, T. Aoki, T. W. Hänsch, and K. Dieckmann, *Quantum Degenerate Two-Species Fermi-Fermi Mixture Coexisting with a Bose-Einstein Condensate*, Phys. Rev. Lett. **100**, 010401 (2008).

[250] M. K. Tey, S. Stellmer, R. Grimm, and F. Schreck, *Double-degenerate Bose-Fermi mixture of strontium*, Phys. Rev. A **82**, 011608 (2010). 113

[251] M. Trippenbach, K. Góral, K. Rzazewski, B. Malomed, and Y. B. Band, *Structure of binary Bose-Einstein condensates*, J. Phys. B: At. Mol. Opt. Phys. **33**, 4017 (2000). 113

[252] E. Altman, W. Hofstetter, E. Demler, and M. D. Lukin, *Phase diagram of two-component bosons on an optical lattice*, New J. Phys. **5**, 113 (2003).

[253] A. Kuklov, N. Prokof'ev, and B. Svistunov, *Commensurate Two-Component Bosons in an Optical Lattice: Ground State Phase Diagram*, Phys. Rev. Lett. **92**, 050402 (2004).

[254] A. Micheli, G. K. Brennen, and P. Zoller, *A toolbox for lattice-spin models with polar molecules*, Nat. Phys. **2**, 341 (2006).

[255] D. DeMille, *Quantum Computation with Trapped Polar Molecules*, Phys. Rev. Lett. **88**, 067901 (2002).

[256] S. Giorgini, L. P. Pitaevskii, and S. Stringari, *Theory of ultracold atomic Fermi gases*, Rev. Mod. Phys. **80**, 1215 (2008). 113

[257] L. D. Carr, D. DeMille, R. V. Krems, and J. Ye, *Cold and ultracold molecules: science, technology and applications*, New J. Phys. **11**, 055049 (2009). 113

[258] T. Köhler, K. Góral, and P. S. Julienne, *Production of cold molecules via magnetically tunable Feshbach resonances*, Rev. Mod. Phys. **78**, 1311 (2006). 113

[259] C. Chin, R. Grimm, P. Julienne, and E. Tiesinga, *Feshbach resonances in ultracold gases*, Rev. Mod. Phys. **82**, 1225 (2010). 113, 143

[260] K. M. Jones, E. Tiesinga, P. D. Lett, and P. S. Julienne, *Ultracold photoassociation spectroscopy: Long-range molecules and atomic scattering*, Rev. Mod. Phys. **78**, 483 (2006). 113

[261] J. M. Sage, S. Sainis, T. Bergeman, and D. DeMille, *Optical Production of Ultracold Polar Molecules*, Phys. Rev. Lett. **94**, 203001 (2005). 113

[262] J. G. Danzl *et al.*, *Quantum Gas of Deeply Bound Ground State Molecules*, Science **321**, 1062 (2008).

[263] F. Lang, K. Winkler, C. Strauss, R. Grimm, and J. H. Denschlag, *Ultracold Triplet Molecules in the Rovibrational Ground State*, Phys. Rev. Lett. **101**, 133005 (2008).

[264] K.-K. Ni *et al.*, *A High Phase-Space-Density Gas of Polar Molecules*, Science **322**, 231 (2008).

[265] M. Viteau *et al.*, *Optical Pumping and Vibrational Cooling of Molecules*, Science **321**, 232 (2008).

[266] J. Deiglmayr *et al.*, *Formation of Ultracold Polar Molecules in the Rovibrational Ground State*, Phys. Rev. Lett. **101**, 133004 (2008). 113

[267] T. Lahaye, C. Menotti, L. Santos, M. Lewenstein, and T. Pfau, *The physics of dipolar bosonic quantum gases*, Rep. Prog. Phys. **72**, 126401 (2009). 113

[268] G. Thalhammer *et al.*, *Double Species Bose-Einstein Condensate with Tunable Interspecies Interactions*, Phys. Rev. Lett. **100**, 210402 (2008). 113

[269] W. Ketterle and M. W. Zwierlein, *Making, probing and understanding ultracold Fermi gases*, Rivista Nuovo Cimento **31**, 247 (2008). 113

[270] J. Weiner, V. S. Bagnato, S. Zilio, and P. S. Julienne, *Experiments and theory in cold and ultracold collisions*, Rev. Mod. Phys. **71**, 1 (1999). 113, 131

[271] M. L. Harris, P. Tierney, and S. L. Cornish, *Magnetic trapping of a cold* Rb–Cs *atomic mixture*, J. Phys. B: At. Mol. Opt. Phys. **41**, 035303 (2008). 113, 131

[272] J. P. Burke, Jr., J. L. Bohn, B. D. Esry, and C. H. Greene, *Prospects for Mixed-Isotope Bose-Einstein Condensates in Rubidium*, Phys. Rev. Lett. **80**, 2097 (1998). 113, 136

[273] J. F. Bertelsen, H. K. Andersen, S. Mai, and M. Budde, *Mixing of ultracold atomic clouds by merging of two magnetic traps*, Phys. Rev. A **75**, 013404 (2007). 114

[274] M. Greiner, I. Bloch, T. W. Hänsch, and T. Esslinger, *Magnetic transport of trapped cold atoms over a large distance*, Phys. Rev. A **63**, 031401 (2001). 114, 120

[275] H. J. Lewandowski, D. M. Harber, D. L. Whitaker, and E. A. Cornell, *Simplified System for Creating a Bose-Einstein Condensate*, J. Low Temp. Phys. **132**, 309 (2003). 114

[276] A. L. Migdall, W. D. Phillips, J. V. Prodan, T. H. Bergeman, and H. J. Metcalf, *First observation of magnetically trapped neutral atoms*, Phys. Rev. Lett. **54**, 2596 (1985). 116

[277] W. Hänsel, J. Reichel, P. Hommelhoff, and T. W. Hänsch, *Magnetic Conveyor Belt for Transporting and Merging Trapped Atom Clouds*, Phys. Rev. Lett. **86**, 608 (2001). 120

[278] J. L. Roberts *et al.*, *Resonant Magnetic Field Control of Elastic Scattering in Cold* ^{85}Rb, Phys. Rev. Lett. **81**, 5109 (1998). 134

[279] T. Volz, S. Dürr, S. Ernst, A. Marte, and G. Rempe, *Characterization of elastic scattering near a Feshbach resonance in* ^{87}Rb, Phys. Rev. A **68**, 010702 (2003). 134

[280] W. Ketterle, D. S. Durfee, and D. M. Stamper-Kurn, *Making, probing and understanding Bose-Einstein condensates*, arXiv:cond-mat/9904034 (1999). 134

[281] T. Guénault, *Statistical Physics* (Chapman & Hall, 1995). 134

[282] J. P. Burke, *Theoretical investigation of cold alkali atom collisions*, PhD thesis, University of Colorado, 1999. 135

[283] P. O. Fedichev, M. W. Reynolds, and G. V. Shlyapnikov, *Three-Body Recombination of Ultracold Atoms to a Weakly Bound s Level*, Phys. Rev. Lett. **77**, 2921 (1996). 137

[284] B. D. Esry, C. H. Greene, and J. P. Burke, *Recombination of Three Atoms in the Ultracold Limit*, Phys. Rev. Lett. **83**, 1751 (1999).

[285] P. F. Bedaque, E. Braaten, and H.-W. Hammer, *Three-body Recombination in Bose Gases with Large Scattering Length*, Phys. Rev. Lett. **85**, 908 (2000). 137

[286] E. A. Burt *et al.*, *Coherence, Correlations, and Collisions: What One Learns about Bose-Einstein Condensates from Their Decay*, Phys. Rev. Lett. **79**, 337 (1997). 137

[287] W. Bao, D. Jaksch, and P. A. Markowich, *Three-dimensional simulation of jet formation in collapsing condensates*, J. Phys. B: At. Mol. Opt. Phys **37**, 329 (2004). 137

[288] S. K. Adhikari, *Mean-field model of jet formation in a collapsing Bose Einstein condensate*, J. Phys. B: At. Mol. Opt. Phys. **37**, 1185 (2004).

[289] A. J. Moerdijk, H. M. J. M. Boesten, and B. J. Verhaar, *Decay of trapped ultracold alkali atoms by recombination*, Phys. Rev. A **53**, 916 (1996). 137

[290] J. L. Roberts, N. R. Claussen, S. L. Cornish, and C. E. Wieman, *Magnetic Field Dependence of Ultracold Inelastic Collisions near a Feshbach Resonance*, Phys. Rev. Lett. **85**, 728 (2000). 137, 149, 150

[291] P. A. Altin *et al.*, *Measurement of inelastic losses in a sample of ultracold* ^{85}Rb, Phys. Rev. A **81**, 012713 (2010). 137

[292] R. V. E. Lovelace, C. Mehanian, T. J. Tommila, and D. M. Lee, *Magnetic confinement of a neutral gas*, Nature (London) **318**, 30 (1985). 139

[293] H. F. Hess, *Evaporative cooling of magnetically trapped and compressed spin-polarized hydrogen*, Phys. Rev. B **34**, 3476 (1986). 139

[294] S. B. Papp, *Experiments with a two-species Bose-Einstein condensate utilizing widely tunable interparticle interactions*, PhD thesis, University of Colorado, 2007. 139

[295] S. E. Pollack *et al.*, *Extreme Tunability of Interactions in a* ^{7}Li *Bose-Einstein Condensate*, Phys. Rev. Lett. **102**, 090402 (2009). 144

[296] T. Weber, J. Herbig, M. Mark, H.-C. Nägerl, and R. Grimm, *Three-Body Recombination at Large Scattering Lengths in an Ultracold Atomic Gas*, Phys. Rev. Lett. **91**, 123201 (2003). 150

[297] Coherent, *Mephisto family of lasers*, Accessed: 18 March 2013, URL: `http://www.coherent.com/products/?2062/Mephisto-Family-of-Lasers`. 155

[298] J. L. Helm, *Private communication*, November 2012. 167

[299] E. Hecht, *Optics (4th Edition)* (Addison Wesley, 2001). 176

[300] National Institute of Standards and Technology, *Persistent Lines of Neutral Rubidium (Rb I)*, Accessed: 24 March 2013, URL: `http://physics.nist.gov/PhysRefData/Handbook/Tables/rubidiumtable3.htm`. 177

[301] M. Antezza, L. P. Pitaevskii, and S. Stringari, *Effect of the Casimir-Polder force on the collective oscillations of a trapped Bose-Einstein condensate*, Phys. Rev. A **70**, 053619 (2004). 184, 185

[302] D. Bloch and M. Ducloy, *Atom-wall interaction*, volume 50 of *Advances In Atomic, Molecular, and Optical Physics*, pp. 91 – 154, Academic Press, 2005. 184

[303] H. B. G. Casimir and D. Polder, *The Influence of Retardation on the London-van der Waals Forces*, Phys. Rev. **73**, 360 (1948). 184

[304] J. F. Babb, *Long-range atom-surface interactions for cold atoms*, J. Phys. Conf. Ser. **19**, 1 (2005). 185

[305] Z.-C. Yan, A. Dalgarno, and J. F. Babb, *Long-range interactions of lithium atoms*, Phys. Rev. A **55**, 2882 (1997). 185, 186

[306] A. Derevianko, S. G. Porsev, and J. F. Babb, *Electric dipole polarizabilities at imaginary frequencies for hydrogen, the alkali-metal, alkaline-earth, and noble gas atoms*, At. Data. Nucl. Data Tables **96**, 323 (2010). 186

[307] M. Born and E. Wolf, *Principles of Optics* (Pergamon Press, 1959). 187, 190, 191

[308] W. Seifert *et al.*, *Reflection of metastable argon atoms from an evanescent wave*, Phys. Rev. A **49**, 3814 (1994). 188

[309] L. H. Malitson, *Interspecimen Comparison of the Refractive Index of Fused Silica*, J. Opt. Soc. Am. **55**, 1205 (1965). 188

[310] G. A. Brooker, *Modern Classical Optics* (Oxford University Press, 2002). 195, 196

[311] G. Woan, *The Cambridge Handbook of Physics Formulas* (Cambridge University Press, 2003). 196